Fiber-coupled nanophotonic devices for nonlinear optics and cavity QED

Thesis by

Paul Edward Barclay

In Partial Fulfillment of the Requirements

for the Degree of

Doctor of Philosophy

California Institute of Technology

Pasadena, California

2007

(Defended May 23, 2007)

In memory of Larry Barclay

Acknowledgments

Since my first visit to Caltech, Oskar Painter has been exceedingly generous with his time, energy, and insight. Oskar's enthusiasm for the work of his students, his curiosity, and his desire to deeply understand whatever he is working on has never ceased to be inspiring, and I feel fortunate to have learned so much about all aspects of research from him.

I have also been fortunate to interact with Hideo Mabuchi, with whom meetings always ended with fresh ideas and optimism. Hideo's combination of creativity and perspective is something I hope to be able to replicate.

In my experience, the greatest strength of Caltech is its students. In Kartik Srinivasan, with whom I have shared an office since arriving in Pasadena, one couldn't ask for a better colleague. Matthew Borselli never ceased being helpful. Thomas Johnson could always be counted on to do things precisely. Building up the lab with this trio was a great experience, and I'm sure that its future will be bright in the hands Raviv Perahia, Jessie Rosenberg, Chris Michael, and Matt Eichenfeld. In the atomic physics lab, I was lucky to work closely with Benjamin Lev. Ben always generously treated his hard work as if it were ours. With help from Michael Armen, John Stockton, Andrew Berglund, Kevin McHale, and everyone else in Mabuchi-lab, Joe Kerckhoff and I have had an exciting time catching up on Ben's considerable knowledge after he graduated, and I am grateful for Joe's dedication.

Two people from my time at the University of British Columbia have had a lasting influence. For two summers, Garry Clarke gave me the best job that I'm likely to ever have, and in the process convinced me to go to graduate school. Jeff Young showed me how much fun doing physics can be. I am ever thankful for their continued support and advice.

Away from school, Graeme Smith, the city of Los Angeles and its dedicated adventurers on two wheels; Jesse Jackson and Nicholas Bradley and the geography of North America; and other Canadian visitors have all kept me measurably distracted, which isn't surprising but is fortunate. Signe Bray could only have been a greater help to me if she had arrived

in Pasadena earlier.

My brother David has always been a great friend and source of ideas, almost all of them original. And of course my parents and grand parents have supported me tremendously. My mother has never ceased giving encouragement, and my father was a tremendous source of strength from whom I learned most of what I know.

Abstract

The sub-wavelength optical confinement and low optical loss of nanophotonic devices dramatically enhances the interaction between light and matter within these structures. When nanophotonic devices are combined with an efficient optical coupling channel, nonlinear optical behavior can be observed at low power levels in weakly-nonlinear materials. In a similar vein, when resonant atomic systems interact with nanophotonic devices, atom-photon coupling effects can be observed at a single quanta level. Crucially, the chip based nature of nanophotonics provides a scalable platform from which to study these effects.

This thesis addresses the use of nanophotonic devices in nonlinear and quantum optics, including device design, optical coupling, fabrication and testing, modeling, and integration with more complex systems. We present a fiber taper coupling technique that allows efficient power transfer from an optical fiber into a photonic crystal waveguide. Greater than 97% power transfer into a silicon photonic crystal waveguide is demonstrated. This optical channel is then connected to a high-Q ($> 4 \times 10^4$), ultra-small mode volume ($V < (\lambda/n)^3$) photonic crystal cavity, into which we couple $> 44\%$ of the photons input to a fiber. This permits the observation of optical bistability in silicon for sub-mW input powers at telecommunication wavelengths.

To port this technology to cavity QED experiments at near-visible wavelengths, we also study silicon nitride microdisk cavities at wavelengths near 852 nm, and observe resonances with $Q > 3 \times 10^6$ and $V < 15\ (\lambda/n)^3$. This Q/V ratio is sufficiently high to reach the strong coupling regime with cesium atoms. We then permanently align and mount a fiber taper within the near-field an array of microdisks, and integrate this device with an atom chip, creating an “atom-cavity chip” which can magnetically trap laser cooled atoms above the microcavity. Calculations of the microcavity single atom sensitivity as a function of Q/V are presented and compared with numerical simulations. Taking into account non-idealities, these cavities should allow detection of single laser cooled cesium atoms.

Contents

List of Figures

List of Tables

Glossary of acronyms

APD Avalanche photodiode.

cQED Cavity quantum electrodynamics.

CCD Charge coupled detector.

CW Continuous wave.

e-beam Electron beam.

FCA Free carrier absorption.

FCD Free carrier dispersion.

FDTD Finite difference time domain.

FEM Finite element method.

FEMLAB Finite element method software package distributed by Comsol.

FSR Free spectral range.

HD Heterodyne.

ICP-RIE Inductively coupled reactive ion etch.

MOT Magneto-optical trap.

LIAD Light induced atom desorption.

LPCVD Low pressure chemical vapor deposition.

SEM Scanning electron microscope.

SNR Signal to noise ratio.

SOI Silicon on insulator.

SPCM Single photon counting module.

TE Transverse electric.

TM Transverse magnetic.

TPA Two photon absorption.

NV Nitrogen vacancy.

PC Photonic crystal.

PCWG Photonic crystal waveguide.

PECVD Plasma enhanced chemical vapor deposition.

PMMA Polymethyl methacrylate.

RPM Revolutions per minute.

Q Quality factor.

QED Quantum electrodynamics.

UV Ultra-violet.

UHV Ultra high vacuum.

V Mode volume.

Publications

- P. E. Barclay, K. Srinivasan, M. Borselli, and O. Painter. Experimental demonstration of evanescent coupling from optical fibre tapers to photonic crystal waveguides. *IEE Elec. Lett.*, 39(11) 842–844, 2003.
- K. Srinivasan, P. E. Barclay, O. Painter, J. Chen, A. X. Cho, and C. Gmachl. Experimental demonstration of a high quality factor photonic crystal microcavity. *Appl. Phys. Lett.*, 83(10) 1915–1917, 2003.
- O. Painter, K. Srinivasan, and P. E. Barclay. Wannier-like equation for the resonant cavity modes of locally perturbed photonic crystals. *Phys. Rev. B*, 68(3) 035214, 2003.
- P. E. Barclay, K. Srinivasan, and O. Painter. Design of photonic crystal waveguides for evanescent coupling to optical fiber tapers and integration with high-Q cavities. *J. Opt. Soc. Am. B*, 20(11) 2274–2284, 2003.
- P. E. Barclay, K. Srinivasan, M. Borselli, and O. Painter. Efficient input and output optical fiber coupling to a photonic crystal waveguide. *Opt. Lett.*, 29(7) 697–699, 2004.
- B. Lev, K. Srinivasan, P. E. Barclay, O. Painter, and H. Mabuchi. Feasibility of detecting single atoms using photonic bandgap cavities. *Nanotechnology*, 15 S556–S561, 2004.
- S. A. Maier, P. E. Barclay, T. J. Johnson, M. D. Friedman, and O. Painter. Low-loss fiber accessible plasmon waveguide for planar energy guiding and sensing. *Appl. Phys. Lett.*, 84(20) 3990–3992, 2004.
- P. E. Barclay, K. Srinivasan, M. Borselli, and O. Painter. Probing the dispersive

and spatial properties of planar photonic crystal waveguide modes via highly efficient coupling from optical fiber tapers. *Appl. Phys. Lett.*, 85(1) 4–6, 2004.

- K. Srinivasan, P. E Barclay, and O. Painter. Fabrication-tolerant high quality factor photonic crystal microcavities. *Opt. Expr.*, 12(7) 1458–1463, 2004.
- K. Srinivasan, P. E. Barclay, M. Borselli, and O. Painter. Optical-fiber based measurement of an ultra-small volume high-Q photonic crystal microcavity. *Phys. Rev. B*, 70 081306(R), 2004.
- M. Borselli, K. Srinivasan, P. E. Barclay, and O. Painter. Rayleigh scattering, mode coupling, and optical loss in silicon microdisks. *Appl. Phys. Lett.*, 85(17) 3693–3695, 2004.
- P. E. Barclay, K. Srinivasan, and O. Painter. Nonlinear response of silicon photonic crystal microresonators excited via an integrated waveguide and a fiber taper. *Opt. Expr.*, 13 801–820, 2005.
- K. Srinivasan, P. E. Barclay, M. Borselli, and O. Painter. An Optical-Fiber-Based Probe for Photonic Crystal Microcavities. *IEEE JSAC*, 23 1321–1329, 2005.
- S. A. Maier, M. D. Friedman, P. E. Barclay, and O. Painter. Experimental demonstration of fiber-accessible metal nanoparticle plasmon waveguides for planar energy guiding and sensing. *Appl. Phys. Lett.*, 86(7) 071103, 2005.
- K. Srinivasan, M. Borselli, T. J. Johnson, P. E. Barclay, O. Painter, A. Stintz, and S. Krishna. Optical loss and lasing characteristics of high-quality-factor AlGaAs microdisk resonators with embedded quantum dots. *Appl. Phys. Lett.*, 86 151106, 2005.
- P. E. Barclay, B. Lev, K. Srinivasan, H. Mabuchi, and O. Painter. Integration of fiber coupled high-Q SiNx microdisks with atom chips. *Appl. Phys. Lett.*, 89 131108, 2006.

Chapter 1

Introduction

From afar, fabrication of nanoscale optical components can appear to be predominantly motivated by the same forces that have driven developments in the microelectronics industry, where we have become accustomed to equating smaller with more powerful. Unsurprisingly, to a large degree this intuition is correct. Optical chips containing dense arrays of devices have the potential for high bandwidth data processing, and already play a role in the telecommunications industry [1, 2, 3]. However, as a scientist, the motivation for miniturization can come from elsewhere: the desire to study optical effects that cannot be observed easily, if at all, without the help of wavelength scale confinement of light. Reassuringly, these two views of optical miniturization are not in conflict. Instead, these interests drive each other: Novel chip-scale optical phenomena often find applications in practical devices, and the usefulness of a scalable, integrated optical platform is not lost on physicists wanting to study increasingly complex systems.

The work in this thesis is focused on optical nanostructures, with both of these perspectives in mind. We study chip-based optical waveguides and microcavities, first developing tools for optically accessing and characterizing them, and then using them in experiments in nonlinear optics and cavity QED [4, 5, 6]. Each of these experiments is immediately relevant to applications that leverage the chip-scale nature of the structures. Nonlinear optical effects in silicon (Si) nanostructures can be used for low power on-chip all-optical switching, while integrated nanophotonic circuits promise to improve the robustness and scalability of cavity QED based quantum information processing resources.

1.1 Microcavities

Optical microcavities [7] confine light to wavelength scale volumes for relatively long times, and are the cornerstone of nanophotonics. At resonant frequencies, they enhance the local electromagnetic energy density, and support extremely large field strengths for low input powers. Generally speaking, the high quality factor (Q) and small mode volume (V) of microcavities make them sensitive to intensive and extensive properties, respectively, of their host environment. For example, a high-Q cavity can be extremely sensitive to small changes in the bulk susceptibility of its environment, while a small V cavity can be sensitive to local changes.

While microcavities can be fabricated from a wide range of geometries, including photonic crystal [8, 9, 10, 11, 12] and whispering gallery mode [13, 14, 15, 16, 17] resonators, any given microcavity can be characterized by Q and V. These quantities are defined in terms of the local field supported by the microcavity. For a microcavity resonance excited by a single photon, the field maxima E_{max} inside the cavity is simply written as

$$E_{\mathrm{max}} = \sqrt{\frac{\hbar\omega}{2\epsilon V}}, \tag{1.1}$$

where ω is the optical frequency of the resonance, and ϵ is the dielectric constant of the microcavity at the field maximum. To maintain this field strength in steady state, it is necessary to replenish the microcavity with new photons at the same rate at which they leak out due to imperfections or limitations in the microcavity design. This decay rate is related to Q:

$$\frac{dN}{dt} = -\frac{\omega}{Q}N, \tag{1.2}$$

where N is the number of photons stored in the cavity at a given time t. From energy conservation, this indicates that the power required to store N photons in the cavity scales as $1/Q$. Using the above two equations, for a given power dropped into a cavity, the peak intracavity energy density can be shown to scale with Q/V.

This enhancement is the basis for a large number of recent experiments in microcavity nonlinear optics, whose power thresholds scale in a nonlinear fashion with V/Q. Examples includes low threshold Raman lasers [18, 19, 20], parametric down conversion [21], and radiation pressure induced mechanical oscilation [22, 23]. Recently, low power nonlinear all-optical switching [24, 25, 26] has been observed. Large Q/V is also essential for experiments in cavity QED [4, 5, 6], which study the coherent energy exchange between single photons and single atoms [27, 28, 29] or quantum dots [30, 31, 32, 33]. Within the cavity, the atom-photon interaction rate and photon dissipation rate scale with $1/V^{1/2}$ and $1/Q$, respectively, and when the atom-photon interaction rate is sufficiently strong compared to the photon and atomic decoherence rates, the coupled atom-cavity system can be used in applications such as single photon generation [34, 35, 36, 37] and quantum state transfer [38, 39] for quantum information processing.

1.2 Fiber optic coupling at the nanoscale

In addition to requiring large field enhancements and photon lifetimes, any useful application of microcavities in nonlinear and quantum optics demands an efficient optical interface between the microcavity and external optics. The mismatch in both spatial dimensions and refractive index between wavelength-scale photonics and conventional fiber optics is severe, and without engineering a transition between the macro- and the nano-scale, the loss of optical fidelity is extremely high.

Fiber tapers [40, 41] are versatile tools that make this transition adiabatically. They have been used to efficiently excite resonances in whispering gallery mode cavities [42, 43, 15, 44, 45], and as discussed in this thesis, photonic crystal waveguides [46, 47, 48] and microcavities [11]. The highly integrated nature of chip based photonics also comes to our aid, as microcavities can be efficiently sourced from on-chip waveguides [25, 49] that are in turn coupled to the outside world. Using these tools to establish efficient optical channels between the laboratory and nanophotonic devices, the next challenge is to integrate fiber coupled devices with more complex experimental systems, such as those used in neutral atom based cavity QED experiments.

1.3 Organization

Many of the topics discussed above are studied in detail in this thesis. In Ch. 2 and Ch. 3, we theoretically examine the problem of coupling light into and out of photonic crystal waveguides, and propose a new technique using fiber tapers. This technique is put into practice in Ch. 4, where we demonstrate nearly perfect coupling at telecommunication wavelengths between a fiber taper and a Si photonic crystal waveguide, and use the taper to probe the dispersive and spatial properties of the bound photonic crystal waveguide modes. Efficient coupling between the photonic crystal waveguide and a high-Q, ultra-small V photonic crystal microcavity is also demonstrated. The nonlinear optical properties of this Si microcavity are studied in Ch. 5, where optical bistability is observed at sub-mW input powers.

In Ch. 6, our focus shifts to studying microcavities suitable for cavity QED experiments with neutral alkali atoms at near visible wavelengths. We show that SiN_x is an excellent material for microcavities operating in this wavelength range, and demonstrate extremely high Q/V microdisk cavities. These microdisks are integrated with atom chips in Ch. 7, where a method for robust fiber coupling is demonstrated, and the resulting atom-cavity chip is installed in an atomic physics apparatus used for neutral atom trapping and manipulation, with the aim of perfoming cavity QED experiments fully "on-chip." Finally, the possibility of detecting single atoms delivered to the microcavity using the atom chip is studied theoretically in Ch. 8, where general scaling laws for single atom sensitivity are derived and verified numerically.

Chapter 2

Interfacing photonic crystal waveguides with fiber tapers: design

The utility of photonic crystal (PC) devices relies heavily upon one's ability to efficiently couple light into and out of them. At the outset of the work contained in this thesis, no efficient technique had been demonstrated for efficiently exciting guided modes of planar photonic crystal waveguide structures. Initial photonic crystal waveguide experiments [52, 53] relied upon end-fire coupling between single mode fibers and the cleaved facet of a PC waveguide, and exbited extremely small coupling efficiency ($<$ 20 dB) because of the extreme spatial and refractive index mismatch between subwavelength high-index PC structures and optical fibers.

A number of methods for overcoming this problem have been studied. Perhaps the most obvious approach is to use adiabatic transitions [54, 55, 56] from "standard" ridge waveguides to source PC waveguides. However, coupling from fibers into high refractive index ridge waveguides poses similar problems, and requires the use of on-chip spot-size converters [57, 49, 58, 53] for high efficiency. Other groups have developed free-space grating assisted coupling techniques [59, 60] that utilize the periodicity of the photonic crystal waveguide to scatter light at near-normal incidence into bound photonic crystal waveguide modes, with modest efficiency.

Our approach differs fundamentally from those described above. Rather than design on-chip coupling interfaces, we decided to bury the transition between fiber optics and nanophotonics within fiber. Evanescent coupling between a fiber taper [40] and a PC waveguide, as detailed schematically in Fig. 2.1, makes use of the inherent dispersive properties of PCs to enable guided-wave coupling between waveguides with nearly ideal coupling efficiency. A single fiber taper used in this manner can function as an adjustable "wafer

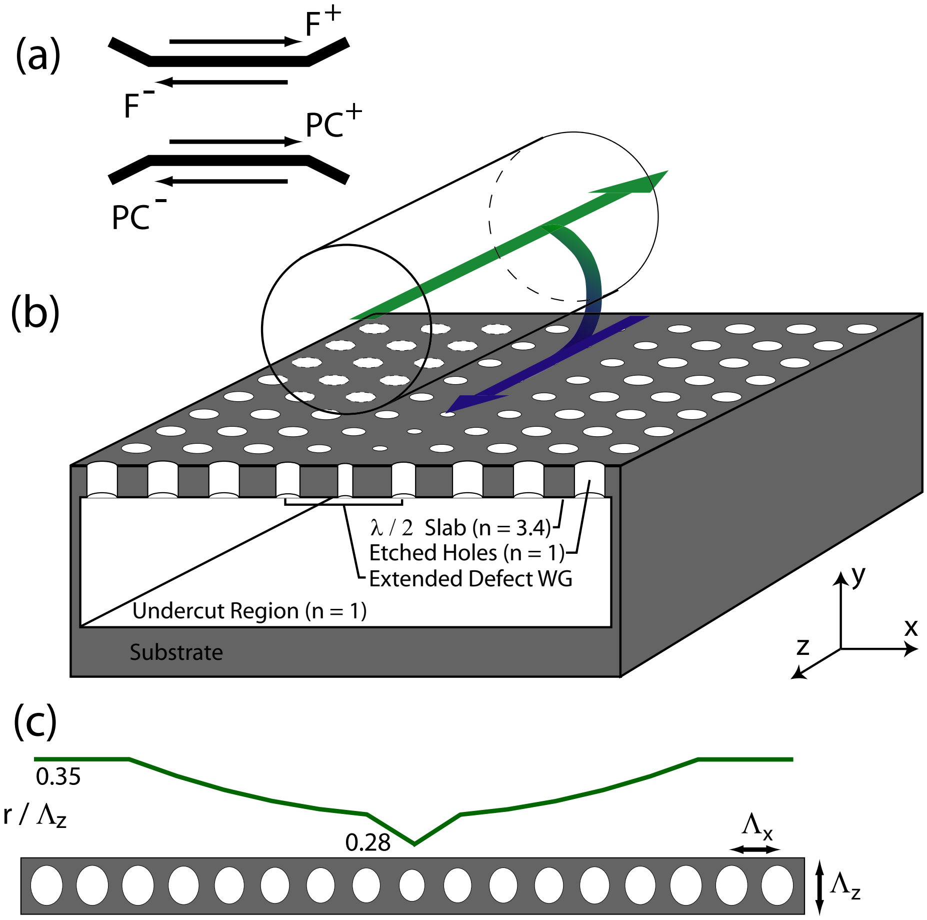

Figure 2.1: (a) Schematic of the coupling scheme, showing the four mode basis used in the coupled mode theory. (b) Coupling geometry. In the case considered here, the coupling is contra-directional. (c) Grading of the hole radius used to form the waveguide, and a top view of the graded-defect compressed-lattice ($\Lambda_x/\Lambda_z = 0.8$) waveguide unit cell.

scale probe" for testing of multiple devices on a planar chip.

Evanescent coupling

In the simplest picture, evanescent coupling between two parallel waveguides requires that there exist (in the frequency range of interest) a pair of modes, one from each waveguide, that share a common momentum component down the waveguide (phase-matching), and for which their transverse profiles and electric field polarizations are similar. A weak spatial overlap of the evanescent tails of each mode can then result in significant power transfer between waveguides. Full power transfer requires that, in addition, no other radiation or guided modes of either waveguide participate in the coupling, either due to a large phase mismatch and/or weak transverse overlap. Fiber taper coupling has been shown to be extremely valuable in this regard (in comparison to simple prism coupling, which involves a continuum of modes), and was first used to provide near perfect single mode coupling to dielectric microsphere [61, 42, 62] and toroid [14] resonators for ultra sensitive measurement of high-Q whispering gallery modes. In a similar manner, fiber taper probes can be used to couple to two dimensional PC membrane waveguides, thanks to their undercut air-bridge structure that suppresses radiation from the fiber into the substrate, and their zone-folded dispersion that enables phase matching between the dissimilar fiber and PC modes. Thus, by designing a PC waveguide whose defect mode has a transverse field profile that sufficiently overlaps the fiber taper's, efficient power transfer between the waveguides can be achieved. Furthermore, the flexibility in lattice engineering afforded by PCs allows this waveguide to be designed to couple efficiently to PC defect cavities, providing a fiber-PC waveguide-PC cavity optical probe.

In the remainder of this chapter, closely following Ref. [63], we discuss the design of a PC waveguide that satisfies the requirements outlined above. In Sec. 2.1, a simple coupled mode theory that models coupling between a fiber taper and a PC is presented, and the desired waveguide properties are illuminated mathematically and discussed in more detail. In Sec. 2.2, a general **k**-space analysis of bulk PC bandstructures is used to determine which types of defect modes have the desired properties. The results from these sections are then applied to the design and analysis of a PC waveguide in a square lattice in Sec. 2.3, and are further illustrated with FDTD supermode calculations in Sec. 2.4.

2.1 Coupled-mode theory

It has long been realized that modes in translationally invariant waveguides with differing dielectric constants can be phase-matched with the aid of a grating, so it is not surprising that the intrinsic discrete translational symmetry of PC waveguides and the resulting zone-folded dispersion of their modes allows PCs to be phase-matched with a large class of dissimilar waveguides, including tapered fibers. Grating mediated phase-matching schemes have been studied extensively, beginning with the research of microwave traveling wave tubes [64], and, more recently, of optical devices such as filters, directional couplers, and distributed feedback lasers (Ref. [65] and references therein). However, because the dielectric contrast of a PC grating is large, the fiber-PC coupling picture differs from that of a traditional (weak) grating assisted coupler, and rather than analyze coupling between plane-waves of the untextured waveguides, we must consider the Bloch eigenmodes of the PC waveguide. Although rigorous coupled mode theories for Bloch modes have been developed in the context of non-linear perturbations to Bragg fibers [66], photonic crystals [67], and coupled-resonator optical waveguides [68], none of these formalisms consider coupling between parallel waveguides. In order to evaluate the properties of evanescent coupling between a fiber and a PC defect waveguide, a coupled mode theory is presented in this section that can approximately predict the power transfer between the PC Bloch modes and the fiber planewave modes as a function of propagation distance, transverse coupling strength, and phase-mismatch. More detailed derivations of the following equations, as well as some useful properties of Bloch modes, are given in Appendix A.

The physical system being modeled is specified by the dielectric constants of the interacting waveguides $\epsilon_\mu(\mathbf{r})$, each of which individually supports a set of modes $\mathbf{E}^\mu_\nu(\mathbf{r})$, where μ labels the waveguides and ν labels the eigenmodes of each waveguide. For $e^{-i\omega t}$ time dependence, Maxwell's equations require that each of these modes satisfies the eigenvalue equation

$$\boldsymbol{\nabla} \times \boldsymbol{\nabla} \times \mathbf{E}^\mu_\nu(\mathbf{r}) = \tilde{\omega}^2 \epsilon_\mu(\mathbf{r}) \mathbf{E}^\mu_\nu(\mathbf{r}) \tag{2.1}$$

where $\tilde{\omega} = \omega/c$ is the free space wavenumber.

The fundamental approximation of waveguide coupled mode theories is that after some propagation distance the field of the composite system represented by $\epsilon(\mathbf{r}) = \epsilon_1 \cap \epsilon_2 ... \cap \epsilon_n$ can be approximated by some linear combination of the modes of the constituent systems represented by $\epsilon_\mu(\mathbf{r})$:

$$\mathbf{E}(\mathbf{r}) = \sum_{\mu\nu} C^\mu_\nu(z) \mathbf{E}^\mu_\nu(\mathbf{r}) \tag{2.2}$$

where it has been assumed that the modes are propagating in the $\pm\hat{\mathbf{z}}$ direction, or more precisely that the power flux of the individual modes in the $\hat{\mathbf{z}}$ direction is constant. When considering continuums of delocalized modes, an integral replaces the discrete sum. If $\epsilon_\mu(\mathbf{r})$ is periodic in z so that $\epsilon_\mu(x, y, z + \Lambda_z) = \epsilon_\mu(x, y, z)$, by Bloch's theorem [69] the eigenmodes have z dependence of the form $\mathbf{E}^{\mu}_{\nu}(x,y,z+\Lambda_z) = e^{i\beta_\nu\Lambda_z}\mathbf{E}^{\mu}_{\nu}(x,y,z)$, and Eq. (2.1) becomes

$$\mathbb{H}_{\beta_\nu}\mathbf{e}^{\mu}_{\beta_\nu}(\mathbf{r}) = \tilde{\omega}^2\epsilon_\mu(\mathbf{r})\mathbf{e}^{\mu}_{\beta_\nu}(\mathbf{r}) \tag{2.3}$$

where

$$\mathbb{H}_{\beta_\nu} = (-\beta_\nu^2\hat{\mathbf{z}}\times\hat{\mathbf{z}} + i\beta_\nu(\hat{\mathbf{z}}\times\boldsymbol{\nabla} + \boldsymbol{\nabla}\times\hat{\mathbf{z}}) + \boldsymbol{\nabla}\times\boldsymbol{\nabla})\times, \tag{2.4}$$

$\mathbf{e}^{\mu}_{\beta_\nu}(x,y,z+\Lambda_z) = \mathbf{e}^{\mu}_{\beta_\nu}(x,y,z)$, and $-\pi/\Lambda_z < \beta_\nu \leq \pi/\Lambda_z$ (i.e., β_ν is restricted to the first Brillouin zone) so that the eigenmodes are not over-counted. Equation (2.3) is often solved as an eigenvalue problem for $\tilde{\omega}_\nu$ parameterized by the wavenumber β, giving a dispersion relation $\tilde{\omega}_\nu = \tilde{\omega}_\nu(\beta)$. In linear media, only modes degenerate in $\tilde{\omega}$ have non-zero time averaged coupling over typical laboratory time-scales, and it is convenient to label the modes at fixed $\tilde{\omega}$ by their wavenumber $\beta_\nu(\tilde{\omega})$. Both conventions are equivalent and interchangeable. Typically (as discussed below), for weak coupling only modes *nearly resonant* in β (modulo a reciprocal lattice vector $2\pi/\Lambda_z$) to the exciting field need to be included in expansion (2.2); this is the basic assumption of the coupled mode theory. For weak coupling, this assumption that only nearly resonant modes interact is reasonable; however, the question of completeness is less clear. In general, Eq. (2.2) cannot satisfy Maxwell's equations since the eigenmodes of waveguide μ_1 do not satisfy the boundary conditions of waveguide μ_2, and vice versa. This issue was debated vigorously in the late 80s, but was not resolved, and is well summarized in Ref. [70]. In Ref. [71], Haus and Snyder showed that in some cases the ansatz Eq. (2.2) can be improved by modifying the modes used in the expansion so that they satisfy the boundary conditions of the composite system. This improvement is non-trivial in the case of a photonic crystal slab, however, and will not be used here. This deficiency is minimized for TE-like modes but exists nonetheless if the waveguides lack translational invariance or planar geometry, as is the case in photonic crystal waveguides and fiber tapers, respectively. Despite this limitation, we proceed under the assumption that in the limit of weak coupling the resulting model is a useful design tool that correctly describes the dependence of the coupling on the physical parameters but whose absolute results may deviate from the exact values.

In order to formulate coupled-mode equations, we assume that ansatz Eq. (2.2) is a solution to Maxwell's equations for the hybrid system and employ the Lorentz reciprocity relationship [72] which must hold for any two solutions to Maxwell's equations in non-magnetic materials:

$$\frac{\partial}{\partial z}\int_z (\mathbf{E}_1 \times \mathbf{H}_2^* + \mathbf{E}_2^* \times \mathbf{H}_1)\cdot \hat{\mathbf{z}}\, dx\, dy = i\,\tilde{\omega}\int_z \mathbf{E}_1 \cdot \mathbf{E}_2^*(\epsilon_1 - \epsilon_2^*) dx\, dy \tag{2.5}$$

where $(\mathbf{E},\mathbf{H})_{1,2}$ satisfy Maxwell's equations for $\epsilon_{1,2}$. Setting

$$\begin{aligned}\mathbf{E}_1 &= \sum_j C_j(z)\mathbf{E}_j(\mathbf{r})\\ \mathbf{E}_2 &= \mathbf{E}_i\end{aligned} \tag{2.6}$$

and correspondingly

$$\begin{aligned}\epsilon_1 &= \epsilon\\ \epsilon_2 &= \epsilon_i\end{aligned} \tag{2.7}$$

where the single index, $i = (\mu_i, \nu_i)$, labeling both the waveguide and the mode is adopted for clarity, and substituting Eqs. (2.6-2.7) into Eq. (2.5), the following power-conserving coupled mode equations are obtained:

$$P_{ij}\frac{dC_j}{dz} = i\,\tilde{\omega} K_{ij} C_j \tag{2.8}$$

where

$$P_{ij}(z) = \int_z (\mathbf{E}_i^* \times \mathbf{H}_j + \mathbf{E}_j \times \mathbf{H}_i^*)\cdot \hat{\mathbf{z}}\, dx\, dy \tag{2.9}$$

$$K_{ij}(z) = \int_z \mathbf{E}_i^* \cdot \mathbf{E}_j(\epsilon - \epsilon_j) dx\, dy \tag{2.10}$$

and it has been assumed that all dielectric constants are real. Equation (2.8) is similar to the coupled mode equations given in Ref. [73], with the only differences arising from the fact that no specific form of z dependence of the eigenmodes has been assumed. When the mode amplitudes are fixed at some $z = z_0$, Eq. (2.8) can easily be solved numerically, giving a transfer matrix that maps the amplitudes at z_0 to $z_0 + L$. In order to correctly model an experimental setup, the amplitude of the modes propagating in the $+\hat{\mathbf{z}}$ direction should be fixed at z_0, and the amplitude of the modes propagating in the $-\hat{\mathbf{z}}$ direction should be fixed at $z_0 + L$. Since Eq. (2.8) is linear and origin independent, Eq. (2.8) can be solved with these mixed boundary conditions by first calculating the transfer matrix (which maps $C_i^{\pm}(z_0) \to C_i^{\pm}(z_0 + L)$ where the sign superscript represents the propagating direction of mode j) and then transforming it to the appropriate scattering matrix (which maps $C_i^{+}(z_0) \to C_i^{+}(z_0 + L)$ and $C_i^{-}(z_0 + L) \to C_i^{-}(z_0)$).

From Eq. (2.5), the diagonal terms, P_{ii}, of the power matrix are constant, and are typically normalized to plus or minus unity depending on the sign of the group velocity of mode i. Additionally it can be shown that Bloch modes of the same waveguide are power orthogonal so that $P_{ij} = 0$ if $\epsilon_i = \epsilon_j$ and $\mathbf{E}_i \neq \mathbf{E}_j$. However, modes from neighboring waveguides are not power orthogonal, resulting in non-zero off-diagonal z-dependent components in P_{ij} which must be retained for Eq. (2.8) to be power conserving. In the fiber taper-PC system, the PC fields' z-dependence is the product of a planewave part and a periodic part, whereas fiber fields have planewave-like z-dependence. Expanding the periodic part of the PC field as well the PC dielectric constant in a Fourier series, the z-dependence of P_{ij} and K_{ij} can be written in terms of superpositions of $\exp\left[i\left(\beta_i - \beta_j - 2\pi m/\Lambda_z\right)z\right]$ terms, where m is an integer. For weak coupling ($dC_j/dz \ll 1/\lambda$), only the slowly varying component (compared to λ) of K_{ij} significantly couples the amplitude coefficients C_i and C_j over laboratory length scales of interest. This reasoning is analogous to (for example) that used in the time-domain rotating-wave approximation in quantum mechanics, and is often used to derive approximate analytic solutions to coupled mode equations describing two mode electromagnetic systems in the presence of weak gratings [3]. Because of the strong dielectric contrast of the PC, the problem here is more complex; however, the fundamental results from the simple cases hold: In order to observe significant power exchange between modes, their wavenumbers' β must differ by approximately a reciprocal lattice vector $2\pi m/\Lambda_z$, and the larger the phase matched driving terms, the stronger the coupling. The mixing of the Fourier components of the PC Bloch mode and dielectric constant is the most significant effect captured by this coupled mode theory compared to standard weak grating theories. Physically, this allows coupling between PC and fiber modes that is mediated either directly by a Fourier coefficient of the PC Bloch mode (the dominant effect here) or indirectly by the PC dielectric acting like a grating (a higher order effect). Optimizing the magnitude of these coefficients, and as a result, the coupling from the fiber mode to the desired photonic crystal waveguide mode is discussed in the next section.

2.2 k-space design

Photonic crystal defect waveguides are formed by introducing a line of defects into an otherwise two or three dimensionally periodic PC. Here we consider pseudo-2D membrane structures whose typical geometry is shown in Fig. 2.1. In absence of the defects, the eigenmodes of the bulk 2D slab are Bloch modes whose in-plane wavenumber, $\mathbf{k}$, is a good mode label and who are bound to the slab if $\omega(\mathbf{k})$ is below the cladding and substrate light-lines; i.e., $\omega(\mathbf{k}) < c\,k/n_{c,\,s}$, where n_s and n_c are the indices of refraction of the substrate and cladding respectively. (We will not consider bound modes that exist at special points in $\omega - \mathbf{k}$ space above the light-line, as shown in [74].) The air-bridge membrane structures considered here have $n_c = n_s = 1$, maximizing the area in $\omega - \mathbf{k}$ space where bound modes exist, and also ensuring that the bound modes of a fiber taper ($n_f \approx 1.45$) do not leak into the PC substrate.

The PC modes can be classified as either even or odd, depending on their parity under inversion about the $x - z$ mirror plane of the slab (see Fig. 2.1 for the coordinate system), and it can be shown that the lowest order even modes (i.e., modes with no zeros in the y direction) are TE-like, while the lowest order odd modes (i.e., modes with one zero in the y direction) are TM-like. We only consider coupling to TE-like modes (the fiber can couple to either). Furthermore, we assume that the slab is thin enough to ensure that the frequencies of the second order odd modes (which are also TE-like) are above the frequency range of interest, so that only the fundamental TE-like mode needs to be considered. Figure 2.2 shows the approximate bandstructure of the fundamental TE-like modes of the bulk square-lattice PC slab considered in this paper. This bandstructure is calculated using an effective index 2D planewave expansion model that takes into account the finite thickness of the slab but neglects the vector nature of the field, providing a useful guide for analyzing the $\omega - \mathbf{k}$ space properties of potential PC waveguide modes.

When a line defect is introduced, the discrete translational symmetry of the PC is reduced from two to one dimension, and consequently only the component β of $\mathbf{k}$ parallel to the line defect remains a good mode-label. The corresponding Bloch eigenmodes must satisfy Eq. (2.3) and the resulting band structure is approximately obtained by projecting the bulk PC bandstructure onto the first Brillouin zone of the defect unit cell ($\omega_{1D}(\beta) = \omega_{2D}(\mathbf{k}\,|\,\mathbf{k}\cdot\hat{\mathbf{u}} = \beta)$ where unit vector $\hat{\mathbf{u}}$ is parallel to the line defect) as shown

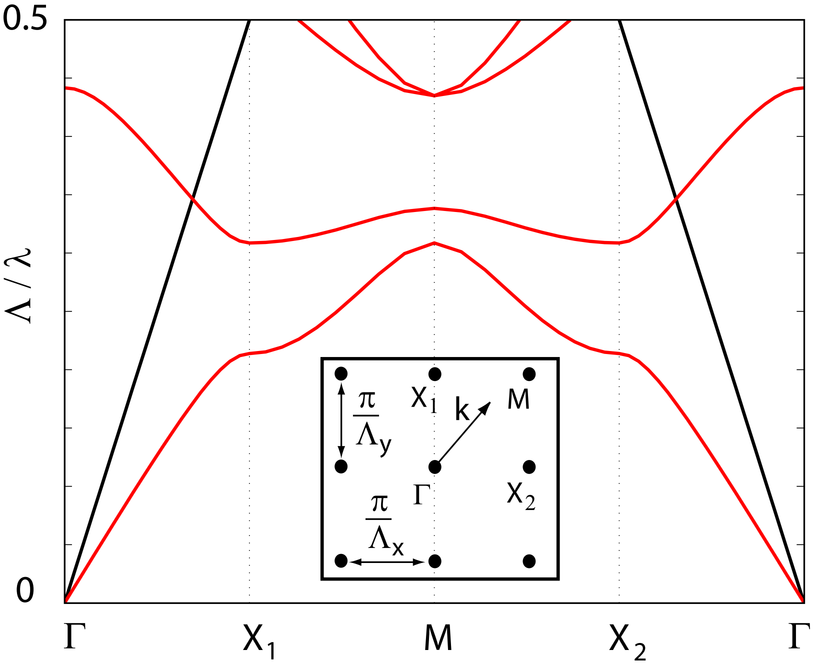

Figure 2.2: Approximate bandstructure of fundamental even (TE-like) modes for a square lattice PC of air holes with radius $r/\Lambda = 0.35$ in a slab of thickness $d = 0.75\Lambda$ and dielectric constant $\epsilon = 11.56$. Calculated using an effective index of $n_{\mathrm{TE}}^{\mathrm{eff}} = 2.64$, which corresponds to the propagation constant of the fundamental TE mode of the untextured slab. The inset shows the first Brillouin-zone of a rectangular lattice.

in Fig. 2.3, and by a discrete set of modes whose field is localized to the defect region. In **k**-space the localized and delocalized modes are characterized by β and a transverse wavenumber *distribution*. The projection creates continuums of delocalized modes in $\omega - \beta$ space over which the *dominant* transverse wavenumber varies smoothly and approximates that of the bulk mode from which it is projected. For small defects, the localized modes are superpositions of the delocalized modes at the top or bottom of the continuum regions, depending on whether the defect is an acceptor or donor type. By identifying from which bulk modes these continuum "band-edges" are projected, we can thus approximately determine the dominant transverse wavenumber of the defect modes. Given a bulk 2D bandstructure, the **k**-space properties of the defect modes associated with any defect geometry can therefore be approximately determined without resorting to computationally expensive waveguide simulations.

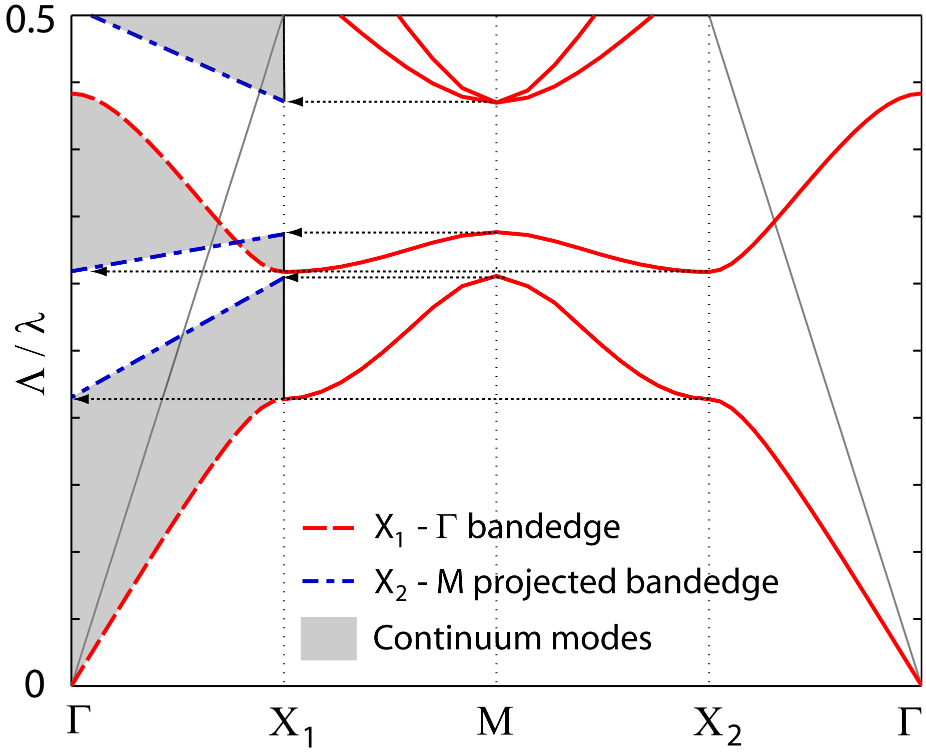

Figure 2.3: Projection of the square lattice bandstructure onto the first Brillouin-zone of a line defect with the same periodicity of the lattice and oriented in the $X_1 \rightarrow \Gamma$ direction. Bandedges whose modes have dominant wavenumbers in the $X_1 \rightarrow \Gamma$ direction (i.e. $\mathbf{k} = k\hat{\mathbf{z}}$) are drawn with solid black lines. Bandedges whose modes have dominant wavenumbers in the $X_2 \rightarrow M$ direction (i.e. $\mathbf{k} = k_z\hat{\mathbf{z}} + \pi/\Lambda_x\hat{\mathbf{x}}$) are drawn with dashed black lines.

To determine what PC waveguide **k**-space properties are desirable for efficient coupling, it is necessary to consider the fiber taper mode properties. Guided fiber taper modes are confined to the region in $\omega - \beta$ space bounded by the air and fiber (usually silica, $n_f \approx 1.45$) light lines, as shown in Fig. 2.4, which immediately limits the PC modes with which the fiber can phase match. A suitable fiber typically has a radius on the order of a PC lattice constant, and the corresponding linearly polarized fundamental fiber mode ($\mathrm{HE}_{11} \pm \mathrm{HE}_{1-1}$) is broad compared to the PC feature size. As a result, PC modes that are highly oscillatory in the transverse direction will not couple well to the fiber, since their transverse coupling coefficients derived in the previous section will be small. PC modes that maximize the coupling coefficient must thus have a transverse wavenumber distribution that is peaked at zero (i.e., has a large transverse DC component). This corresponds to defect modes that are dominantly formed from bulk PC modes whose **k** is parallel to the defect (the $X_1 \rightarrow \Gamma$

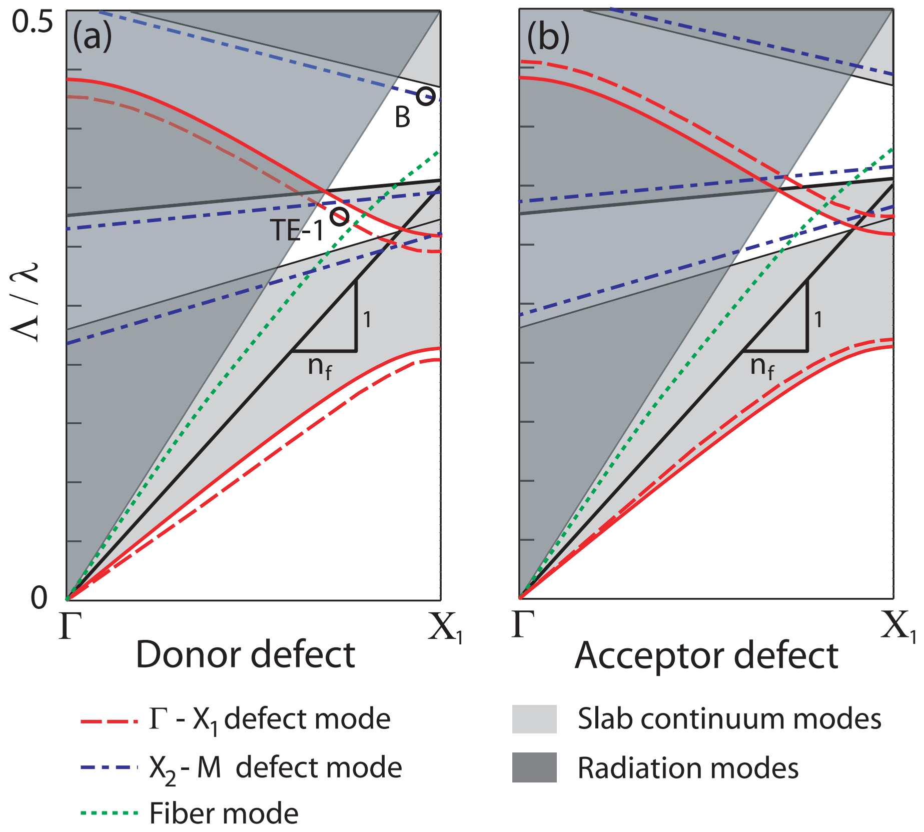

Figure 2.4: Approximate projected bandstructure for (a) donor type and (b) acceptor type, compressed square lattice waveguides. Possible defect modes and the fundamental fiber taper mode are indicated by the dashed lines.

direction here).

These ideas are illustrated in Fig. 2.4, which shows a bulk compressed square lattice band structure projected onto the first Brillouin zone of a line defect in the $X_1 \rightarrow \Gamma$ direction. The compressed lattice is used for reasons discussed below and is not essential for the analysis. The approximate dispersion of localized modes formed by both donor and acceptor type defects are shown, and modes whose transverse wavenumber distribution satisfy the requirements discussed above are indicated. It is not required that the defect modes be in a full photonic bandgap for the coupling scheme considered here. As in the case of other novel PC devices such as lasers [75] and high-Q cavities [76] that have been realized in small bandgap square lattice PCs, localized waveguide modes can exist without a full in-plane bandgap [77]. That being said, for mode selective coupling to be possible it is necessary that the defect mode exists in a “window” in $\omega - \beta$ space, where the nearest mode degenerate in ω is detuned sufficiently in β to suppress coupling, due to its large phase mismatch. Although lattice compression is not required to achieve this, it is sometimes advantageous to distort the lattice in order to optimize the window in $\omega - \beta$ space, as was done here. Compressing the lattice in the transverse direction effectively raises the energy of the bands at the X_2 point and M point in Fig. 2.3, modifying the projection of the full bandstructure onto the first Brillouin zone of the defect waveguide, as reflected in Fig. 2.4.

Once an appropriate lattice and defect waveguide type have been selected, and the approximate location of the desired mode in $\omega - \beta$ space determined using these approximate 2D techniques, 3D finite-difference time-domain (FDTD) can be used to numerically calculate the field profiles and exact dispersion of the 3D PC waveguide eigenmodes. The numerical results are used in turn in the coupled mode theory to model the coupling to the tapered fiber modes. These design principles are applied in the next section to design a compressed square lattice PC defect waveguide that can couple efficiently to fiber tapers.

2.3 Contradirectional coupling in a square lattice PC

The PC waveguide modes considered in this paper are formed within an optically thin (thickness $t_g = 3/4\,\Lambda_x$) semiconductor ($n = 3.4$) membrane perforated with a square array of air holes. From the approximate band structure for the bulk compressed square lattice waveguide shown in Fig. 2.4, there are several potential defect waveguide modes that are not in a continuum and that can phase match with a fiber taper (whose typical dispersion is also shown). Of these modes, only waveguide mode A has the desired transverse wavenumber components: It comes off a bandedge projected from the $X_1 \rightarrow \Gamma$ band of the bulk bandstructure, while the other modes come from $M \rightarrow X_2$ bandedges. Because mode TE_1 is not in a full frequency bandgap, it is not an obvious candidate in the context of the existing literature, which focuses on waveguide modes within a full bandgap. However, as we will show, this mode is confined to the defect region, can be coupled selectively with a fiber taper, and can be used to probe high-Q cavity modes (Ch. 3).

A 3D FDTD calculation of the even bandstructure for the graded waveguide of Fig. 2.1(c) in a compressed ($\Lambda_x/\Lambda_z = 0.8$) square lattice is shown in Fig. 2.5. Modes that are odd about the $x - z$ mirror plane are not shown in this plot; however, it was verified that the frequencies of the TE-like odd modes were higher than that of mode TE_1 in the region

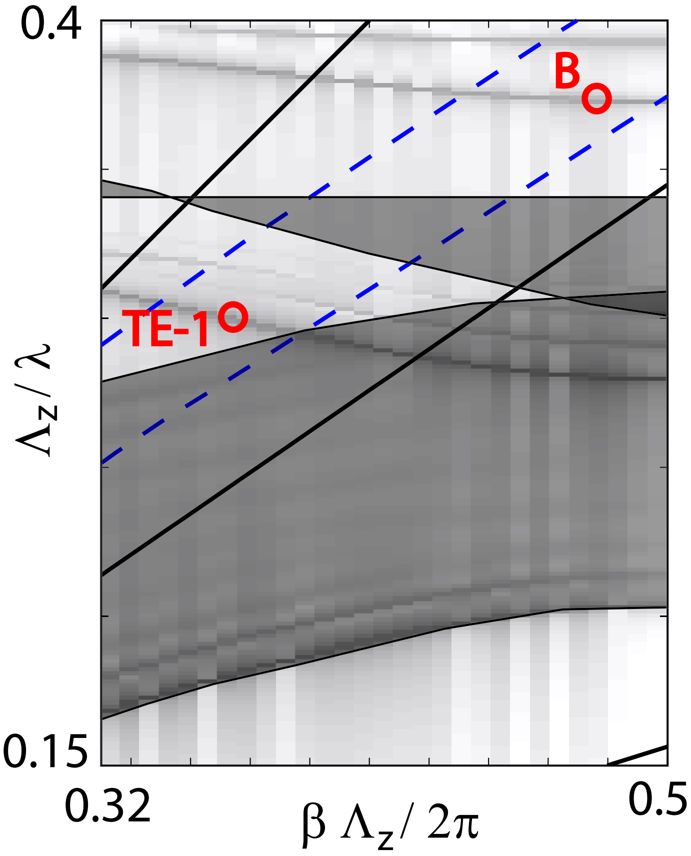

Figure 2.5: 3D FDTD calculated bandstructure for the waveguide shown in Fig. 2.1(c). The dark shaded regions indicate continuums of unbound modes. The dashed lines are the dispersion of fiber tapers with radius $r = 0.8\Lambda_z = 1\Lambda_x$ (upper line) and $r = 1.5\Lambda_z = 1.875\Lambda_x$ (lower line). The solid black lines are the air (upper line) and fiber (lower line) light lines. The energies and wavenumbers of modes TE_1 and B are $\tilde{\omega}\Lambda_z/2\pi = 0.304$ and 0.373 at $\beta\Lambda_z/2\pi = 0.350$ and 0.438 respectively.

of interest (circle "TE_1" in Figs. 2.4 - 2.5). Although other donor defect geometries could have been used, the hole radius grading and the lattice compression used here are important design features of the waveguide for a number of reasons. As discussed in Ch. 3, the field profile of Ref. [76]'s graded cavity mode is very similar to that of waveguide mode TE_1 suggesting that this waveguide mode is ideal for tunneling light into and out of these cavities. In addition, the compressed lattice provides for: (i) expansion of the window in $\omega - \beta$ space supporting defect donor type modes that can phase match with the taper; (ii) an increase in the slope of the defect mode dispersion, resulting in increased coupler bandwidth; and (iii) matching of the frequencies of the waveguide mode and the uncompressed defect cavity

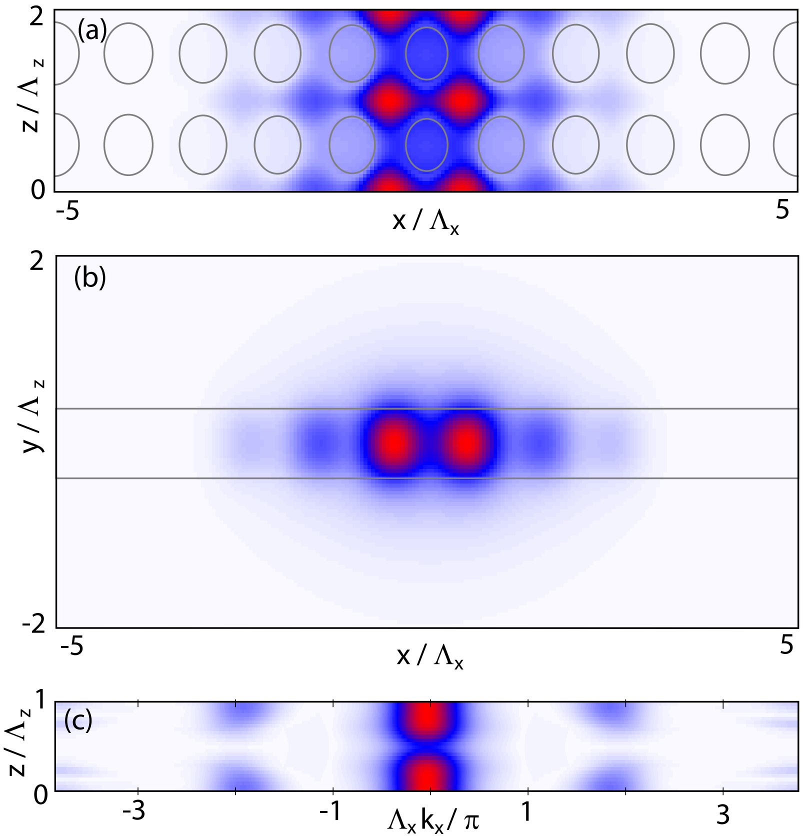

Figure 2.6: Mode TE$_1$ field profiles calculated using FDTD. Dominant magnetic field component (a) $|B_y(x, y = 0, z)|$; and (b) $|B_y(x, y, z = 0)|$; (c) Dominant electric field component transverse Fourier transform $|\tilde{E}_x(k_x, y = 0, z)|$. Note that the dominant transverse Fourier components are near $k_x = 0$.

donor mode without any stitching of the lattice required. (Choosing $\Lambda_x^{\text{PC}} = \Lambda_x^{\text{Cav}}$ requires that $\Lambda_z^{\text{PC}}/\Lambda_z^{\text{Cav}} = \tilde{\omega}^{\text{Cav}}/\tilde{\omega}^{\text{PC}}$.) The two sets of localized states expected from Fig. 2.4 are seen to form, one originating from the X_1-point in the 2D reciprocal lattice, and the other from the M-point. The most localized of each set are the *fundamental* (transverse) modes, which we label as mode TE$_1$ and mode B in Figs. 2.4 - 2.5. The magnetic field profiles and the transverse Fourier transforms of these localized modes are shown in Figs. 2.6 - 2.8. The Fourier transforms confirm that the dominant transverse Fourier components of mode TE$_1$ are centered about $k_x = 0$, while those of mode B are centered about $k_x = \pm\pi/\Lambda_x$. Both of these modes have negative group velocity, indicating that coupling to them from the fiber will be *contradirectional* in nature.

Using the FDTD calculated fields for the PC modes, the exactly calculated fields of a

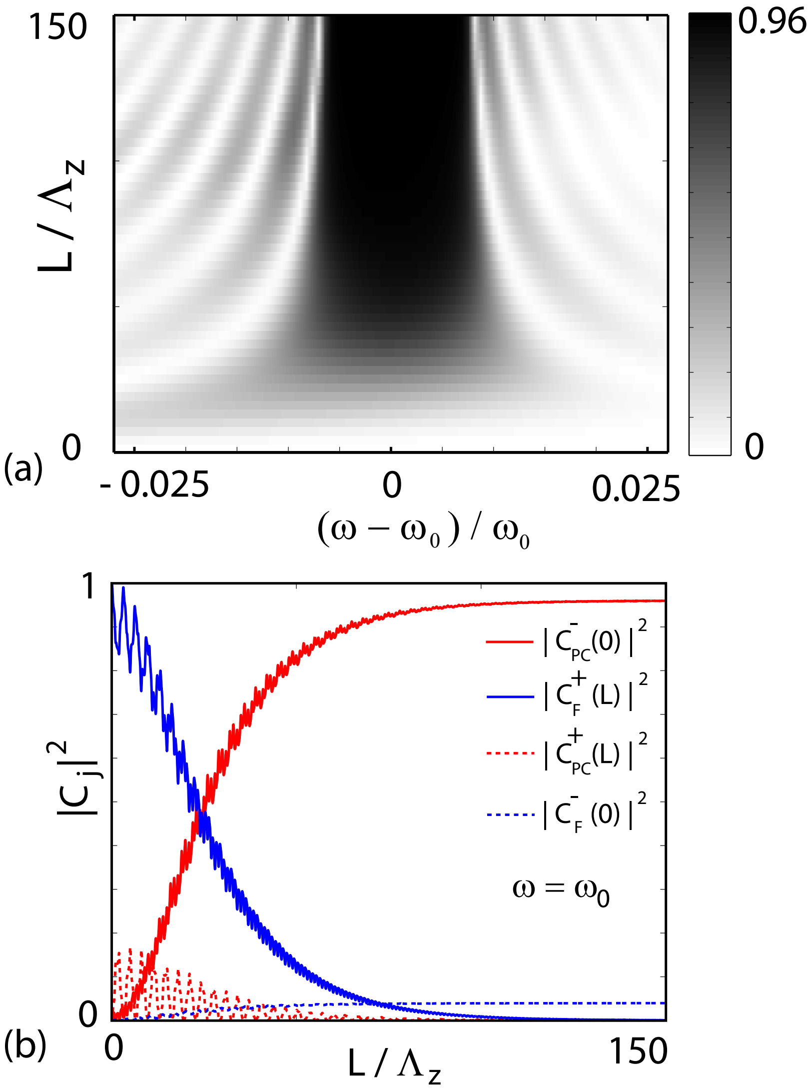

Figure 2.7: (a) Power coupled to PC mode TE$_1$ from a tapered fiber with radius $r = 1.15\Lambda_x$ placed with a $d = \Lambda_x$ gap above the PC as a function of detuning from phase matching and coupler length. (b) Power coupled at $\omega = \omega_0$ to the forward and backward propagating PC and fiber modes as a function of coupler length.

fiber taper, and including only those PC and fiber modes that are nearly phase-matched (as well as their backward propagating counterparts) in the coupled mode theory, the mode amplitudes at the coupler outputs were calculated as a function of coupler length and detuning of ω from the phase matching frequency ω_0. Figure 2.7(a) shows the resulting coupling to mode TE_1 from the fundamental mode of a taper with radius $r \approx 1.15\,\Lambda_x$ placed $d = \Lambda_x$ above the PC. Figure 2.7(b) shows the power in all four modes as a function

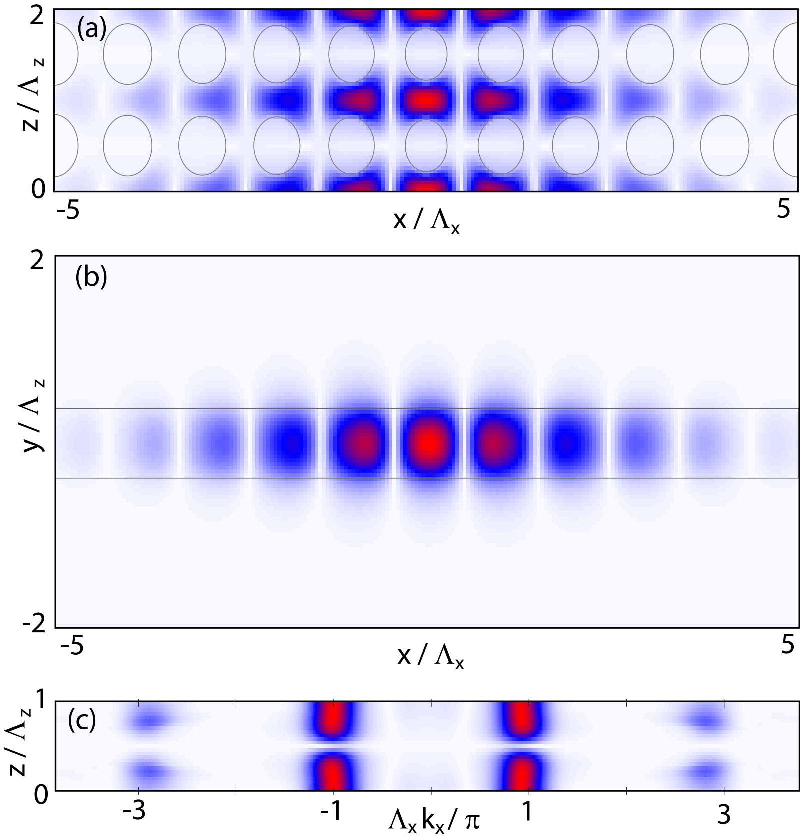

Figure 2.8: Mode B field profiles calculated using FDTD. Dominant magnetic field component (a) $|B_y(x, y = 0, z)|$, (b) $|B_y(x, y, z = 0)|$. (c) Dominant electric field component transverse Fourier transform $|\tilde{E}_x(k_x, y = 0, z)|$. Note that the dominant transverse Fourier components are near $k_x = \pm\pi/\Lambda_x$.

of coupler length at the phase matching condition. For reference, at an operating wavelength (λ_0) of 1.55μm, $\Lambda_x \approx 0.5\mu$m, which corresponds to a taper diameter ($2r$) of roughly 1μm and a waveguide-to-waveguide gap (d) of 0.5μm in this case. For $\omega = \omega_0$ and $L = 50\Lambda_z$ the coupled power is greater than 80%, and reaches 95% for $L = 80\Lambda_z$ ($\approx 40\mu$m). The remaining power is coupled to the backward propagating fiber mode. Note that because the PC mode has negative group velocity, this is contra-directional coupling resulting in monotonically increasing power transfer as a function of coupler length when the transverse coupling is stronger than the detuning in β [78]. The bandwidth is approximately 1.5% of ω_0, and it was verified that within this frequency range coupling to other modes is negligible due to large phase-mismatching. It should be noted that shorter coupling lengths and larger coupling bandwidths could be obtained by reducing the coupling gap, d; however, in the model used here this results in stronger coupling to the backward propagating fiber mode and a decreased asymptotic coupling efficiency. In addition, such strong coupling is best modeled using a more complete basis within coupled mode theory or using a fully numerical approach such as FDTD.

To illustrate the importance of a mode's dominant transverse Fourier components for efficient coupling, Fig. 2.9 shows the power transfer as a function of coupler length and detuning to mode B in Fig. 2.5 from an appropriately phase matched fiber taper placed $d = \Lambda_x$ above the PC [1].

Although mode B is even about the mirror plane in the center of the waveguide, because it is constructed from Bloch modes around the M-point it has relatively small amplitude for transverse Fourier components near zero, resulting in a small transverse overlap factor (K_{ij}) with the fiber taper mode. This results in a coupler length ≈ 200 times longer than that for mode TE$_1$, as well as an extremely narrow bandwidth of $\approx 10^{-4}\%$ of ω_0 (a property further amplified by mode B's low group velocity). Calculations not shown here that studied acceptor defect modes arising from the valence band edge ($M - X_2$) yield similar results, despite their very broad field profiles, which would be expected to match well with the fiber.

These calculations demonstrate that by selecting a mode composed from the appropriate regions in $\mathbf{k}$ space, efficient power transfer between a tapered fiber and the PC can be achieved that is mode selective and that (thanks to its contradirectional character) does not depend critically on the coupling length above some critical minimum. Using a more numerically intensive supermode calculation, we now confirm that the simple coupling analysis used above is valid.

2.4 Supermode calculations

In order to verify the coupling picture between the individual waveguide modes presented in the previous section, it is useful to calculate the bandstructure of the hybrid fiber taper-PC waveguide system. Because this system retains the discrete translational symmetry of the PC waveguide, the bandstructure of its modes (the *supermodes*) can be calculated using FDTD with a combination of Bloch and absorbing boundary conditions in a similar manner

---

[1] Besides the very weak coupling between this mode and the fiber taper, higher order odd slab modes may make coupling in this region of $\mathbf{k}$ space impractical. Nonetheless, the calculations shown here demonstrate the importance of a mode's transverse Fourier components.

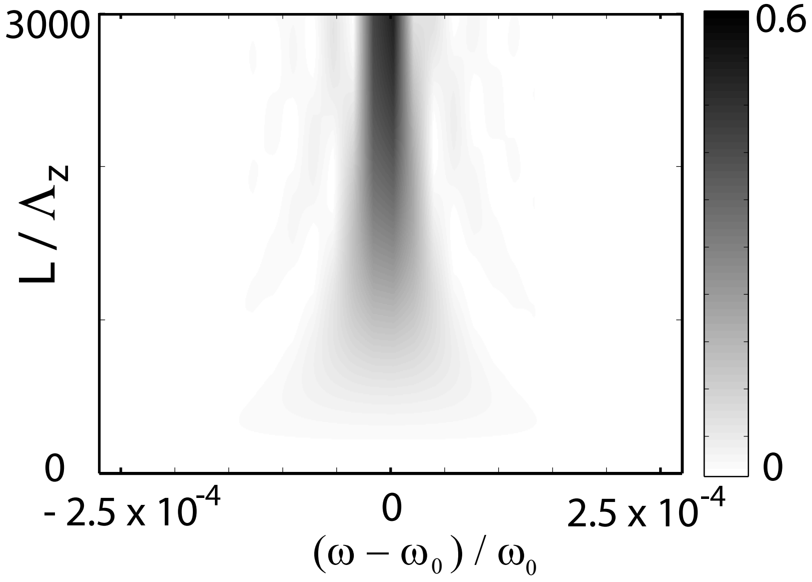

Figure 2.9: Power coupled to PC mode B from a tapered fiber with radius $r = 1.55\Lambda_x$ placed with a $d = \Lambda_x$ gap above the PC as a function of detuning from phase matching and coupler length.

as the bandstructure of the isolated PC waveguide. The resulting bandstructure provides information about the coupling between the modes of the individual waveguides. For weak coupling, it resembles the superposition of the individual waveguide bandstructures (for example Fig. 2.5), but with anti-crossings where the modes intersect and are coupled. The amount of deflection at an anti-crossing is related to the strength of the coupling between the modes, and can be used to back out physical parameters that describe the power transfer.

Figure 2.10(a) shows the bandstructure for a fiber taper of radius $r = 1.17\Lambda_z = 1.46\Lambda_x$ placed $d = \Lambda_z = 1.25\Lambda_x$ above the PC waveguide studied in the previous sections. These parameters differ slightly from those used in the previous section, but do not change the results significantly; the larger separation results in a longer coupling length and a smaller bandwidth, while the larger fiber radius lowers the phase matching frequency slightly. The mirror symmetry about the $y - z$ plane of the fiber-PC system is used to filter for modes that are even about this plane, but the fiber breaks the mirror symmetry in the $x - z$ plane, and the bandstructure contains PC modes that are *odd* in the vertical direction, and that are not shown in the bandstructures from the previous sections. The dispersion of the individual fiber mode and the PC waveguide mode TE_1 can be identified, and the anti-

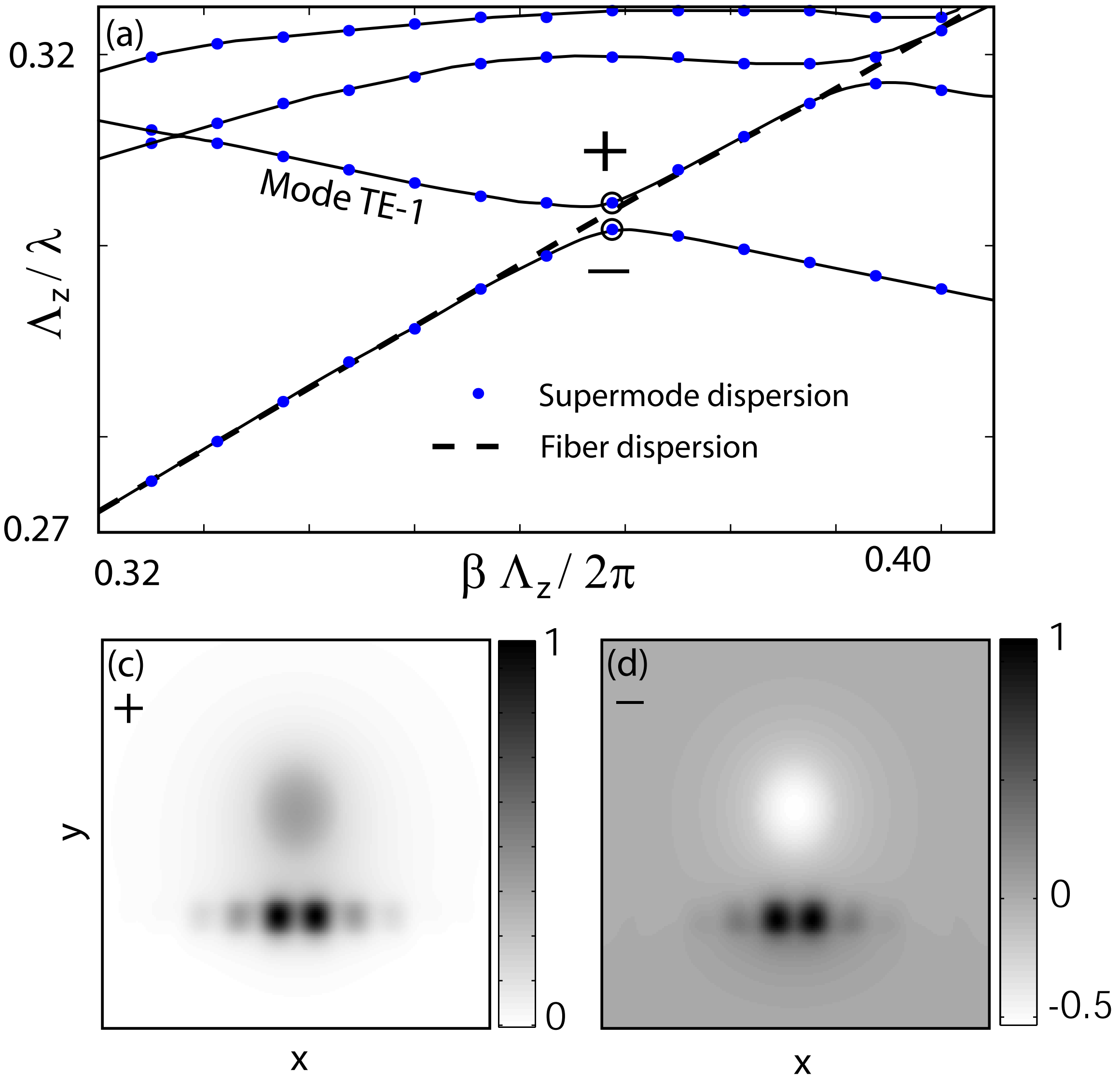

Figure 2.10: (a) FDTD calculated bandstructure of the full fiber taper photonic crystal system. The fiber taper has a radius $r = 1.17\Lambda_z = 1.46\Lambda_x$, and is $d = \Lambda_z = 1.25\Lambda_x$ above the PC waveguide. The TE_1-like and fiber-like dispersion is identified, and the symmetric and antisymmetric superpositions of these modes at the anti-crossing are labeled by the ± signs. (b) The $B_y(x, y, 0)$ component of the symmetric supermode. (c) The $B_y(x, y, 0)$ component of the antisymmetric supermode.

crossing where they intersect indicates that the two modes are coupled. In addition, the fundamental fiber taper mode couples strongly to a series of PC modes at higher frequencies than mode TE_1, which was not predicted from the analysis in the previous section. These are the aforementioned second order odd (about the $x - z$ plane) valence band TE-like PC modes. These modes can be pushed to higher frequencies faster than the fundamental TE-like modes by reducing the slab-thickness (i.e., they can be “frozen out” of the frequency range of interest), and are typically not studied. However, their odd parity in the vertical direction results in an electric field amplitude maxima near the PC surface, and they interact strongly with the fiber taper. Figures 2.10(b,c) show the field profiles of the supermodes from either side of the anti-crossing of interest. The low and high frequency supermodes closely resemble odd and even superpositions, respectively, of the individual waveguide modes, consistent with standard results for coupling between degenerate modes in guided wave optics [3].

Since PC mode TE_1 and the fiber mode have group velocities with opposite signs, a bandgap is formed where they anti-cross. This is consistent with the physical picture of the coupling: On resonance, a contradirectional coupler acts like a mirror, and reflects the power from the forward propagating mode into the backward propagating mode. Mathematically, this is manifest in a non-zero imaginary part of the propagation constant, β, inside the gap. Thus, the supermodes propagate evanescently inside the gap, and complete contradirectional coupling is possible over a bandwidth equal to the size of the gap. The gap at the anti-crossing of mode TE_1 and the fiber mode in Fig. 2.10(a) has a width of 1% of its center frequency ω_0. Coupled mode calculations similar to those of the previous section for a fiber radius and PC-taper gap equal to those used in this section also yield a bandwidth of 1% of ω_0.

2.5 Conclusion

Using the general analysis presented in this chapter, photonic crystal waveguide modes suitable for efficient coupling to optical fiber tapers can be identified. The photonic crystal waveguide design presented here is predicted to allow contradirectional fiber-PC power transfer of 95% after an 80 lattice constant ($\approx 50\,\mu$m) long interaction region. In the following chapter, it will be shown that this photonic crystal waveguide can be efficiently integrated with a photonic crystal cavity.

Chapter 3

Efficient fiber to cavity coupling: theory and design

Optically accessing PC microcavities is difficult due to their ultra-small mode volume and their external radiation pattern, which, unlike micropost [36] and Fabry-Pérot [34] cavities, is not inherently suited to coupling with conventional free-space or fiber optics. However, the planar, chip-based nature of PC cavities lends itself naturally to integration with other planar nanophotonic structures, such as PC waveguides [79, 80]. Initial passive studies of PC cavities took advantage of this, and employed PC "bus" waveguides to probe the cavity [81, 82, 83]. However, neither the coupling into the waveguide nor the waveguide-cavity interface were designed carefully, and the total fiber to cavity coupling efficiency of these studies was very low.

In the previous chapter, we addressed the fiber waveguide coupling problem. In this chapter, we study how the PC waveguide can be engineered to "mode match" with the cavity, ensuring efficient and "ideal" [84] waveguide-cavity coupling. The resulting fiber-waveguide-cavity coupling geometery is illustrated in Figs. 3.1(a) and 3.1(b), and functions as follows. Light is coupled evanescently from the fiber taper onto the PC chip via a PC waveguide, where it is guided to the PC microcavity at the terminus of the PC waveguide. Photons that are reflected from the PC cavity are then recollected into the backward propagating fiber taper mode, where they are separated from the forward propagating input signal using a fiber splitter. In this way, a single optical fiber is used to both source and collect light from the PC microcavity.

When presented with this coupling scheme, an obvious question is whether the PC waveguide is necessary. Can the fiber taper be efficiently coupled directly to the cavity? Kartik Srinivasan from our group demonstrated [11] that it is possible to couple directly

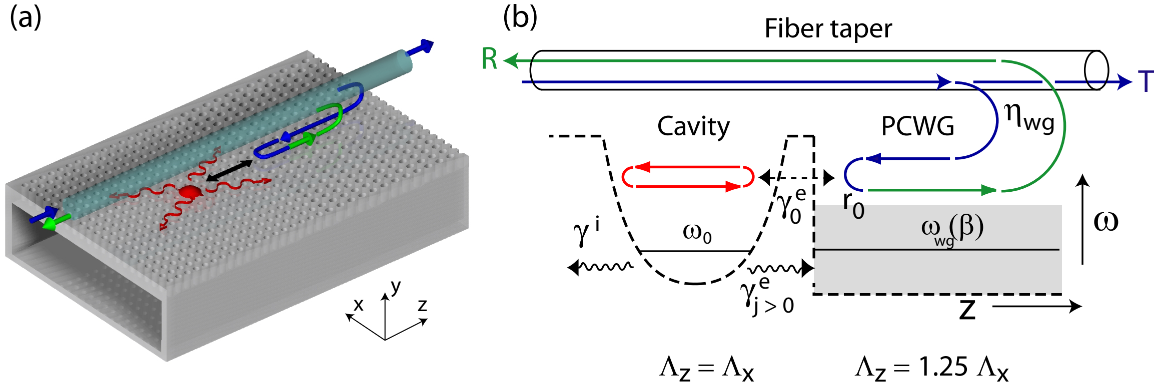

Figure 3.1: (a) Schematic of the fiber taper to PC cavity coupling scheme. The blue arrow represents the input light, some of which is coupled contradirectionally into the PC waveguide. The green arrow represents the light reflected by the PC cavity and recollected in the backwards propagating fiber mode. The red colored region represents the cavity mode and its radiation pattern. (b) Illustration of the fiber-PC cavity coupling process. The dashed line represents the "local" band-edge frequency of the photonic crystal along the waveguide axis. The step discontinuity in the bandedge at the PC waveguide - PC cavity interface is due to a jump in the longitudinal ($\hat{z}$) lattice constant. The parabolic "potential" is a result of the longitudinal grade in hole radius of the PC cavity. The bandwidth of the waveguide is represented by the gray shaded area. Coupling between the cavity mode of interest (frequency ω_0) and the mode matched PC waveguide mode ($\omega_{\mathrm{WG}} = \omega_0$) is represented by γ_0^e, coupling to radiating PC waveguide modes is represented by $\gamma_{j>0}^e$, and intrinsic cavity loss is represented by γ^i.

between fiber tapers and PC cavities, but that because of parasitic losses from the cavity induced by the fiber taper, this coupling is typically neither efficient nor ideal. To emphasize the importance of ideality, we begin in Sec. 3.1 with a review of some of the key parameters describing the loading of a general resonant structure, including coupling efficiency and ideality, and point out specific implications for planar PC microcavities. In Sec. 3.2 we then present a design that attempts to optimize these parameters while allowing for efficient evanescent coupling between a fiber and the waveguide. This work was first presented in Refs. [63] and [25].

3.1 Efficient and ideal waveguide-cavity loading

As proposed in Ref. [84] in the context of microsphere resonators, the interaction between a PC cavity and an external PC waveguide can be described by two key parameters, the *coupling parameter*, K, and the *ideality factor*, I:

$$K \equiv \frac{\gamma_0^e}{\gamma^i + \sum_{j\neq 0} \gamma_j^e}, \tag{3.1}$$

$$I \equiv \frac{\gamma_0^e}{\sum_j \gamma_j^e}, \tag{3.2}$$

where the cavity mode is characterized by its resonance frequency (ω_o), its intrinsic photon loss rate in the absence of the external PC waveguide (γ^i), and its coupling rates to the fundamental TE$_1$ mode (γ_0^e) and higher order (including radiating) modes of the external PC waveguide ($\gamma_{j>0}^e$). I describes the degree of "good" loading, via the fundamental PC waveguide mode in this case, relative to the total loading of the resonator. K is the ratio of "good" loading to the parasitic and intrinsic loss channels of the resonator.

The on-resonance fraction of optical power reflected by the cavity back into the PC waveguide mode is determined by the coupling parameter, K,

$$R_o(\omega_o) = \frac{(1-K)^2}{(1+K)^2}. \tag{3.3}$$

The remaining fractional power, $1 - R_o(\omega_o)$, is absorbed inside the PC cavity or radiated into the parasitic output channels. The reflection resonance full-width at half-maximum (FWHM) linewidth is given by the sum of the loss rates for *all* of the loss channels of the cavity, $\delta\omega = \gamma^i + \sum_j \gamma_j^e$. From $R_o(\omega_o)$ and $\delta\omega$, the quality factor of the PC cavity mode due to intrinsic and parasitic loss (i.e., those loss channels other than the "good" PC waveguide TE$_1$ channel) can be determined:

$$Q_{i+P} = 2Q_T \frac{1}{1 \pm \sqrt{R_o(\omega_o)}} = Q_T(1+K), \tag{3.4}$$

where the total loaded quality factor is $Q_T = \omega_o/\delta\omega$, and where the $\pm$ corresponds to the under- and over-coupled ($K \lessgtr 1$) loading condition. On resonance, full power transfer (critical coupling) from the "good" loading channel to the resonant PC cavity mode occurs when $K = 1$.

Whereas K determines the amount of power dropped by the resonator, the role of I is more subtle. In the case of an internal emitter, the collection efficiency (η_0) of emitted photons into the "good" loading channel is given by,

$$\eta_0 = \frac{\gamma_0^e}{\gamma^i + \sum_j \gamma_j^e} = \frac{1}{1+1/K}, \tag{3.5}$$

which depends only upon the coupling parameter K. However, the cost of obtaining a large collection efficiency is measured by the drop in loaded quality factor of the resonant cavity mode, which can be written in terms of K, I, and Q_i as

$$\frac{Q_T}{Q_i} = 1 - \frac{K}{I(1+K)} = 1 - \frac{\eta_0}{I}. \tag{3.6}$$

Thus, for a given collection efficiency, to maintain a long cavity photon lifetime, I should be maximized.

Utilizing a cavity loading method with $I \sim 1$ is also important for cavity based nonlinear optics. A simple argument can be made by studying the stored energy inside a resonant cavity for a given input power. One can write for the on-resonance internal stored energy, U,

$$U = (1 - R_o(\omega_o))\frac{Q_{i+P}}{\omega_o}P_i = \frac{4K}{(1+K)^2}\frac{I - K(1-I)}{I}\frac{Q_i}{\omega_o}P_i \tag{3.7}$$

where P_i is the input power in the "good" loading channel. The maximum stored energy in the resonator occurs at $K_{\max} = I/(2-I)$, giving a peak stored energy, $U_{\max} = I(Q_i/\omega_o)P_i$, which scales directly with I.

3.2 Mode-matched cavity-waveguide design

For integrated PC cavities and waveguides, in order to maximize I it is necessary to restrict the cavity-waveguide coupling to a single dominant waveguide mode so that $\gamma_0^e \gg \gamma_{j>0}^e$. Parasitic waveguide modes with cavity coupling rates $\gamma_{j>0}^e$ may come from a number of sources: (i) radiation modes above the light cone of the PC slab, (ii) bulk PC slab modes that are not laterally confined, and (iii) other laterally confined PC slab modes. In order to effectively *load* the cavity with the waveguide so that $I \sim 1$, the cavity mode of interest must radiate preferentially into a single waveguide mode[1]. To satisfy this criteria, the design

---

[1] Note that a single *guided*-mode PC waveguide (i.e., a waveguide mode in a full in-plane photonic bandgap) does not guarantee efficient waveguide-cavity coupling, as the cavity mode may still couple radiate into leaky modes of the PC waveguide.

described in this chapter has two important features: (i) the waveguide and cavity modes of interest have similar transverse field profiles (see Fig. 3.2), which allows the cavity to be efficiently loaded end-on, and (ii) the end-fire PC waveguide-cavity geometry restricts the cavity to a single output channel, in a manner analogous to a Fabry-Pérot cavity with a high reflectivity back mirror and a lower reflectivity front mirror[2].

The PC cavity that we wanted to out-couple with a PC waveguide was studied in Ref. [76]. There, Srinivasan, et al. used a group theoretical analysis to design a cavity in a square lattice PC slab that supports a high-Q ($\approx 10^5$) donor defect mode, whose FDTD calculated field profile is shown in Figs. 3.2(a,b). The defect cavity was formed by introducing a donor defect with C_{2v} symmetry in the form of a parabolic grading of the hole radius in both in-plane directions (the $\hat{x}$- and $\hat{z}$-directions, as depicted in Figure 3.2(a)). Since the first order bandgap energy minima of the conduction band in a square lattice occur at the $X_{1,2}$ points of the IBZ, donor modes from this band are expected to be composed of Fourier components in a neighborhood of the $\pm\mathbf{k}_{X_1}$ and $\pm\mathbf{k}_{X_2}$ points in $\mathbf{k}$ space. The high-Q mode transforms as the A_2 representation of the C_{2v} [76], and its dominant $\mathbf{k}$-space components result in a highly directional mode profile along the $\hat{z}$-direction, parallel to the $\Gamma - X_1$ direction of the reciprocal lattice. In anticipation of integration with this cavity, the waveguide studied in Ch. 2 shares an identical grade in hole radius as that in the $\hat{x}$-direction of the defect cavity. The resultant similarity in the lateral ($\hat{x}$-direction) mode profile of the A_2 cavity and TE_1 waveguide modes is clear from the field plots in Fig. 3.2. The lateral overlap factor of these two modes is $|\langle B_y^{\text{WG}} | B_y^{\text{Cav}} \rangle_{xy}| \sim 0.98$, where the waveguide and cavity fields are evaluated at their anti-nodes in the $\hat{z}$-direction. This near unity modal overlap suggests that the cavity mode will radiate dominantely into the TE_1 mode, i.e., $I \sim 1$.

Because of the similarity between the lateral grade in the hole radius of the PC in the waveguide and cavity sections, the coupled waveguide-cavity illustrated in Fig. 3.1 can be approximately viewed as a one dimensional system along the $\hat{z}$-direction. This simplified picture is schematically represented in Fig. 3.1(b), where the frequency of the (local) fundamental "waveguide" mode is plotted versus z for a fixed lateral grading in the PC hole radius. A *buffer* region consisting of a variable number of periods of the square photonic lattice is placed between the end of the waveguide and the defect cavity. As

---

[2] This is in contrast to side-coupled [10], in-line [82], and direct taper coupled [11] geometries, in which the cavity radiates equally into backward and forward propagating waveguide modes (bounding $K \leq 1$ and $I \leq 0.5$)

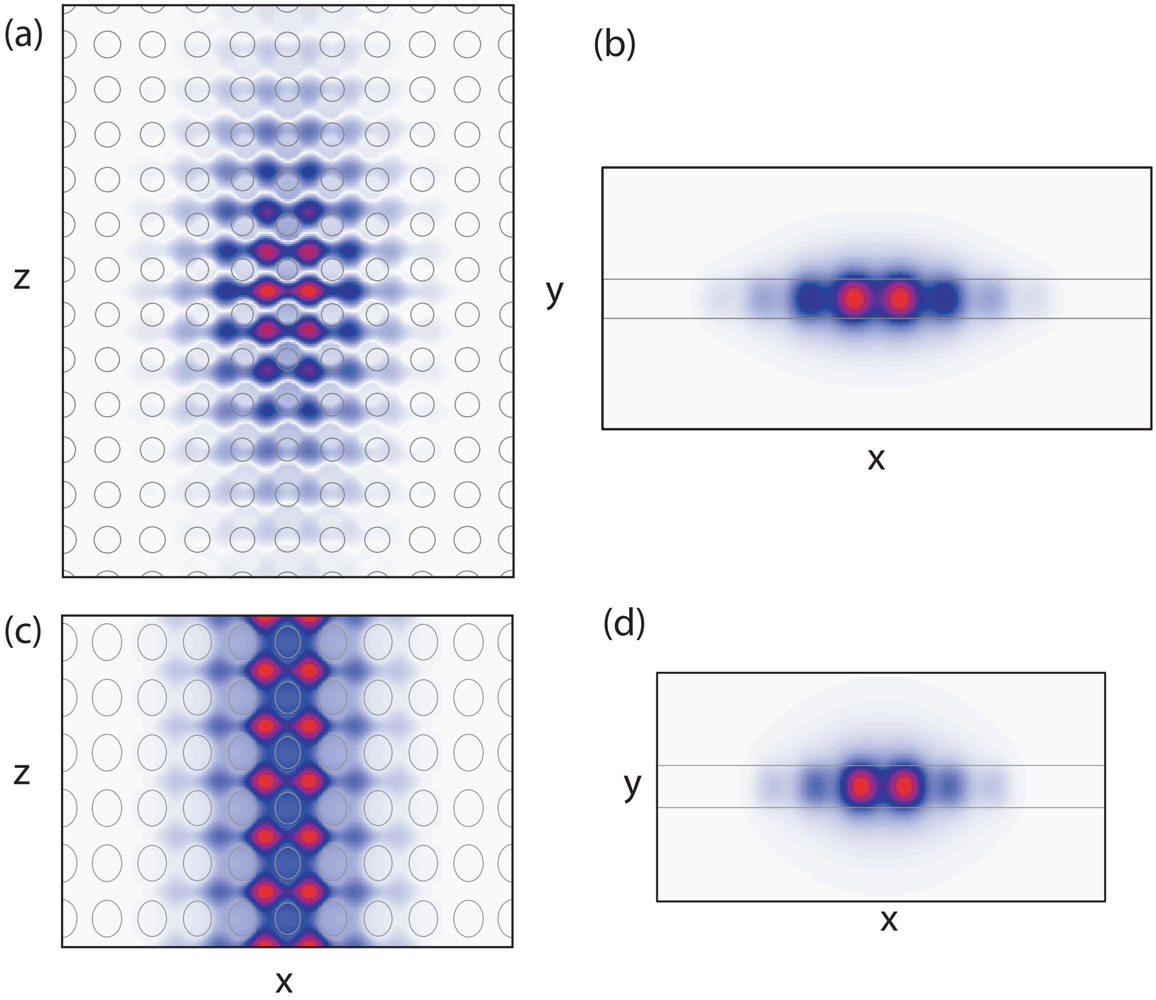

Figure 3.2: (a,b) High-Q defect cavity mode profiles. Plots of the magnetic field pattern are shown in (a) the $x - z$ plane ($|B_y(x, y = 0, z)|$), and (b) the $x - y$ plane ($|B_y(x, y, z = 0)|$). (c,d) PC waveguide TE_1 mode field profiles, taken in the (a) the $x - z$ plane and (b) the $x - y$ plane.

illustrated schematically in Figure 3.1(b), light tunnels between the cavity and waveguide through the barrier. In general, the efficiency and strength of coupling between the cavity and waveguide are tuned by: (i) adjusting the compression and/or the filling fraction of the waveguide lattice so that the TE_1 waveguide mode is resonant with the cavity mode, and (ii) tailoring the waveguide defect so that the waveguide and cavity modes have similar transverse field profiles. The frequency of the lateral guided mode is tuned at different positions in z by adjusting the nominal hole radius (lattice filling fraction) and/or the lattice constant in the $\hat{z}$-direction (lattice compression/stretching). The mode's dispersion in the

PC waveguide section results in a finite frequency bandwidth and is represented in the figure by a shaded region. So as to avoid stitching different lattices, the lateral lattice constant is kept constant ($\Lambda_x^{\text{cav}} = \Lambda_x^{\text{WG}}$). In this way, we can engineer band-offsets to produce tunneling barriers and create localized resonant cavities along the $\hat{z}$-direction. In order to couple from the waveguide to the cavity, the waveguide mode must be in resonance with the localized cavity mode. For the waveguide and cavity mode system considered here, this degeneracy is achieved by adjusting the waveguide lattice compression $\Lambda_x^{\text{WG}}/\Lambda_z^{\text{WG}}$. Additionally, for the designs studied here there is no discontinuity in the hole size, so that the strength of the coupling between the resonant cavity and waveguide modes is determined by the band-offset due to the lattice compression of the waveguide (height of the barrier) and the number of buffer periods between the waveguide and cavity sections (width of the barrier).

An analysis of the coupling between the waveguide the cavity was performed using a 2D effective index FDTD simulation of the full cavity-waveguide system. Although these 2D simulations neglect vertical radiation loss, this analysis can determine how effectively the lateral profile of the waveguide mode has been matched to that of the cavity mode, a major consideration in our waveguide design and a necessity for efficient waveguide-cavity coupling as discussed above. Figure 3.3 shows the cavity mode in the presence of a series of waveguides with different lattice compressions. The magnetic field is shown at instants in time when it is a maximum (confined) and a minimum (radiating) in the cavity. Coupling to the TE_1 waveguide is negligible when the lattice is uncompressed, since its lowest frequency (which occurs at the X point) is higher than the cavity mode frequency. In this case the cavity radiates as if it were *unloaded* and its dominant in-plane radiation is in the $\mathbf{k}_M$ directions. When the lattice is compressed, the waveguide mode frequencies are lowered, and the cavity becomes resonant with the TE_1 waveguide mode labeled by some propagation constant, β (see Fig. 3.1(b)). The *loaded* cavity couples to the TE_1 waveguide mode, but not into other (degenerate in ω but detuned in β) *parasitic* waveguide modes. As discussed above, this mode-selective coupling does not rely on a full photonic bandgap and is due to the similarity between the transverse profiles of the cavity and waveguide modes of interest. The simulations also show that because of the TE_1 dispersion and its corresponding frequency bandwidth, the waveguide-cavity coupling does not depend critically on the amount of lattice compression, so long as the compression is sufficient to lower the frequency at the X point of the TE_1 mode below the cavity mode frequency. By tuning the lattice compression

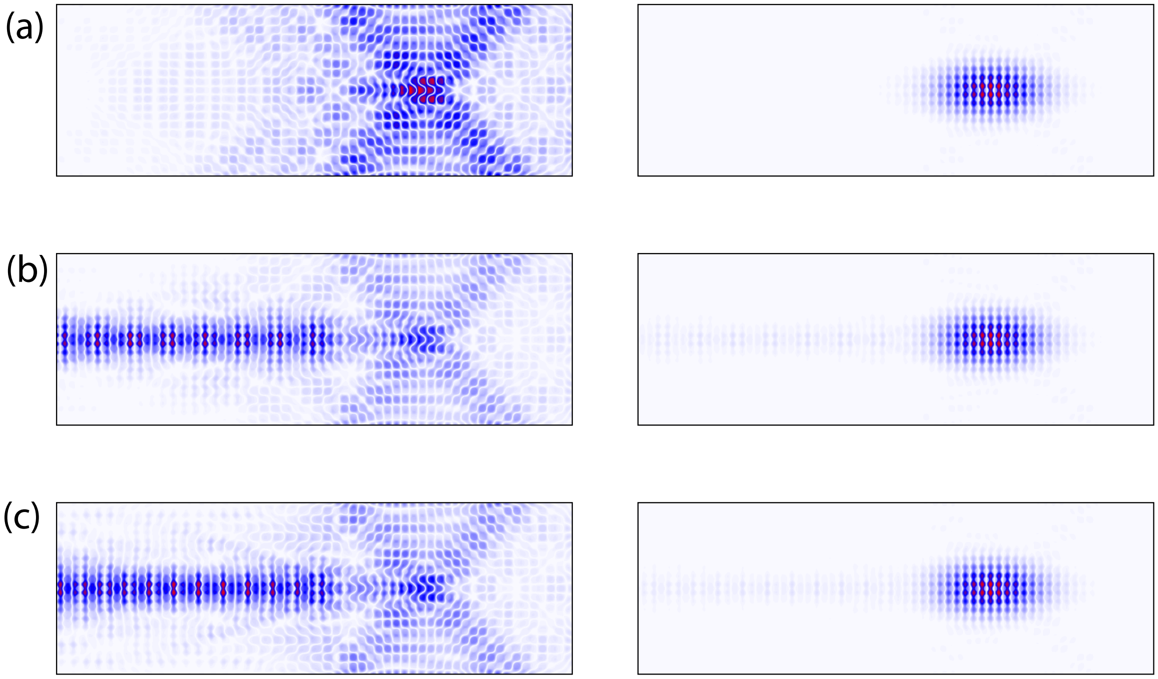

Figure 3.3: Coupling from the defect cavity to the PC waveguide for varying waveguide lattice compression at instances in time when the cavity magnetic field is a minimum (left) and a maximum (right). The envelope modulating the waveguide field is a standing wave caused by interference with reflections from the boundary of the computational domain. The diagonal radiation pattern of the cavity is due to coupling to the square lattice M points, and is sufficiently small to ensure a cavity Q of $\approx 10^5$. $|B|$ for (a) $\Lambda_x^{\text{WG}}/\Lambda_z^{\text{WG}} = 20/20$ (b) $\Lambda_x^{\text{WG}}/\Lambda_z^{\text{WG}} = 20/25$ (ratio used in the previous section) (c) $\Lambda_x^{\text{WG}}/\Lambda_z^{\text{WG}} = 20/29$.

beyond this minimum, the propagation constant (and group velocity) of the TE_1 mode when it is resonant with the cavity mode is adjusted. By choosing the compression such that this propagation constant phase matches with a fiber taper ($\Lambda_x/\Lambda_z = 20/25$ for the case considered in the previous section), an efficient *fiber-taper/PC-waveguide/PC-cavity* probe is theoretically realized.

3.3 Conclusion

The fiber-waveguide-cavity coupling technique studied in this chapter provides highly efficient fiber to PC cavity coupling. By designing the PC waveguide so that it is mode-matched with the PC cavity, nearly ideal loading of the cavity by the waveguide is possible, ensuring that the cavity-Q is not degraded by parasitic waveguide loss. The resulting fiber-to-cavity coupling channel can be used to study nonlinear effects within the PC cavity for low fiber input power, as shown in Ch. 5, and will also be useful as an efficient photon collector in future single photon source experiments using PC cavities.

Chapter 4

Probing photonic crystals with fiber tapers: experiment

In this chapter, the evanescent coupling scheme described theoretically in Ch. 2 and Ch. 3 is demonstrated experimentally. It is shown that in addition to providing efficient fiber-to-chip coupling, a fiber taper can be used as a wafer-scale probe to study the spectral and spatial properties of the optical modes supported by photonic crystal devices. By circumventing the intrinsic spatial and refractive index mismatch between optical fiber and PC devices, and taking advantage of the strong dispersion and undercut geometry inherent to PC membrane structures, efficient power transfer and rapid characterization of optical modes of a PC waveguide using fiber tapers are possible. This tool significantly simplifies and accelerates the design and fabrication cycle that must often be iterated in order to realize high quality nanophotonic elements, and provides an interface between wavelength scale nanophotonic circuits and fiber optics.

This work was originally presented in Refs. [48, 47, 25]. Section 4.2 presents experimental results demonstrating that the coherent interaction over the length of the coupling region between phase matched modes of a fiber taper and Si photonic crystal waveguide manifests in 97% power transfer. In Sec. 4.3, the fiber taper is used to probe the dispersive and spatial properties of Si PC waveguide modes. These techniques are then leveraged in Sec. 4.4 to achieve high coupling efficiency ($> 44\%$) from a fiber taper into a Si PC microcavity that is integrated with a photonic crystal waveguide.

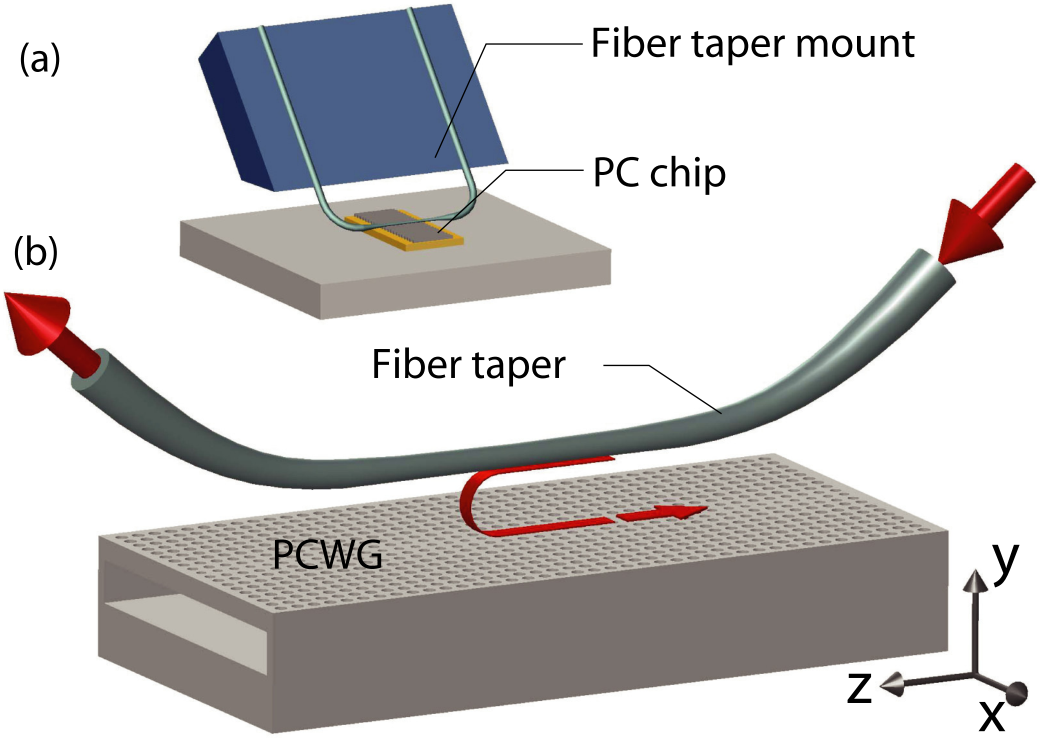

Figure 4.1: Schematic of the coupling scheme. (a) Illustration of the fiber taper in the "U-mount" configuration that is employed during taper probing of the PC chip. (b) Illustration of the fiber taper positioned in the near field of the PC waveguide, and the contra-directional coupling between waveguide that occurs on-resonance.

4.1 Experimental details

The optical coupling scheme used in this work is shown schematically in Fig. 4.1. An optical fiber taper, formed by heating and stretching a standard single-mode silica fiber, is placed above and parallel to a PC waveguide. The fiber diameter changes continuously along the length of the fiber taper, reaching a minimum diameter on the order of the wavelength of light. Light that is initially launched into the core-guided fundamental mode of the optical fiber is adiabatically converted in the taper region of the fiber into the fundamental air-guided mode, allowing the evanescent tail of the optical field to interact with the PC waveguide; coupling occurs to *phase-matched* PC waveguide modes that share a similar momentum component down the waveguide at the frequency of interest. The undercut geometry of the PC waveguide prevents the fiber taper from radiating into the PC substrate.

4.1.1 Fiber taper fabrication

The fiber tapers are fabricated by simultaneously heating and stretching a standard single mode fiber until the minimum diameter of the fiber is on the order of a wavelength. A detailed description of the apparatus and fabrication is given by M. Borselli's thesis [85]; what follows is a brief outline. Detailed descriptions of the theory of fiber taper formation can be found in Refs. [40, 41].

A standard single mode fiber designed for operation at the wavelength of interest (SMF 28 for operation at 1550 nm, Nufern 780HP for operation at 852 nm, etc.) is stripped of its protective acrylate cover over a 1 cm length. This stripped region is then placed between two magnetic fiber clamps, each of which is attached to a computer controlled single axis linear translation stage. Care is taken to ensure that the clamped section of fiber is well tensioned, and that the clamps do not impart any torque. A hydrogen torch flowing a small amount of H_2 is ignited, resulting in a gentle flame. The torch is mounted on a computer controlled single axis linear translation stage (Suruga Seiki), which controls the separation between the torch and the fiber in the direction perpendicular to the fiber. A manual three axis micrometer attaches the torch to the translation stage, and is used to fine tune the position of the flame.

Using a LabView program, the stages holding the fiber are commanded to begin moving in opposite directions at a constant speed of 1-2 μm/s, further tensioning the fiber. Simultaneously, the stage holding the H_2 flame is quickly moved to position the flame directly below the tensioned fiber. The flame heats the fiber above the glass softening point, allowing it to be stretched by the continuously moving stages holding the fiber. As the fiber is stretched, its diameter shrinks (by conservation of volume).

During this process, the optical transmission through the fiber is monitored by coupling a laser source to one end of the fiber and monitoring the output of the other end with a photodetector. As the minimum fiber diameter shrinks, the tapered region of the fiber transitions from being single-mode to multimode, often resulting in oscillations in the fiber transmission as a function of pull length due to coupling and interference between the fundamental mode and higher order modes within the fiber. However, as the minimum fiber diameter shrinks below a wavelength, the fiber becomes single-mode once again, and the transmission becomes independent of pull length[1]. This "feature" in the transmission as a function of pull time can be used to calibrate the size of the fiber taper in situ.

Once the fiber taper has reached the desired minimum diameter (usually between 0.5 μm and 1.5 μm, after $\sim$ 10-15 mm of pulling) the computer control halts the movement of the stages holding the fiber, and moves the stage positioning the H_2 flame away from the fiber. The mounts holding the fiber are then released, and the tapered fiber can then be picked up manually. Despite its small minimum diameter, the tapered region is strong enough to support the weight of a 1m long fiber tail. The fiber taper is then manually bent into a "U" shape, before being attached to a flat holder (with specially machined grooves) using adhesive tape, as illustrated in Fig. 4.1(a). Putting the fiber in a "U" shape is easily achieved by holding the two fiber tails in one hand, usually by pinching both fiber tails between the thumb and index finger. The tapered region then naturally takes on the desired "U" geometry. The fiber can then be spliced into the experimental setup, and is ready to be used for coupling to PC devices. As long as the taper is adiabatic (compared to the wavelength of light), the overall insertion loss in the fiber at the end of the pull can be extremely low, and is typically below 10%.

As discussed in Sec. 4.2, the fiber tapers fabricated as described above can only be used to probe one-dimensional arrays of devices. Recently our group [45] as well as groups in Korea [86], and Australia [87], have developed "dimpled" fiber tapers, which require an additional local heating step after the initial taper formation to create local curvature in the otherwise straight fiber taper, allowing the taper to be used to probe two-dimensional arrays of devices. These tapers are not used in the results presented here however.

4.1.2 Fiber probing measurement apparatus

The measurement apparatus necessary for fiber taper probing of PC devices is very simple. The "U"-mounted fiber taper [Fig. 4.1(a)] is attached to a three-axis stage that has manual micrometer control in the horizontal axes and a computer controlled 50 nm resolution motorized stepper in the vertical axis. The sample is mounted on a micrometer controlled goniometer (for tip-tilt adjustment) attached to a rotation stage, which in-turn is attached to a two horizontal axis computer controlled 50 nm resolution motorized stepper

---

[1] An air clad fiber with refractive index n_f is single mode if its diameter $d < 2.405\lambda/\pi\sqrt{n_f^2 - 1}$ [3]. For glass, $n_f = 1.45$, requiring $d < 0.73\lambda$.

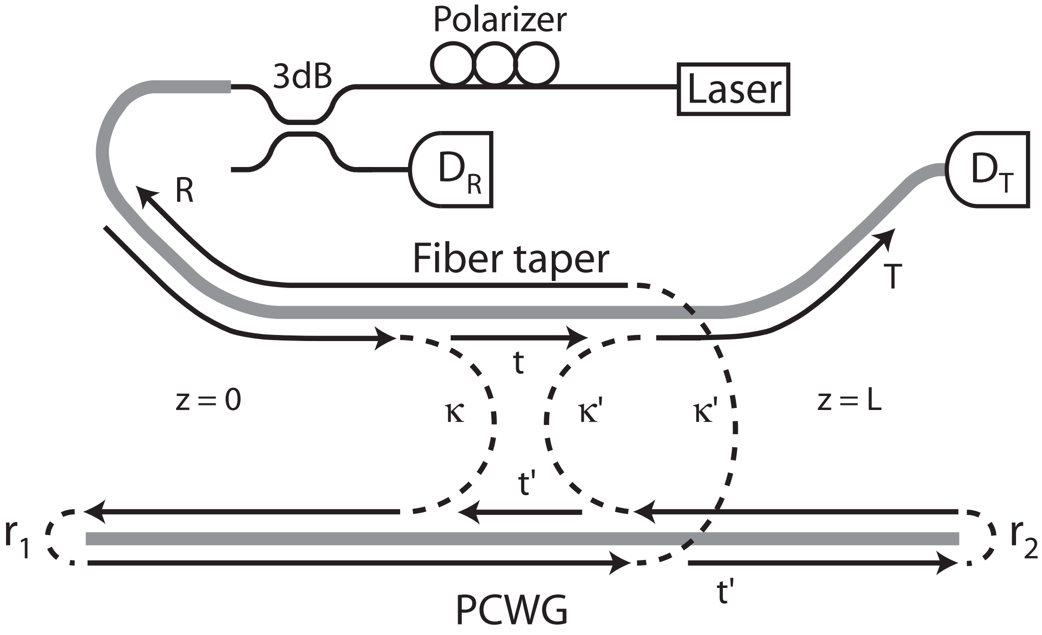

Figure 4.2: Illustration of the optical path within the fiber optic measurement apparatus. D_T and D_R represent photodetectors used to measure the transmitted and reflected signals respectively.

stage. This allows the fiber taper to be accurately positioned at varying heights and lateral displacements relative to individual PC devices, as in Fig. 4.1(b).

All of the optics used in the results presented in this chapter are fiber based. A schematic detailing the optical path within the fiber and PC device is shown in Figure 4.2. To spectrally characterize the taper-PC waveguide coupler, an external cavity swept wavelength source (New Focus "Vidia") with wavelength range 1565-1625 nm was connected to the fiber taper input via a polarizer and a 3dB coupler. At the fiber taper output, a photodetector (D_T) was connected to measure the transmitted power past the taper-PC interaction region. An additional photodetector (D_R) was connected to the second 3dB coupler input to measure the light reflected by the PC interaction region.

4.1.3 Photonic crystal fabrication

A typical fabricated array of PC waveguides is shown in Fig. 4.3. These PC devices were fabricated from a silicon-on-insulator (SOI) wafer purchased from Soitec. The Si thickness was 340 nm, and the underlying oxide was 2 μm thick. Arrays of PC devices are defined using electron beam lithography and other semiconductor processing techniques, details of which are given here and in K. Srinivasan's thesis [88].

Samples are first spin coated with a thin layer of ZEP-520 (Zeon Corporation, Japan) electron beam resist (5000 RPM for 60 seconds, followed by a 20 minute 180^{o}C bake). Electron beamwriting is used to create etch masks on the SOI wafer from the electron beam resist. The etch masks are defined using AutoCAD generated pattern files that are read by a computer program called "Bewitch" written by Oliver Dial, a former Caltech undergraduate student. Bewitch converts the AutoCAD .dxf file into a raster pattern that is output to a Hitachi S-4300 cold field emission scanning electron microscope (SEM) in the form of a set of two voltages that control the SEM x and y scan coils. The raster rate is determined by the desired electron dose per pixel; for doses between 30-60 μC/cm^2, speeds ranging from 10-250 kHz are typical, depending on the pixel size and electron beamcurrent. For the photonic crystals fabricated here, low beamcurrent (5 pA), low speed (35 kHz) beamwrites were used, with the SEM accelerating voltage set at 15 kV and the SEM magnification between 450X-1000X. This beamwriting system does not have stitching capabilities, and the maximum pattern size is limited by the field of view of the SEM at the desired beamwriting magnification (up to $\sim 100\mu\text{m} \times 100\mu\text{m}$). Arrays of patterns are written by moving the stage after a pattern is complete, and repeating the beamwrite. Often, within an array of masks employing identical input beamwriting patterns, both the lattice constant and nominal hole radius are varied by adjusting the "scaling" of the Bewitch output voltages, and the beamwriting speed (dwell time per pixel), respectively. "Proximity effects", in which the post-beamwrite hole size deviates from the desired size due to exposure of neighboring holes, are compensated for a priori in the pattern files.

For the beamwrite, it is crucial that the sample surface is level along the axis of the stage movement so that the electron beam remains focused on the surface for the entire beamwrite. In practice, the SEM sample mount surface has a slight tilt. This sample mount consists of a 2 cm diameter aluminum sample holder that is screwed into a chuck that, in turn, is interfaced with the SEM positioning stage. By rotating the position of the top sample holder surface (by adjusting how far it is screwed into the chuck), the tilt axis can be rotated relative to the beamwriting stage movement axis. At a unique position, these axes are aligned, and the height of the sample surface at the beam position does not change when the sample stage is moved along a desired axis. This setting can be determined by

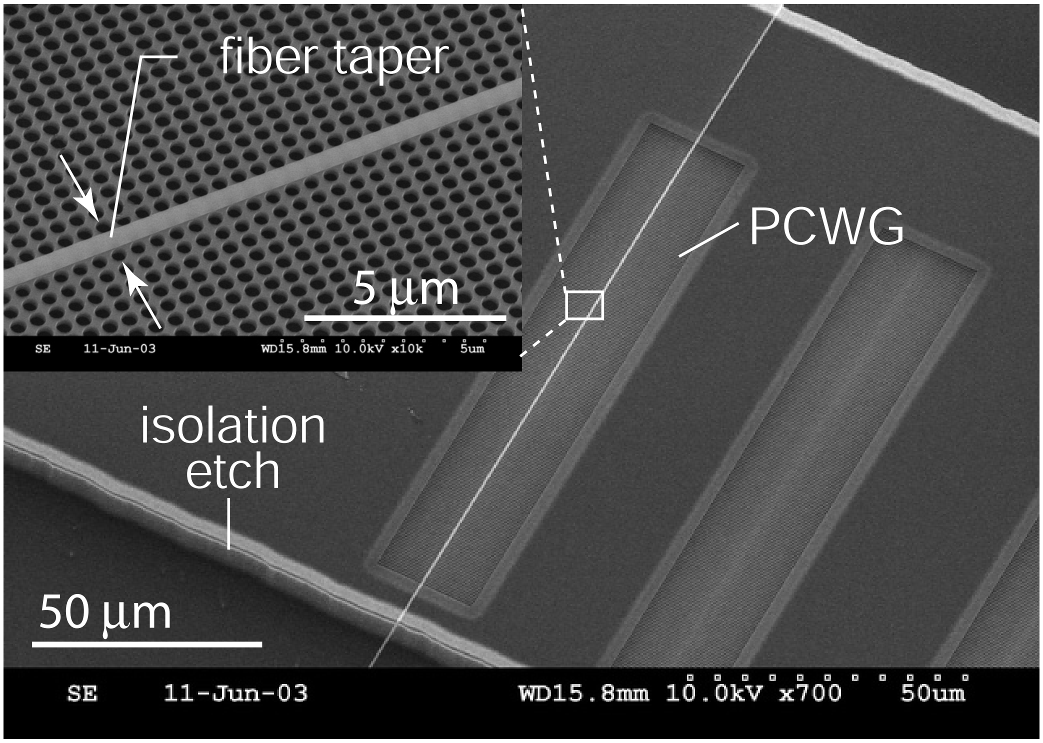

Figure 4.3: SEM image of a fabricated photonic crystal array. One of the devices is positioned below a fiber taper. Also visible is the edge of the “isolation” mesa on which the PC array is defined.

trial and error, checking each new setting by imaging an array of devices and confirming that the SEM focus does not need to be adjusted when the sample is moved along the axis of interest. Once the setting has been determined, it is important to never inadvertently adjust the sample holder, and to be consistent with the orientation of the sample on the holder. A better long term solution would be to have a custom sample holder, with a top flat surface, machined to our specifications.

After the beamwrite, a SF_6/C_4F_8 based inductively coupled plasma reactive ion etching (ICP-RIE) is used to selectively remove Si material not covered by the ZEP mask. The ratio of SF_6 to C_4F_8 was optimized to provide smooth and vertical sidewalls; too much SF_6 results in roughness, while too much C_4F_8 results in angled sidewalls. After this dry etch, the remaining ZEP is removed using acetone or an acidic H_2SO_4:H_2O_2 “Piranha” cleaning step. Photolithography is then used to cover the etched patterned regions with a photoresist mask (Shipley 5214); and a SF_6 isolation etch, > 10 μm in depth, is performed to remove unpatterned material surrounding the PC devices (Fig. 4.3). This step ensures that the fiber taper only evanescently interacts with the PC regions, and not with the surrounding unpatterned material. The suspended membrane structure is created by selectively removing the underlying silicon dioxide layer using a hydrofluoric acid wet etch for approximately three minutes at room temperature. In some cases, a short ICP-RIE etch is used to uniformly thin the top Si layer, depending on the Si thickness required by the device design. Finally, a H_2SO_4:H_2O_2 cleaning step is used to remove any organic material (such as ZEP) on the device surface.

4.2 Efficiently coupling into photonic crystal waveguides

Using the fabrication techniques described above, and the design presented in Ch. 2, PC waveguides were formed in a 300 nm thick Si membrane by introducing a grade in hole radius along the transverse direction of a compressed square lattice of air holes, as shown by Figure 4.4(a-b). As described in Ch. 2, the coupling of interest for this PC waveguide design occurs between the fundamental linearly polarized fiber mode and the TE_1 PC waveguide mode, whose field profile is shown in Fig. 4.4(a) and dispersion is shown in Fig. 4.4(c). This PC waveguide mode has a negative group velocity, resulting in *contradirectional* coupling, as depicted in Fig. 4.1(b) and Fig. 4.2.

Although the coupling efficiency of this technique can be inferred by analyzing the signal transmitted through the fiber taper as a function of wavelength and fiber taper position, a more direct measurement is to study the power coupled into and then back out of a PC waveguide. This measurement allows a lower bound for the input-output coupling efficiency to be absolutely established. In this section, by studying light that is coupled into a PC waveguide, reflected by an end-mirror at the PC waveguide termination, and then coupled into the backward propagating fiber mode, as depicted in Fig. 4.2, it is shown that the coupling has near unity efficiency.

In initial studies of evanescent coupling to such PC waveguides [46], the waveguide termination consisted of a 2 μm region of undercut Si, followed by an 8 μm length of non-undercut SOI and a final air interface. The interference from multiple reflections at the three interfaces within the waveguide termination resulted in a highly wavelength dependent reflection coefficient, making quantitative analysis of signals reflected by the PC waveguide

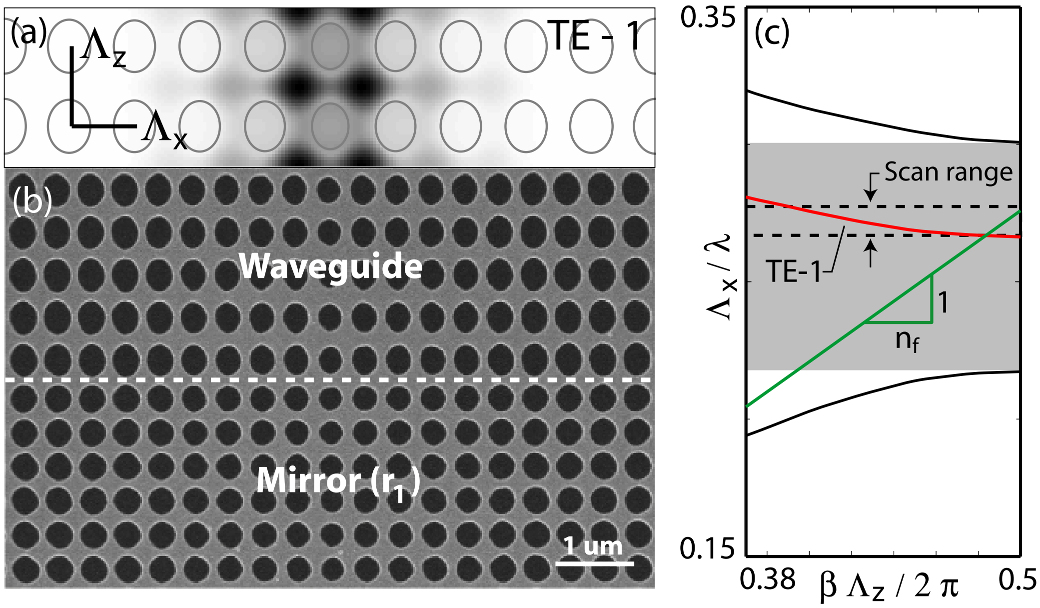

Figure 4.4: (a) Waveguide geometry and finite-difference time-domain (FDTD) calculated magnetic field profile (B_y) of the TE$_1$ mode. (b) SEM image of the high (r_1) reflectivity waveguide termination. The PC waveguide has a transverse lattice constant $\Lambda_x = 415$ nm, a longitudinal lattice constant $\Lambda_z = 536$ nm, and length $L = 200\Lambda_z$. (c) Dispersion of the PC waveguide mode, and the band edges of the mirror termination for momentum along the waveguide axis ($\hat{z}$). The shaded region is the reflection bandwidth of the mirror.

difficult. In order remove effects from multiple reflections, we engineered the waveguide terminations to have either high or low *broadband* reflectivity. On one end of the PC waveguide, shown in Figure 4.4(b), a photonic crystal mirror with high modal reflectivity (r_1) for the TE$_1$ PC waveguide mode was used. This high reflectivity end mirror was formed by removing the lattice compression of the waveguide while maintaining the transverse grade in hole radius. The change in lattice compression results in the TE$_1$ PC waveguide mode lying within the partial bandgap of the high reflectivity end mirror section (Figure 4.4(c)), while the transverse grade in hole radius reduces diffraction loss within the mirror. On the opposite end of the PC waveguide, a poor reflector with low reflectivity (r_2) was realized by removing (over several lattice constants) the transverse grade in hole radius while keeping the central waveguide hole radius fixed, resulting in a loss of transverse waveguiding within the end mirror section and allowing the TE$_1$ PC waveguide mode to diffract into the unguided bulk modes of the PC.

In the absence of reflections due to the PC waveguide termination (i.e., $r_{1,2} = 0$), the fiber-PC waveguide junction can be characterized by

$$\begin{bmatrix} a_{\mathrm{F}}^{+}(L) \\ a_{\mathrm{PC}}^{-}(0) \end{bmatrix} = \begin{bmatrix} t & \kappa' \\ \kappa & t' \end{bmatrix} \begin{bmatrix} a_{\mathrm{F}}^{+}(0) \\ a_{\mathrm{PC}}^{-}(L) \end{bmatrix}, \tag{4.1}$$

where κ and κ' are coupling coefficients, t and t' are transmission coefficients, and $a_{\mathrm{F}}^{+}(z)$ and $a_{\mathrm{PC}}^{-}(z)$ are the amplitudes of the forward propagating fundamental fiber taper mode and the backward propagating TE_1 PC waveguide mode, respectively. The coupling region extends along the z-axis, with $z = 0$ corresponding to the input and $z = L$ to the output of the coupler. As illustrated by Figure 4.2, non-zero $r_{1,2}$ introduce feedback into the system. This allows input light coupled from the forward propagating fundamental fiber taper mode into the TE_1 PC waveguide mode to be partially reflected by the PC waveguide termination, and subsequently coupled to the backward propagating fundamental fiber taper mode. In the presence of this feedback within the PC waveguide, the normalized reflected and transmitted powers in the fiber taper are given by [89]

$$\overline{T} = \left|a_{\mathrm{F}}^{+}(L)\right|^2 = \left|t + \frac{\kappa\kappa' t' r_1 r_2}{1 - r_1 t' r_2 t'}\right|^2, \tag{4.2}$$

$$\overline{R} = \left|a_{\mathrm{F}}^{-}(0)\right|^2 = \left|\frac{\kappa\kappa' r_1}{1 - r_1 t' r_2 t'}\right|^2, \tag{4.3}$$

for $a_{\mathrm{F}}^{+}(0) = 1$ and $a_{\mathrm{PC}}^{-}(L) = 0$. By measuring $\overline{T}$ and $\overline{R}$, and considering Eqs. (4.2) and (4.3), we can determine the efficiency of the fiber-PC waveguide coupling as measured by $|\kappa\kappa'|$.

In the measurements presented here, a fiber taper with 2 μm diameter was used to probe the PC waveguide of Figure 4.4(b). Figures 4.5(a) and 4.5(b) show $\overline{T}$ and $\overline{R}$ as a function of wavelength when the taper is aligned with the PC waveguide at a height of $g = 0.20$ μm, and indicate that the phase-matched wavelength is $\lambda \sim 1598 \pm 5$ nm. Data for $\overline{T}$ is normalized by the taper transmission when it is not interacting with the device. Asymmetry in the fiber taper loss about the coupling region was taken into account by repeating the measurements with the direction of propagation through the taper and the orientation of the PC waveguide sample reversed; the geometric mean of the values for $\overline{R}$ obtained from the two orientations takes any asymmetry into account. As described in Section 4.3, coupling to the guided TE_1 mode of the PC waveguide was confirmed by studying the coupling dependence upon polarization, lateral taper displacement, and fiber taper diameter. Figure 4.5(c) shows $\overline{T}$ and $\overline{R}$ at the resonant wavelength of the PC waveguide nearest the phase-matching condition [the minima and maxima in $\overline{T}(\lambda)$ and $\overline{R}(\lambda)$], as a function of taper height, g, above the PC waveguide. Included in Figure 4.5(c) is the off-resonant (away from phase-matching) transmission, $\overline{T}_{\mathrm{off}}$, through the fiber. A maximum normalized reflected power $\overline{R}_{\mathrm{max}} \sim 0.88$ was measured at a height of $g \sim 0.25$ μm, where the corresponding transmission was $\overline{T} < 0.01$. As can be seen in the wavelength scans of Figure 4.5(a), at this taper height the Fabry-Pérot resonances due to multiple reflections from the end mirrors of the PC waveguide are suppressed for wavelengths within the coupler bandwidth due to strong coupling to the fiber taper. Ignoring for the moment the effects of multiple reflections in Eq. 4.3, the maximum optical power coupling efficiency is then $|\kappa\kappa'| = \sqrt{\overline{R}_{\mathrm{max}}}/|r_1|$, where the square root dependence upon $\overline{R}_{\mathrm{max}}$ is a result of the light passing through the coupler twice in returning to the backward propagating fiber mode. Assuming the high reflectivity mirror is perfect (unity reflection), for the measured $\overline{R}_{\mathrm{max}} = 0.88$ this implies 94% coupling of optical power from taper to PC waveguide (and vice-versa).

By further comparison of $\overline{T}(g)$ and $\overline{R}(g)$ with the model given above, this time including feedback within the PC waveguide, we find that the high reflectivity PC waveguide end-mirror is imperfect and that $\overline{R}_{\mathrm{max}}$ is in fact limited by mirror reflectivity, not the efficiency of the coupling junction. For this comparison, we take the elements of the coupling matrix to satisfy the relations $|t|^2 + |\kappa|^2 = 1$, $\kappa' = \kappa$, and $t' = t^*$ of an ideal (lossless) coupling junction [89]. For the phase matched contradirectional coupling considered here, the dependence of κ on g can be approximated by $|\kappa(g)| = \tanh\left[\kappa_{\perp,0}\exp(-g/g_0)L\right]$ [78], where $\kappa_{\perp,0}$ and g_0 are constants. Substituting these relations into Eqs. (4.2) and (4.3), $\overline{T}$ and $\overline{R}$ can be fit to the experimental data with $r_{1,2}$, $\kappa_{\perp,0}$ and g_0 as free parameters[2]. Note that waveguide loss can also be included in the model; however, it is found to be small compared to the mirror loss. Figure 4.5(c) shows the fits to the data for $g \geq 0.20$ μm; for $g < 0.20$ μm non-resonant scattering loss is no longer negligible and the ideal coupling junction model breaks down. Note that the off-resonant scattering loss is observed to effect the reflected signal at a smaller taper-PC waveguide gap than for the transmitted signal, indicating that within the coupler bandwidth $1 - \overline{T}_{\mathrm{off}}$ is an overestimate of the amount of power scattered into

---

[2] We take $r_1 t' r_2 t' / |r_1 t' r_2 t'| = 1$, corresponding to a resonant condition within the PC waveguide..

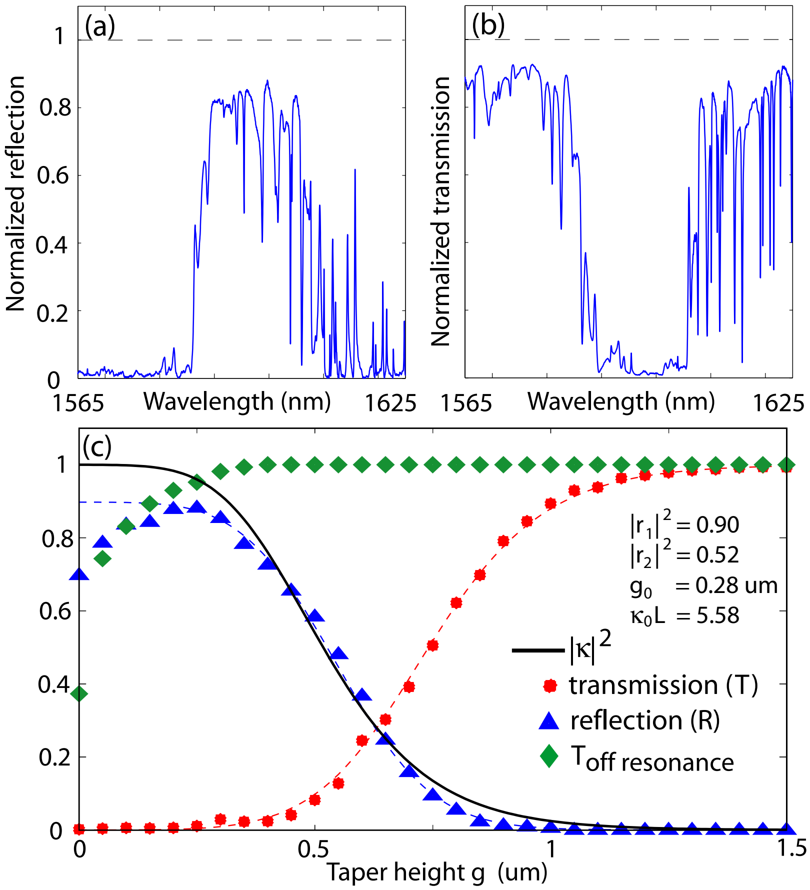

Figure 4.5: (a) Reflection and (b) transmission of the fiber taper as a function of wavelength for a taper height of 0.20 μm. Both signals were normalized to the taper transmission with the PC waveguide absent. (c) Measured taper transmission minimum, reflection maximum, and off-resonant transmission as a function of taper height. Also shown are fits to the data, and the resulting predicted coupler efficiency, $|\kappa|^2$.

radiation modes. From the fits in Figure 4.5(c), the PC waveguide end-mirror reflectivities are estimated to be $|r_1|^2 = 0.90$ and $|r_2|^2 = 0.52$, and the optical power coupling efficiency ($|\kappa|^2$) occurring at $\overline{R}_{\text{max}}$ ($g = 0.25$ μm) is approximately 97%.

4.3 Real- and k-space waveguide probing

In this section, we demonstrate that by utilizing the micron-scale lateral size and the dispersion of the fiber taper, the evanescent coupling technique can be used for mapping the bandstructure and spatial profile of PC waveguide modes. A device similar to that studied in Sec. 4.2 is characterized in this section, but with two important differences: (i) It does not have a high reflectivity end mirror, and (ii) the Si slab thickness is varied from 340 nm to 300 nm during the testing, in order to study the dispersive properties of the waveguide modes, as described below.

4.3.1 Bandstructure mapping

Figure 4.6(a) shows an approximate bandstructure of the TE-like modes of the host compressed square lattice PC slab whose dominant Fourier components are in the direction of the waveguide, and that will consequently couple most strongly with the fundamental fiber taper mode. Superimposed upon this bandstructure are the important *donor*-type defect waveguide modes. In addition to the dispersion of the TE_1 mode studied in Sec. 4.2, which has a negative group velocity and originates from the conduction band edge, the dispersion of a defect mode labeled TE_2, which has positive group velocity and originates from the second order (in the vertical direction) valence band-edge, is shown. A typical fiber taper dispersion curve is also shown, lying between the air and silica light lines.

In Figure 4.7(a-b), 3D FDTD simulations were used to accurately calculate the PC waveguide bandstructure in the regions where phase-matching to the fiber taper is expected to occur. The FDTD-calculated in-plane magnetic field profiles of the TE_1 and TE_2 PC waveguide modes (taken in the mid-plane of the dielectric slab) near their respective phase-matching points are shown in Figs. 4.6(b,c). Although one can couple to either of the TE_1 or TE_2 modes, the TE_1 mode is of primary interest here because of its fundamental nature in the vertical direction and its similar properties to that of the high-Q cavity mode discussed in Ch. 2.

In order to probe the bandstructure of the PC waveguide, the transmitted power through the fiber taper was monitored as a function of wavelength, taper position relative to the PC waveguide, and taper diameter. By varying the position along the fiber taper of the interaction region between the PC waveguide and taper (as measured by l_c, the distance from the fiber taper diameter minimum), the diameter (d) of the fiber taper, and hence the propagation constant (β) of the fiber taper mode interacting with the PC waveguide mode, could be tuned. Tuning from just below the air light-line ($d = 0.6$ μm, $n_{\mathrm{eff}} = \beta c/\omega \sim 1.05$), to just above the silica light-line ($d = 4.0$ μm, $n_{\mathrm{eff}} \sim 1.40$) was possible. Figure 4.7(c) shows the taper transmission as a function of wavelength and sample position (l_c) when the taper is centered above the PC waveguide at a height $g \sim 700$ nm from the PC waveguide surface.

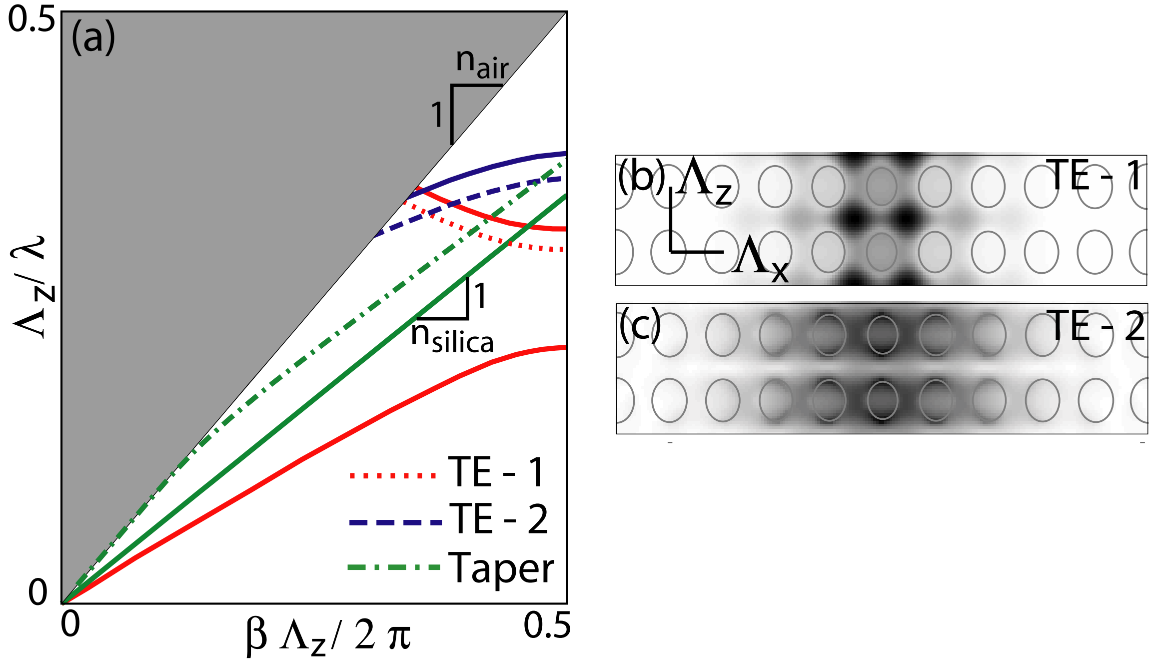

Figure 4.6: (a) Approximate bandstructure of the PC waveguide studied in Sec. 4.3. Only the TE-like modes that couple most strongly with the fiber taper are shown. The dispersion of a typical fiber taper is also indicated. (b) FDTD calculated magnetic field profile for the TE_1 mode, taken in the mid-plane of the dielectric slab. (c) Same as (b), but for the TE_2 mode.

Resonances corresponding to both the TE_1 counter- and TE_2 co-propagating modes can be identified. SEM measurements of the taper diameter as a function of position (l_c) were used to calculate the propagation constant of each resonance, allowing the PC waveguide modes' dispersion to be plotted [Fig. 4.7(e)]. The measured bandstructure is in close agreement with the FDTD calculated dispersion of Fig. 4.7(a), replicating both the negative group velocity of the TE_1 mode and the anti-crossing behavior of the odd vertical parity TE_2 and TM_1 modes. Figures 4.7(d,f) show analogous data obtained by probing the sample after the Si slab thickness, t_g, has been thinned using a short ICP-RIE dry etch to better isolate the TE_1 mode in $\omega - \beta$ space. As predicted by the FDTD simulation (Fig. 4.7(b)), the TE_1 mode is seen to shift slightly higher in frequency due to the sample thinning, whereas the higher-order TE_2 mode shifts more quickly with slab thickness and is effectively "frozen" out of the laser scan range.

As in Sec. 4.2, the dependence of the waveguide power transfer on coupling strength,

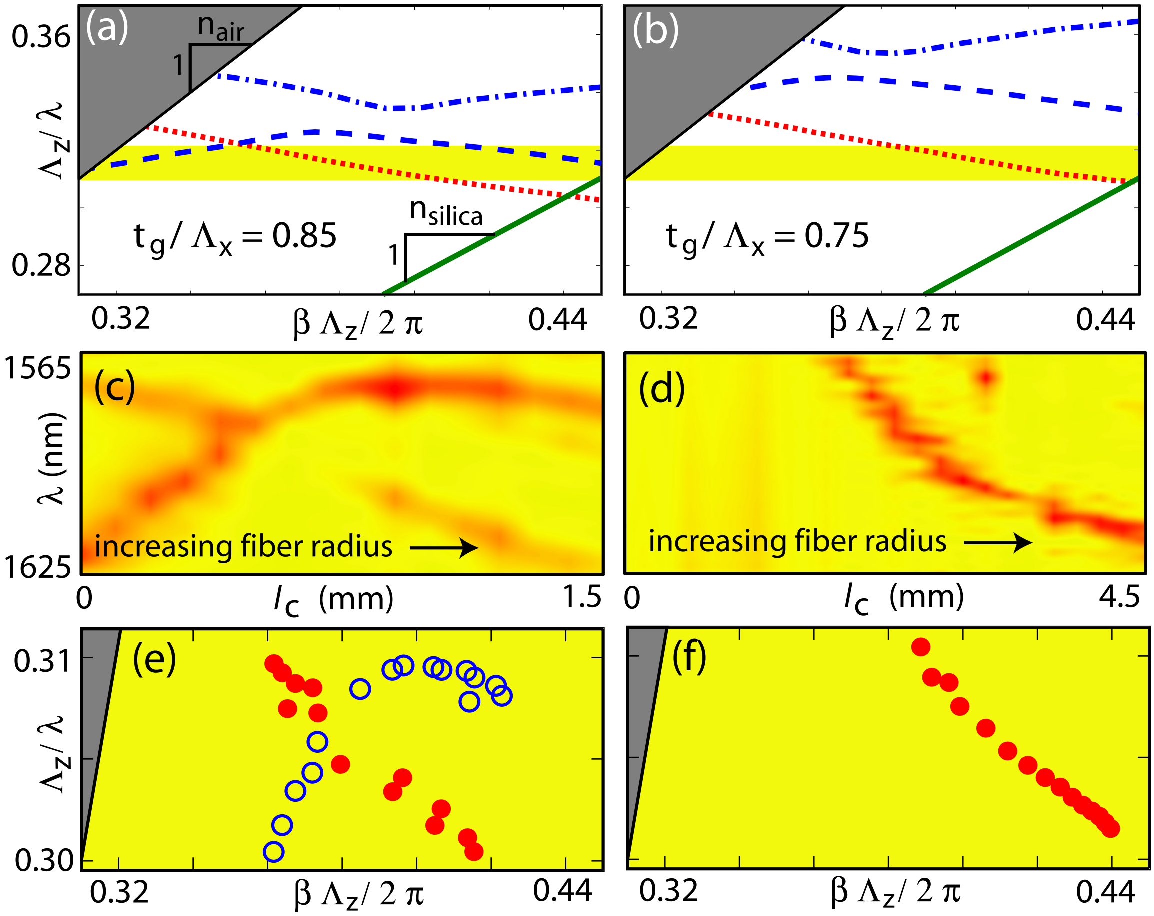

Figure 4.7: 3D FDTD calculated dispersion of the TE_1 (dotted line), TE_2 (dashed line), and TM_1 (dot-dashed line) modes for the (a) un-thinned (t_g = 340 nm), and (b) thinned (t_g = 300 nm) graded lattice PC waveguide membrane structure ($n_{Si} = 3.4$). Measured transmission through the fiber taper as a function of wavelength and position along the tapered fiber for (c) un-thinned sample and (d) thinned sample (different tapers were used for the thinned and un-thinned samples, so the transmission versus l_c data cannot be compared directly). Transmission minimum (phase-matched point) for each mode in the (e) un-thinned and (f) thinned sample as a function of propagation constant. In (a-b), the lightly shaded regions correspond to the tuning range of the laser source used.

and the overall efficiency of the coupling process were studied by varying the gap between the fiber taper and PC waveguide. Figure 4.8(a) shows the transmission through the fiber taper, with the coupling region occurring at a taper diameter of $d = 1.9$ μm for varying taper heights above the thinned PC waveguide. Figure 4.8(b) shows the same measurement, but with the coupling region occurring at a taper diameter of $d = 1.0$ μm, and for a PC waveguide with slightly smaller nominal hole size. In both cases, the central resonance

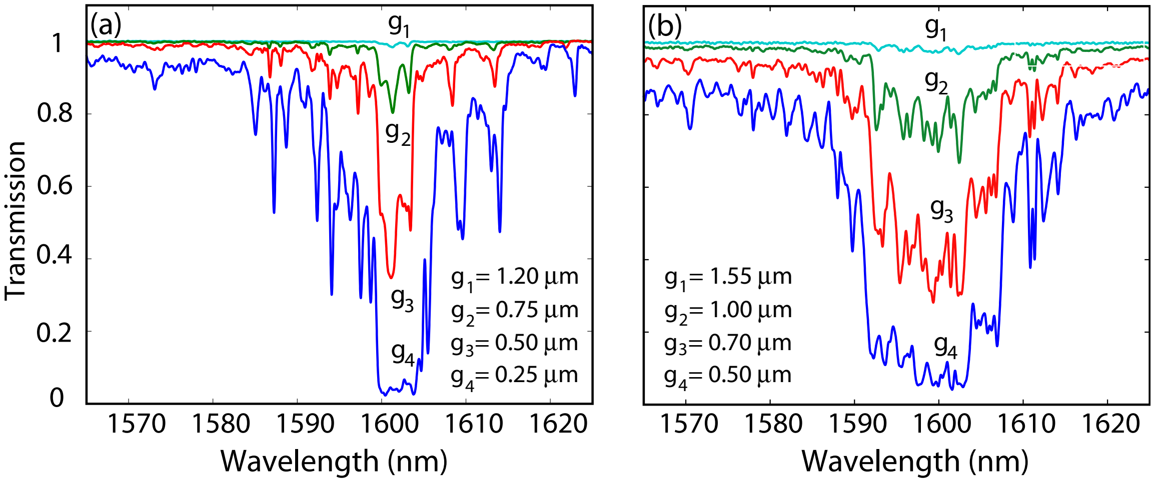

Figure 4.8: Coupling characteristics from the fundamental fiber taper mode to the TE$_1$ PC waveguide mode of the thinned sample ($t_g = 300$ nm). Transmission versus wavelength for (a) 1.9μm and (b) 1.0 μm diameter taper coupling regions for varying taper-PC waveguide gap, g. Transmission in (a,b) has been normalized to the transmission through the fiber-taper in absence of the PC waveguide.

feature occurring around $\lambda = 1600$ nm is the coupling to the TE$_1$ mode of the PC waveguide.

The coupler bandwidth was 20 nm for coupling with small diameter taper regions ($d \sim 1.0$ μm) and less than 10 nm for coupling to regions of large taper diameter ($d \sim 1.9$ μm). This effect has two main contributions: the variation of the TE$_1$ PC waveguide mode group velocity at different points in the bandstructure ($|n_{\text{g}}| = |c\,\delta\beta/\delta\omega| \sim 4$ - 6); and the variation in the taper diameter and, hence, propagation constant along the length of the 100 μm PC waveguide, ($\delta\beta/\delta d \sim (0.084, 0.36)\,\omega/c$ μm^{-1}, for $d = (1.9, 1.0)$ μm).

4.3.2 Real-space mapping

The micron-scale lateral extent of the fiber taper was also used as a near-field probe of the localized nature of the PC waveguide modes. Fig. 4.9(a) shows the coupling dependence of the TE$_1$ PC waveguide mode as a function of lateral displacement of the taper from the center of the PC waveguide (Δx). The full-width at half-maximum of $1 - \overline{T}_{\text{min}}$ versus Δx (for a 1.0 μm diameter taper coupling region) was measured to be ~ 1.84 μm, in close agreement with the value (2.08 μm) obtained using a simple coupled mode theory from Ch. 2. When the taper is displaced laterally, coupling to a second resonance [see Fig. 4.9(b)] is observed. This resonance has dispersion that is similar to that of the TE$_1$ mode, but shifted

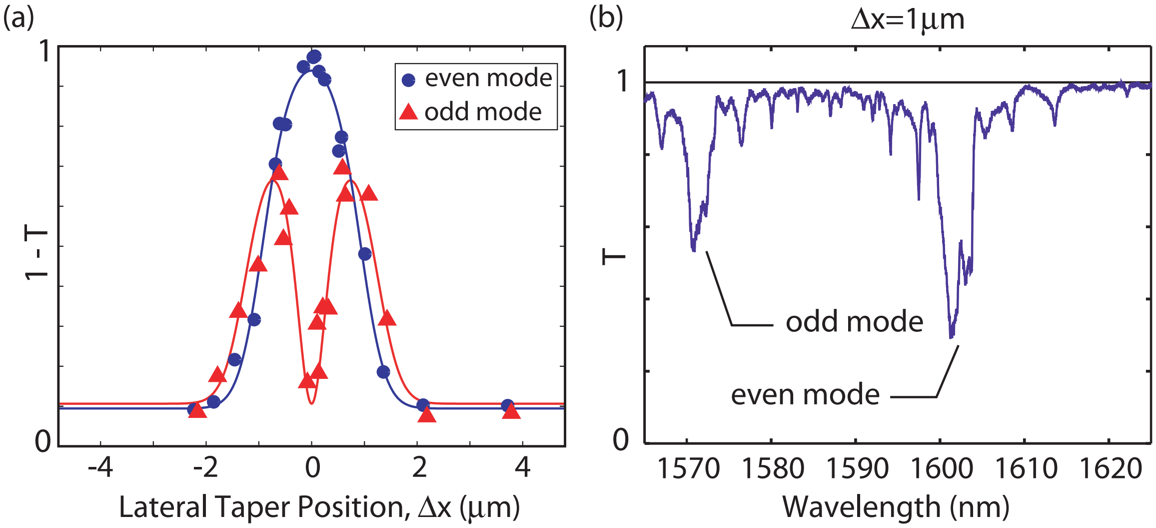

Figure 4.9: Coupling characteristics from the fundamental fiber taper mode to the TE_1 PC waveguide mode of the thinned sample ($t_g = 300$ nm). (a) $1 - \overline{T}_{\mathrm{min}}$ versus lateral position (Δx) of the 1.0 μm diameter fiber taper relative to the center of the PC waveguide ($g = 400$ nm). (b) Transmission versus wavelength for $\Delta x \sim 1$ μm. Transmission in (a-b) has been normalized to the transmission through the fiber-taper in absence of the PC waveguide.

~ 30 nm lower in wavelength, and corresponds to coupling to the odd (about x) counterpart to the TE_1 mode. The coupling is a result of the broken mirror symmetry about x induced by the taper when $|\Delta x| > 0$, and is a further demonstration of the local nature of the taper probe.

4.4 Efficient coupling into PC microcavities

Having demonstrated above that nearly ideal coupling from a fiber taper into a well characterized PC waveguide mode is possible, the next step was to integrate the fiber-coupled PC waveguide with a PC microcavity, and efficiently fiber couple light into and out of the wavelength scale resonator. Following the design presented in Ch. 2, and using the same fabrication techniques described Sec. 4.1.3 to realize the PC waveguide devices discussed above, integrated PC cavity-PC waveguide devices were fabricated in a $t_g = 340$nm thick layer of Si. A typical device is shown in Fig. 4.10, which also shows regions in which unpatterned silicon was removed to allow taper probing of the device. In addition to isolating the PC devices on a mesa of height ~ 10 μm, a trench extending diagonally from the cavity

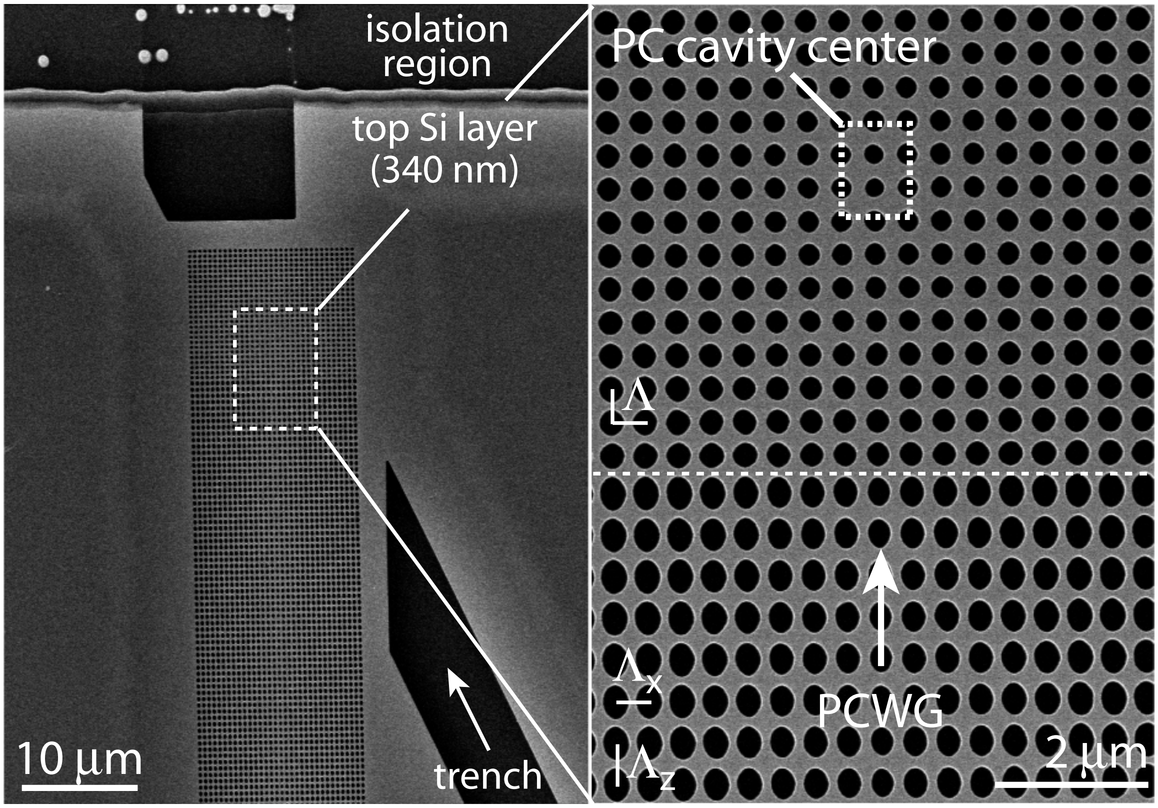

Figure 4.10: SEM image of an integrated PC waveguide-PC cavity sample. The PC cavity and PC waveguide have lattice constants $\Lambda \sim 430$ nm, $\Lambda_x \sim 430$ nm, and $\Lambda_z \sim 550$ nm. The surrounding silicon material has been removed to form a diagonal trench and an isolated mesa structure to enable fiber taper probing.

was defined. This allowed the cavity to be probed directly by the fiber taper, independently from the waveguide, as in Ref. [11]. However, as described below, much more efficient coupling to the PC cavity was also performed by aligning the fiber taper along the axis of the PC waveguide and coupling through the PC waveguide into the PC cavity, as described theoretically in Ch. 2

Direct taper-cavity probing

With the taper aligned with the etched trench, the spectral and spatial properties of the PC cavity modes were probed directly [Fig. 4.11(a), taper position (ii)], as in Ref. [11]. The trench prevented the fiber taper from interacting with the unpatterned silicon, and light was coupled directly from the fiber taper into the high-Q PC cavity modes. Although this

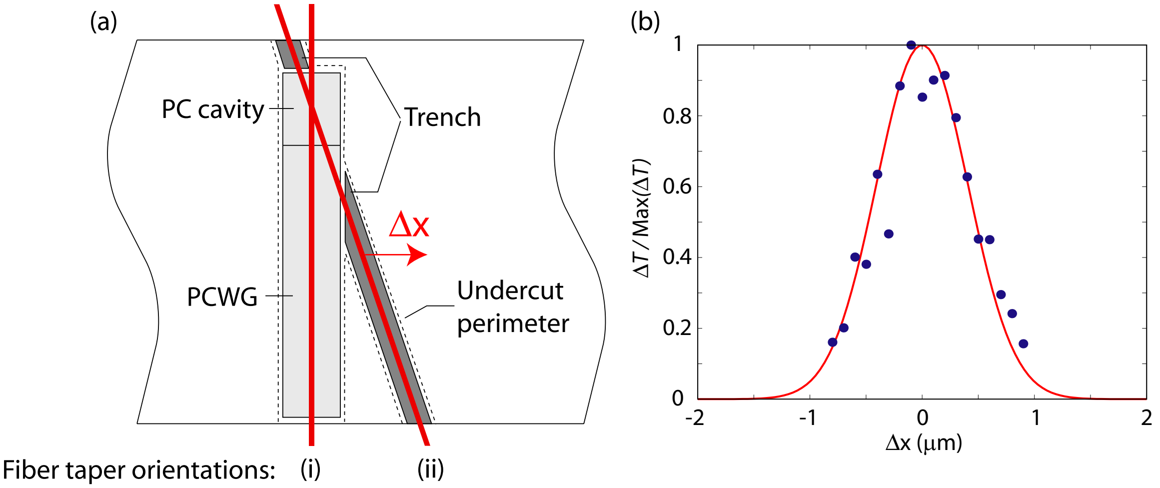

Figure 4.11: (a) Illustration of the device and fiber taper orientation for (i) efficient PC waveguide mediated taper probing of the cavity, and (ii) direct taper probing of the cavity. (b) Normalized depth of the transmission resonance ($\Delta\overline{T}$) at $\lambda_o \sim 1589.7$, as a function of lateral taper displacement relative to the center of the PC cavity, during direct taper probing (taper in orientation (ii)).

coupling is inefficient ($\Delta\overline{T}$ =1-10%, $I \ll 1$), it allowed the frequency of the A_2^0 cavity mode to be independently determined.

In the device studied here, when the taper was aligned with the trench and positioned ~ 500 nm above the cavity, a sharp dip in $\overline{T}$ was observed at a wavelength of $\lambda_o \sim 1589.7$ nm. It was confirmed that this was due to coupling to a localized cavity mode by studying the depth of the resonance as the taper was displaced laterally ($|\Delta x| > 0$) relative to the center of the PC-cavity. The measured normalized resonance depth as a function of taper displacement is shown in Fig. 4.11(b), and has a halfwidth of 480 nm, consistent with previous studies of the localized A_2^0 cavity mode [11]. To further aid with the initial differentiation between resonant features in the transmission that are due to cavity modes from those that are due to delocalized Fabry-Pérot reflections within the PC lattice, it is useful to monitor the reflected signal in the fiber taper during this step. Because of their localized nature, PC cavity modes couple into the backward and forward propagating fiber taper modes with equal efficiency, usually resulting in distinct features in the reflected signal.

PC waveguide mediated taper-cavity probing

The fiber taper was then aligned above and parallel to the PC waveguide (Fig. 4.11(a), taper position (i)). At taper-PC waveguide phase-matching wavelengths, $\overline{T}$ decreases resonantly as power is coupled from the taper into the PC waveguide; coupling to the TE$_1$ PC waveguide mode was verified by studying the dispersive and spatial properties of the coupling, as in Sec. 4.3. The fiber taper-PC waveguide coupling bandwidth was adjusted to overlap with the wavelength of the A_2^0 cavity mode using two mechanisms. Coarse tuning was obtained by adjusting, from sample to sample, the nominal hole size and longitudinal lattice constant (Λ_z) of the PC waveguide. Fine tuning of the coupler's center wavelength over a 100 nm wavelength range was obtained by adjusting the position, and, hence, the diameter of the fiber taper region coupled to the PC waveguide [47]. Different degrees of cavity loading were also studied by adjusting the number of periods (9-11) of air holes between the center of the PC cavity and the end of the PC waveguide. In the device studied below (shown in Fig. 4.10) the PC cavity was fabricated with nine periods on the side adjacent to the PC waveguide and 18 periods on the side opposite the PC waveguide .

Figure 4.12(a) shows the normalized reflected fiber signal, $\overline{R}$, for a taper diameter $d \sim 1$ μm, which aligns the taper-PC waveguide coupler bandwidth with the A_2^0 PC cavity mode wavelength. This signal is normalized to the taper transmission in absence of the PC waveguide, and since light passes through the taper-PC waveguide coupler twice, the signal is given by $\overline{R} = \eta_{wg}^2 R_o$, where η_{wg} is the taper-PC waveguide coupling efficiency. Note that both R_o and η_{wg} are frequency dependent. In Fig. 4.12(a), the peak in $\overline{R}$ around $\lambda \sim 1590$ nm corresponds to the phase-matched point of the fiber taper and the TE$_1$ PC waveguide mode. From the peak value of $\overline{R}_{\max} = 0.53$, a maximum taper-PC waveguide coupling efficiency of $\eta_{wg} \sim 73\%$ was estimated, where the off-resonant R_o is taken to be unity. This value is lower than the 97% obtained in Sec. 4.2 due to coupling to additional higher-order (normal to the Si slab) PC waveguide modes that interfere with the coupling to the fundamental TE$_1$ PC waveguide mode for strong taper-PC waveguide coupling. This can be avoided in future devices by increasing the nominal PC waveguide hole size relative to that in the PC-cavity or reducing the Si slab thickness, effectively freezing out the higher-order PC waveguide modes [47].

The sharp dip in reflection at $\lambda \sim 1589.7$ nm, shown in detail in Fig. 4.12(b), corresponds

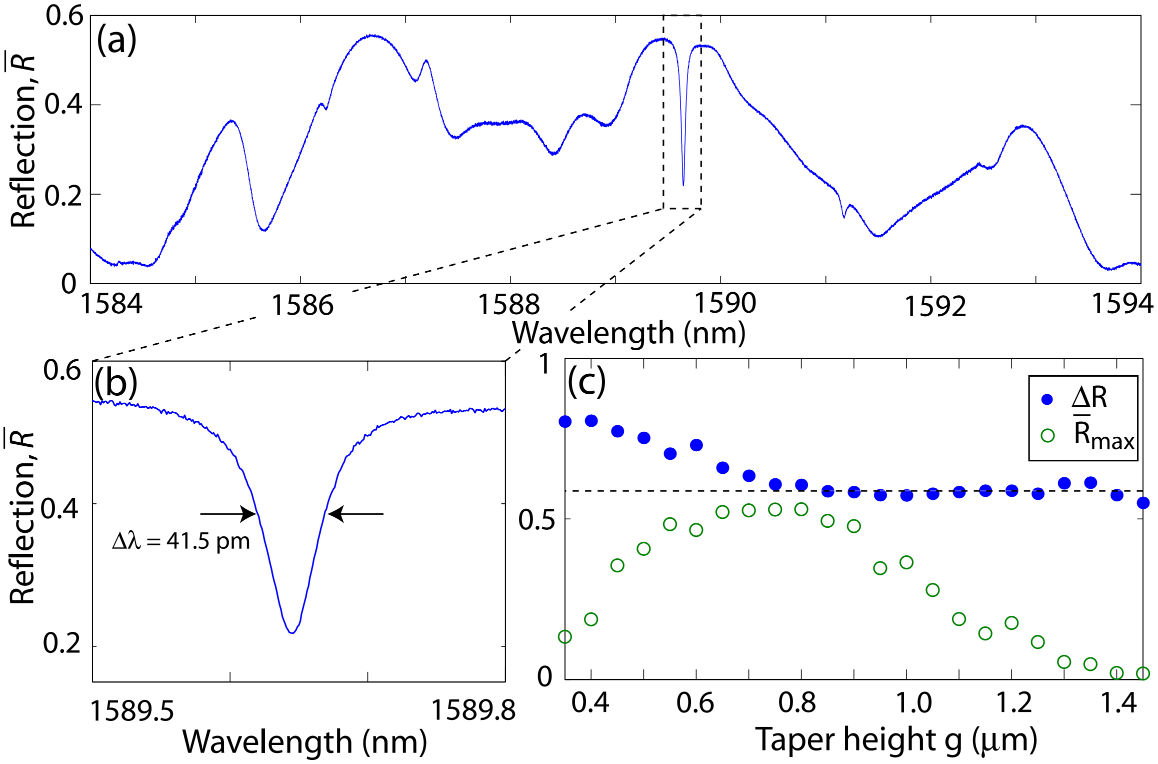

Figure 4.12: (a) Measured reflected taper signal as a function of input wavelength (taper diameter $d \sim 1$ μm, taper height $g = 0.80$ μm). The sharp dip at $\lambda \sim 1589.7$ nm, highlighted in panel (b), corresponds to coupling to the A_2^0 cavity mode. (c) Maximum reflected signal (slightly detuned from the A_2^0 resonance line), and resonance reflection contrast as a function of taper height. The dashed line at $\Delta R = 0.6$ shows the PC waveguide-cavity drop efficiency, which is independent of the fiber taper position for $g \geq 0.8$ μm.

to resonant excitation of the A_2^0 PC cavity mode, as confirmed by the direct fiber probing of the cavity described above. The other broad features in $\overline{R}$ correspond to weak Fabry-Pérot effects of the PC waveguide, and weak interference between the TE_1 mode and higher order PC waveguide modes. The reflected fiber taper signal as a function of taper-PC waveguide gap height, g, is shown in Fig. 4.12(c). For $g \geq 0.8$ μm, $\overline{R}_{\text{max}}$ increases with decreasing g as the coupling from the fiber taper to the TE_1 PC waveguide mode becomes stronger. The resonance contrast, $\Delta R = 1 - R_o(\omega_o) = (\overline{R}_{\text{max}} - \overline{R}(\omega_o))/\overline{R}_{\text{max}}$, remains constant, since the PC waveguide-cavity interaction is independent of the fiber taper to PC waveguide coupling. For smaller taper-PC waveguide gap heights, $g < 0.8$ μm, fiber taper coupling into higher order PC waveguide modes and radiation modes becomes appreciable, and $\overline{R}_{\text{max}}$ decreases for decreased taper height. The corresponding increase in ΔR seen in Fig. 4.12(c) is a result of interference between the TE_1 mode and higher-order PC waveguide modes that are excited and collected by the taper, and is not a manifestation of improved coupling between the TE_1 PC waveguide mode and the A_2^0 PC cavity mode. Direct coupling between the taper and the cavity is negligible here.

From a Lorentzian fit to the A_2^0 cavity resonance dip in $R_o(\omega)$, the normalized on-resonance reflected power is estimated to be $R_o(\omega_o) = 0.40$, corresponding to an undercoupled $K = 0.225$. The loaded quality factor as measured by the reflected signal linewidth is $Q_T = 3.8 \times 10^4$. Substituting these values into Eq. (3.4) gives the cavity mode quality factor due to parasitic loading and intrinsic losses, $Q_{i+P} = 4.7 \times 10^4$. Previous measurements of similar PC cavity devices without an external PC waveguide load yielded intrinsic quality factors of 4×10^4 [11], strongly indicating that the parasitic loading of the PC cavity by the PC waveguide is minimal, and $I \sim 1$ for this PC cavity-waveguide system. The high ideality of this coupling scheme should be contrasted with previous direct taper measurements of the PC cavities [11], whose coupling was limited to a maximum value, $K = 0.018$, with an ideality of $I \sim 0.035$ (corresponding to a resonance depth of 7%, $Q_T = 2.2 \times 10^4$).

The efficiency of power transfer from the fiber taper into the PC cavity is given by $\eta_{in} = \eta_{wg}\Delta R \approx 44\%$. This corresponds to the *total* percentage of photons input to the fiber taper that are dropped by the PC cavity. Based upon these measurements, in the case of an internal cavity source, such as an atom or a quantum dot, the efficiency of light collection into the fiber taper for this PC cavity system would be $\eta_{out} = \eta_{wg}\eta_0 \approx 13\%$ ($\eta_0 \approx 18\%$). As the tapers themselves are of comparably very low loss, with typical losses associated with the tapering process less than 10%, these values accurately estimate the *overall* optical fiber coupling efficiency. Finally, note that previous measurements of near-ideal coupling between the fiber taper and PC waveguide indicate that by adjusting the PC waveguide as described above to improve η_{wg}, η_{in}, and η_{out} can be increased to 58% and 18%, respectively. More substantially, adjustments in the coupling parameter, K, towards over-coupling by decreasing the number of air-hole periods between the PC cavity and the PC waveguide can result in significant increases in η_{in} and η_{out}, with minimal penalty in loaded Q-factor for $I \sim 1$.

4.5 Conclusion

The evanescent fiber taper to PC waveguide coupling technique demonstrated is this chapter provides unprecedentedly high coupling efficiency, as well as a means to study both the dispersive and spatial properties of bound photonic crystal waveguide modes, and an optical channel to source high-Q PC microcavities. These results confirm the theoretical predictions of the previous chapters, and reinforce the utility of fiber tapers as wafer-scale probes for photonic crystal devices. In the next chapter, we will leverage this technique to study the nonlinear optical properties the PC microcavity.

Chapter 5

Nonlinear optics in silicon photonic crystal cavities

Owing to the ultra-small mode volume and long resonant photon lifetimes of PC cavities, the resulting stored electromagnetic energy density can be extremely large even for modest input powers ($<$ mW), resulting in highly nonlinear behavior of the resonant cavity system. Having demonstrated in Ch. 4 a technique for efficiently coupling light into a small mode volume, high-Q, silicon PC cavity, we now have the tools necessary to study nonlinear optical properties intrinsic to these devices.

In this chapter, we present results demonstrating optical bistability in a silicon PC cavity for 100 μW dropped CW cavity power. By comparing a model of the relevant nonlinear optical process within these devices with the observed results, we are able to understand which nonlinear effects play the largest role, and extract parameters describing physical properties of Si within nanophotonic devices. In particular, we predict sub-nanosecond free carrier lifetimes in the cavity, which, due to the small mode volume and large effective surface area of these devices, are significantly shorter than are found in bulk Si.

Since the publication of these results in Ref. [25], a number of groups have observed similar nonlinear effects in PC microcavities, and have taken advantage of them to implement low-power high-speed optical switches [26, 90, 91, 92]. In addition, from a technological perspective, the importance of nonlinear absorption and free-carriers effects in nanophotonic devices fabricated from silicon has continued to grow, as recent progress in optical modulators [93] and wavelength converters [94, 95] has relied upon engineering devices while taking these effects into careful consideration.

We begin in Sec. 5.1 by generalizing the linear waveguide-cavity coupling theory of Sec. 3.1 to include nonlinear processes that depend upon the magnitude of the internally stored cavity energy. Higher power measurements in which nonlinear effects become apparent are studied in Sec. 5.2, and the model presented in Sec. 5.1 is used to estimate the scale of the various nonlinear effects within the silicon PC cavity.

5.1 Modeling nonlinear absorption and dispersion in a microcavity

In order to account for nonlinear effects one may modify the (linear) analysis of Sec. 3.1 by allowing the various cavity and coupling parameters to depend upon the stored cavity energy, a reasonably easy quantity to estimate from experimental measurements. In this section, relevant nonlinear processes are explicitly incorporated into the description of the cavity response through use of carefully defined effective modal volumes and confinement factors appropriate to nonlinear processes in high-index contrast photonic crystal structures. We begin with a description of nonlinear absorption, which tends to drive the steady-state nonlinear response of the PC cavities studied here.

5.1.1 Nonlinear absorption

Nonlinear absorption adds power dependent loss to the photonic crystal cavity, degrading the quality factor as the internal cavity energy is increased, which in turn modifies the coupling efficiency from the PC waveguide loading channel. This effect is incorporated into the formalism presented in Sec. 3.1 by writing the intrinsic cavity loss rate, γ^i, explicitly in terms of its various linear and nonlinear components:

$$\gamma^i(U) = \gamma_{\text{rad}} + \gamma_{\text{lin}} + \overline{\gamma}_{\text{TPA}}(U) + \overline{\gamma}_{\text{FCA}}(U). \tag{5.1}$$

At low power, the "cold cavity" loss rate is given by γ_{rad} and γ_{lin}, which represent loss due to radiation and linear material absorption, respectively. Power dependent nonlinear loss is given here by $\overline{\gamma}_{\text{TPA}}$ and $\overline{\gamma}_{\text{FCA}}$, which represent two-photon and free-carrier absorption, respectively; other nonlinear absorption processes can be included analogously. The coupling parameter K and the quality factor Q_{i+P} depend on γ^i, requiring the solution of a system of self-consistent equations for U in order to determine the on-resonance cavity response for a given PC waveguide input power P_i:

$$U = \frac{4K(U)}{(1+K(U))^2}\frac{Q_{i+P}(U)}{\omega_o}P_i, \tag{5.2}$$

$$K(U) = \frac{\gamma_o^e}{\gamma^i(U) + \sum_{j>0}\gamma_j^e}, \tag{5.3}$$

$$\frac{\omega_o}{Q_{i+P}(U)} = \gamma^i(U) + \sum_{j>0}\gamma_j^e. \tag{5.4}$$

Before Eqs. (5.2-5.4) can be solved, explicit expressions for the energy-dependent contributions to γ^i are required. Beginning with relations for nonlinear absorption in bulk media, and taking into account the complicated geometry of the PC cavity, we now derive expressions for $\overline{\gamma}_{\text{TPA}}$ and $\overline{\gamma}_{\text{FCA}}$. These expressions can be written in terms of the internal cavity energy, known material parameters, and modal parameters that account for the mode shape and localization of the PC cavity field.

Two-photon absorption

The 1500 nm operating band of the devices studied in this work lies in the bandgap of the host silicon material. For the doping densities of the p-type silicon membrane used to form the PC cavity ($\rho \sim 1-3\ \Omega\cdot\text{cm}$, $N_A < 10^{16}\ \text{cm}^{-3}$), free-carrier absorption due to ionized dopants is small ($\alpha_{fc} \sim 10^{-2}\ \text{cm}^{-1}$). Two-photon absorption, however, is significant[60, 96, 97, 98, 99], especially in the highly localized PC cavities. For a given field distribution, the (time-averaged) two-photon absorption loss rate at position $\mathbf{r}$ can be written as

$$\gamma_{\text{TPA}}(\mathbf{r}) = \beta'(\mathbf{r})\frac{1}{2}\epsilon_o n^2(\mathbf{r})E^2(\mathbf{r}), \tag{5.5}$$

where $E(\mathbf{r})$ is the *amplitude* of the complex electric field pattern, $\mathbf{E}(\mathbf{r})$, of the resonant mode of the cavity; ϵ_o is the permittivity of free space; and $n(\mathbf{r})$ is the local (unperturbed) refractive index. The real, physical electric field of the resonant cavity mode can be written in terms of the complex mode pattern as $\mathbf{E}(\mathbf{r},t) = (\mathbf{E}(\mathbf{r})e^{-i\omega_o t} + \mathbf{E}^*(\mathbf{r})e^{+i\omega_o t})/2$. The *material* parameter, β', describes the strength of the two-photon absorption process, and can be related to the usual two-photon absorption coefficient, β, that relates intensity to loss per unit length, by $\beta' = (c/n_g)^2\beta$, where c is the speed of light in vacuum and n_g is the group velocity index associated with the measurement of β. Typically, for bulk material measurements where waveguiding is minimal and material dispersion is small, n_g can be taken to be equal to n.

In high-index-contrast photonic crystals, E, n, and β' depend strongly on the spatial coordinate $\mathbf{r}$. Equation (5.5) describes the local two-photon absorption rate; the effective modal two-photon absorption rate that characterizes the absorption of the entire cavity mode is given by a weighted average of the local absorption rate [100, 101],

$$\overline{\gamma}_{\text{TPA}} = \frac{\int \gamma_{\text{TPA}}(\mathbf{r}) n^2(\mathbf{r}) E^2(\mathbf{r}) d\mathbf{r}}{\int n^2(\mathbf{r}) E^2(\mathbf{r}) d\mathbf{r}} = \overline{\beta'} \frac{U}{V_{\text{TPA}}}, \tag{5.6}$$

where $\overline{\beta'}$ and V_{TPA} are defined as

$$\overline{\beta'} = \frac{\int \beta'(\mathbf{r}) n^4(\mathbf{r}) E^4(\mathbf{r}) d\mathbf{r}}{\int n^4(\mathbf{r}) E^4(\mathbf{r}) d\mathbf{r}} \tag{5.7}$$

$$V_{\text{TPA}} = \frac{\left(\int n^2(\mathbf{r}) E^2(\mathbf{r}) d\mathbf{r}\right)^2}{\int n^4(\mathbf{r}) E^4(\mathbf{r}) d\mathbf{r}}. \tag{5.8}$$

In a photonic crystal formed by air holes in silicon, $\beta'(\mathbf{r}) = \beta'_{\text{Si}}$ inside the silicon, and $\beta'(\mathbf{r}) = 0$ in the air, so that Eq. (5.6) can be written as,

$$\overline{\gamma}_{\text{TPA}} = \Gamma_{\text{TPA}} \beta'_{\text{Si}} \frac{U}{V_{\text{TPA}}} \tag{5.9}$$

$$\Gamma_{\text{TPA}} = \frac{\int_{\text{Si}} n^4(\mathbf{r}) E^4(\mathbf{r}) d\mathbf{r}}{\int n^4(\mathbf{r}) E^4(\mathbf{r}) d\mathbf{r}}, \tag{5.10}$$

for which $\int_{\text{Si}}$ only integrates over the silicon region of the PC cavity.

Free-carrier absorption

Although, as mentioned above, the (linear) free-carrier absorption due to the ionized dopants of the silicon layer used for the PC cavities in this work is negligible on the scale of other losses, two-photon absorption gives rise to a steady-state population of electron and hole free-carriers far above this equilibrium value. Two-photon absorption induced free-carrier absorption thus plays a significant role in the silicon PC cavity nonlinear response. At position $\mathbf{r}$ in the cavity, assuming a simple Drude model, the optical loss rate due to free-carrier absorption is

$$\gamma_{\text{FCA}} = \sigma'(\mathbf{r}) N(\mathbf{r}), \tag{5.11}$$

where σ' is related to the material dependent free-carrier cross-section, σ, by $\sigma' = \sigma(c/n_g)$, and $N(\mathbf{r})$ is the free-carrier density. In silicon, it has been demonstrated experimentally [102] that this model correctly describes absorption by both electrons and holes, albeit with unique values of $\sigma'_{e,h}$ for each carrier type. Here we let N represent the number of electron-hole pairs and take $\sigma' = \sigma'_e + \sigma'_h$. We neglect the small ($< 1 \times 10^{16}$ cm^{-3}) background free-carrier hole density due to the ionized acceptors of the p-type Si layer used in this work.

In general, the derivation of the free-carrier density for a given two-photon absorbed power distribution requires a microscopic theory that takes into account carrier diffusion, carrier-carrier scattering effects (Auger recombination, for instance), and, in the highly porous PC cavities, local surface recombination effects. In lieu of such an analysis, we approximate the free-carrier density distribution by considering the local two-photon absorbed power,

$$N(\mathbf{r}) = \frac{\tau p_{\text{TPA}}(\mathbf{r})}{2\hbar\omega_o}, \tag{5.12}$$

where τ is a free-carrier lifetime, and $p_{\text{TPA}}(\mathbf{r})$ is the local absorbed power *density* due to two-photon absorption,

$$p_{\text{TPA}}(\mathbf{r}) = \frac{1}{2}\epsilon_o n^2(\mathbf{r}) E^2(\mathbf{r}) \gamma_{\text{TPA}}(\mathbf{r}). \tag{5.13}$$

Equation (5.12) neglects non-local effects due to spatial carrier diffusion by assuming that $N(\mathbf{r})$ depends only on the power absorbed at position $\mathbf{r}$; however, it does correlate regions of strong two-photon absorption with high free-carrier density. Also, since τ generally depends on N and on the proximity to surfaces, τ will have a spatial dependence within the cavity. We neglect this effect here, and let τ represent an effective free-carrier lifetime for all the carriers in the cavity region[1]. Combining Eqs. (5.11), (5.12), and (5.13), an effective modal free-carrier absorption rate can be written as

$$\overline{\gamma}_{\text{FCA}} = \frac{\frac{\tau}{2\hbar\omega_o}\int \left(\sigma'(\mathbf{r})\frac{1}{2}\epsilon_o n^2(\mathbf{r}) E^2(\mathbf{r}) \gamma_{\text{TPA}}(\mathbf{r})\right) n^2(\mathbf{r}) E^2(\mathbf{r}) d\mathbf{r}}{\int n^2(\mathbf{r}) E^2(\mathbf{r}) d\mathbf{r}}. \tag{5.14}$$

Substituting Eq. (5.5) for $\gamma_{\text{TPA}}(\mathbf{r})$, the modal loss rate due to free-carrier absorption in the

---

[1] In using the approximate theory above, in which regions of high two-photon absorbed power are correlated with high steady-state carrier density, we better approximate the cavity "volume" of interest, and consequently the effective free-carrier lifetime better represents the average time a free-carrier stays in the region of the PC cavity mode.

porous silicon photonic crystals considered here can be written as

$$\overline{\gamma}_{\mathrm{FCA}} = \Gamma_{\mathrm{FCA}} \left(\frac{\tau \sigma'_{\mathrm{Si}} \beta'_{\mathrm{Si}}}{2\hbar\omega_o} \frac{U^2}{V^2_{\mathrm{FCA}}} \right), \tag{5.15}$$

with effective confinement factor and mode volume defined as

$$\Gamma_{\mathrm{FCA}} = \frac{\int_{\mathrm{Si}} n^6(\mathbf{r}) E^6(\mathbf{r}) d\mathbf{r}}{\int n^6(\mathbf{r}) E^6(\mathbf{r}) d\mathbf{r}} \tag{5.16}$$

$$V^2_{\mathrm{FCA}} = \frac{\left(\int n^2(\mathbf{r}) E^2(\mathbf{r}) d\mathbf{r}\right)^3}{\int n^6(\mathbf{r}) E^6(\mathbf{r}) d\mathbf{r}}. \tag{5.17}$$

Equations (5.15) and (5.9) represent the total loss rate of photons from the cavity due to free-carrier and two-photon absorption, respectively. These expressions depend only on material parameters; modal confinement factors, $\Gamma_{\mathrm{TPA,FCA}}$; effective mode volumes, $V_{\mathrm{TPA,FCA}}$; and the internal cavity energy, U. The modal parameters take into account the non-trivial geometry and field distribution of the cavity mode, and can be determined for a given mode from FDTD simulations. Including expressions (5.9) and (5.15) in γ^i, Eqs. (5.2-5.4) can be solved iteratively for Q_{i+P} and K, which characterize the on-resonance nonlinear response of the cavity for a given input power.

5.1.2 Nonlinear and thermal dispersion

In addition to modifying the cavity quality factor, large cavity energy densities also modify the refractive index of the cavity, resulting in a power dependent resonance frequency. Here we consider the role of the Kerr effect, free-carrier dispersion, and heating due to linear and nonlinear absorption, on the dispersive response of the PC cavity. The refractive index shift induced through the processes considered here is a function of both space and internal cavity energy. The corresponding renormalization of the resonant cavity frequency can be approximated using first order perturbation theory as

$$\frac{\Delta\omega_o(U)}{\omega_o} = -\Delta\overline{n}(U), \tag{5.18}$$

where the normalized modal index shift, $\Delta\overline{n}(U)$, is given by an average of the (normalized) local refractive index shift, $\Delta n(\mathbf{r})/n(\mathbf{r})$:

$$\Delta\overline{n}(U) = \frac{\int\left(\frac{\Delta n(\mathbf{r})}{n(\mathbf{r})}\right)n^2(\mathbf{r})E^2(\mathbf{r})d\mathbf{r}}{\int n^2(\mathbf{r})E^2(\mathbf{r})d\mathbf{r}}. \tag{5.19}$$

This energy dependent frequency shift, together with the energy dependent loss described in Sec. 5.1.1, modifies the Lorentzian frequency dependence of the cavity response:

$$R_o(\omega) = 1 - \frac{4K(U)}{(1+K(U))^2}\frac{(\delta\omega/2)^2}{(\omega-\omega_o-\Delta\omega_o(U))^2+(\delta\omega(U)/2)^2}. \tag{5.20}$$

For a given input power P_i and frequency ω, U is given by

$$U = \frac{P_d}{\gamma_{i+P}} = (1-R_o(\omega))\frac{Q_{i+P}(U)}{\omega_o}P_i, \tag{5.21}$$

where $P_d = (1-R_o(\omega))P_i$ is the frequency dependent dropped power in the resonant cavity.

For input powers sufficient to shift $\Delta\omega_o > \sqrt{3}\delta\omega/2$, the frequency response described by Eq. (5.20) is bistable, and can be exploited for applications including temperature locking and optical switching [103, 24, 104]. In order to solve Eq. (5.20) for the cavity response, it is necessary to derive expressions for each of the constituents of $\Delta\overline{n}$ as a function of U. We begin with the Kerr effect.

Kerr effect

The time-averaged local index shift induced by the Kerr effect is

$$\Delta n_{\text{Kerr}}(\mathbf{r}) = n_2'(\mathbf{r})\frac{1}{2}\epsilon_o n^2(\mathbf{r})E^2(\mathbf{r}), \tag{5.22}$$

where $n_2'(\mathbf{r})$ is a material parameter, and is related to the usual n_2 coefficient relating intensity to refractive index shift [105] by $n_2' = (c/n_g)n_2$. In a silicon PC cavity, neglecting the tensor nature of the third order susceptibility, the normalized modal index change due to the Kerr effect can be written as

$$\Delta\overline{n}_{\text{Kerr}}(U) = \frac{\Gamma_{\text{Kerr}}}{n_{\text{Si}}}\left(n_{2,\text{Si}}'\frac{U}{V_{\text{Kerr}}}\right), \tag{5.23}$$

with $n'_{2,\mathrm{Si}}$ and n_{Si} being the Kerr coefficient and linear refractive index of Si, respectively. A similar, more general expression, is given in Ref. [106]. As both the Kerr effect and two-photon absorption (TPA) share the same dependence on field strength, the confinement factor and effective mode volume associated with the Kerr effect are equal to those of TPA:

$$\Gamma_{\mathrm{Kerr}} = \Gamma_{\mathrm{TPA}} \tag{5.24}$$

$$V_{\mathrm{Kerr}} = V_{\mathrm{TPA}}. \tag{5.25}$$

Free-carrier dispersion

Dispersion due to free-carrier electron-hole pairs is given by[2]

$$\Delta n_{\mathrm{FCD}}(\mathbf{r}) = -\zeta(\mathbf{r})N(\mathbf{r}), \tag{5.27}$$

where $\zeta(\mathbf{r})$ is a material parameter with units of volume. Following the derivation of $\overline{\gamma}_{\mathrm{FCA}}$, the normalized modal index change is

$$\Delta\overline{n}_{\mathrm{FCD}}(U) = -\frac{\Gamma_{\mathrm{FCD}}}{n_{\mathrm{Si}}}\left(\frac{\tau\zeta_{\mathrm{Si}}\beta'_{\mathrm{Si}}}{2\hbar\omega_o}\frac{U^2}{V_{\mathrm{FCD}}^2}\right), \tag{5.28}$$

with

$$\Gamma_{\mathrm{FCD}} = \Gamma_{\mathrm{FCA}} \tag{5.29}$$

$$V_{\mathrm{FCD}} = V_{\mathrm{FCA}}. \tag{5.30}$$

Thermal dispersion

It is also necessary to consider the effect of thermal heating due to optical absorption on the refractive index of the PC cavity. The normalized modal index shift is given by

$$\Delta\overline{n}_{\mathrm{th}} = \frac{\int\left(\frac{1}{n(\mathbf{r})}\frac{dn}{dT}(\mathbf{r})\Delta T(\mathbf{r})\right)n^2(\mathbf{r})E^2(\mathbf{r})d\mathbf{r}}{\int n^2(\mathbf{r})E^2(\mathbf{r})d\mathbf{r}}. \tag{5.31}$$

---

[2] Experimental results [102] indicate that this Drude model must be modified slightly to accurately describe the contribution from hole free-carriers in silicon, which scales with $N_h^{0.8}$:

$$\Delta n_{\mathrm{FCD,Si}} = -\left[\zeta_{e,\mathrm{Si}}N_e + (\zeta_{h,\mathrm{Si}}N_h)^{0.8}\right]. \tag{5.26}$$

For simplicity, we ignore this in the following analysis, and note that the modification is straightforward, and is included in later numerical results.

Here $\Delta T(\mathbf{r})$ is the local temperature change due to the absorbed optical power density within the cavity, and dn/dT is a material dependent thermo-optical coefficient. Neglecting differences in the spatial distributions of the contributions to $\Delta T(\mathbf{r})$ from the various absorption processes, and assuming that $\Delta T(\mathbf{r})$ scales linearly with absorbed power density for a fixed spatial heating distribution, the modal thermal shift can be written as

$$\Delta\overline{n}_{\text{th}}(U) = \frac{\Gamma_{\text{th}}}{n_{\text{Si}}}\left(\frac{dn_{\text{Si}}}{dT}\frac{dT}{dP_{\text{abs}}}P_{\text{abs}}(U)\right) \tag{5.32}$$

where,

$$P_{\text{abs}}(U) = \left(\gamma_{\text{lin}} + \overline{\gamma}_{\text{TPA}}(U) + \overline{\gamma}_{\text{FCA}}(U^2)\right)U. \tag{5.33}$$

$\Gamma_{\text{th}} = \int_{\text{Si}} n^2E^2d\mathbf{r}/\int n^2E^2d\mathbf{r}$ is a confinement factor that accounts for the fact that only the semiconductor experiences an appreciable index shift, and dT/dP_{abs} is the thermal resistance of the PC cavity, which relates the mean modal temperature change to the total absorbed power. In what follows, we lump these two factors together, yielding an effective thermal resistance of the PC cavity.

From Eqs. (5.23), (5.28), and (5.32), the total modal index change and corresponding resonance frequency shift can be determined as a function of cavity energy. The nonlinear lineshape described by Eq. (5.20) can then be calculated iteratively as a function of input power when combined with the power dependent loss model of sub-section 5.1.1. This is used below in Sec. 5.2 to estimate the scale of the different nonlinear processes in silicon PC microcavities.

As a final comment, we note that the above analysis has assumed steady-state optical, carrier, and thermal distributions, whereas the transient response of such structures is of significant practical interest for applications such as high speed switching. Although the Kerr nonlinearity, two-photon absorption, free-carrier absorption, and free-carrier dispersion all depend on the electronic structure of the semiconductor material, the sub-micron geometry typical of photonic crystals can also play an important role. For example, the surfaces introduced by the slab and air hole geometry of planar PC cavities can significantly modify the free-carrier lifetime, τ, compared to that in bulk material [103, 107, 108]. Similarly, the thermal response time scales inversely with the spatial scale of the optically absorbing region, and depends upon the geometry and the material dependent thermal properties of a given structure [105]. Although not the focus of the work presented here, an inkling of these effects is seen in the sub-nanosecond estimated effective free-carrier lifetime in the silicon PC cavity studied below.

5.2 Nonlinear measurements

The nonlinear response of the PC cavity was studied by measuring the dependence of the reflected signal lineshape on the power input to the PC waveguide. Figure 5.1 shows wavelength scans of the cavity response, R_o, for varying power, P_t, input to the fiber taper. Each scan was obtained by dividing the normalized reflected signal, $\overline{R}$, by the slowly varying taper-PC waveguide coupler lineshape, $\eta_{wg}^2(\omega)$. In all of the measurements, the fiber taper was aligned near the optimal taper-PC waveguide coupling position, and the wavelength of the laser source was scanned in the direction of increasing λ. P_t was determined by taking taper insertion loss into account, and measuring the taper input power with a calibrated power meter.

Increasing the power in the fiber taper, and consequently the PC waveguide, results in three readily observable changes in R_o: (i) a decrease in the resonance contrast, ΔR_o; (ii) a shift $\Delta\omega_o$ in the resonance frequency ω_o; and (iii) the broadening and asymmetric distortion of the resonance lineshape, eventually leading to a "snap" in the reflection response characteristic of bistability [109]. Here we use the theory presented in Sec. 5.1 to show that these features are due to nonlinear absorption and dispersion in the PC cavity.

Figure 5.2(a) shows P_d, the on-resonance power dropped into the PC cavity, as a function of P_i, the power incident on the cavity from the PC waveguide. P_d is measured from $P_d = \Delta R_o(P_i)P_i$, and P_i is related to the taper input power by $P_i = \eta_{wg}(\omega_o)P_t$. For small P_i, P_d increases with a constant slope equal to the "cold cavity" value of $\Delta R_o = 0.60$ measured in Sec. 4.4. For larger P_i, P_d becomes sub-linear versus P_i, as loss due to nonlinear absorption becomes appreciable compared to the other loss channels of the PC cavity. In the context of the analysis of Sec. 5.1, γ^i increases with increasing P_d, degrading K, and decreasing ΔR_o (for $K < 1$). From the "cold cavity" η_0 and Q_T measured in the previous

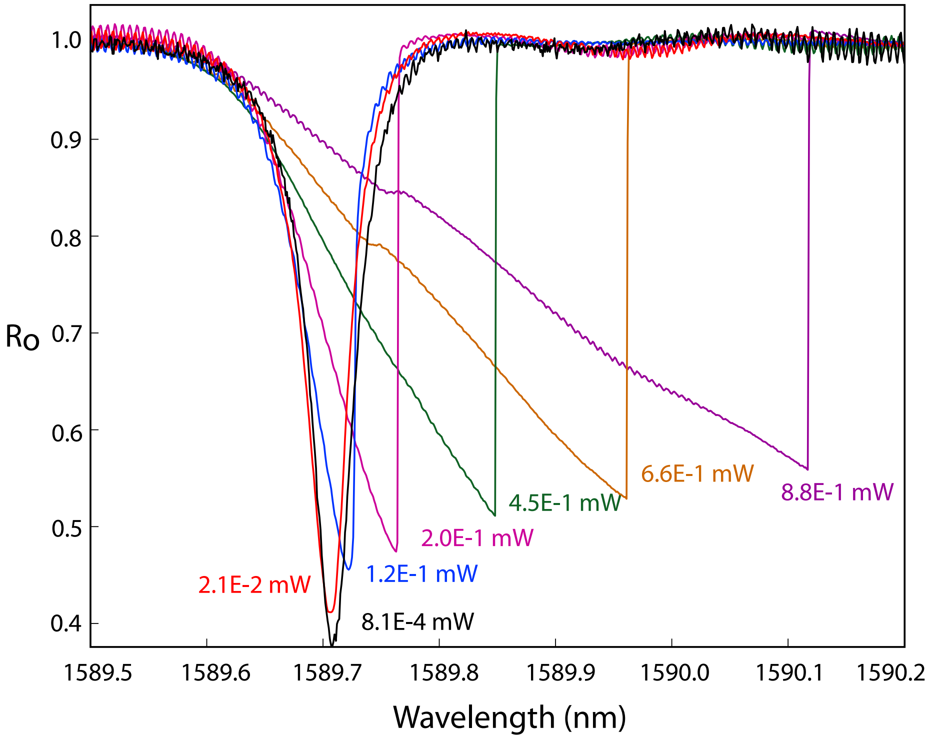

Figure 5.1: (a) Measured cavity response as a function of input wavelength, for varying PC waveguide power (taper diameter $d \sim 1$ μm, taper height $g = 0.80$ μm).

section, the power dependent $Q_{i+P}(P_i)$ can be extracted from $\Delta R_o(P_i)$ through the relation:

$$Q_{i+P}(P_i) = K(\Delta R_o(P_i))\frac{Q_T(P_i = 0)}{\eta_0(P_i = 0)}. \tag{5.34}$$

Equation (5.34) is useful for powers where nonlinear effects distort the Lorentzian lineshape, and $\lambda_o/\delta\lambda$ is not an accurate measure of $Q_T(P_i)$. Using Eqs. (5.34) and (3.7), the internal cavity energy, U, can be calculated from P_i and ΔR_o.

Figure 5.2(b) shows a plot of the measured $\Delta\lambda_o$, the resonance wavelength shift, as a function of U [3]. This plot has several noteworthy properties: First, the wavelength shift is nonlinear in U, indicating that nonlinear processes such as free-carrier dispersion and heating through nonlinear absorption must be taking effect. Also, for small U, the resonance wavelength is seen to blue shift. In the 1550 nm wavelength band of operation, both dn_{Si}/dT and $n_{2,\text{Si}}$ are > 0, while $d(\Delta n_{\text{FCD}})/dU < 0$, indicating that free-carrier dispersion is the

---

[3] Note that the sharp transition edge associated with optical bistability occurs at the cavity resonance wavelength when scanning from blue to red, thus an accurate measure of $\Delta\lambda_o$ can be made.

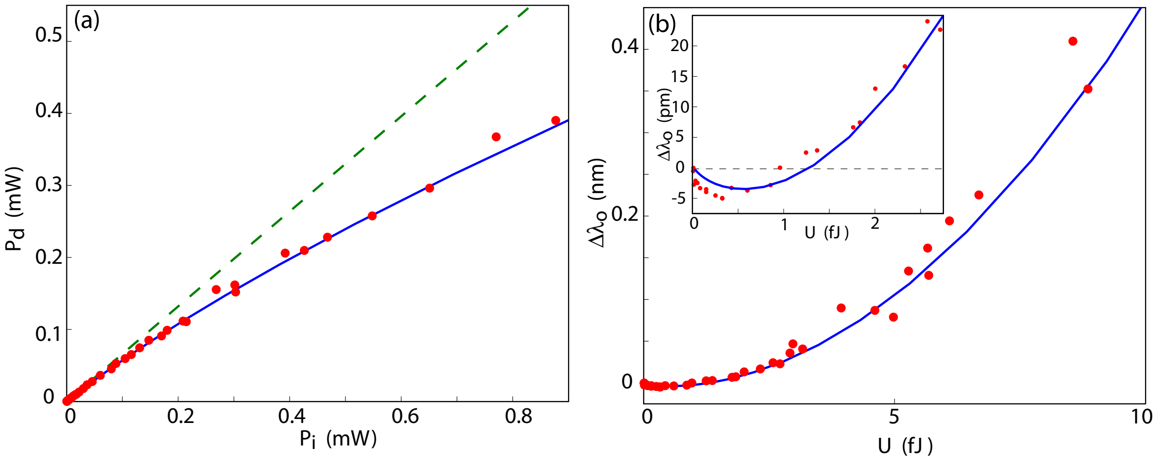

Figure 5.2: (a) Power dropped (P_d) into the cavity as a function of power in the PC waveguide (P_i). The dashed line shows the expected result in absence of nonlinear cavity loss. (b) Resonance wavelength shift as a function of internal cavity energy. Solid blue lines in both Figs. show simulated results.

dominant dispersive process at low input powers. For $U > 0.34$ fJ ($P_d > 10$ μW), the resonance wavelength begins to red shift, indicating that thermal or Kerr effects dominate for large internal cavity energy. Also, note that for a stored cavity energy as low as $U \sim 3$ fJ ($P_d \sim 100$ μW) the cavity response is bistable with $\Delta\lambda_o = 35$ pm $\sim \sqrt{3}\delta\lambda/2$.

In order to estimate the contributions of the various nonlinear processes to the effects discussed above, the absorptive, $P_d(P_i)$, and dispersive, $\Delta\lambda(P_i)$, data were fit using the model presented in Sec. 5.1. Specifically, Eqs. (5.2-5.4) were solved for P_d and U as a function of P_i, and Eq. (5.18) was used to calculate $\Delta\lambda_o$. The free parameters in this model were taken as: (i) the effective free-carrier lifetime, τ; (ii) the effective thermal resistance of the PC cavity, $\Gamma_{\text{th}} dT/dP_{\text{abs}}$; and (iii) the fraction of the "cold cavity" loss that is due to linear absorption (as opposed to radiation), $\eta_{\text{lin}} = \gamma_{\text{lin}}/(\gamma_{\text{lin}} + \gamma_{\text{rad}})$. The material and modal constants used are listed in Table 5.1.

Table 5.1: Nonlinear optical coefficients for the Si photonic crystal microcavity.

Parameter	Value	Units	Source
V_{TPA}	4.90	$(\lambda_o/n_{\mathrm{Si}})^3$	FDTD[b]
V_{FCA}	3.56	$(\lambda_o/n_{\mathrm{Si}})^3$	FDTD[b]
Γ_{TPA}	0.982	-	FDTD[b]
Γ_{FCA}	0.997	-	FDTD[b]
n_{Si}	3.45	-	[110, 102]
σ_{Si}	14.5×10^{-22}	m^2	[110, 102]
ζ^e_{Si}	8.8×10^{-28}	m^3	[110, 102]
ζ^h_{Si}	4.6×10^{-28}	m^3	[110, 102]
$n_{2,\mathrm{Si}}$	4.4×10^{-18}	$\mathrm{m}^2 \cdot \mathrm{W}^{-1}$	[96]
β_{Si}	8.4×10^{-12}	$\mathrm{m} \cdot \mathrm{W}^{-1}$	[96][a]
dn_{Si}/dT	1.86×10^{-4}	K^{-1}	[111]

[a] Average of the two quoted values for Si⟨110⟩ and Si⟨111⟩.

[b] Calculated from FDTD generated fields of the A_2^0 cavity mode of the graded square lattice cavity studied here.

As has been observed in studies of silicon optical waveguides [97], we find that a strong dependence of τ on carrier density is required for our model, to accurately reproduce *both* the dispersive and absorptive data represented in Figs. 5.3(a) and (b). In order to account for a carrier density dependent lifetime in our model the following procedure was used: With $\Gamma_{\mathrm{th}} dT/dP_{\mathrm{abs}}$ and η_{lin} held fixed, $\tau(P_i)$ was determined for each input power from a least squares fit to $\Delta\lambda_o(P_i)$ and $P_d(P_i)$. Since there are two data points for each input power, one dispersive and one absorptive, the optimum $\tau(P_i)$ has a non-zero residual error.

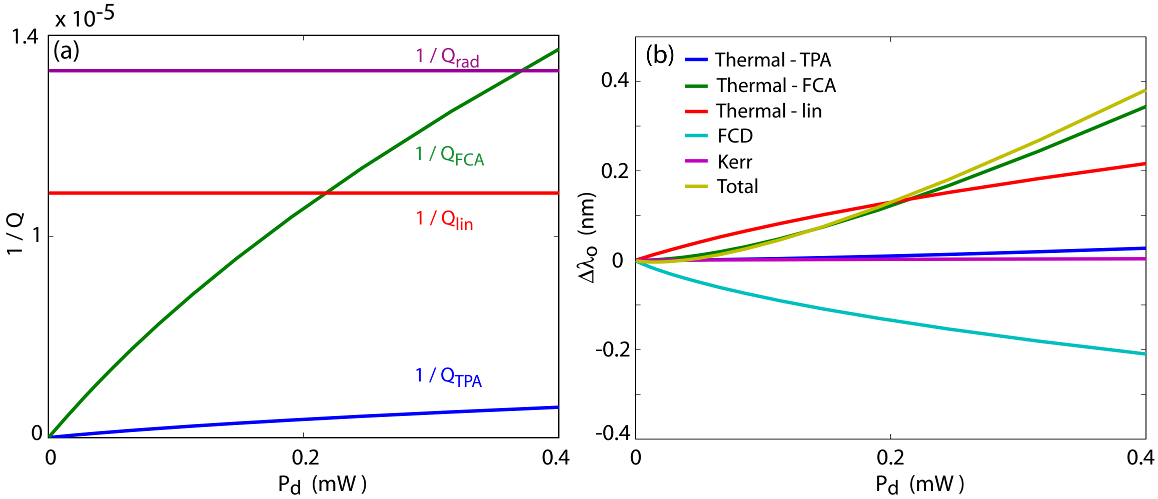

Figure 5.3: (a) Simulated effective quality factors for the different PC cavity loss channels as a function of power dropped into the cavity. (b) Contributions from the modeled dispersive processes to the PC cavity resonance wavelength shift as a function of power dropped into the cavity. (Simulation parameters: $\eta_{\text{lin}} \sim 0.40$, $\Gamma_{\text{th}} dT/dP_{\text{abs}} = 27$ K/mW, $\tau^{-1} \sim 0.0067 + (1.4 \times 10^{-7}) N^{0.94}$ where N has units of cm^{-3} and τ has units of ns.)

This procedure was repeated for a range of values for $\Gamma_{\text{th}} dT/dP_{\text{abs}}$ and η_{lin}. For a fixed value of η_{lin}, the fits were robust in $\Gamma_{\text{th}} dT/dP_{\text{abs}}$ with the sum of the least square residual of $\tau(P_i)$ clearly minimized for an optimal value of $\Gamma_{\text{th}} dT/dP_{\text{abs}}$. This procedure, however, was only found to constrain $\eta_{\text{lin}} > 0.15$. Within this range of η_{lin} the quality of the fits does not change significantly, with the optimal functional form of τ changing slightly and the optimal value of $\Gamma_{\text{th}} dT/dP_{\text{abs}}$ varying between $\sim 15 - 35$ K/mW. Based on estimates of η_{lin} from studies of loss in silicon microdisk resonators fabricated using the same SOI wafers and the same processing techniques [44], and by comparing the etched surface area seen by the PC cavity mode to that seen by a microdisk mode, we chose to use $\eta_{\text{lin}} \sim 0.40$ for the PC cavity. With this value of η_{lin} the optimal value of the effective cavity thermal resistance, $\Gamma_{\text{th}} dT/dP_{\text{abs}}$, was found to be 27 K/mW, of the same order of magnitude as the result calculated in Ref. [112] for a similar membrane structure. Finally, the point-by-point least-squared optimum values of $\tau(P_i)$ were then fit as a function of the effective free-carrier density N, using a curve of the form $\tau^{-1} = A + BN^{\alpha}$. Using this $\tau(N)$, smooth fits to measured $P_d(P_i)$ and $\Delta\lambda(P_i)$ were obtained, shown as solid blue lines in Fig. 5.2.

Fig. 5.3 shows the various components of the total cavity loss rate, and resonance shift,

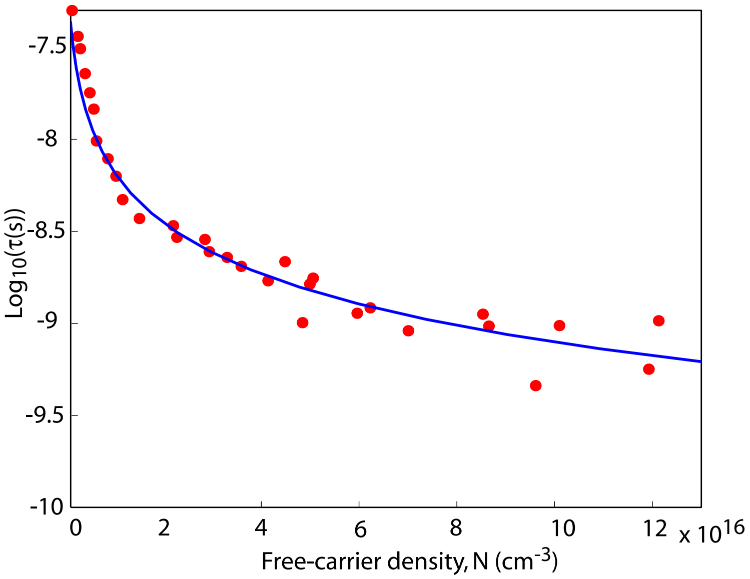

Figure 5.4: Dependence of free-carrier lifetime on free-carrier density (red dots) as found by fitting $\Delta\lambda_o(P_i)$ and $P_d(P_i)$ with the constant material and modal parameter values of Table 5.1, and for effective PC cavity thermal resistance of $\Gamma_{\text{th}}dT/dP_{\text{abs}} = 27$ K/mW and linear absorption fraction $\eta_{\text{lin}} = 0.40$. The solid blue line corresponds to a smooth curve fit to the point-by-point least-squared fit data given by $\tau^{-1} \sim 0.0067 + (1.4 \times 10^{-7})N^{0.94}$, where N is in units of cm^{-3} and τ is in ns.

for the parameters used in the fits to the measured data. It can be seen that although TPA does not dominate the PC cavity response, the free-carriers it generates and the resulting free carrier dispersion and absorption drive the nonlinear behavior of the silicon PC cavity at low and high input powers, respectively. The fit effective free-carrier lifetime, shown in Fig. 5.4, shows similar characteristics to that obtained by Liang et al. [97], demonstrating a significant fall-off in τ for large N, but with a smaller saturated lifetime. Both the pronounced decay in τ and the low ~ 0.5 ns value of the high-carrier density free-carrier lifetime are significantly different from that found in bulk Si, and are most likely related to carrier diffusion and surface effects owing to the extremely large surface-to-volume ratio of the PC cavity, the small length scales involved (~ 200 nm feature size), and the small size scale of the optical mode [107]. This small effective free-carrier lifetime is consistent with other recent experimental results of highly porous silicon optical structures [99, 103, 108]. It should, however, be noted that the bulk Si TPA coefficient was used in modeling the nonlinear response of the PC cavity, which, given the above comments, may not be accurate due to surface modification of TPA. As the effects of free-carrier lifetime and two-photon absorption on the behavior of the dispersive and absorptive nonlinear response of the PC cavity are somewhat intertwined, further studies will be necessary to concretely separate these two phenomena in porous Si structures such as the photonic crystals of this work.

5.3 Conclusion

In this chapter, the evanescent coupling scheme presented in Ch. 4 was exploited to probe the steady-state nonlinear optical properties of a PC cavity. The influence of two-photon absorption, free-carrier absorption and dispersion, Kerr self-phase modulation, and thermo-optic dispersion, on the response of the PC cavity was considered theoretically. Optical bistability at fiber input powers of 250 μW was measured, and by fitting the theoretical model to the data, a free-carrier lifetime within the PC cavity as low as ~ 0.5 ns was inferred.

Chapter 6

Silicon nitride microdisk resonators

The ideal microcavity host material should have a high index of refraction and a low intrinsic optical absorption rate over the wavelength range of interest. For telecommunications applications operating in the 1.3-1.5 μm wavelength band, as in Ch. 4 - 5, it has been demonstrated in recent years that Si exhibits these properties and can be used to form low loss ultrasmall cavities [11, 12, 16] and waveguides [113, 58]. At shorter wavelengths, where Si is opaque and other semiconductors such as Al_xGaAs_{1-x} have relatively high optical absorption rates [114], silicon nitride (SiN_x) [115, 116, 117, 118] is an excellent substitute.

In addition to sharing the obvious benefits of the maturity of Si based processing, SiN_x has a moderately high index of refraction ($n \sim 2.0$-2.5, compared to $n \sim 3.5$ in Si and $n \sim 1.45$ in SiO_2) and a large transparency window (6 $\mu m > \lambda > 300$ nm) [119, 118]. This low absorption loss across visible and near-IR wavelengths allows SiN_x to be used with a diverse set of atomic and atomic-like (colloidal quantum dots, color centers, etc.) species with optical transitions in the visible wavelength range. The high refractive index of SiN_x permits the creation of a variety of wavelength scale, high-Q microcavity geometries such as whispering-gallery [120, 121] and planar photonic crystal structures [122]. Combined with a lower index SiO_2 cladding and/or substrate, waveguiding in a SiN_x layer [117, 123, 124] can be used to distribute light within a planar microphotonic circuit suitable for high-density integration. Similarly, SiN_x microphotonic devices are well suited to experiments involving moderate refractive index environments, such as sensitive detection of analytes contained in a fluid solution [125] or absorbed into a low index polymer cladding [126].

In this chapter, we study SiN_x microdisk cavities at wavelengths near 852.34 nm, corresponding to the D2 transition of Cs atoms, and show that they are suitable for cavity QED experiments operating within the strong-coupling regime. An outline of the chapter is as follows. Fabrication of high quality ($Q > 3 \times 10^6$), small mode volume (9 μm diameter, $V < 15(\lambda/n)^3$) SiN$_x$ microdisks is described in Sec. 6.1. Finite-element-method (FEM) simulations of the optical modes of these devices are presented in Sec. 6.2, and fiber tapers are used to characterize the optical properties of fabricated structures in Sec. 6.3. A technique for tuning the resonance wavelength of these device is presented in Sec. 6.4, and a demonstration of multiple microdisks coupled to a single fiber taper waveguide is presented in Sec. 6.5. Finally, the prospect of utilizing these microdisks in cavity QED experiments involving Cs atom and diamond nanocrystals is discussed in Sec. 6.6, where it is predicted that these devices will simultaneously support GHz photon-emitter coupling rates and sub-GHz photon decay rates. Portions of the work contained in this chapter originally appeared in Ref. [17].

6.1 SiN$_x$ Microdisk fabrication

An advantage of fabricating devices from SiN$_x$ is the availability of existing processing expertise, originally developed for microelectronics, MEMS, and silicon photonics, that can be applied to SiN$_x$ device fabrication. The SiN$_x$ devices studied here were fabricated from Si wafers with a 250 nm thick SiN$_x$ layer deposited on the surface. These wafers are available commercially from, for example, Silicon Valley Microelectronics Inc. (SVMI), at a relatively low per-wafer cost. In our wafers, the SiN$_x$ layer was grown-to-order using low pressure chemical vapor deposition (LPCVD), and is stoichiometric in composition ($n \sim 2.0$). Higher index, non-stoichiometric films are also available, as are wafers with multiple dielectric layers.

Some initial devices were also fabricated from plasma enhanced chemical vapor deposition (PECVD) films that were made in our lab using the Oxford Plasmalab tool. However, as discussed in Sec. 6.3.3, PECVD material has a high impurity density compared to LPCVD material, and as a result has more optical absorption [127]. This is primarily due to the lower hydrogen impurity density of the LPCVD material, and can be reduced with a high temperature (1000 °C) anneal of the PECVD material, so that its optical performance approaches that of LPCVD material.

Fabrication of the microdisk resonators follows a similar process flow as the Si photonic crystal devices in Ch. 4 and 5. An array of highly circular electron beam (e-beam) resist

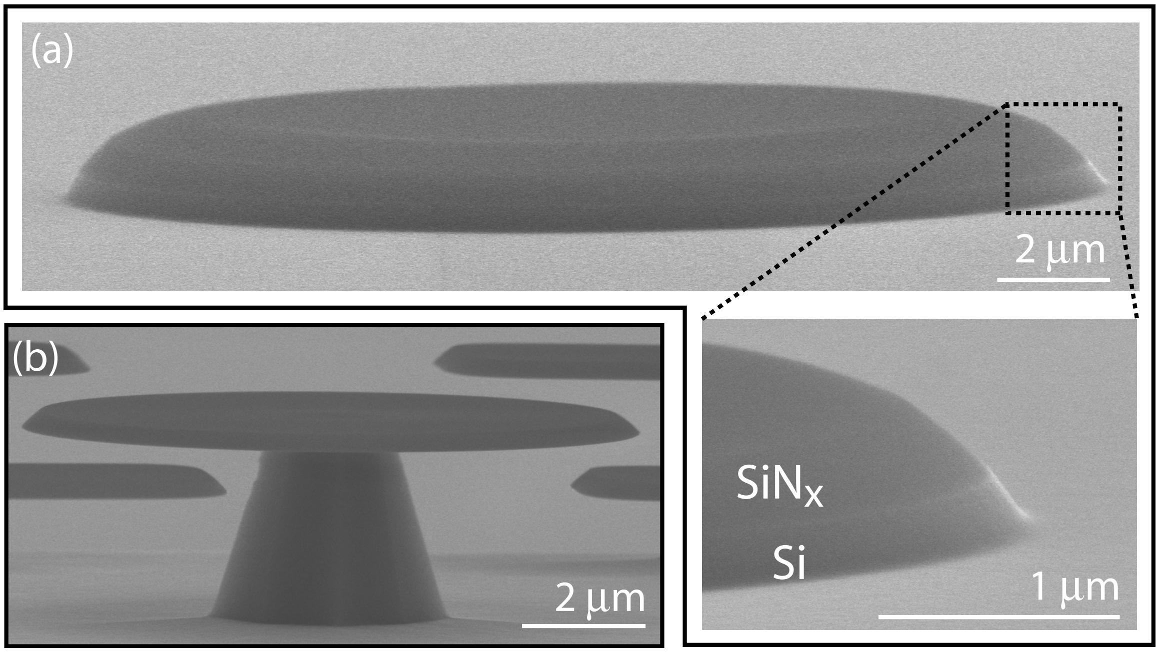

Figure 6.1: (a) SEM image of a SiN$_x$ microdisk after the ICP-RIE dry etching, but before the resist removal and undercutting of the underlying Si layer. Note the smoothness of the sidewalls. (b) SEM image of a fully processed SiN$_x$ microdisk.

(ZEP 520 spun on at 3500 rpm) masks are created using e-beam lithography. Depending on the application, the diameter of individual masks within an array can be varied by adjusting the electron dose, by adjusting the pattern file input to the electron beamwriting software, or by scaling the software output signal that controls the SEM during the beamwrite. After developing the exposed resist, a five minute, 160°C bake is then used to reflow and smooth any roughness in the mask [16]. This reflow also reduces the verticality of the resist profile, which, while problematic for photonic crystal devices requiring vertical sidewalls, is not detrimental to the quality of microdisk resonators. A C_4F_8/SF_6 plasma dry etch is then used to transfer the resist etch mask into the SiN$_x$ layer as smoothly as possible. This etch is similar in chemistry and power to the Si etch, but with a higher C_4F_8 flow rate. The increased C_4F_8 content results in a smoother etch profile, at the expense of sidewall verticality and etch rate. Figure 6.1(a) shows a microdisk at this stage of the fabrication process. After this step, the remaining e-beam resist mask is removed using acetone or a short H_2SO_4:H_2O_2 acid bath. Typically, as with the Si photonic crystal devices, to aid with future fiber taper testing, the array of etched structures is then covered with a photoresist mask, and a long SF_6 isolation etch is used to remove $\sim$ 10-20 μm of the surrounding SiN_x and underlying Si, leaving the etched devices on a mesa. This step is not necessary if the devices are to be tested using a "dimpled" fiber taper [45]. Next, a heated potassium hydroxide wet etch is used to selectively remove the underlying $\langle 100 \rangle$ Si substrate. This undercut etch time is maximized, depending on the microdisk diameter, so that the SiN_x microdisks are supported by a sub-micron diameter Si pillar, as shown in Fig. 6.1(b). It is important to minimize the size of this pillar to prevent it from overlapping with the field of the microdisk whispering gallery modes, since Si has a higher refractive index than SiN_x and is absorbing at near-visible wavelengths, resulting in significant radiation and absorption loss. A final cleaning step to remove organic materials from the disk surface was performed using a H_2SO_4:H_2O_2 acid etch, followed by a short (30-60 s) dilute (20:1) HF etch to remove any surface oxide [128].

6.2 Microdisk mode simulations

Microdisk resonators rely upon total internal reflection to support whispering gallery modes with extremely small intrinsic radiation loss [129, 15, 44, 16, 85, 130, 14]. Although exact analytic solutions to Maxwell's equations for these modes cannot generally be calculated, an approximate scalar analysis can be employed to gain insight into their properties, as described in Refs. [16, 85]. The important result from this analysis is that the microdisk modes can be labeled by indices $\{m, p, q, \sigma\}$ corresponding to the azimuthal, radial, vertical, and polarization quantum numbers respectively, and the field has the approximate functional form

$$E_z(\rho, \phi, z) = e^{im\phi} \psi_p(\rho) Z_{q,\sigma}(z), \tag{6.1}$$

where ρ, z, and ϕ are the radial, vertical, and azimuthal coordinates respectively. For microdisks with perfect cylindrical symmetry, the azimuthal $\exp(im\phi)$ dependence is exact. The radial mode profile, $\psi_p(\rho)$ is given approximately by Bessel and Hankel functions inside and outside the disk, respectively. The vertical field dependence $Z_{q,\sigma}(z)$ is given by the mode profiles of a two dimensional slab waveguide [3]. For $\sigma = \pm 1$, the field is even/odd (TE/TM-like) about the center of the microdisk slab. In practice, the microdisk thickness is chosen to be small enough such that only the lowest order in z ($q = 1$) TE and TM modes have resonance wavelengths, λ_o, close to the operating wavelength, and for the remainder of the chapter we assume that $q = 1$.

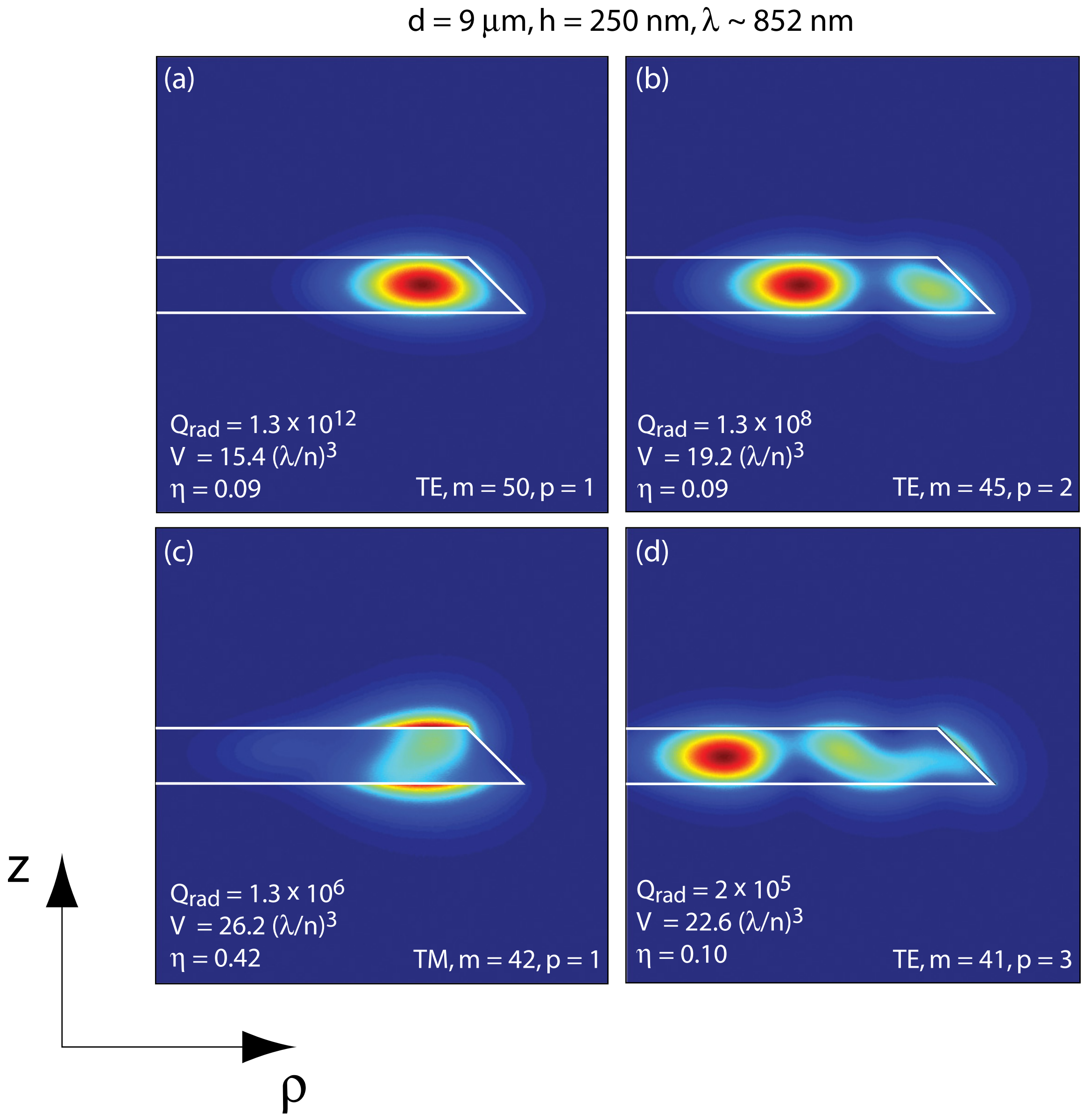

Figure 6.2: Electric field magnitude distribution of the four highest Q_{rad} modes with resonance wavelengths near 852 nm for a 9 μm diameter, 250 nm thick SiN$_x$ microdisk with a 45 degree sidewall profile. The calculated radiation quality factor Q_{rad}, optical mode volume V_o (assuming a standing wave mode), and normalized peak exterior energy density η are also indicated for each mode.

This approximate analysis does not allow the microdisk modes to couple to external "leaky" radiation modes. In order to account for this coupling, and to accurately predict the radiation limited quality factor, Q_{rad}, of these devices, fully vectorial finite-element simulations of Maxwell's equations can be used to calculate the eigenfunctions and complex eigenfrequencies of these structures. FEMLAB, a commercial software package from Comsol, was adapted by Sean Spillane [131], and later by Matt Borselli [16, 85] and Kartik Srinivasan [88] for this purpose.

Using this software, we modeled the microdisks described in Sec. 6.1, and studied the properties of the whispering gallery modes supported by these devices. In addition to Q_{rad}, the figures of merit of particular interest are the mode volume, V_o, and the peak normalized external energy density, η. Both V_o and η are defined in terms of the peak energy density:

$$V_o = \frac{\int n^2(\mathbf{r}')E^2(\mathbf{r}')d\mathbf{r}'}{\left(n^2(\mathbf{r})E^2(\mathbf{r})\right)|_{\text{max}}} = \frac{\int n^2(\mathbf{r}')E^2(\mathbf{r}')d\mathbf{r}'}{n_o^2 E_o^2} \tag{6.2}$$

$$\eta = \frac{E^2(\mathbf{r}|n^2(\mathbf{r})=1)|_{\text{max}}}{\left(n^2(\mathbf{r})E^2(\mathbf{r})\right)|_{\text{max}}} = \frac{E^2(\mathbf{r}|n^2(\mathbf{r})=1)|_{\text{max}}}{n_o^2 E_o^2} \tag{6.3}$$

where E_o and n_o are the electric field magnitude and index of refraction at the position of maximum energy density, respectively.

6.2.1 High Q modes of 9 μm diameter microdisks at 852 nm

Figure 6.2 shows cross sections of the electric field magnitude and the relevant modal figures of merit of the four highest Q modes supported by these devices at wavelengths within a few nm of 852 nm. The fundamental ($p = 1$) TE-like mode has $Q_{\text{rad}} > 10^{12}$, indicating that radiation is not likely to be a limiting loss mechanism for this mode in the microdisk considered here. However, as discussed below in Sec. 6.2.2, when the disk diameter is decreased, Q_{rad} falls rapidly, and radiation can become the dominant loss mechanism of these devices. Similarly, note that as the radial order p increases, m and Q_{rad} decrease. This is because higher radial order modes have a larger proportion of radial momentum components, that are not bound to the microdisk volume by total internal reflection. For the total in-plane momentum of the eigenmodes to remain invariant (for fixed $\{q, \sigma\}$), the relative azimuthal ("tangential") momentum, which is proportional to m, must decrease. The dependence of λ_o and Q_{rad} on m, n and polarization is illustrated in Fig. 6.3, which shows that modes with larger m have higher Q_{rad}. Nonetheless, all of the modes shown in Fig. 6.2 have $Q_{\text{rad}} > 10^5$.

In order to predict the interaction strength between a microcavity field and a dipole or

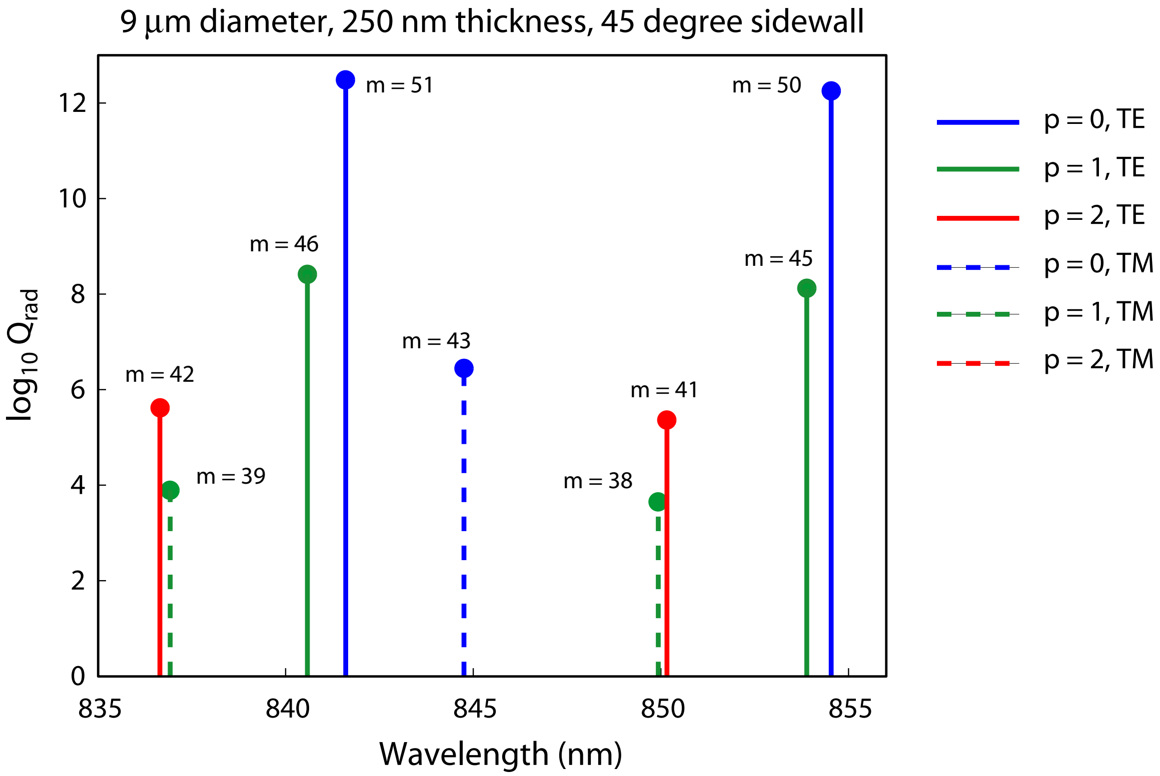

Figure 6.3: Resonance wavelength and Q_{rad} of the lowest radial order (highest m and Q_{rad}) modes with resonance wavelengths near 852 nm for a 9 μm diameter, 250 nm thick SiN$_x$ microdisk with a 45 degree sidewall profile.

other perturbation within its near field, it is necessary to calculate the per photon electric field envelope. In general, since the time averaged energy stored by the electric field of a single photon is $\hbar\omega/2$ (the magnetic field stores another $\hbar\omega/2$ of energy), the spatially varying single photon electric field amplitude for a given microcavity mode can be written as:

$$E(\mathbf{r}) = \sqrt{\frac{\hbar\omega}{2\epsilon_o n^2(\mathbf{r})V_r(\mathbf{r})}} \tag{6.4}$$

where $V_r(\mathbf{r})$ is a generalized position dependent mode volume, and is given by

$$V_r(\mathbf{r}) = \frac{\int n^2(\mathbf{r}')E^2(\mathbf{r}')d\mathbf{r}'}{n^2(\mathbf{r})E^2(\mathbf{r})} = \frac{n_o^2 E_o^2}{n^2(\mathbf{r})E^2(\mathbf{r})}V_o. \tag{6.5}$$

For many applications it is also often convenient to define an “exterior” mode volume, which is determined by the maximum field strength outside of the microdisk, and is given in terms of η and V_o by

$$V_e = \frac{1}{\eta} V_o, \tag{6.6}$$

so that the maximum field strength outside of the microdisk is given by

$$E_e = \sqrt{\frac{\hbar\omega}{2\epsilon_o V_e}}. \tag{6.7}$$

TE vs. TM: mode volume

Of the high-Q modes shown in Fig. 6.2, one is dominantly TM polarized. Although this mode has a relatively low Q_{rad} compared to the fundamental TE mode, it is potentially useful for applications that place a premium on maximizing the field strength near the surface, since the electric field exterior to the microdisk is larger for this mode compared to the fundamental TE-like mode. Comparing the "exterior" mode volumes of the TE and TM $p = 1$ modes,

$$\frac{V_e^{\text{TM}}}{V_e^{\text{TE}}} = \frac{\eta^{\text{TE}}}{\eta^{\text{TM}}} \frac{V_o^{\text{TM}}}{V_o^{\text{TE}}}. \tag{6.8}$$

For the values of η and V_o given in Fig. 6.2(a) and 6.2(c), Eq. 6.8 gives,

$$\frac{V_e^{\text{TM}}}{V_e^{\text{TE}}} \sim 0.38, \tag{6.9}$$

confirming that although V_o of the TE mode is smaller than that of the corresponding TM mode, the maximum local field outside the microdisk is more intense for the TM mode than for the TE mode. Because of this, depending on the requirements placed on Q, the TM mode may be suited for applications studying coupling between the cavity field and emitters located on or near the surface of these microdisks.

6.2.2 Scaling of Q_{rad} and V with microdisk diameter

As shown in Fig. 6.4, FEM simulations were also used to calculate the variation in Q_{rad}, V_o, and V_e of the fundamental ($p = 1$) TE and TM modes as a function of microdisk diameter, d. The microdisk thickness, h, was fixed at 250 nm for these simulations, as this is the thickness of our commercially purchased LPCVD SiN$_x$ films. As a result, the microdisk is not scaled isotropically when d is varied, and Q_{rad} and V_o are not independent of λ for a given λ/d. For the simulations presented here, we considered $\lambda \sim 852$ nm and 637 nm, corresponding to optical transitions in Cs [132] and diamond NV centers [133].

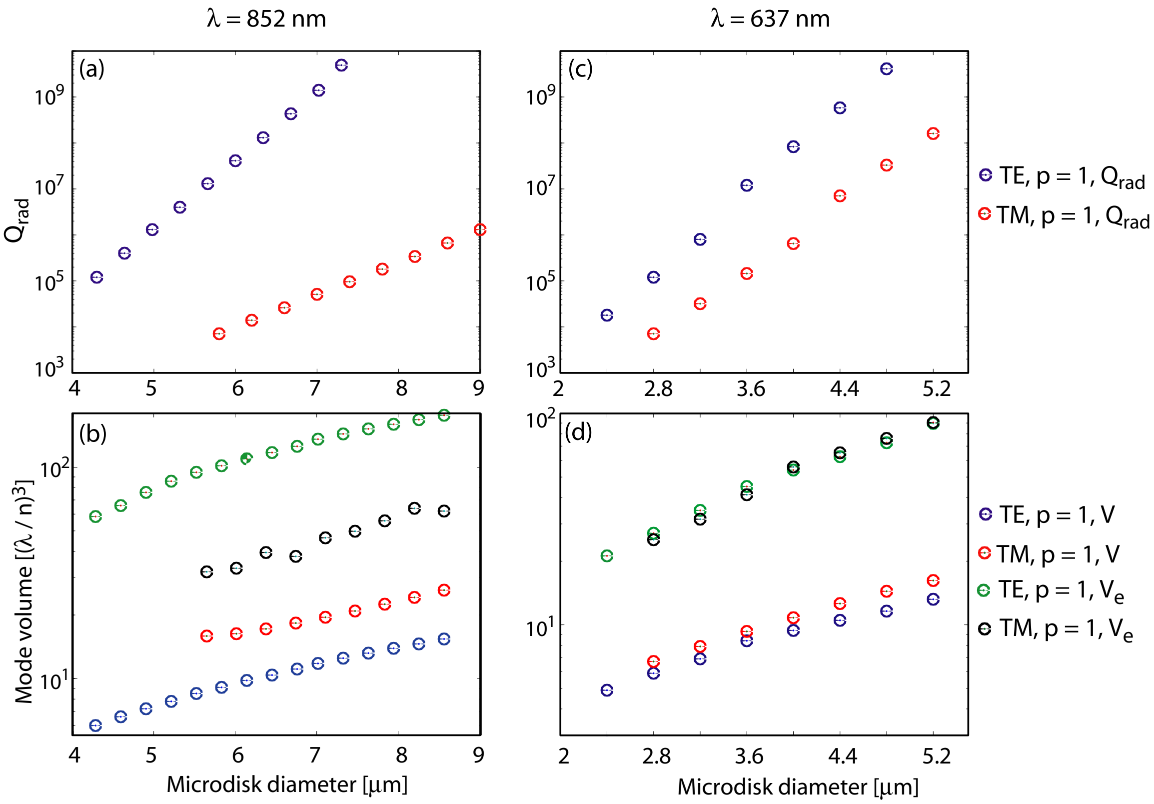

Figure 6.4: FEM calculated V_o and Q_{rad} of the $p = 1$ TE and TM modes as a function of microdisk diameter, for $h = 250$ nm. (a) Q_{rad} at $\lambda = 852$ nm. (b) V_o at $\lambda = 852$ nm. (c) Q_{rad} at $\lambda = 637$ nm. (d) V_o at $\lambda = 637$ nm. In all of the mode volume calculations, it was assumed that the microdisk supports standing wave modes.

From Figs. 6.4(a-d) it clear that Q_{rad} falls exponentially as d decreases, while V_o falls more slowly. Comparing the dependence of V_o and V_e of the TE and TM modes on d and λ in Fig. 6.4(b) and 6.4(d), we see that at the longer wavelength, the difference in V_o and V_e of the TE and TM modes is significant, whereas at the shorter wavelength it is small. This is due to the TM mode being increasingly strongly confined to the microdisk as h/λ is increased.

This effect is illustrated by considering specific value of V_o and V_e for each mode, when d is chosen such that Q_{rad} is fixed at some threshold. In the case of the TE (TM) mode at $\lambda \sim 852$ nm, Q_{rad} drops below 10^6 for $d < 5$ μm (9 μm). The corresponding mode volume given by Fig. 6.4(b) is $V_o \sim 7(\lambda/n)^3$ $(22(\lambda/n)^3)$. However, since the TE mode field is largely confined inside the microdisk, while the TM mode has field maxima close to the surface of the disk, the exterior mode volume for $Q_{\text{rad}} \sim 10^6$ of the TE mode is larger than that of the TM mode: $V_e \sim 75(\lambda/n)^3$ for the TE mode, while $V_e \sim 60(\lambda/n)^3$ for the TM mode. At $\lambda \sim 637$ nm, for the TE (TM) mode, from Figs. 6.4(c,d), Q_{rad} drops below 10^6 for $d < 3.2$ μm (4.0 μm), where $V_o \sim 6.5(\lambda/n)^3$ $(10(\lambda/n)^3)$. In this case, the exterior mode volume, $V_e \sim, 35(\lambda/n)^3$ of the TE mode is smaller than $V_e \sim 55(\lambda/n)^3$ of the TM mode.

6.3 Microdisk testing using a fiber taper

As with the photonic crystal devices studied in Ch. 4, fiber tapers can be used to excite optical resonances in microdisks [42, 15, 44, 43, 84]. When a fiber taper is placed within the near field of the microdisk, as illustrated in Fig. 6.5(a), efficient coherent fiber-cavity power transfer can be realized. In this section, fiber tapers are used to efficiently couple light into and characterize the LPCVD SiN_x microdisks described above.

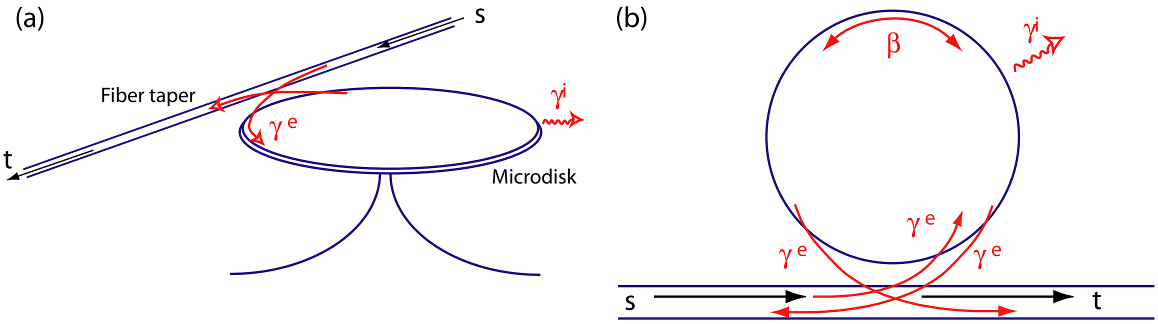

Figure 6.5: (a) Schematic of fiber taper coupling to a microdisk traveling wave mode. (b) Generalization of the coupling process depicted in (a) to represent a microdisk that supports standing wave modes. s and t are the input and output field amplitudes of the fiber taper field, respectively (see Ch. 8).

6.3.1 Waveguide microdisk coupling

This section gives a brief overview of waveguide-microdisk coupling basics, sharing similar notation as used in Sec. 3.1 and Ch. 8. Derivations of the basic equations presented below can be found in a number of references, including [89, 134, 135, 84, 85, 88], and Ch. 8 of this thesis.

As indicated in Fig. 6.5(b), the fiber-microdisk coupling is characterized by coupling rate γ_0^e. Phase matching between the fiber taper mode and the whispering gallery mode plays an important role in the determining the magnitude of γ_0^e, and the degree of phase matching can vary considerably depending on the refractive index and the thickness of the microdisk, as well as on the m number of a given microdisk mode [85]. Generally, the fiber couples preferentially to co-propagating traveling wave microdisk modes. The transmission through the fiber taper in this case is similar to Eq. 3.3 for the waveguide coupled PC cavity response, and is given on resonance by

$$T_o(\omega_o) = \frac{(1-K)^2}{(1+K)^2}, \tag{6.10}$$

where

$$K = \frac{\gamma_0^e}{\gamma^i + \sum_{j\neq 0} \gamma_j^e}. \tag{6.11}$$

In the limit that there is no parasitic loss, $K \to \gamma_0^e/\gamma^i$, and critical coupling ($K = 1$, $T_o = 0$) can be achieved when $\gamma_0^e = \gamma^i$ [43]. Off-resonance, the transmission is given by

$$T(\omega) = 1 - \frac{4K}{(1+K)^2} \frac{(\gamma_t/2)^2}{(\omega-\omega_o)^2 + (\gamma_t/2)^2}. \tag{6.12}$$

where $\gamma^t = \gamma^i + \sum_j \gamma_j^e$.

In practice, for imperfectly smooth microdisks, the degenerate ($\pm m$) clockwise and counter-clockwise traveling wave modes are coupled within the microdisk at a rate, β, due to surface roughness induced coherent backscattering [15, 136, 44, 16]. The coupled modes are standing wave superpositions of the clockwise and counter-clockwise traveling wave modes, and have renormalized eigenfrequencies, $\omega_o \pm \beta$. In the regime that $\beta \gg \gamma^t$, the two standing wave modes, treated individually, accurately describe the microcavity response. In this limit, the on-resonance transmission for each of these modes is again given by

$$T_o(\omega_o \pm \beta) = \frac{(1-K)^2}{(1+K)^2}. \tag{6.13}$$

However, since standing wave modes couple equally to each of the forward and backward propagating waveguide modes[1], in the limit that there is no additional parasitic loss $K \to$

---

[1] In the same way as side-coupled photonic crystal cavities [83].

$\gamma_0^e/(\gamma^i + \gamma_0^e) < 1$, and $T_o = 0$ can never be achieved.

6.3.2 Microdisk testing at 852 nm

In order to characterize the microdisk resonances at 852 nm, near the D2 transition of Cs, a swept wavelength source (New Focus Velocity) covering the 840-856 nm wavelength band was coupled into the fiber taper waveguide, and the transmission spectra was measured for varying fiber taper position relative to the fabricated microdisks. Figure 6.6 shows a typical spectra when the fiber taper is positioned such that it is significantly loading the cavity. In this wide wavelength spectrum, obtained by using a DC motor to scan the external grating of the diode laser, at four resonant wavelengths a significant fraction of the power in the fiber taper is dropped into the cavity. As indicated in the figure, these resonances correspond to the TE-like microdisk modes discussed in Sec. 6.2. The different coupling depth and linewidth of each mode is due to differences in their γ^i and γ_j^e, and, as a result, K and γ^t.

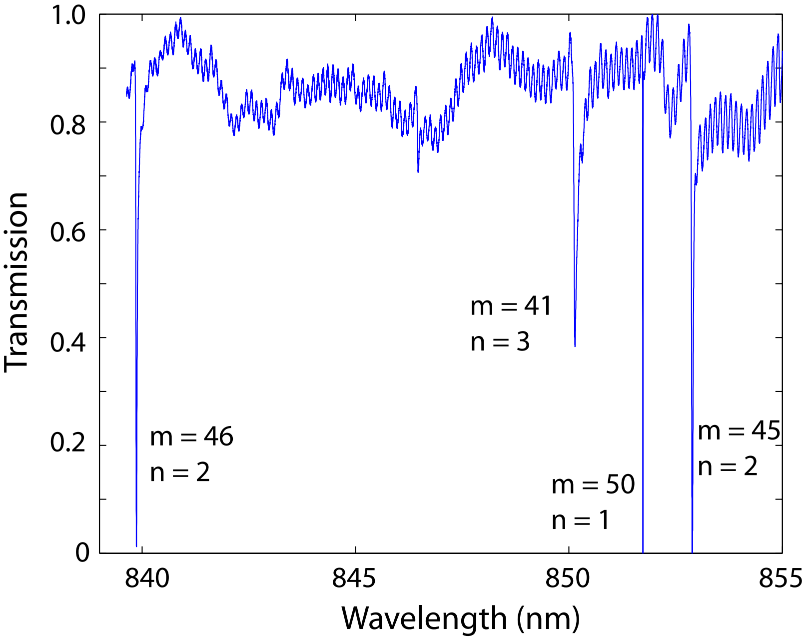

Figure 6.6: Taper transmission when the taper is aligned close the perimeter of a 9 μm diameter microdisk. This wide wavelength scan was obtained by performing a DC motor sweep of the laser diode grating position. This data shows a typical “family” of microdisk modes. The high frequency noise on the off-resonance background is due to etalon effects in the laser.

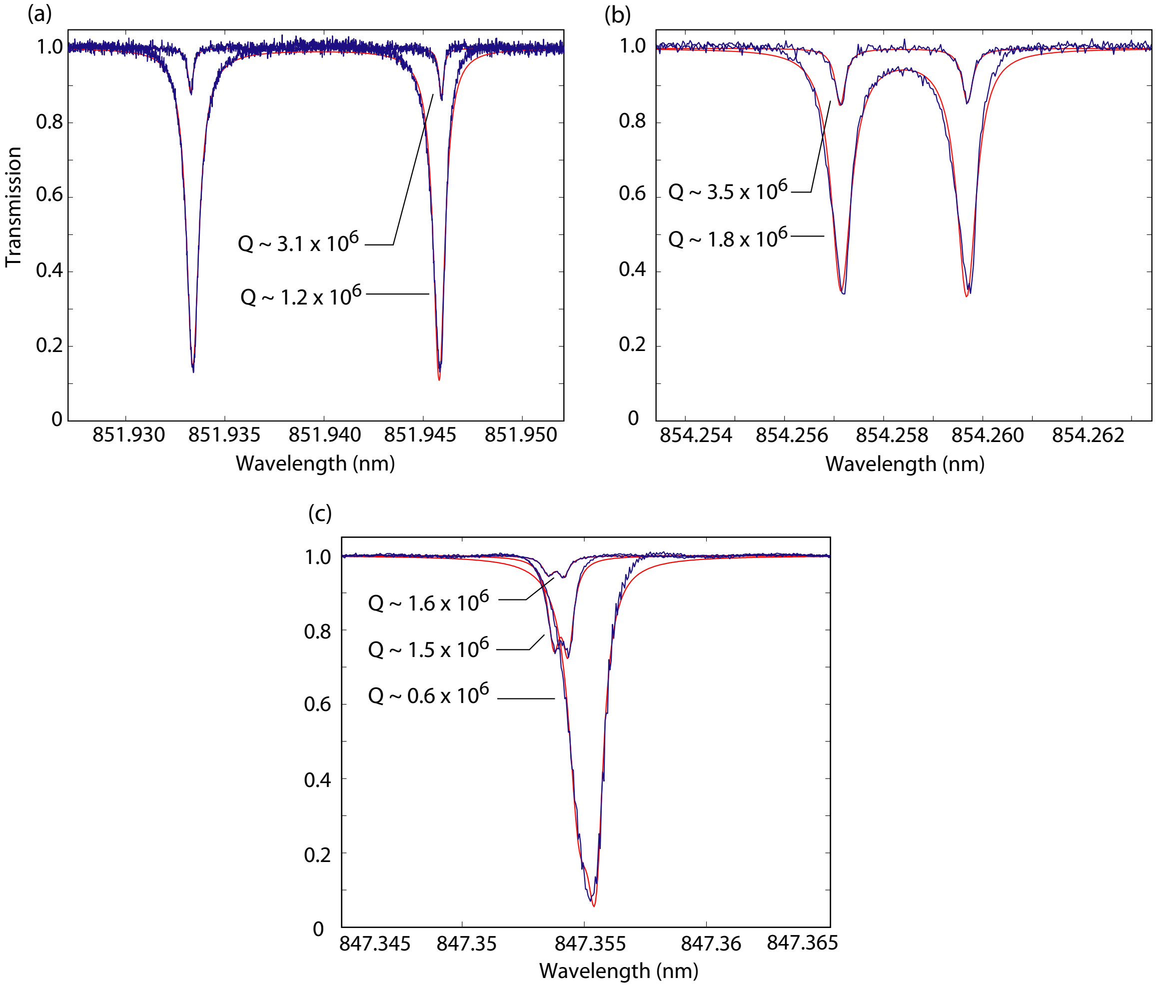

Figure 6.7: Fiber taper transmission when the taper is positioned in the near field of a 9 μm diameter microdisk, for two fiber taper positions. The data in (a), (b), and (c) are for different nominally identical microdisks fabricated simultaneously on the same chip. The red lines are fits using a model that includes coupling between the microdisk and the tapers, as well as between traveling wave modes of the microdisk.

Figure 6.7 shows typical narrow range wavelength scans, obtained by using a piezo to scan the external grating of the diode laser, of the lowest radial order ($p = 1$) TE-like mode of three 9 μm diameter SiN$_x$ microdisks, for varying taper positions. When the taper is weakly coupled to the microdisk, the resonances in Fig. 6.7 have linewidths, $\delta\lambda_o$, ranging between 0.26-0.56 pm, corresponding to intrinsic quality factors $Q = 1.5 \times 10^6 - 3.5 \times 10^6$. From Fig. 6.6(a), the free spectral range between modes of the same radial order but different azimuthal number (m) was measured to be 5.44 THz (13 nm), resulting in a finesse of

$\mathcal{F} = 5 \times 10^4$ for the fundamental $p = 1$ mode measured in Fig. 6.7(a). The doublet structure in the transmission spectra is due to mode-coupling between the clockwise and counter-clockwise modes of the disk due to surface roughness induced backscattering, as described above. For these devices, as well as other microdisks from the same sample, the splitting between resonances varies between $\Delta\lambda = 0.5$-12 pm, and no correlation between $\delta\lambda_o$ and $\Delta\lambda$ is observed. When the taper is positioned more closely ($\sim$ 200 nm) to the microdisk so that the on-resonance transmission decreases, the loaded Q decreased non-ideally. Although the degree of non-ideal loading depends on the taper diameter, as does the coupling strength, the loaded resonances in Fig. 6.7(a-c) are typical, with $I \sim 0.4$-0.6 for $K \sim 0.25$-0.6, corresponding to 65%-95% input coupling efficiency from the fiber taper, and $20\% - 40\%$ collection efficiency into the fiber taper. Reaching critical coupling, where $T_o = 0$, is increasingly difficult and non-ideal as $\Delta\lambda$ increases. However, for microdisks supporting resonances with low intrinsic splitting, such as that shown in Fig. 6.7(c), it is possible to approach $T_o = 0$ for loaded $Q \sim 8 \times 10^5$.

Comparing the measured values of $Q \sim 10^6$ for the fundamental $p = 1$ mode presented here with the FEM simulated radiation loss ($Q_{\text{rad}} = 10^{12}$) results in Sec. 6.2.1, it is clear that the measured values are not radiation limited. Tests of less surface sensitive, larger diameter microdisks showed similar or reduced doublet splitting but no reduction in linewidth, indicating that Q is most likely limited by material absorption and not surface roughness [16].

6.3.3 Comparison with PECVD microdisks

The first SiN_x microdisks fabricated in our lab were made from “home-grown” PECVD deposited films. The processing of these device is identical to that of the LPCVD microdisks, with the exception that PECVD SiN_x is etched approximately twice as fast by the ICP-RIE dry etch as the LPCVD material, somewhat reducing the difficulty of the fabrication. However, PECVD SiN_x has a much higher impurity density (primarily H_2), and generally has higher optical absorption [127]. Devices fabricated from this material typically had $Q \sim 3 \times 10^5$ for wavelengths in the 852 nm range. Tests of larger microdisks at 1550 nm had similar results. However, it was observed that by annealing the microdisks at 900^{o}C temperatures, the quality of the material could be improved dramatically, and $Q > 10^6$ could be observed in the 1550 nm range. Not surprisingly, the annealed PECVD material has similar dry etching characteristics as the LPCVD material. A shortcut to fabricating high quality devices without etching the "hard" LPCVD material is to anneal devices initially fabricated from "soft" PECVD SiN_x. This is not necessary for the microdisks studied here, but may be useful for fabricating photonic crystal devices in the future.

6.4 Resonance wavelength positioning

Using the above fabrication procedure, the resonance wavelength of the microdisk modes could be positioned with an accuracy of ±0.5 nm. In order to finely tune λ_o into alignment with the D2 atomic Cs transition, or any other wavelength of interest, a series of timed etches in 20:1 diluted H_2O:49% HF solution can be employed [116, 137, 138]. As the HF slowly etches the SiN_x, the resonance wavelength of the high-Q, 9 μm diameter disk modes was observed to blue shift at a rate of 1.1 nm/min (Fig. 6.8(a)). With this technique, the cavity resonance could be positioned with an accuracy of ±0.05 nm without degrading the Q factor (Figs. 6.8(b,c)). Further fine tuning can be accomplished by heating and cooling of the sample; a temperature dependence of $d\lambda_o/dT \sim 0.012$ nm/^{o}C was measured for the $p = 1$, TE-like microdisk modes.

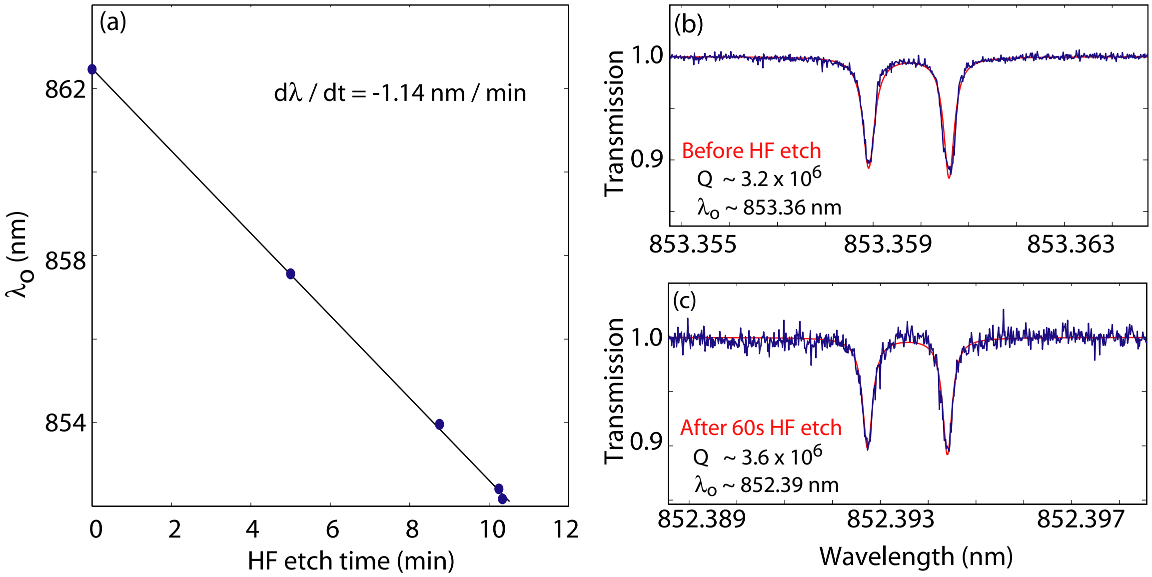

Figure 6.8: (a) Shift in resonance wavelength as a function of HF dip time. Resonance lineshape (b) before, and (c) after a 60 s HF dip. Note that the Q of the resonance has not degraded.

6.5 Multidisk arrays

As stated throughout this thesis, a driving force behind the development of optical microcavities has been their promise of inherent scalability and compactness. An example that takes advantage of these properties is the integration of many microcavities with a single waveguide. Multicavity devices have applications in wavelength division multiplexing [139], in creating "slow light" optical buffers [140, 141, 142], and in nonlinear optics [143, 144, 68]. Future cavity QED experiments incorporating multiple coupled atom-cavity systems also stand to benefit from these devices.

From a practical perspective, these devices also have an immediate application in microcavity experiments that simultaneously require a large density of modes and a small microcavity mode volume. An example of such an experiment is given in Ch. 7, where a device is installed in a vacuum chamber used for cavity QED experiments with Cs. Once the microcavity is installed in the chamber, its resonance wavelength drifts away from the desired set point due to Cs accumulation on the cavity surfaces. For a cavity with a small free spectral range, this drift would not be a problem if it was guaranteed that a "new" cavity mode were always within tuning range of the desired wavelength. However, wavelength-scale microcavities are characterized by large mode spacing, or, in the case of photonic crystal cavities, are essentially single mode. By coupling with the same waveguide to an array of cavities with a range of resonant frequencies, we can effectively realize a device with ultra-small mode volume *and* small mode spacing.

Arrays of ten nominally identical microdisks were fabricated using the procedure described in Sec. 6.1 for individual microdisks. The spatial alignment of each microdisk was ensured by incorporating the entire array in a single e-beam mask. Figure 6.9(a) shows an optical image of part of an array, aligned with a fiber taper. A typical transmission spectra through the fiber taper is shown in Fig. 6.9(b). The spectrum looks similar to ten offset copies of a single microdisk spectrum (Fig. 6.6). "Families" of resonances, corresponding to coupling between the fiber taper and the same mode in different microdisks within the array, are clearly identifiable. By monitoring the scattered light from the array when the source laser is tuned onto one of the resonances, individual resonances can be identified with a unique microdisk. The variation in resonance wavelengths of a given mode family is due to the microdisk size dispersion inherent to the fabrication process. For the device

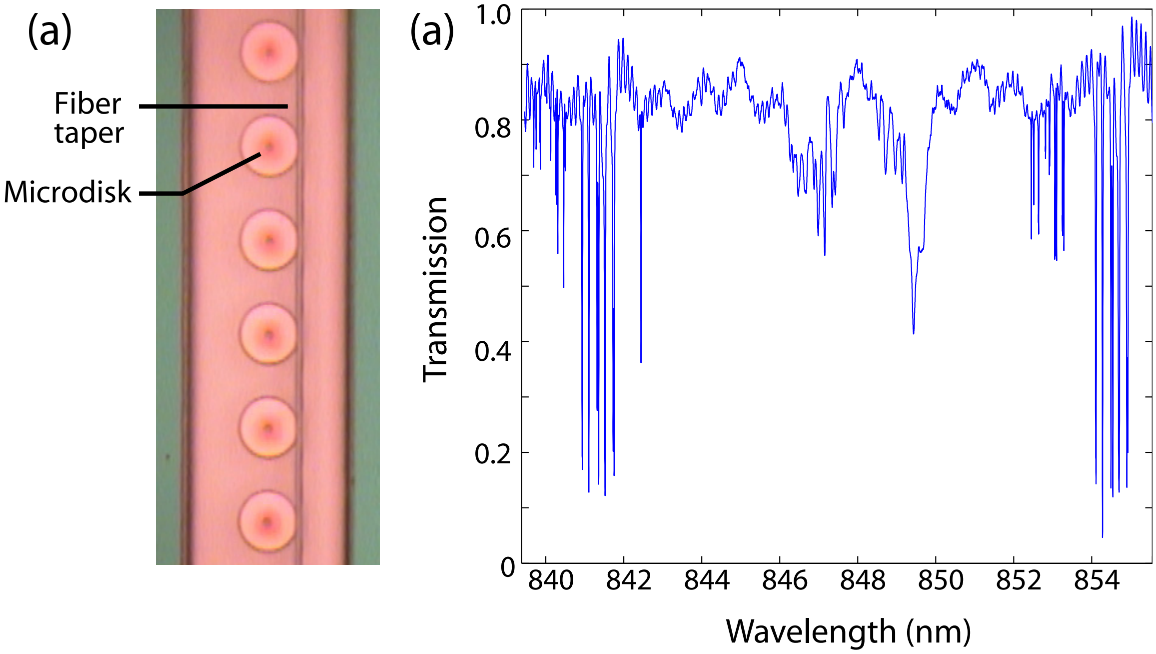

Figure 6.9: (a) Optical microscope image of part of an array of 10 microdisks, aligned with a fiber taper. (b) Transmission spectra of the fiber taper when it is aligned with an array of 10 microdisks.

tested here, the set of resonance wavelengths of a given mode varies over $\Delta\lambda_o \sim 0.5$-1.0 nm, and typical spacing between resonances is $\sim$ 0.1 nm, corresponding to $\Delta T < 10^{o}$C of temperature tuning. Larger variation can be realized by slightly adjusting the microdisk diameter in the e-beam mask definition. The broad resonance features in Fig. 6.9(b) are a result of coupling to low-Q microdisk modes; that then bleed together, forming a broad "coupled-cavity" resonant feature.

The maximum number of microdisks that can be incorporated in an array is currently limited by the field of view of the SEM. If a dedicated beamwriter (as opposed to our modified SEM) with stitching capabilities were used, larger arrays could be fabricated. Also, the larger write speeds and better beamcurrent stability attainable with dedicated beamwriters would possibly reduce the size dispersion of the microdisks, enabling the precise spectral alignment of resonances required for slow-light experiments.

6.6 Predicted microdisk cavity QED parameters

As we are particularly interested in studying interactions between the microcavity field and single atoms or solid state quantum emitters, it is useful to calculate expected parameters governing the dynamics of cavity-QED systems [5, 4] employing the devices discussed above. The key physical parameters are the cavity field decoherence rate, κ; the atom-photon interaction rate, g; and the atomic decoherence rate, $\gamma_a = \gamma_{\text{sp}} + \gamma_{\text{nr}}$, where γ_{sp} is the spontaneous emission rate and γ_{nr} is the non-radiative decoherence rate. The atomic decoherence rate, γ_a, is a property of the quantum emitter of interest, and the cavity field decoherence rate is determined entirely by the cavity quality factor, Q:

$$\kappa = \frac{\omega_o}{2Q} = \frac{\gamma_t}{2}. \tag{6.14}$$

The single photon coupling rate, g, depends on both the local cavity field strength, and the dipole moment of the quantum emitter. In general, g can be written in terms of the electric field, $\mathbf{E}$, and dipole moment, $\mathbf{d}$:

$$g(\mathbf{r}) = \frac{\langle \mathbf{E}(\mathbf{r}) \cdot \mathbf{d} \rangle_{12}}{\hbar} = \frac{\mathbf{E}(\mathbf{r}) \cdot \mathbf{d}_{12}}{\hbar} = \frac{\zeta E(\mathbf{r}) d_{12}}{\hbar} \tag{6.15}$$

where $\mathbf{d}_{12} = \langle \mathbf{d} \rangle_{12}$ is the dipole matrix element connecting the excited and ground state eigenfunctions of the atom-like system of interest, and ζ is determined by the polarization of $\mathbf{E}$ relative to $\mathbf{d}_{12}$. We take $\zeta = 1$ in the following.

For a single photon confined to a microcavity, the local field strength can be written in terms of a position dependent mode volume, V_r, as in Eq. 6.4. Although d_{12} is tabulated for some atoms and solid state emitters of interest, it is often more convenient to express d_{12} in terms of the more routinely measured spontaneous emission lifetime, τ. From quantum mechanical perturbation theory, it can be shown [145] that τ (measured in volume V with index of refraction n_e), is given by

$$\frac{1}{\tau} = \frac{2\pi}{\hbar^2} |E d_{12}|^2 \frac{\omega^2 n_e^3 V}{3\pi^2 c^3}. \tag{6.16}$$

Substituting for the single photon field strength,

$$E = \sqrt{\frac{\hbar\omega}{2\epsilon_o n_e^2 V}}, \tag{6.17}$$

gives an expression for d_{12} in terms of τ:

$$d_{12} = \sqrt{\frac{3\pi\epsilon_o c^3\hbar}{\tau n_e \omega^3}}. \tag{6.18}$$

Using Eqs. 6.4 and 6.15, g can be written in terms of τ and the cavity mode volume:

$$g(\mathbf{r}) = \sqrt{\frac{3\pi c^3}{2\tau n_e \omega^2 n^2(\mathbf{r}) V(\mathbf{r})}} = \frac{1}{2}\sqrt{\frac{3c\lambda^2}{2\pi\tau n_e n^2(\mathbf{r}) V(\mathbf{r})}}. \tag{6.19}$$

In the case of an emitter placed inside the microdisk (e.g., an embedded quantum dot), the maximum interaction rate, assuming the emitter in aligned with the field maxima, is

$$g_o = \frac{1}{2}\sqrt{\frac{3c\lambda^2}{2\pi\tau n_e n_o^2 V_o}}. \tag{6.20}$$

When the emitter is placed at the field maxima exterior of the cavity (e.g., in the case of a neutral atom or nanocrystal near the surface of the cavity), the interaction rate is given by

$$g_e = \frac{1}{2}\sqrt{\frac{3c\lambda^2}{2\pi\tau n_e V_e}} = \frac{\sqrt{\eta}}{2}\sqrt{\frac{3c\lambda^2}{2\pi\tau n_e V_o}}. \tag{6.21}$$

Two regions of parameter space of particular interest in cavity QED experiments are the strong-coupling regime and the bad-cavity regime. The strong-coupling criterion is satisfied when the atom-photon coupling rate exceeds the decoherence rates of the system: $g \gg [\kappa, \gamma_a]$. In this regime, energy can be coherently exchanged between the atom and the cavity mode, and the system can be approximated by the dressed-state solutions of the Jaynes-Cummings Hamiltonian [146]. The bad cavity limit is realized when the cavity decay rate exceeds the atom-photon interaction rate, but the Purcell enhanced [147] atomic radiative decay rate into the cavity mode exceeds the free space atomic decoherence rate: $\kappa \gg g^2/\kappa \gg \gamma_a$. In both of these regimes, the atom decays predominantly into the cavity mode, permitting efficient photon collection. In practice, $g_e^2/\kappa\gamma_a > 1$ and $g_e/\max[\kappa, \gamma_a] > 1$

are useful criteria for determining whether the Q and V of a given microdisk will permit it to operate in the bad cavity or strong-coupling regimes when interacting with a given quantum emitter.

6.6.1 Cavity QED with Cs atoms

The $6^2\mathrm{S}_{1/2} \rightarrow 6^2\mathrm{P}_{3/2}$ (D_2) hyperfine transitions of atomic Cs occur at wavelengths centered around $\lambda_{\mathrm{Cs}} = 852.34$ nm, and the excited states have spontaneous emission lifetimes of $2\pi/\gamma_{\mathrm{sp}} = \tau \sim 30$ ns [132]. There is no non-radiative decay of excited D_2 states in atomic Cs, so $\gamma_a = \gamma_{\mathrm{sp}}$. Figures 6.10(a) and 6.10(b) show the predicted values of κ and g_e for the fundamental TE-like and TM-like microdisk modes simulated in Sec. 6.2 at λ_{Cs}, as well as γ_{sp}. Equation 6.21 was used to calculate g_e using the V_e values from Sec. 6.2.2 and the value for τ given above (with $n_e = 1$). The cavity decay rate was calculated assuming that the cavity Q is limited to 4×10^6, as per the measurements in Sec. 6.3. For microdisk diameters with simulated $Q_{\mathrm{rad}} < 4 \times 10^6$, it was assumed that $Q = Q_{\mathrm{rad}}$, i.e., material losses were neglected. The validity of this assumption is discussed in Sec. 6.6.3.

Encouragingly, for the TE-like fundamental mode, we can see from Fig. 6.10(a) that $g_e/2\pi$ associated with these microdisk modes can approach 2 GHz with a radiation limited $\kappa \sim 0.1$ GHz. In particular, $g_e/2\pi \sim 1.3$ GHz is expected for the $p = 1$ TE mode of the 9 μm diameter microdisks studied experimentally in Sec. 6.3.2; this was measured to have $\kappa/2\pi \sim 0.05$ GHz. By reducing the diameter of the microdisk, it is possible to increase $g_e/2\pi$ to 1.8 GHz without radiation loss degrading Q below this value. Clearly, this cavity should be able to operate in the strong-coupling regime when interacting with a single Cs atom. This is illustrated in Fig. 6.10(c), which shows $g_e/\max\,[\kappa, \gamma_{\mathrm{sp}}]$ as a function of microdisk diameter. For the experimentally demonstrated 9 μm diameter microdisks, $g_e/\max\,[\kappa, \gamma_{\mathrm{sp}}] > 25$, and could increase further for smaller microdisks. Additionally, as shown in Fig. 6.10(d), the bad-cavity parameter, $g_e^2/\kappa\gamma_{\mathrm{sp}} > 10^3$, indicating that the cavity will serve as an extremely efficient photon collector, even with a significant degradation in κ.

For a given microdisk diameter, the $p = 1$ TM-like mode has slightly larger g_e than the TE-like mode; however, κ becomes radiation limited for much larger diameter microdisks than does the TE-like mode. Nonetheless, it should also be possible to reach the strong-coupling regime with this mode.

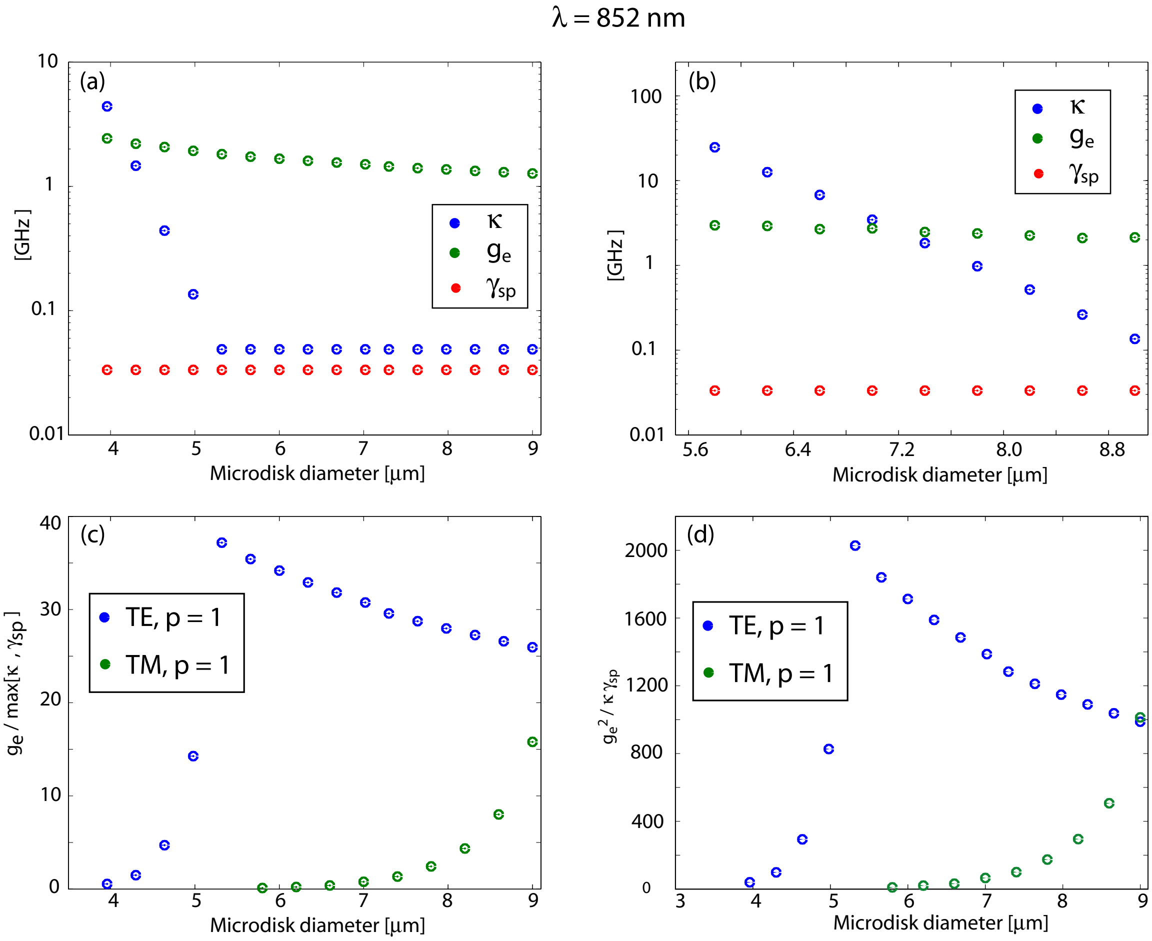

Figure 6.10: Cavity QED parameters for a Cs atom in the microdisk near field, as a function of microdisk diameter. The Cs atom is taken to be at the field maximum outside of the microdisk. The microdisk thickness is $h = 250$ nm, and $\lambda \sim 852$ nm. In calculating κ, $Q = \min\left[4 \times 10^6, Q_{\text{rad}}\right]$. (a,b) Interaction and decoherence rates for the fundamental (a) TE mode, (b) TM mode. (c) Strong-coupling parameter. (d) Bad cavity parameter.

6.6.2 Cavity QED with diamond NV centers

Single nitrogen-vacancy (NV) defects [133] in diamond share many properties associated with atomic systems. Namely, they emit single (non-classical) photons at well defined wavelengths [148], and have relatively large dipole moments. The NV defect center, formed by an N substitutional defect adjacent to an empty lattice site, has attracted significant interest because it is relatively abundant in most diamond samples, it emits photons in the easily detectable visible wavelength band ($\lambda_{\text{NV}} \sim 637$ nm), and it can be varied in density by subjecting the sample to MeV electron irradiation in order to damage the diamond lattice and create vacancies. By forming the NV centers in diamond nanocrystals [149], it should be possible to place these "artificial atoms" within the near field of the SiN_x microcavities discussed here.

An analysis identical to that used above with Cs atoms can be applied to predict the cavity QED parameters when the microdisk interacts with an NV center. Although NV centers have a spontaneous emission lifetime of $2\pi/\gamma_{\mathrm{sp}} = \tau \sim 12$ ns [150] when formed in bulk diamond, and $2\pi/\gamma_{\mathrm{sp}} = \tau \sim 20$ ns when formed in diamond nanocrystals [149], at room temperature, γ_{nr} in NV centers is very large due to coupling with phonons. At liquid-He temperatures (2 K), $\gamma_a/2\pi$ as low as 13 MHz has been measured [151] in bulk diamond, but results vary, depending on material quality. In the following, we take $\gamma_a = \gamma_{\mathrm{sp}} = 2\pi/20\ \mathrm{ns}^{-1}$.

Figures 6.11(a) and 6.11(b) compare γ_{sp} with the predicted values for g_e and κ for the TE- and TM-like $p = 1$ modes at $\lambda \sim 637$ nm of the microdisks simulated in Sec. 6.2.2, as a function of microdisk diameter. For both the TE- and TM-like modes, $g_e = $ 2-3 GHz is predicted before the microdisk becomes radiation limited, and $Q < 4 \times 10^6$ ($\kappa > 0.1$ GHz). As shown in Fig. 6.11(c), the coupled NV-center cavity system should be able to reach the regime of strong-coupling, with $g_e/\kappa > 20$. In Fig. 6.11(d), the bad cavity factor, $g_e^2/\kappa\gamma_{\mathrm{sp}}$, exceeds 10^3. This factor is of particular importance when considering NV-centers or other solid-state emitters with potentially large γ_{nr}, as it indicates how large γ_a can be with the system remaining in the bad-cavity regime. For $g_e^2/\kappa\gamma_{\mathrm{sp}} = 10^3$, the system can tolerate $\gamma_a \sim 10^3\gamma_{\mathrm{sp}} \sim 50$ GHz while remaining in the bad cavity regime. Finally, note that at this wavelength the TM-like mode performs equally, if not better, than the TE-like mode.

6.6.3 Practical limitations

The above analysis assumes that the cavity Q is limited by either material or radiation loss. In practice, effects such as surface roughness and surface state absorption can become the dominant microcavity loss channels [16]. Although experimental evidence in Sec. 6.2.1 indicates that this was not the case for the microdisks studied there, surface effects become increasingly pronounced as the microdisk diameter shrinks and the field becomes less confined. Similarly, the TM-like mode is a comparatively better sensor of the microdisk surface than is the TE-like mode, and is more sensitive to surface related loss mechanisms. Further systematic experimental studies of Q vs. microdisk diameter and mode polarization are needed to better understand the impact of these effects.

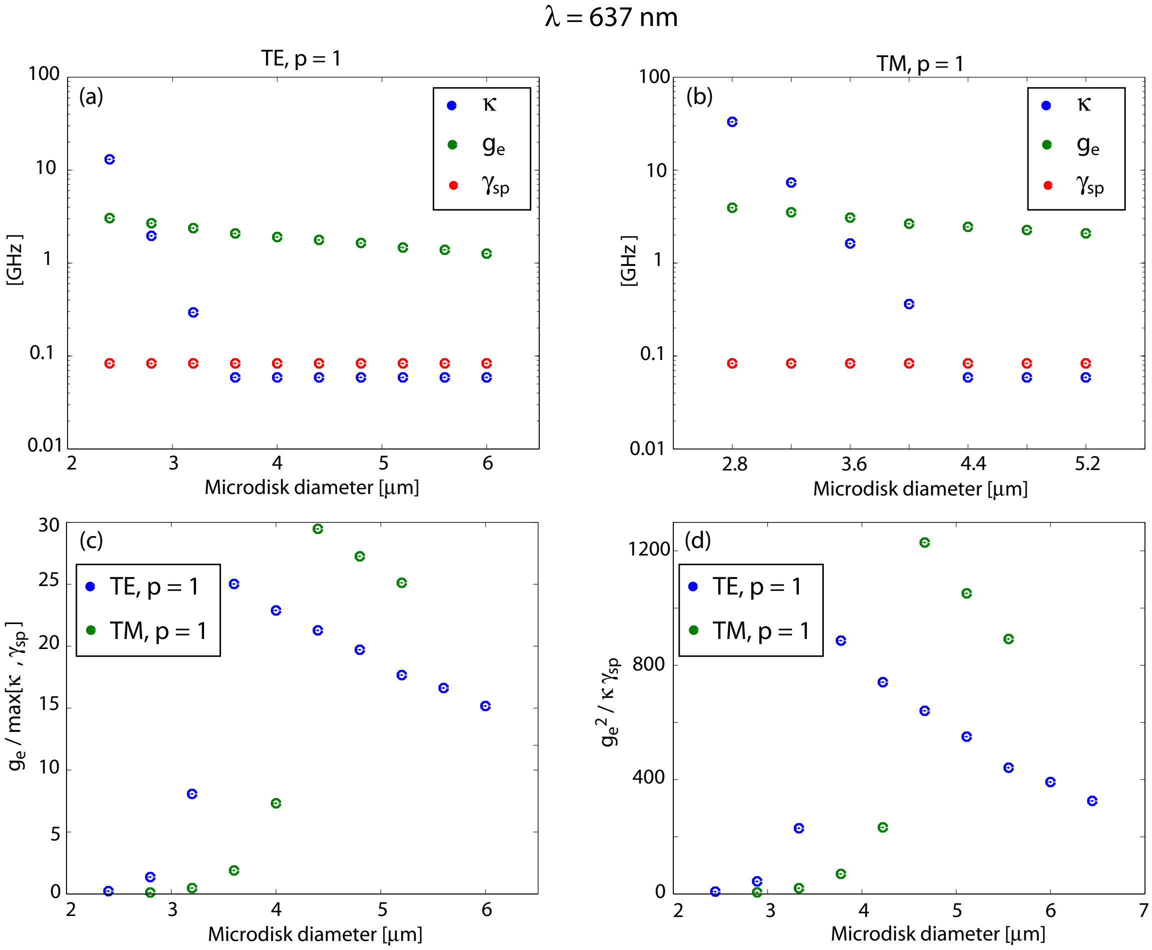

Figure 6.11: Cavity QED parameters for an diamond NV center interacting with the microdisk near field, as a function of microdisk diameter. The NV center is taken to be at the field maximum outside of the microdisk. The microdisk thickness is $h = 250$ nm, and $\lambda \sim 637$ nm. In calculating κ, $Q = \min\left[4 \times 10^6, Q_{\text{rad}}\right]$. (a,b) Interaction and decoherence rates for the fundamental (a) TE mode, (b) TM mode. (c) Strong coupling parameter. (d) Bad cavity parameter.

Wavelength dependent material absorption was also ignored in the analysis of the microdisk modes at 637 nm. A difference in the intrinsic material optical loss rate at 637 nm compared with that at 852 nm would modify the maximum obtainable Q for devices in this wavelength range. However, based on existing literature [119, 118], we expect the optical attenuation coefficient of SiN_x to fall within the same order of magnitude at both wavelengths.

6.7 Conclusion

In this chapter, we have shown that microdisk optical cavities fabricated from SiN_x have sufficiently low optical loss rates and sufficiently large single photon peak field strengths for cavity QED experiments with Cs atoms operating within the strong-coupling regime. These cavities should allow GHz atom-photon coupling rates, which are higher than any other high-Q microcavity operating at $\lambda = 852$ nm demonstrated to date. Because of the low optical loss of SiN_x in the visible wavelength range, these cavities should also be useful for experiments studying a wide class of solid state quantum emitters, such as diamond NV centers. Ultimately, by taking advantage of the planar, CMOS compatible nature of the SiN_x material system, fully integrated photonic chips for visible wavelengths, consisting of many cavities connected through on-chip waveguides, can be designed and fabricated. In the next chapter, we will show how these devices can be integrated with atom chips, eventually promising fully “on-chip” cavity QED and quantum information processing with neutral atoms.

Chapter 7

An atom-cavity chip

Atom chips [152, 50, 51, 153] have rapidly evolved over the last decade as a valuable tool in experiments involving the cooling, trapping, and transport of ultra-cold neutral atom clouds. Fabricated using standard semiconductor processing techniques, atom chips are formed by conducting microwires lithographically patterned on a planar insulating substrate. For modest microwire currents, extremely high magnetic field gradients can be formed close to the atom chip surface [154], and by combining appropriate microwire configurations with externally generated magnetic bias fields, magnetic traps for cold atoms can be realized [155, 156, 157]. Crucially, the position of the magnetic trap, and hence the atoms, can be moved dynamically by varying the current through the microwire configuration.

Examples of experiments that leverage the planar, scalable, micron-sized features of atom chips include studies of Bose-Einstein condensates [158, 159] and degenerate Fermi gases [160] "on-chip", "portable" Bose-Einstein condensates [161], atom waveguides [162] and conveyer belts [163], and atom interferometers [164, 165, 166, 167]. The field of cavity QED [6, 5, 4] and, in particular, cavity QED with neutral atoms and microphotonic devices [168, 169, 170, 171, 172, 173, 131, 29] is poised to significantly benefit from atom chips. Integration of atomic and microphotonic chips [170, 173, 171, 174, 175] offers several advancements to the current state-of-the-art Fabry-Pérot cavity QED systems [176, 34, 177, 178, 179], most notably a scalable platform for locally controlling multiple quantum bits. Ultimately, the atom chip can be used to deliver and possibly trap single atoms within the near field of a microcavity.

In this chapter, we describe and demonstrate a technique for integrating the fiber coupled microcavities studied in previous chapters with atom chips developed by Benjamin Lev [180]. Integrated "atom-cavity" chips fabricated using this technique can be installed in atom trapping vacuum systems while maintaining an efficient fiber input and output channel between the microcavity and the outside world. By taking advantage of the small size of the microcavities, we show that they can be directly integrated with the metal layer used in optically and magnetically trapping atoms near the surface the atom chip, and hence, the cavity. In Sec. 7.1, we describe the fiber mounting technique, and in Sec. 7.2 use a fiber coupled device installed in the atom trapping UHV system to study the sensitivity of a SiN_x microdisk to a dilute cesium (Cs) vapor. In Sec. 7.3, we show how Cs atoms can be trapped directly above an array of microdisks integrated with a mirrored surface attached to an atom chip. Much of the work presented in Sec. 7.1 and Sec. 7.2 first appeared in Ref. [17].

7.1 Fiber coupled microcavities for atom chips

7.1.1 Robust fiber mounting

The ability to align fiber tapers within the near fields of microcavities is crucial for establishing an efficient optical channel into and out of these devices. As described in Ch. 4 and 6, this can be achieved using computer controlled positioning stages. However, these stages are not compatible with ultra-high vacuum (UHV) systems required for atomic physics experiments. Rather than attempt to integrate vacuum-safe piezo [181] or mechanical [29] positioning stages with the atom chip apparatus, our solution to this problem was to develop a technique to permanently attach an optimally aligned fiber taper to the microcavity chip.

A practical fiber-to-microcavity mounting technique must (i) permit high resolution (< 100 nm) positioning of the fiber relative to the microcavity for optimal coupling, (ii) not create significant optical loss, and (iii) be robust to any mechanical impulses imparted during the installation of the device in the experimental apparatus. In addition, for experiments with atom chips, the mounting technique must (iv) be UHV compatible, (v) be able to withstand elevated temperatures (~ 150 ^{o}C) required during vacuum chamber bakes, and (vi) not interfere with the atom cooling and trapping optics.

The solution discussed here is to use UV curable epoxy to permanently and robustly fix the position of a fiber taper that is initially aligned with the microcavity using computer controlled stages. The critical features of this technique are epoxy “microjoints” that fix

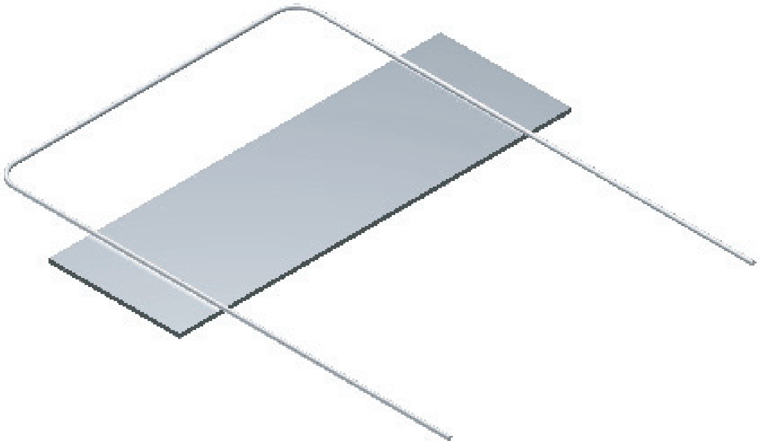

Figure 7.1: Illustration of a fiber taper mounted in a “U” configuration to a glass slide. The fiber taper is bonded to the glass slide using UV curable epoxy.

the position of the taper in the immediate vicinity of the microcavity, in addition to epoxy “macrojoints” that fix the position of the fiber pig-tails relative to the atom chip. A brief description of the mounting procedure follows.

The microcavity chip (3-5 mm × 3-8 mm × 0.3 mm) is first aligned and bonded using polymethyl methacrylate (PMMA) to the desired location on a rigid planar substrate, which, for the purpose of the experiments being considered here, is an atom chip. The fiber taper is placed in a self-tensioning “U” configuration, and is bonded to and supported by a glass slide (1 cm × 1.5 cm, $\sim 200\ \mu$m thick) as illustrated in Fig. 7.1. The top surface of the glass slide is suctioned to a vacuum chuck that is attached to a computer controlled vertical positioning stage. The substrate supporting the microcavity (i.e., the atom chip) is positioned on the computer controlled horizontal positioning stage used in Ch. 4. Using these high resolution stages, the taper is aligned with the microdisk. Adjustment in the lateral gap between the taper and the microdisk is used to optimize the level of cavity loading. As shown in Fig. 7.2, the fiber taper and microdisk are then permanently attached using UV curable epoxy in two regions: (i) Microscopic glue joints between the fiber taper and lithographically defined supports fix the position of the taper relative to the disk, and (ii) macroscopic glue joints between the taper support slide and the atom chip fix the position of the taper support relative to the chip and serve as stress relief points for the fiber pig-tails. The glue for each

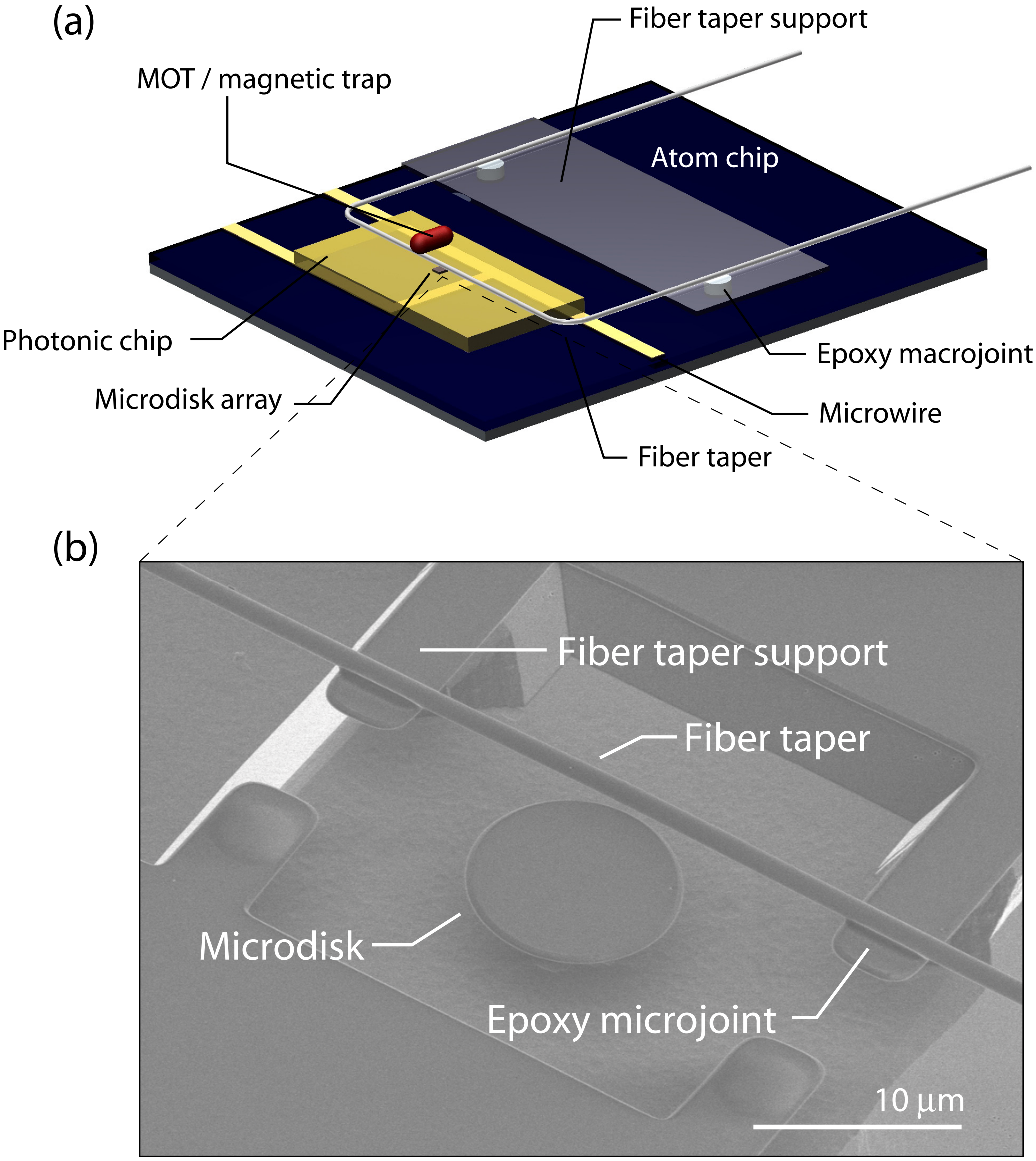

Figure 7.2: (a) Illustration of a fiber coupled photonic chip integrated with an atom chip. (b) SEM image of a fiber taper permanently mounted to a microdisk using epoxy microjoints.

of these joints is dispensed in advance, prior to the taper alignment.

The microjoint glue (Dymax OP-4-20632) is applied to the supports using a sacrificial fiber taper as a “brush.” When a fiber taper “brush” is dipped in epoxy, beads of glue whose diameter are on the same order as the taper diameter are formed. These beads can be transfered onto the supports on the optical chip by contacting the taper “brush” with the supports using the high precision stages. Only glue with a low enough viscosity (~ 500 cP) can be transfered in this way. To minimize optical loss, it is important to minimize the quantity of glue deposited in the anticipated bonding region. In the example shown in Fig. 7.2, the epoxy was actually deposited on the supports adjacent to the eventual bonding region; from there it was transfered using the fiber taper that ultimately was bonded to the chip. The macrojoint glue (Dymax OP-4-20663) is applied to the atom chip manually using a syringe or sharp point.

The glue is cured using a UV spot lamp (Dymax BlueWave 50, 3000 mW/cm^2) coupled to a lightguide that directs the light onto the sample. The macrojoints cure after a few seconds of direct exposure. Somewhat surprisingly, the microjoints take much longer: Typically, a cure time of at least 5 min is used. During this process, it is important that the UV source have an unobstructed line of sight to the microjoint regions. Once the macrojoints have cured, it is difficult to non-destructively test the strength of the microscopic joints. Test trials with no macrojoints, in which the stages are used to raise the fiber taper to stress the microjoints after curing, indicate that a correctly bonded microjoint will not fail before the SiN$_x$ support breaks.

To guarantee robustness, it is important that the microcavity array be isolated on a mesa by $>$ 10-20 μm, as described in Ch. 4. This ensures that in the case of a mechanical impulse, the fiber taper does not contact the edge of the photonic chip, which would result in significant insertion loss. To avoid blocking trapping laser beams or obscuring imaging, the entire fiber taper mount must lie below the plane of the optically and magnetically trapped atoms ($\sim$ 600 μm above the atom chip surface). A sufficiently low-profile is achieved by aligning and bonding the taper support slide parallel to and below the plane of the microcavity top surface. Geometric requirements of the trapping beams are discussed further below.

During the taper mounting procedure, the taper-microdisk coupling is monitored by measuring the microdisk resonance wavelength (λ_o) and contrast (ΔT) through the fiber taper, with no noticable change being observed during the curing of the epoxy joints. The microjoints incur taper diameter dependent broadband insertion loss; approximately 10-15% optical loss per joint is optimal. Post-cure, the fiber-cavity alignment is extremely robust, withstanding all of the vacuum installation procedures described below.

7.1.2 Installation in a UHV chamber

The ultimate test of the robustness of the fiber coupled device is its installation in the vacuum chamber used for performing atom chip trapping experiements. This installation requires that the atom-cavity chip be transported across the Caltech campus from Oskar Painter's photonics lab to Hideo Mabuchi's atomic physics lab. There, the atom chip is mounted onto a copper chassis that also holds several wire coils used for generating the magnetic fields required for atom trapping [180]. The chassis is then turned upside down, so that the atom chip top surface is facing down, and installed in the vacuum chamber. Once in the vacuum chamber, a number of wires used to pass current to the microwires are connected to the atom chip. Vacuum-safe fiber feedthroughs [182] are used to pass the fiber-pigtails out of the chamber. The chamber is then evacuated to the 10^{-3} Torr range using a turbo pump backed by a mechanical roughing pump. Following this initial pump down, the chamber is heated to 120 °C for 24-48 hours. During the bake, when the pressure reaches $\sim 10^{-4}$ Torr, an ion pump is turned on. Finally, when the chamber pressure reaches $\sim 10^{-7}$ Torr, the chamber is slowly cooled to room temperature where the final chamber pressure is typically in the 10^{-9} Torr range.

During this installation process the fiber coupled atom-cavity chip is manipulated significantly, and sometimes jostled. In order to be sure that the taper-cavity coupling is not disturbed as a result, the microcavity resonance is monitored continuously during these procedures. For a successfully mounted device, the fiber-cavity coupling, as measured by the fiber off-resonance transmission T_{off} and ΔT, is impervious to these disturbances, illustrating the robustness of this technique. In fact, tests have shown that the atom-cavity chip can be dropped centimeters onto the optical table without disturbing the coupling, so long as the fiber taper is not contacted directly.

In contrast, the resonance wavelength λ_o of high-Q small V microcavities is very sensitive to the microcavity environment, and to sub-monolayer changes to the microcavity surfaces. In the case of the SiN_x microdisks used in the experiments to date, after the initial pump down but before the chamber bake, λ_o typically blue shifts by -0.1 nm. This shift is due in part to the difference between the refractive index of air and vacuum ($\Delta n \sim 10^{-5}$), and in part due to the desorption of molecules that may have accumulated on the microcavity surface before it was installed in the vacuum chamber. As the chamber is heated during the bake, the resonance shifts reversibly at a rate of ~ 0.012 nm/^{o}C. Additionally, while the chamber is in steady state at an elevated temperature, λ_o can be observed to red-shift slowly at a rate that depends on the recent history of the chamber. This shift, $\Delta\lambda_{o,\text{bake}} \sim 0.1-0.3$ nm is not reversible, typically saturates over the course of the bake, and is presumed to be due to contaminants on the chamber sidewalls and in the pumping system that outgas during the bake and collect on the cavity surface.

7.2 Microcavity surface sensitivity to Cs vapor

Of significant concern is the effect of Cs and other related compounds on the optical properties of microcavities installed in the vacuum chamber. Cs and other contaminants are introduced into the chamber from a heated Cs source ("oven") attached to the chamber via a UHV valve. During a typical lifetime of a microcavity installed in the UHV system, the Cs valve is opened in two scenarios: periodically during the inital pump down and/or bake, to equilibrate the pressure in the Cs oven with that in the chamber, and during the operation of the atom trapping experiments in order to source the atom trap with Cs atoms. In both scenarios, opening the Cs valve is observed to be directly correlated with a red shifting of λ_o. This is problematic when using microcavities in atomic cQED experiments, where it is required that the microcavity resonance wavelength be maintained close to that of the atomic transition of interest. Ultra small mode volume microcavities are either single mode (in the case of PC cavities) or have a large mode spacing (~ 13 nm for the microdisks studied in here and in Ch. 6). Since thermal tuning of the cavity resonance is typically limited to $\sim 0.1-0.2$ nm, lacking another high bandwidth tuning technique, it is necessary that $\Delta\lambda_o$ be minimized and/or controlled during the experiment.

During the chamber pump-down, the most successful protocol in practice is to open the Cs valve for ~ 30 minutes prior to beginning the bake, and for several ~ 10 minute intervals during the bake, once the chamber pressure is below 10^{-4} Torr. This allows the Cs oven to be "pumped on," and maintained at a pressure close to that of the main chamber. When the Cs valve is opened during the bake[1], it is usually possible to observe a shift in λ_o at rate of roughly 1-10 pm/min. In some instances, opening the Cs oven during the bake has resulted in rapid deterioration of the microcavity resonance Q, accompanied by a rapid shift

---

[1] The Cs oven is tyically at 60 °C during the bake.

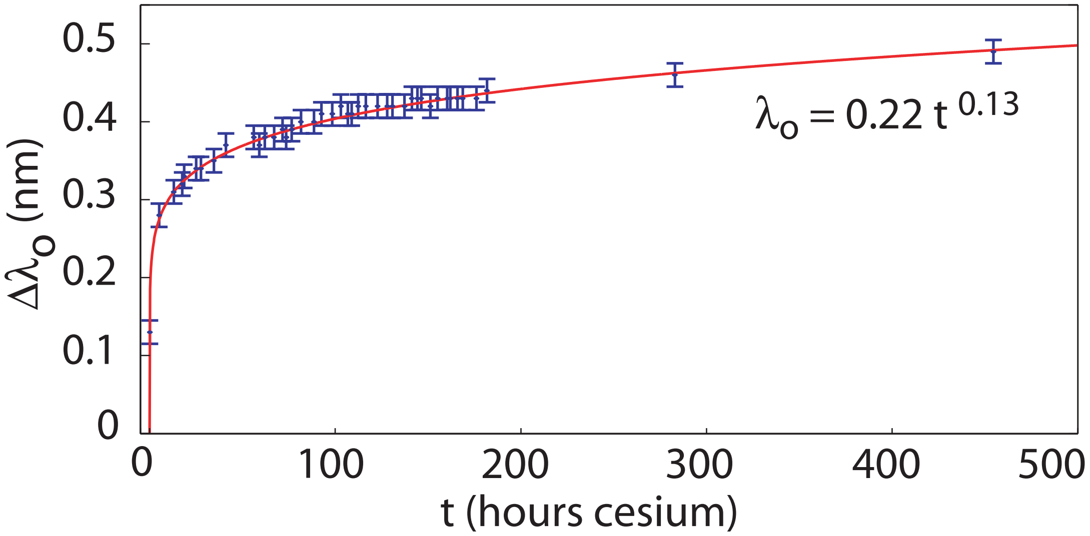

Figure 7.3: Resonance wavelength shift of the 9 μm diameter SiN$_x$ microdisk studied in Ch. 6 as a function of time exposed to Cs. The Cs partial pressure was $10^{-9} - 10^{-8}$ Torr.

in λ_o. Trials indicate that initially pumping on the Cs oven at room temperature before beginning the bake is important in order to avoid this problem.

During the operation of the experiment, it is necessary to operate the Cs oven at 40-50 $^{\rm o}$C with the valve open completely in order to reach a sufficiently high Cs partial pressure ($\sim 10^{-8} - 10^{-9}$ Torr) in the chamber to enable formation of a relatively large MOT. Atoms from this Cs vapor adsorb on the microcavity surface with a logarithmic time dependence, i.e., in a "glassy" manner [183], where interactions between deposited atoms quench the rate of adsorption. As shown in Fig. 7.3, typical "saturated" shifts in λ_o are $\Delta\lambda_{o,\rm Cs} \sim 0.5$ nm; however, $\Delta\lambda_{o,\rm Cs}$ can vary depending on the conditions of the Cs oven.

Quantitatively, a shift, $\Delta\lambda_o$, of the disk resonances can be related to a deposited surface film of thickness, s, by

$$s = \Delta\lambda_o/(\lambda_o(n_{\rm f} - 1)\Gamma'), \tag{7.1}$$

where $\Gamma' s$ represents the fraction of modal energy in the film [85] and $n_{\rm f}$ is the refractive index of the film. From finite element simulations of the 9 μm diameter microdisk used in collecting the data in Fig. 7.3, $\Gamma' = 0.0026$ nm^{-1} for the $p = 1$ TE-like mode. Assuming a film index of refraction equal to that of SiN$_x$, the measured wavelength shift at the longest measured time ($t = 450$ h) corresponds to roughly a half-monolayer coverage of Cs on the disk surface (monolayer thickness ~ 4 $\AA$ [184]).

The time dependence of this film growth can be approximately modeled as follows. Roughly,

$$\frac{ds}{dt} = Pe^{-ks} \tag{7.2}$$

where s is the fractional number of monolayers coating the microcavity surface, P is proportional to the Cs partial pressure, and k is a constant describing a repulsive interaction between adsorbed Cs atoms. According to this model,

$$s(t) = \frac{\ln(kPt + c)}{k}, \tag{7.3}$$

where c is determined by $s(t = 0)$, and is equal to 1 for $s(0) = 0$. A saturated film thickness, s_{sat}, can be defined in terms of the rate of accumulation, $\dot{s}$: When $\dot{s}$ is lower than a practical threshold, $\dot{s}_{\text{sat}}$, changes in s (and therefore λ_o) can be ignored over the course of the experiment. Using this definition, s_{sat} is given by

$$s_{\text{sat}} = \frac{1}{k}\ln(\frac{P}{\dot{s}_{\text{sat}}}). \tag{7.4}$$

Equation (7.4) clearly indicates that for a given $\dot{s}_{\text{sat}}$, s_{sat} scales logarithmically with P. This indicates that working in a UHV systems with a lower non-Cs background pressure, which would enable the formation of a MOT with a similarly lower Cs partial pressure, would reduce s_{sat}. Ultimately, a two chamber atom trapping system, comprised of a MOT chamber connected to a magnetic trapping chamber, could be used to significantly reduce P in the vicinity of the microcavity.

Interestingly, assuming that the model described above is valid, this background pressure dependence potentially can be exploited to semi-permanently tune a microcavity into resonance after installing the cavity in the vacuum chamber but prior to beginning the experiment. This tuning mechanism is in the spirit of work that used noble gas condensation on low temperature semiconductor microcavities to tune their resonances [185, 186]. The envisioned tuning procedure is illustrated in Fig. 7.4: By initially elevating the Cs partial pressure significantly, for example, to $10P_o$, where P_o is the normal operating Cs partial pressure, a film of thickness $\gg s_{sat}|_{P=P_o}$ can be deposited. The Cs partial pressure can then be reduced to P_o, at which point the rate of Cs accumulation is predicted to be slow on the

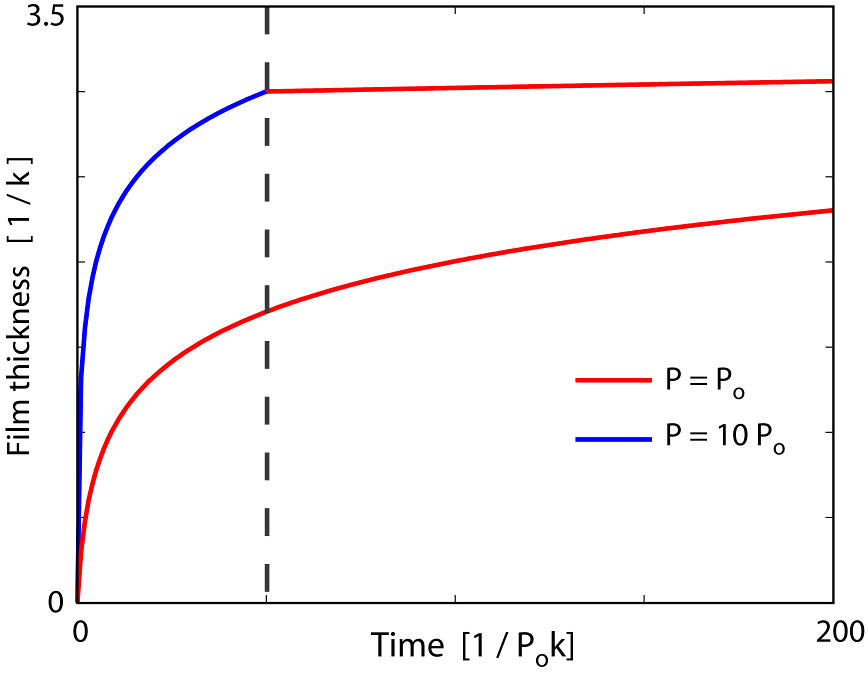

Figure 7.4: Simulated accumulated Cs film thickness as a function of time for varying background pressure. For the upper curve, at the time indicated by the dashed vertical line the Cs partial pressure is reduced by an order of magnitude.

time scale of the lifetime of the experiments (ideally, hundreds of hours). In practice, experimental efforts to realize this tuning have been unsuccessful, due to a tendency for the Q of the microcavity resonance to degrade when the Cs oven is opened at elevated temperatures. This Q degradation is not always observed (it was not noticed for the device from which the data in Fig. 7.3 was taken), and is currently thought to be related to contamination of the Cs oven. The use of atom "dispensers" as an alternative source of Cs [187] is currently being investigated.

A potentially simpler alternative to the above techniques for reducing the effects of Cs is to investigate treatments of the microcavity surface. In Ref. [188], Ghosh et al. coated the inside surfaces of a photonic crystal fiber with an organosilane, which in combination with light induced atomic desorption (LIAD), prevents room temperature Rubidium atoms from interacting with the photonic crystal fiber walls. It is possible that a similar process can be used with the microcavities studied here.

7.3 Atom trapping on the atom-cavity chip

Atom chips employ a combination of external optical cooling and on-chip magnetic trapping to assemble clouds of cold atoms from a dilute thermal gas. When integrated with a fiber coupled cavity, it is crucial that the cavity not interfere with these trapping fields, and that the atom chip have the ability to deliver the trapped atoms to the vicinity of the cavity. Experiments with cold atoms and Fabry-Pérot cavities typically source atoms from free space MOTs, formed far from the cavity and transfered to the cavity via either gravity [176] or an optical potential [178]. When the cavity is integrated with an atom chip, the atoms can be transfered from a mirror-MOT [50], formed near the surface of the atom chip, into a purely magnetic trap, and then magnetically waveguided into the cavity [175, 173]. Compared to Fabry-Pérot cavities, microcavities are a much smaller geometric obstacle. By taking advantage of microcavities' small size, it is possible to directly integrate them with the atom chip, and to form a MOT within tens of microns from the cavity surface. In this section, after a brief overview of the operation of the atom chip used in these experiments, a fully integrated atom-cavity chip that permits trapping directly above a microdisk cavity is presented.

7.3.1 Atom chip basics

This subsection briefly reviews the basic operation of the atom chips fabricated by Benjamin Lev with which the microcavities were integrated. A detailed description can be found in B. Lev's thesis [180], and an excellent general overview of this type of atom chip is given in Ref. [50].

Ultimately, the atom chip confines atoms within a purely magnetic trap that is formed by a superposition of magnetic fields generated by currents in microscopic (on-chip) and macroscopic (external) wires. An example of a canonical microwire magnetic trap is illustrated in Fig. 7.5(a): A two dimensional trap is formed by superimposing a homogeneous bias field with the radially decaying field of a microwire, resulting in a field minima at a fixed height above the wire. By dynamically varying the microwire current and the magnetic bias field, the height of the trap above the microwire can be adjusted. Three dimensional magnetic trapping can be achieved by breaking the translational symmetry of the wire, and patterning "u" or "z" shaped microwires, as illustrated in Fig. 7.5(b). More complicated

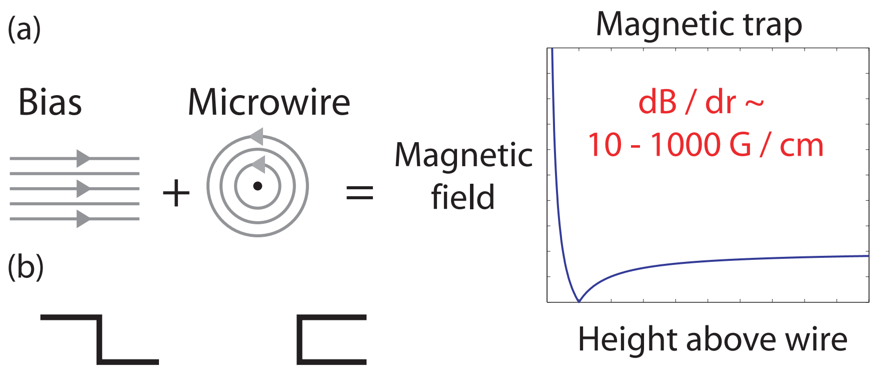

Figure 7.5: (a) Illustration of a magnetic trap formed by superimposing a homogeneous magnetic bias field with the magnetic field generated from current in a wire directed out of the page. This trap offers confinement in the 2D plane of the page. (b) Top view of two wire configurations that provide 3D magnetic trapping when combined with a homogeneous bias field.

microwire circuits permit the atom trap position to be adjusted in all three dimensions by dynamically reconfiguring the current path.

However, in order to magnetically trap a significant number of atoms, it is first necessary to cool and trap them in a MOT [189]. A generic MOT is formed when the intersection of three sets of red-detuned counter-propagating and orthogonally polarized laser beams, oriented along orthogonal axes, is aligned with an externally generated magnetic quadrapole field. The surface of an atom chip cuts off optical access from the half-space below it, necessitating the use of a "mirror-MOT", in which a surface on the atom chip is used to reflect a pair of orthogonal 45° beams that intersect a pair of counter-propagating beams aligned parallel and close to the surface of the atom chip, as illustrated in Fig. 7.6. This geometry provides three dimensional optical cooling at the point where all of the beams intersect; when combined with a magnetic quadrapole field, this allows the formation of a MOT. The magnetic quadrapole field can either be supplied by microwires on the atom chip surface, or by macroscopic wires. The resulting traps are referred to as "micro mirror-MOTs" and "macro mirror-MOTs", respectively.

In the atom trapping apparatus used here, atoms are first collected in a macro mirror-MOT, then transferred into a micro mirror-MOT, before undergoing optical pumping and sub-Doppler polarization gradient cooling, and finally being transfered into a purely magnetic trap. A "u" shaped microwire, positioned below a mirrored region of the atom chip, is

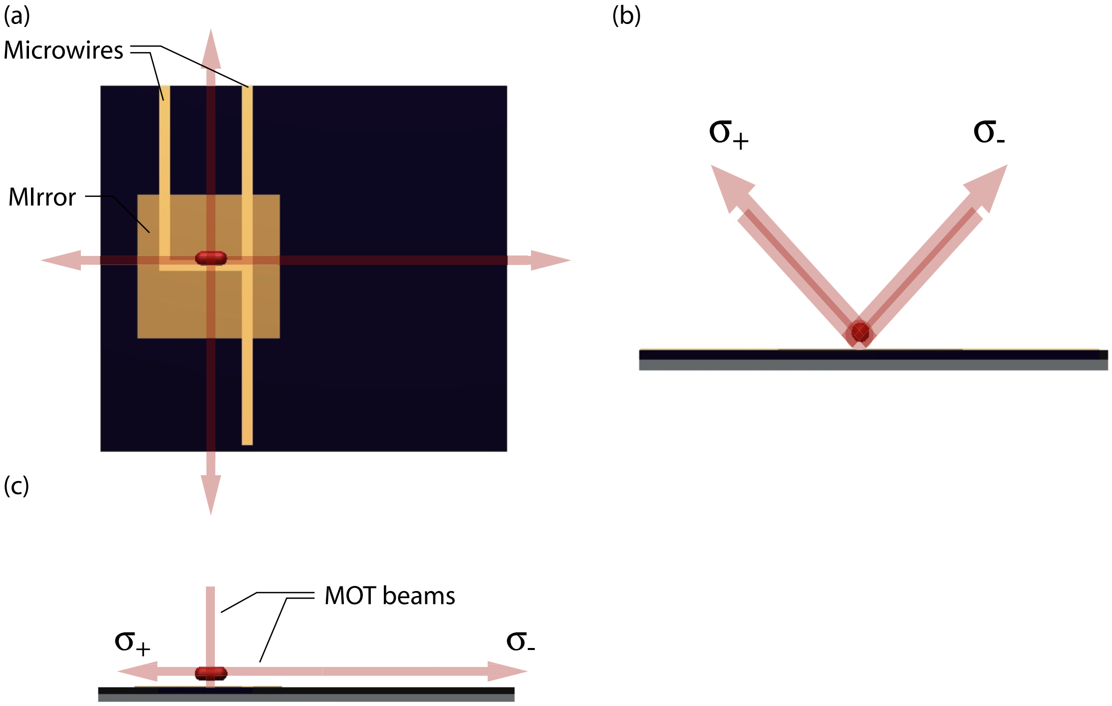

Figure 7.6: Illustration of the laser beam and microwire geometry used to form the atom chip mirror-MOT. During the MOT formation, current flows through the "u" section of the "h" microwire circuit.

used to generate the quadrapole field for the micro mirror-MOT. After sub-Doppler cooling, the temperature of the trapped atoms is $< 10\ \mu$K, and they are optically pumped into the $m_f = |l|$ state, where the quantization axis $\hat{\mathbf{z}}$ is defined by a bias field. The optical fields are then turned off, and since the potential energy of an atom in a magnetic field $\mathbf{H}$ is given by

$$V_m(\mathbf{r}) = -\mu m_f H_z(\mathbf{r}), \tag{7.5}$$

atoms in the $m_f = |l|$ state are trapped in magnetic field minima. If the magnetic trap position and shape are closely matched with those of the micro mirror-MOT, and if the sub-Doppler cooling and optical pumping are optimized, a large fraction of the atoms in the micro mirror-MOT can be transfered into the purely magnetic trap. The magnetic trap position can then be adjusted by dynamically varying the path of current flow through the microwire circuit on the atom chip. Practically, the degree and extent to which this position can be controlled is limited by the microwire geometry, the maximum current allowed by the microwires, and the trap lifetime.

7.3.2 Integrating cavities with atom chips

The initial proposal in Ref. [173] to integrate microcavities with atom chips anticipated using atom waveguiding [162, 163] to move atoms from a magnetic trap formed at the micro mirror-MOT location to a microcavity positioned several mm away. As the experiment progressed, however, it was realized that because of the small size of the microdisks, the atom delivery could be simplified by initially trapping the atoms in a micro mirror-MOT directly above the microcavity. The atoms could then be moved into the cavity near-field from either a magnetic trap or directly from the mirror-MOT, without requiring the extra waveguiding step. However, in order to form the initial micro mirror-MOT directly above the cavity, it is necessary that the cavity not disrupt the mirror region. In the case of "macroscopic" cavities, this is not possible. Conversely, the small footprint of microcavities (1- 100 μm) has a minimal effect on the comparatively large (1 cm) MOT beams being reflected by the mirror, and it is possible to form a mirror-MOT directly above them. As illustrated in Fig. 7.7(d), so long as the MOT is formed at a height above the surface greater than the microcavity footprint, it should be largely unaffected.

Implementing this experimentally requires that the cavity be integrated with the mirrored region of the atom chip, so that the cavity region forms a small "defect" in the otherwise uniform mirror, and is aligned with the microwire that sets the micro mirror-MOT position. Ultimately, this could be achieved by fabricating the cavity from the same substrate as the atom chip, creating a monolithic atom-cavity chip. A simpler short-term solution is illustrated in Fig. 7.7: Incorporate a mirror on the same chip as the microcavity, and then bond the resulting cavity-mirror chip to the desired location on the independently fabricated atom chip. Note that the fiber mounting technique described in Sec. 7.1 is compatible with this scheme, and that the low profile of the mounted fiber ensures that it does not interfere with any of the optical beams.

It is straightforward to modify the fabrication process of the SiN$_x$ cavities described in Ch. 6 to include a mirror layer. Briefly, the procedure is as follows. The lithography, dry etching, and isolation steps are unchanged. After the isolation etch, before removing the photoresist that masks the device mesa, an optically thin layer of gold is evaporated onto the entire microcavity chip. A gentle acetone bath is then used to lift-off the gold coated

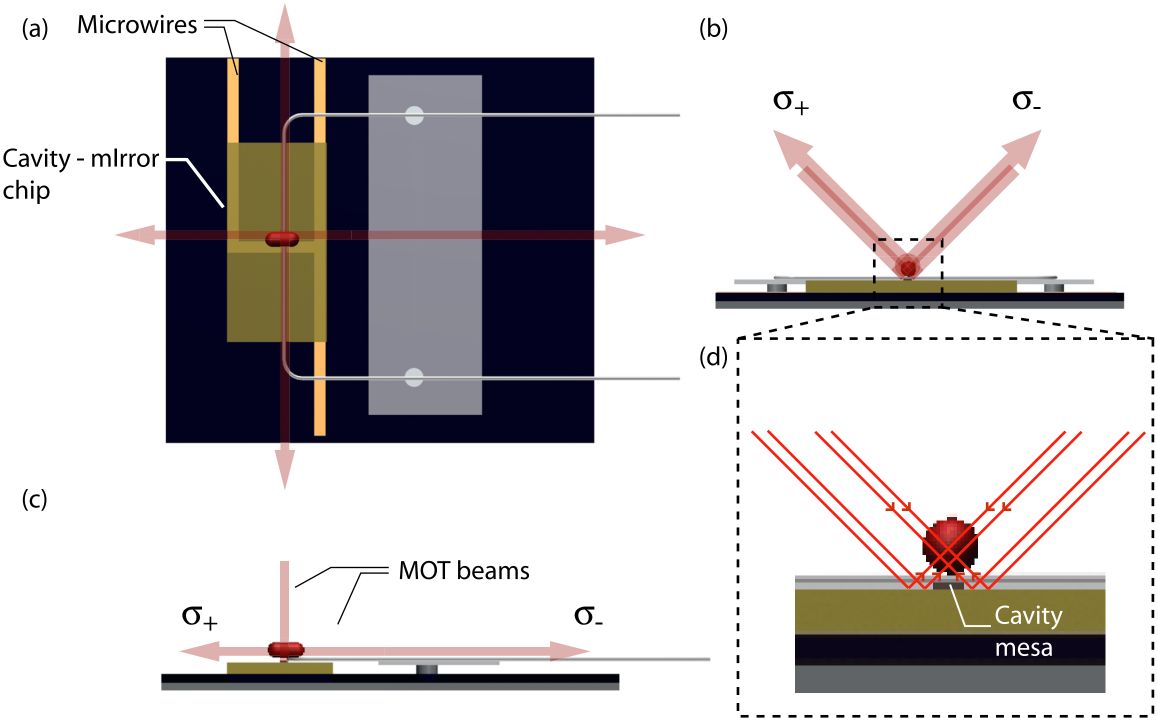

Figure 7.7: Illustration of the laser beam and microwire geometry used to form a mirror-MOT when the cavity-mirror is integrated with the atom chip. (a) Top view, (b) end view, (c) side view. The zoomed-in detail (d) shows how a MOT can be formed above an array of cavities on an otherwise uniform mirror. The shadow from the cavities only extends above the surface as high as the cavity footprint.

photoresist mask. This leaves the device mesa uncovered, while the rest of the chip surface is coated with gold. The final undercutting and cleaning steps are unchanged.

A device fabricated using this process is shown in Fig. 7.8. This device consists of a 3×10 array of 9 μm diameter SiN$_x$ microdisks that are isolated on a mesa ~ 20 μm above the gold coated Si substrate surface. The microdisk array dimensions are 100 μm $\times$ 100 μm, and the chip dimensions are 4 mm $\times$ 6 mm $\times$ 0.3 mm. The device was bonded to the atom chip, as described in Sec. 7.1.1, positioned so that the microdisk array was aligned above the "u" microwire, as illustrated in Fig. 7.7. A fiber taper was mounted to the device, and the resulting fiber-coupled atom-cavity chip was installed in B. Lev's atom trapping UHV system.

Using this device, and following the MOT operation and magnetic trapping procedure described in Ref. [180], it was confirmed that $\sim 10^6$ Cs atoms could be trapped ~ 200 μm

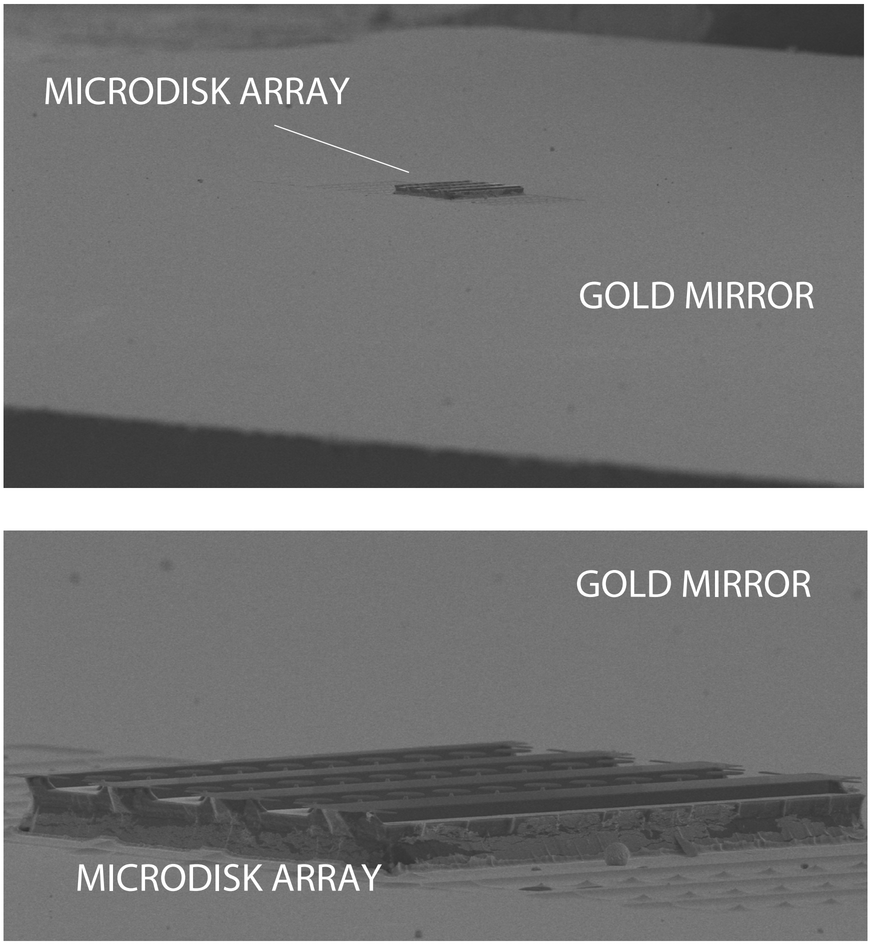

Figure 7.8: SEM images of a cavity-mirror chip. The mesa contains a 3 × 10 array of 9 μm diameter microdisks, and is isolated by ~ 20 μm above the surrounding gold coated Si substrate.

above the surface of the microdisk array in macro mirror-MOT, then transferred to a micro mirror-MOT ~ 100 μm above surface, and finally lowered into the device array using a purely magnetic trap. Figure 7.9 shows fluorescence images of the laser cooled atoms being delivered to the microcavity array in this way. The images were generated by precisely halting the experiment at the instant of interest, zeroing the magnetic fields, exciting the atoms using the MOT beams, and measuring the resulting photoluminescence and scattered light with a CCD camera. Sub-ms timing relative to the beginning of the transfer from the macro-MOT to the micro-MOT was realized using computer controlled external delayed pulse generators, as described in Ref. [180]. Scattering of the excitation (MOT) beams by the surface of the atom-cavity chip made it difficult to identify the position of the

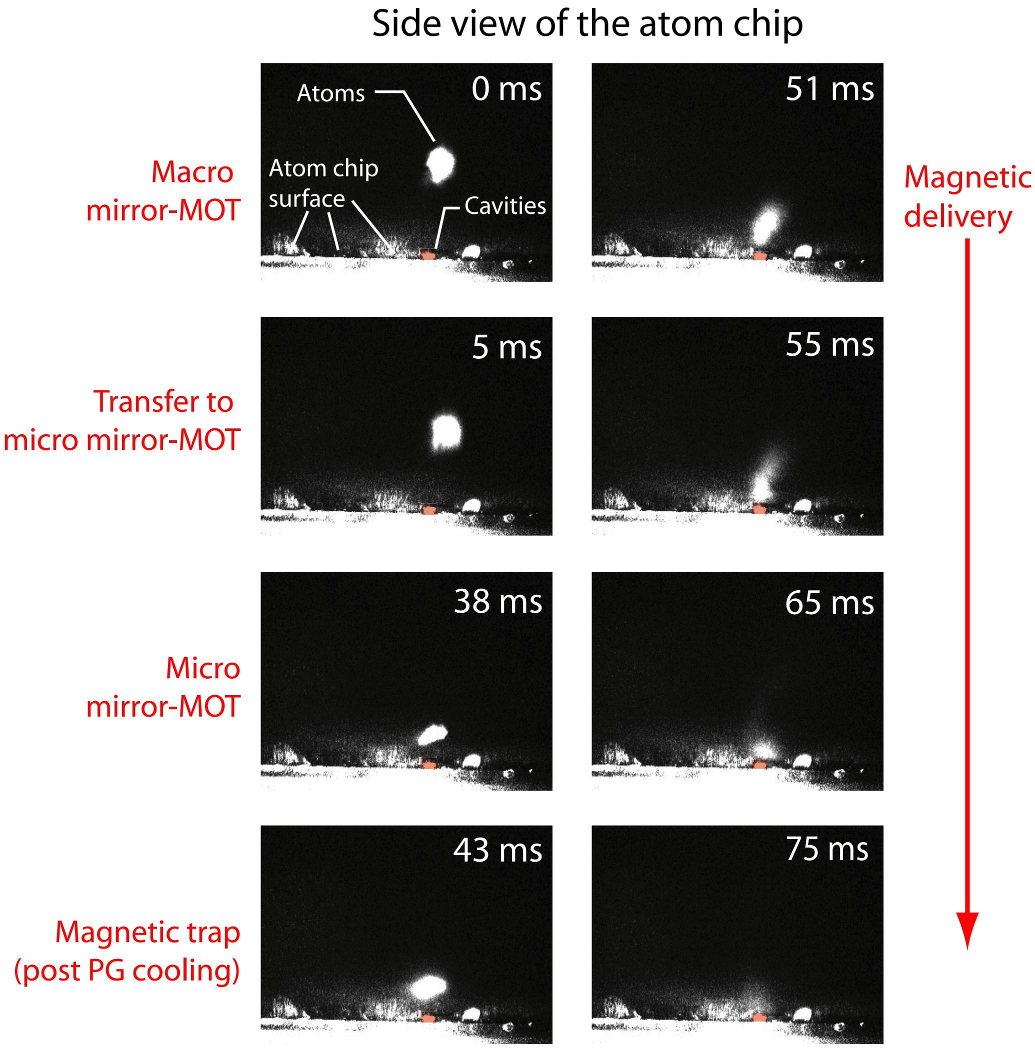

Figure 7.9: Photoluminescence images of laser cooled atoms being delivered to the micro-cavity array on the atom chip. The red-colored area highlights the position of the cavity array. The atom-cavity chip is oriented as in Fig. 7.7(b). Each image is taken by halting the experiment at the specified time after the transfer from the the macro mirror-MOT to the cavity has begun, zeroing the magnetic fields, and exciting the atoms using the MOT beams. The resulting photoluminescence, as well as light scattered by the atom chip surface, is imaged using a zoom lens, and is collected by a CCD camera.

cavity array in Fig. 7.9, so it has been highlighted in red. This position was confirmed by extinguishing all of the excitation beams and coupling light into the cavity via the mounted fiber taper. The light radiated by the cavity and scattered by the microjoints fixing the taper to the device could be imaged with the CCD, providing an accurate indicator of the cavity position. In addition, top view images [same perspective as in Fig. 7.7(a)] were used to verify that the atom cloud was positioned directly above the cavity array. It was also confirmed that when the light input to the cavity was tuned close to resonance with a Cs transition, for sufficiently high input power ($\sim \mu$W), the scattered light destroyed the Cs magnetic trap, further confirming that the microcavity is positioned near the trap.

7.4 Conclusions and outlook

With the fiber mounting and cavity-mirror integration techniques presented in this chapter, it is possible to integrate efficiently fiber-coupled microcavities with an atom chip, and deliver MOT and/or magnetically trapped atoms to the cavities. These techniques are not specific to the types of microcavities and atom chips considered here, or to any of the atom trapping apparatus. For example, this technology could easily be adapted to work with fiber coupled photonic crystal devices integrated with atom chips designed for vacuum glass cell systems [161]. A particularly exciting direction for future work on atom-cavity chips is the monolithic integration of the cavities studied in this thesis with the atom chip substrate. This could be easily realized by fabricating the atom chip from a Si/SiO$_2$/SiN$_x$ wafer underlying an Au microwire layer. The SiN$_x$ layer would provide optical waveguiding, with the lower refractive index SiO$_2$ layer suppressing optical radiation loss. Advances in atom chip technology may eventually allow single atom [190] magnetic trapping and manipulation, enabling the controlled interaction of atoms with arrays of individually addressed optical microcavities.

Of immediate importance is to understand the interaction between Cs vapor in the UHV system and the microcavity surfaces. A technique for decreasing or compensating for this interaction is necessary if large FSR (free spectral range) or single mode micro- and nanocavities are to be used for cavity QED with alkali atoms. Installing arrays of fiber coupled microcavities, whose resonances are distributed over a range of frequencies, as in Ch. 6, is a short term solution. Possible long term approaches for addressing this issue are (i) passivation of the microcavity surface, (ii) investigation of LIAD of accumulated Cs atoms, (iii) "deterministic" saturation induced tuning of the Cs film thickness (Sec. 7.2), and (iv) design of an atom trapping system that operates with a lower Cs background pressure in the vicinity of the microcavity. Additionally, on-going studies are examining whether Cs dispensers provide improved repeatability of Cs accumulation on the microcavity surface, which may allow a-priori biasing of the microcavity resonance wavelength, assuming that the Cs accumulation saturates. Simultaneously, work developing high bandwidth tunable cavities and integrated multicavity devices may relax the tolerances on the microcavity resonance frequencies.

Chapter 8

Microcavity single atom detection

Detection and trapping of single atoms within the vicinity of an optical cavity is a critical tool in the effort to realize the canonical system of cavity QED: A single trapped (spatially localized) atom interacting with the quantized photon field of an optical cavity [6, 5, 4]. By continuously monitoring the optical field of a cavity, it is possible to sense the presence of an atom if the interaction rate between the cavity field and the atom is sufficiently high relative to the decoherence rates of the system [176]. Using the cavity itself as a single atom detector, pioneering work with Fabry-Pérot cavities has succeeded in trapping single atoms within the cavity field using optical forces [191, 178, 179], enabling implementation of quantum information processing resources such as the controlled generation of sequences of single photon pulses [34, 35], as well reversible quantum state transfer between photonic and atomic states [38, 39].

As mentioned elsewhere in this thesis, compared to state-of-the-art Fabry-Pérot experiments, microcavity-based cavity QED systems offer, in addition to the possibility of being scaled to more complex configurations, orders of magnitude higher atom-photon interaction rates, leading directly to higher bandwidth and more robust operation [173, 169, 170, 171, 172, 192, 180, 131, 29]. While these advantages stem directly from the ultrasmall mode volume and associated sub-wavelength length scale of the microcavities considered in this thesis, their small size also introduces further technical challenges from an atom detection perspective: It becomes increasingly difficult to localize atoms within the cavity near-field as the cavity volume shrinks. This fact is exemplified by comparing recent [29] single-atom detection signals obtained using a microtoroid [14] cavity with those observed using much larger mode volume Fabry-Pérot systems [176, 27, 193, 28].

In this chapter, we theoretically examine the technical feasibility of detecting single laser

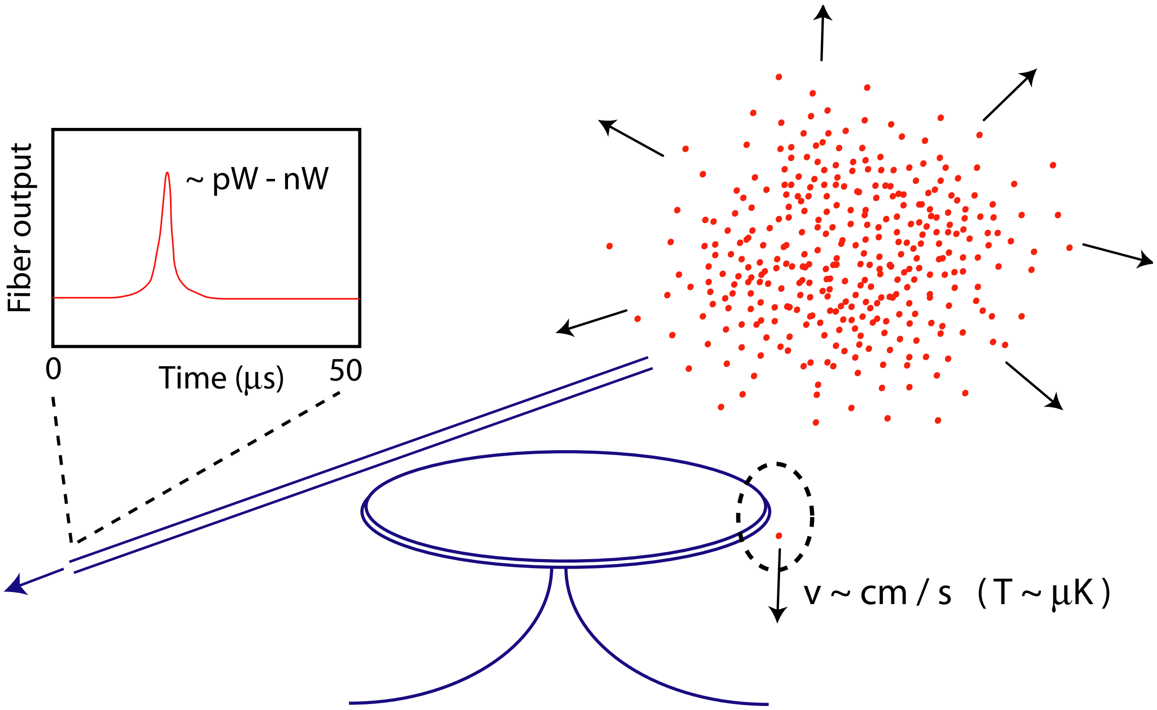

Figure 8.1: Depiction of microdisk atom detection experiment.

cooled atoms, moving with ultra-cold velocities, as they "transit" through the near field of the microcavities studied in Ch. 4 and 6. The single atom detection experiment that we are analyzing is depicted in Fig. 8.1: By monitoring changes in the transmission through a fiber taper that is coupled to a microcavity, in this case a microdisk, we hope to observe single atoms passing through the near field of the microcavity. In the experiment, clouds of cold atoms are delivered to the microcavity using a magnetic trap, as described in Ch. 7, and single atoms are expected to be moving at thermal velocities of ~ 2.5 cm/s [173]. For a 250 nm thick microdisk, the transit time over which an atom moving in a vertical trajectory senses the cavity field will be on the order of a few μs, so that the necessary detection bandwidth is > 1 MHz. This, combined with the relatively low light levels necessary for single-photon single-atom experiments, makes single atom detection technically non-trival.

This work extends results presented in Refs. [173, 180] to study the sensitivity of microcavities to single atoms. The central result, presented in Sec. 8.1, is that the maximum atom-induced change in waveguide output signal scales, to a very good approximation, with Q/V. This analysis includes non-idealities, such as coupling between degenerate cavity modes, non-ideal fiber-cavity coupling, and operation of the system in the bad-cavity regime. In Sec. 8.2, suitable photodetection schemes are analyzed, and an atom-detection figure of merit is calculated for realistic detector noise figures and atom transit times, as a function of microcavity and experiment parameters.

8.1 Atom induced modification of fiber coupled cavity response

In this section, we use a quantum master equation [194] formalism to calculate the transmission through a waveguide coupled to a microcavity when an atomic dipole is interacting with the cavity near field. A semiclassical [195, 196] analysis in the weak driving regime is also used to derive analytic expressions that provide insight into the maximum expected change in waveguide output power that can be induced by an atom interacting with the cavity, as a function of cavity parameters. We begin in Sec. 8.1.1 by considering a single mode microcavity before analyzing a whispering gallery mode microcavity with degenerate travelling wave modes in Sec. 8.1.2. Finally, simulation results for realistic cavity and atomic dipole parameters are given in Sec. 8.1.3.

A note on notation: Thoughout this analysis, we use similar notation as in Ch. 3, with some simplifications. Here, we write the intrinsic cavity loss rate as γ_i, the waveguide-cavity coupling rate as γ_e, and the total cavity loss rate as γ_t. We do not explicitly include parastic waveguide loss, but it is straighforward to modify the analysis to include it. The cavity and atomic decay rates used in this chapter are related to the standard cavity QED notation as follows: $\gamma_t = 2\kappa$, $\gamma_a = \gamma_{||} + \gamma_{\perp}$.

8.1.1 Single mode cavity

For a given cavity field amplitude, a, the amplitude of the fiber field transmitted past the cavity is given by

$$t = s + i\sqrt{\gamma_e}a, \tag{8.1}$$

where s is the amplitude of the fiber input field, and γ_e is the fiber-cavity coupling rate (see Fig. 6.5) [134]. In this formalism, $|s|^2$ has units of power (i.e., photons per unit of time), and $|a|^2$ has units of energy (i.e., photons). The magnitude of γ_e is determined by the evanescent field overlap and the degree of phase matching between the waveguide and cavity modes.

Writing the cavity field amplitude as a_c when there is no atom in the cavity, from standard cavity-waveguide coupled mode theory [89, 134, 84], the equation of motion for $a_c(t)$ is

$$\frac{da_c}{dt} = -\left(\frac{\gamma_i}{2} + \frac{\gamma_e}{2} + i\Delta\omega_c\right) a_c + is\sqrt{\gamma_e}, \tag{8.2}$$

where γ_i is the loss rate of the cavity in the absence of the waveguide, and $\Delta\omega_c$ is the detuning between the input field and the cavity resonance frequency. In steady state, this gives for the empty cavity field amplitude

$$a_c = \frac{is\sqrt{\gamma_e}}{i\Delta\omega_c + \gamma_t/2}, \tag{8.3}$$

where $\gamma_t = \gamma_i + \gamma_e$ is the total energy decay rate of the cavity. On-resonance, $\Delta\omega_c = 0$, and

$$a_{c,o} = i\frac{2s\sqrt{\gamma_e}}{\gamma_t}. \tag{8.4}$$

The corresponding intracavity photon number is

$$n_{c,o} = |a_{c,o}|^2 = \frac{s^2}{\gamma_t}\frac{4\gamma_e}{\gamma_t} = \frac{s^2}{\gamma_t}\frac{4K}{1+K} = \frac{s^2}{\gamma_i}\frac{4K}{(1+K)^2} \tag{8.5}$$

where K is the coupling parameter defined in Ch. 3. If the cavity only radiates into a single waveguide channel (e.g., as is the case with the photonic crystal cavity studied in Ch. 3 and Ch. 4), then $K = \gamma_e/\gamma_i$. The above expression for $a_{c,o}$, combined with Eq. 8.1, gives the usual result for the empty cavity, on-resonance, normalized transmission:

$$T_{c,o} = \left|\frac{t}{s}\right|^2 = \left|1 - 2\frac{\gamma_e}{\gamma_t}\right|^2 = \left|\frac{1-K}{1+K}\right|^2. \tag{8.6}$$

When an atom is present in the cavity, the equation of motion for the cavity field is modified, as it is necessary to consider coupling between the electric field and the atomic states. We will do this, and then calculate the modification to the waveguide transmission when there is an atom in the cavity, by first writing the fully quantized master equation for the atom-cavity system, and then considering the semiclassical limit.

Quantum master equation

In the rotating frame of the input optical field, the Hamiltonian for a two level atom coupled to a quantized cavity mode is

$$\hat{H} = \Delta\omega_a \hat{\sigma}_+ \hat{\sigma}_- + \Delta\omega_c \hat{a}^\dagger \hat{a} + ig\left(\hat{a}^\dagger\ \hat{\sigma}_- - \hat{a}\ \hat{\sigma}_+\right) + i\left(\varepsilon\ \hat{a}^\dagger - \varepsilon^*\ \hat{a}\right), \tag{8.7}$$

where $\hat{\sigma}_\pm$ are the raising and lowering operators of the two level atomic system, g is the atom-photon coupling rate (which can be written in terms of the cavity mode volume and the atomic dipole strength: see Sec. 6.6), $\varepsilon = is\sqrt{\gamma_e}$ is the amplitude of the incident field driving the system at frequency ω_p, $\Delta\omega_a = \omega_a - \omega_p$ is the detuning between the driving field and the atomic transition, and $\Delta\omega_c = \omega_c - \omega_p$ is the detuning between the driving field and the cavity resonance, as in Eq. 8.2.

In order to calculate the steady state expectation value of $\hat{a}$ in the presence of dissipation, we can employ a quantum master equation [194]:

$$\frac{d\hat{\rho}}{dt} = -i\left[\hat{H}, \hat{\rho}\right] + \hat{L}\hat{\rho}, \tag{8.8}$$

where $\hat{L}$ permits decoherence to be taken into account. For the atom-cavity system studied here, it is

$$\hat{L}\ \hat{\rho} = \frac{\gamma_t}{2}\left(2\hat{a}\hat{\rho}\hat{a}^\dagger - \hat{a}^\dagger\hat{a}\hat{\rho} - \hat{\rho}\hat{a}^\dagger\hat{a}\right) + \frac{\gamma_a}{2}\left(2\hat{\sigma}_-\hat{\rho}\hat{\sigma}_+ - \hat{\sigma}_+\sigma_-\hat{\rho} - \hat{\rho}\hat{\sigma}_+\hat{\sigma}_-\right), \tag{8.9}$$

where γ_a is the atomic decoherence rate due to spontaneous emission. Solving Eq. 8.8 for $\hat{\rho}_{ss}$ in steady state (setting $d\hat{\rho}/dt = 0$), we can calculate the steady state expectation value of $\hat{a}$ when there is an atom interacting with the cavity field:

$$a_a = \langle \hat{a} \rangle_{ss} = \mathrm{Tr}\left(\hat{\rho}_{ss}\hat{a}\right). \tag{8.10}$$

The taper transmission, T_a, in the presence of an atom is then simply given by

$$T_a = \left|1 + i\frac{a_a}{s}\sqrt{\gamma_e}\right|^2, \tag{8.11}$$

and the change in photon flux exiting the fiber taper when an atom is coupled to the cavity with interaction strength, g, is,

$$\Delta P = s^2 \big| T_a - T_c \big|. \tag{8.12}$$

In general, we can caculate a_a numerically from Eq. 8.8 for a finite-sized photon Fock-space using tools such as the Quantum Optics Toolbox [197]. However, we can also gain some valuable intuition by considering the semiclassical equations of motion.

Semiclassical analysis

The equations of motion for the expectation values of $\hat{a}$ and $\hat{\sigma}_\pm, \hat{\sigma}_z$ can be derived from $d\langle \hat{A} \rangle / dt = d/dt \left(\mathrm{Tr} \left(\hat{\rho} \; \hat{A} \right) \right)$, the canonical commutation and completeness relations that define $\hat{a}$ and $\hat{\sigma}_\pm, \hat{\sigma}_z$, and Eq. 8.8. In the semiclassical approximation, expectation values of operator products are evaluated as products of the expectation values of the individual operators [196, 195]; for example, $\langle \hat{\sigma}_z \hat{a} \rangle = \langle \hat{\sigma}_z \rangle \langle \hat{a} \rangle$. This analysis gives the semiclassical optical Maxwell-Bloch equations,

$$\frac{da_a}{dt} = -\left(i\Delta\omega_c + \frac{\gamma_t}{2} \right) a_a + g\sigma_- + \varepsilon, \tag{8.13}$$

$$\frac{d\sigma_-}{dt} = -\left(i\Delta\omega_a + \frac{\gamma_a}{2} \right) \sigma_- + g\sigma_z a_a, \tag{8.14}$$

$$\frac{d\sigma_z}{dt} = -2g \left(\sigma_- a_a^* + \sigma_+ a_a \right) - \gamma_a \left(1 + \sigma_z \right). \tag{8.15}$$

which can be solved in steady state for a_a as a function of drive strength, ε, and detunings, $\Delta\omega_c$ and $\Delta\omega_a$. Because of the $g\sigma_z a_a$ term in Eq. 8.14, the solution is nonlinear in a_a, and is typically refered to as the optical bistability equation. Note that when $g \to 0$, Eq. 8.13 is identical to Eq. 8.2 with $\varepsilon = is\sqrt{\gamma_e}$. For a weak driving field, ε, we will find that the semiclassical equations acurately predict the intracavity photon number.

Weak driving regime

Further simplification can be obtained by limiting ourselves to the weak driving regime, where we assume that the atomic state is never inverted, i.e., $\sigma_z \sim -1$. In this limit, the optical Maxwell-Bloch equations are linearized [196], and give

$$a_a = \frac{\varepsilon \left(\gamma_a/2 + i\Delta\omega_a \right)}{\left(\gamma_t/2 + i\Delta\omega_c \right) \left(\gamma_a/2 + i\Delta\omega_a \right) + g^2}. \tag{8.16}$$

Equation 8.16 can be used to illustrate the effect of the atom on the fiber coupled cavity response. Note that in the limit that $g \rightarrow 0$, $a_a \rightarrow a_c$ given by Eq. 8.3, as expected.

To illustrate the effect of the atom on the cavity response, consider the special case where the cavity, atom, and driving field are all on resonance: $\Delta\omega_c = \Delta\omega_a = 0$. In this case,

$$a_{a,o} = \frac{2\varepsilon}{\gamma_t + 4g^2/\gamma_a} = \frac{2is\sqrt{\gamma_e}}{\gamma_t + 4g^2/\gamma_a}, \tag{8.17}$$

and

$$T_{a,o} = \left|1 - \frac{2\gamma_e/\gamma_t}{1 + 4g^2/\gamma_t\gamma_a}\right|^2. \tag{8.18}$$

In the limit that $4g^2/\gamma_t \gg \gamma_a$,

$$T_{a,o} \rightarrow \left|1 - \frac{2\gamma_e}{4g^2/\gamma_a}\right|^2 \sim 1, \tag{8.19}$$

and the relative change in the waveguide transmission due to the atom is

$$\frac{T_{a,o}}{T_{c,o}} \sim \left(\frac{1+K}{1-K}\right)^2 \tag{8.20}$$

which can be abritrarily large as $K \rightarrow 1$.

We can also predict what the maximum absolute change in waveguide output power induced by the atom. From the Maxwell-Bloch equations, it can be shown that

$$1 + \sigma_z \sim 2s^2\frac{\gamma_e}{g^2}, \qquad \text{for } \ 4g^2/\gamma_t \gg \gamma_a, \tag{8.21}$$

so that the weak driving condition $\sigma_z \sim -1$ is satisfed when

$$s^2 \ll P_s = s_s^2 = \frac{g^2}{2\gamma_e} = \frac{1}{K}\frac{g^2}{2\gamma_i}, \qquad \text{for } \ 4g^2/\gamma_t \gg \gamma_a. \tag{8.22}$$

where we call P_s the saturation input power. Subsituting Eqs. 8.19 and 8.6 into Eq. 8.12, the change in the power exiting the waveguide when an atom is coupled to the cavity is approximately given by

$$\Delta P_o = s^2\left|1 - \left(\frac{1-K}{1+K}\right)^2\right|, \qquad \text{for } \ 4g^2/\gamma_t \gg \gamma_a, \quad s \ll s_s \tag{8.23}$$

which is simply the power dropped into the empty cavity from the waveguide. From Eq. 8.22, the maximum atom induced change in power is

$$\Delta P_o \ll \frac{2g^2}{\gamma_i}\frac{1}{(1+K)^2}. \qquad \text{for} \;\; 4g^2/\gamma_t \gg \gamma_a \tag{8.24}$$

It is also convenient to write this in terms of the maximum on-resonance empty cavity intracavity photon number, n_s, at which the weak driving approximation is valid:

$$\Delta P_o \ll \gamma_i \; n_s, \qquad \text{for} \;\; 4g^2/\gamma_t \gg \gamma_a \tag{8.25}$$

where $n_s = 2g^2/\gamma_t^2$.

From Eq. 8.24, we can clearly see that the maximum atom induced change in power increases as the intrinsic loss rate (γ_i) and the mode volume ($\propto g^{-1/2}$) of the cavity decrease. Another important observation is that the above analysis does not require the atom-cavity system to be in the strong coupling regime. Rather, it is sufficient for the system to be in the "bad-cavity" regime for single atom detection. Finally, recall that the example considered above is on resonance ($\Delta\omega_c = \Delta\omega_a = 0$), and that full quantum simulations are required to predict the cavity response for larger drive fields. Later in this section, we will examine the dependence of T_a on detuning for cavities in both the strong and weak coupling regimes, using both the semiclassical solution and fully quantum simulations.

8.1.2 Whispering gallery mode cavity

The presence of a degenerate or nearly denegerate mode significantly affects the cavity response to an atomic dipole [198]. Even when the cavity modes are exactly orthogonal, if the atom interacts with each mode, the modes become coupled. In the case of whispering gallery mode cavities such as microdisks, a dipole scatters light from a single travelling wave mode into both the clockwise and counterclockwise travelling modes, in a manner analogous to surface roughness induced modal coupling [16, 15, 136, 198]. In this section, we will augment the analysis given above to include a second cavity mode.

Assume that the cavity supports two degenerate, counter-propagating, whispering gallery modes whose fields have amplitude a and b. Here we label a and b as the *ccw* (counter-clockwise) and *cw* (clockwise) propagating modes, respectively. Because of the necessity of phase matching, the waveguide will only couple to the co-propagating mode, which we will assume is a. As in the single mode case, the normalized transmission through the waveguide is

$$T = \left| 1 + i\frac{a}{s}\sqrt{\gamma_e} \right|^2 . \tag{8.26}$$

Any photons scattered into the counter-propagating mode b will couple to the backward propagating waveguide mode; the normalized reflected waveguide signal is

$$R = \left| i\frac{b}{s}\sqrt{\gamma_e} \right|^2 . \tag{8.27}$$

In absence of coupling to an atom, the equations of motion for the empty cavity mode amplitudes, $a_c(t)$ and $b_c(t)$, are

$$\frac{da_c}{dt} = -\left(\frac{\gamma_i}{2} + \frac{\gamma_e}{2} - i\Delta\omega_c\right) a_c + i\beta b_c + is\sqrt{\gamma_e}, \tag{8.28}$$

$$\frac{db_c}{dt} = -\left(\frac{\gamma_i}{2} + \frac{\gamma_e}{2} - i\Delta\omega_c\right) b_c + i\beta^* a_c, \tag{8.29}$$

where β is the coupling rate between modes intrinsic to the cavity (e.g., due to surface scattering), and we have assumed that both modes have equal γ_i and γ_e.

In the limit that $|\beta| \ll \gamma_t$, we say that the cavity supports degenerate whispering gallery modes. In this limit, a_c and T_c are identical to those obtained for the single mode cavity. However, as we will show below, when an atom interacts with a cavity in this limit, a_a and T_a are modified significantly relative to the single-mode result obtained above.

In the limit that $|\beta| \gg \gamma_t$, the cavity eigenmodes are most intuitively represented by standing waves formed by even and odd supperpositions of the *cw* and *ccw* modes [16, 15, 136, 198]. These standing waves are uncoupled, and have resonant frequencies $\omega_c \pm \beta$. Because the standing waves have no azimuthal momentum, they radiate equally into both the forward and backward waveguide modes, and the waveguide-cavity coupling is modified. For $\omega_p = \omega_c \pm |\beta|$, $T_{c,o}$ can be calculated using the identical expression (Eq. 8.6) for the single mode cavity, but with $K \to K' = \gamma_e/(\gamma_i + \gamma_e) = K/(K+1)$.

The following analysis is valid for all values of β. However, we only consider limiting on-resonance cases when $\beta \to 0$, since in the $|\beta| \gg \gamma_t$ limit, the single mode cavity results with $K \to K'$ can be used.

Quantum master equation

The quantum master equation for a two-mode cavity is a simple generalization of the result for the single mode cavity presented in Sec. 8.1.1 [198]. In the rotating frame of the input optical field, the Hamiltonian for a two level atom coupled to the two quantized cavity modes is

$$\begin{aligned}\hat{H} = \Delta_a \hat{\sigma}_+ \hat{\sigma}_- + \Delta_c \left(\hat{a}^\dagger \hat{a} + \hat{b}^\dagger \hat{b}\right) + ig\left(\hat{a}^\dagger\ \hat{\sigma}_- - \hat{a}\ \hat{\sigma}_+\right) + \\ ig\left(\hat{b}^\dagger\ \hat{\sigma}_- - \hat{b}\ \hat{\sigma}_+\right) + i\left(\varepsilon\ \hat{a}^\dagger - \varepsilon^*\ \hat{a}\right).\end{aligned} \tag{8.30}$$

We have assumed that the atomic coupling strength, g, is equal for both modes of the cavity; this is valid for degenerate whispering gallery modes that only differ in their direction of propagation, but is not generally true.

For the degenerate whispering gallery mode cavity, L is given by

$$\hat{L}\ \hat{\rho} = \frac{\gamma_t}{2}\left(2\hat{a}\hat{\rho}\hat{a}^\dagger - \hat{a}^\dagger\hat{a}\hat{\rho} - \hat{\rho}\hat{a}^\dagger\hat{a}\right) + \frac{\gamma_t}{2}\left(2\hat{b}\hat{\rho}\hat{b}^\dagger - \hat{b}^\dagger\hat{b}\hat{\rho} - \hat{\rho}\hat{b}^\dagger\hat{b}\right) \tag{8.31}$$

$$+\frac{\gamma_a}{2}\left(2\hat{\sigma}_-\hat{\rho}\hat{\sigma}_+ - \hat{\sigma}_+\sigma_-\hat{\rho} - \hat{\rho}\hat{\sigma}_+\hat{\sigma}_-\right). \tag{8.32}$$

After calculating the steady state master equation,ρ_{ss}, from Eq. 8.8, the amplitudes of the forward and backward propagating waveguide fields are:

$$a_a = \langle\hat{a}\rangle_{ss} = \mathrm{Tr}\left(\hat{\rho}_{ss}\hat{a}\right), \tag{8.33}$$

$$b_a = \langle\hat{b}\rangle_{ss} = \mathrm{Tr}\left(\hat{\rho}_{ss}\hat{b}\right). \tag{8.34}$$

As in the single-mode case, a_a and b_a can be calculated numerically and substituted into Eqs. 8.26 and 8.27 to determine R and T when an atom is coupled to the cavity.

Semiclassical analysis

The semiclassical equations of motion for an atomic dipole coupled to a degenerate whispering gallery mode cavity are [198]

$$\frac{da_a}{dt} = -\left(i\Delta\omega_c + \frac{\gamma_t}{2}\right) a_a + i\beta\ b_a + g\sigma_- + \varepsilon, \tag{8.35}$$

$$\frac{db_a}{dt} = -\left(i\Delta\omega_c + \frac{\gamma_t}{2}\right) b_a + i\beta^*\ a_a + g\sigma_- \tag{8.36}$$

$$\frac{d\sigma_-}{dt} = -\left(i\Delta\omega_a + \frac{\gamma_a}{2}\right) \sigma_- + g\sigma_z(a_a + b_a), \tag{8.37}$$

$$\frac{d\sigma_z}{dt} = -2g\left(\sigma_-(a_a^* + b_a^*) + \sigma_+(a_a + b_a)\right) - \gamma_a\left(1 + \sigma_z\right). \tag{8.38}$$

Note that these equations do not reduce to the equations of motion for an atom coupled to a single mode cavity when $|\beta| = 0$, except in the limit that $g = 0$, i.e., when the cavity modes do not interact with the atom.

Weak driving regime

In the weak driving regime, where $\langle\sigma_z\rangle = -1$ for all time, the semiclassical equations of motion can be solved for a_a and b_a,

$$a_a = \frac{\varepsilon(\theta_c + g^2/\theta_a)}{\theta_c(\theta_c + g^2/\theta_a) + g^2/\theta_c\left(i\beta + i\beta^*\right) + g^2\theta_c/\theta_a + |\beta|^2}, \tag{8.39}$$

$$b_a = a_a \frac{i\beta^* - g^2/\theta_c}{\theta_c + g^2/\theta_a}, \tag{8.40}$$

where $\theta_c = i\Delta\omega_c + \gamma_t/2$, and $\theta_a = i\Delta\omega_a + \gamma_a/2$.

We can make further simplifications in the special case that $|\beta| = 0$, where Eq. 8.39 simplifies to:

$$a_a = \frac{\varepsilon(\theta_a + g^2/\theta_t)}{\theta_a\theta_t + 2g^2}. \qquad \text{for} \quad |\beta| = 0 \tag{8.41}$$

Comparing this expression with the analogous expression (Eq. 8.16) for the single mode cavity, we see that they are only equal in the limit that $g \to 0$. If the atom and cavity are on resonance with the drive field ($\Delta\omega_a = \Delta\omega_c = 0$), Eq. 8.41 reduces to

$$a_{a,o} = \frac{2\varepsilon}{\gamma_t}\frac{4g^2/\gamma_t\gamma_a + 1}{8g^2/\gamma_t\gamma_a + 1}, \qquad \text{for} \quad |\beta| = 0 \tag{8.42}$$

and in the limit ($g^2 \gg \gamma_t\gamma_a$),

$$a_{a,o} = \frac{\varepsilon}{\gamma_t} = \frac{is\sqrt{\gamma_e}}{\gamma_t}. \qquad \text{for } 4g^2/\gamma_t \gg \gamma_a,\ |\beta| = 0 \tag{8.43}$$

The corresponding waveguide transmission is

$$T_{a,o} = \left(1 - \frac{\gamma_e}{\gamma_t}\right)^2 = \frac{1}{(1+K)^2}. \qquad \text{for } 4g^2/\gamma_t \gg \gamma_a,\ |\beta| = 0 \tag{8.44}$$

For no-zero waveguide-cavity coupling ($K > 0$), $T_{a,o}$ for the degenerate whipering gallery mode cavity is clearly less than the unity transmission that was calculated in the single mode case (Eq. 8.19). The maximum relative change in the waveguide transmission induced by the atom is

$$\frac{T_{a,o}}{T_{c,o}} \sim \frac{1}{(1-K)^2}, \qquad \text{for } 4g^2/\gamma_t \gg \gamma_a,\ |\beta| = 0 \tag{8.45}$$

and the change in waveguide output power is

$$\Delta P = s^2 \frac{K(2-K)}{(1+K)^2}. \qquad \text{for } 4g^2/\gamma_t \gg \gamma_a,\ |\beta| = 0 \tag{8.46}$$

Note that as $K \to 1$, $\Delta P \to s^2/4$.

From the optical Bloch equations, the input power below which $\sigma_z \sim -1$ in the degenerate whispering gallery mode cavity is

$$s^2 \ll P_s = s_s^2 = \frac{2g^2}{\gamma_e}, \qquad \text{for } 4g^2/\gamma_t \gg \gamma_a,\ |\beta| = 0 \tag{8.47}$$

and the maximum absolute change in waveguide output power induced by the atom is

$$\Delta P_o \ll \frac{2g^2}{\gamma_i} \frac{|2-K|}{(K+1)^2} = \gamma_i\ n_s \frac{|2-K|}{4}, \qquad \text{for } |\beta| = 0 \tag{8.48}$$

where $n_s = 8g^2/\gamma_t^2$ for the degenerate whispering gallery mode cavity. Note that for $K = 1$, this is the same result as in the single mode cavity case, i.e., Eqs. 8.48 and 8.24 are equivalent. Although the atom induces a smaller change in cavity transmission in degenerate whispering gallery mode cavities than in single mode cavities, the saturation input power is higher, so that the maximum atom induced change in output power is equal for both cases.

As with the single mode cavity analysis, from Eq. 8.48, we can clearly see that the maximum atom induced change in power increases as the intrinsic loss rate (γ_i) and the mode volume ($\propto g^{-1/2}$) of the cavity decrease. Again, to observe single atom effects, the above analysis does not require that the atom-cavity system be in the strong coupling regime, but only in the "bad-cavity" regime.

Finally, recall that the above analysis assumes $|\beta| = 0$. In the limit that $|\beta| \gg \{g, \gamma_t, \Delta\omega_c, \Delta\omega_a\}$, it is more intuitive to analyze the cavity in the renormalized standing wave basis, with detunings measured relative to the "new" modes. As discussed above, in this case one finds that the atom-cavity system dynamics are similar to those of the single-mode cavity presented in Sec. 8.1.1, with a modification to the coupling parameter K to account for coupling between the standing wave modes and the backward propagating waveguide modes.

8.1.3 Simulations

In this section, we simulate the effect of an atom on the waveguide coupled cavity response for varying system parameters, by both numerically solving the quantum master equation, and using the analytic expressions obtained from the semiclassical equations of motion in Secs. 8.1.1 and 8.1.2. We find that at low powers is it sufficient to rely upon the semiclassical, weak driving solution; but for powers approaching $P_s = s_s^2$, it is necessary to solve the fully quantized quantum master equation. First we consider the behavior of a single mode cavity, before studying a degenerate whispering gallery mode cavity.

Single mode cavity

Figure 8.2 compares the transmission, T_c, through a waveguide coupled to a bare cavity with $Q = \{10^4, 10^5, 10^6\}$ ($\gamma_t/2\pi = \{0.35, 3.5, 35\}$ GHz), with the transmission T_a when an atom is coupled to the same cavity. For these simulations, $g/2\pi = 1$ GHz and $\gamma_a/2\pi = 0.005$ GHz, representing a Cs atom coupled to a cavity similar to the ~ 9 μm diameter SiN$_x$ microdisk studied in Ch. 6. As expected from the analysis in Sec. 8.1.1, at $\Delta\omega_c = 0$, an atom induced change in the waveguide transmssion is observed for input power P_i less than P_s. As the input power increases above s_s^2, the change in transmission, $|T_a - T_c|$, decreases. It is useful to note that when $P_i \ll P_s$, the semiclassical, weak driving regime solution given by Eq. 8.16 gives essentially indentical results to those obtained from a numerical solution of the density matrix for the fully quantized systems (Eq. 8.8). For varying Q, the spectra of $T_a(\Delta\omega_c)$

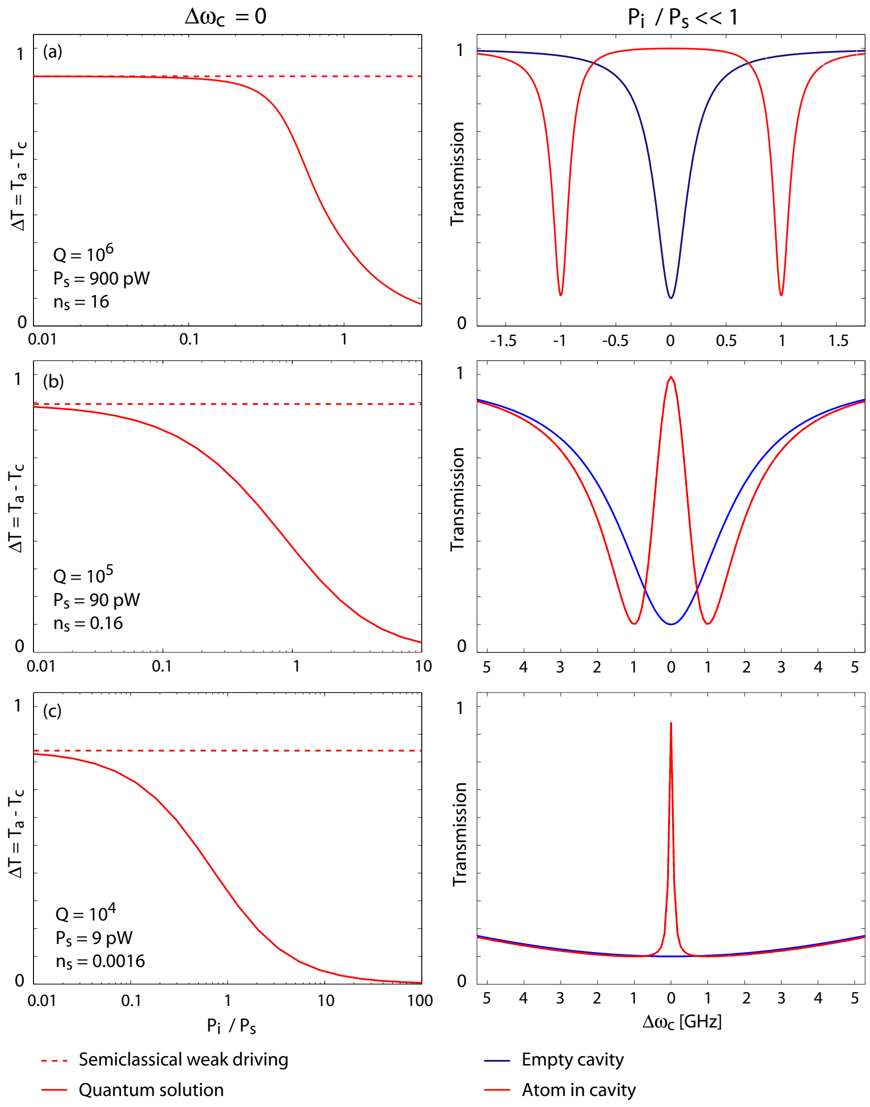

Figure 8.2: Effect of an atom on the response of a fiber coupled single-mode cavity as a function of (left) on-resonance waveguide input power ($\Delta\omega_c = \Delta\omega_a = 0$), and (right) drive field detuning $\Delta\omega_c$ with $P_i \ll P_s$ and $\Delta\omega_a = \Delta\omega_c$, for varying cavity quality factor: (a) $Q = 10^6$, (b) $Q = 10^5$, (c) $Q = 10^4$. In all of the simulations, $\lambda_o = 852$ nm, $g/2\pi = 1$ GHz, $\gamma_a/2\pi = 0.005$ GHz, $K = 0.52$ ($T_{e,o} = 0.1$), and both fully-quantum and semiclassical solutions were used, as indicated. For the spectra on the right, the semiclassical and fully-quantum results cannot be differentiated by eye.

differ dramatically, consistent with the atom-cavity system being in the strong-coupling, bad-cavity, and weak coupling regimes, as shown in Fig. 8.2(a-c), respectively [5].

In strong coupling [Fig. 8.2(a)], the coupled atom-cavity system forms dressed-states that are shifted in frequency by $\pm g$ from the bare cavity resonance frequency, and the waveguide transmission spectrum is dramatically modified. As γ_t increases [Fig. 8.2(b-c)], the dressed states no longer form spectrally distinct features in the waveguide transmission. However, on-resonance, the waveguide transmission continues to be affected by the atom, due to coherent reflection by the atomic dipole. The resulting electromagnetic induced transparancy-like feature persists even for very large γ_t. Using the semiclassical analysis from Sec. 8.1.1, it can be verified that the spectral width of this feature is approximately $\Delta\omega \sim \gamma_a + g^2/\gamma_t$, i.e., the Purcell enhanced spontaneous emission rate.

Degenerate whispering gallery mode cavity

As discussed in Sec. 8.1.2, the cavity response is significantly modified by coupling between degenerate counter-propagating cavity modes, mediated by the atomic dipole as well as by cavity imperfections. Figure 8.3 compares the waveguide transmission past a degenerate whispering gallery mode cavity with no intrinsic mode-coupling ($|\beta| = 0$), with and without an atom, for the same parameters as in Fig. 8.2.

The atom-cavity spectrum is most dramatically modified by the coupling from the atom into both the *cw* and the *ccw* cavity modes when the system is in strong coupling. As shown in Fig. 8.3(a), three resonant dips in the transmission are predicted. Notably, the resonant frequencies of the outer dips are split by $\pm\sqrt{2}g$ relative to the center dip. The factor of $\sqrt{2}$ is due to the standing wave nature of the coupled *cw* and *ccw* modes, and the resulting enhancement of the maximum field strength. From an atom detection perspective, note that the maximum atom induced change in transmission, ΔT, is smaller than in the single mode cavity case. Also, note that a non-zero reflected signal is generated, which potentially can be used for atom detection. The power dependence and onset of saturation of ΔT is consistent with predictions from Sec. 8.1.2. Note that because of the large Fock space associated with simulating two cavity modes at large drive strengths, the less memory intensive stochastic Schrödinger equation (SSE) technique [199, 200, 201, 197] was employed to calculate $\Delta T(P_i)$.

In the bad cavity limit, shown in Figs. 8.3(b,c), the effect of the degenerate cavity mode on the atom-cavity spectrum is less dramatic: The spectra has a similar shape as in the single mode case [Fig. 8.2(b)], with a notch in the transmission centered at $\Delta\omega_c = 0$. However, as in the strong coupling case, $T_{a,o}$ does not reach unity, and the maximum atom induced change in transmission is smaller than in the single mode cavity. Again, the reflected signal

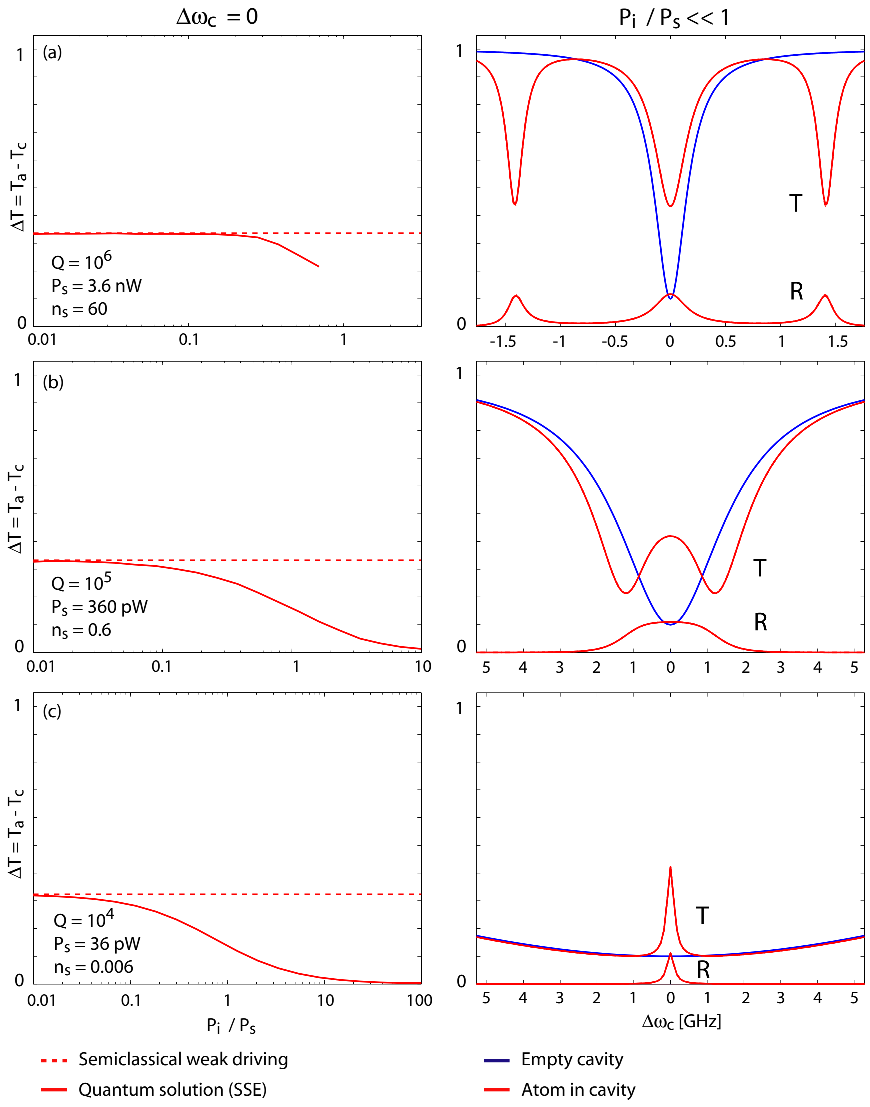

Figure 8.3: Same simulations as in Fig. 8.3, but including a degenerate whispering gallery mode ($|\beta| = 0$). Also shown is the reflected waveguide signal. Both fully-quantum and semiclassical solutions were used, as indicated. For the spectra on the right, the semiclassical and fully-quantum results can not be differentiated by eye. The power dependent calculations in (a) were limited to $P_i < P_s$ for computational reasons.

is non-zero.

Standing wave whispering gallery mode cavity

Fig. 8.4 shows typical waveguide-coupled cavity response spectra when $\beta = 9$ GHz, and the atomic dipole is on resonance with the standing wave cavity mode at $\omega_o - \beta$. In the

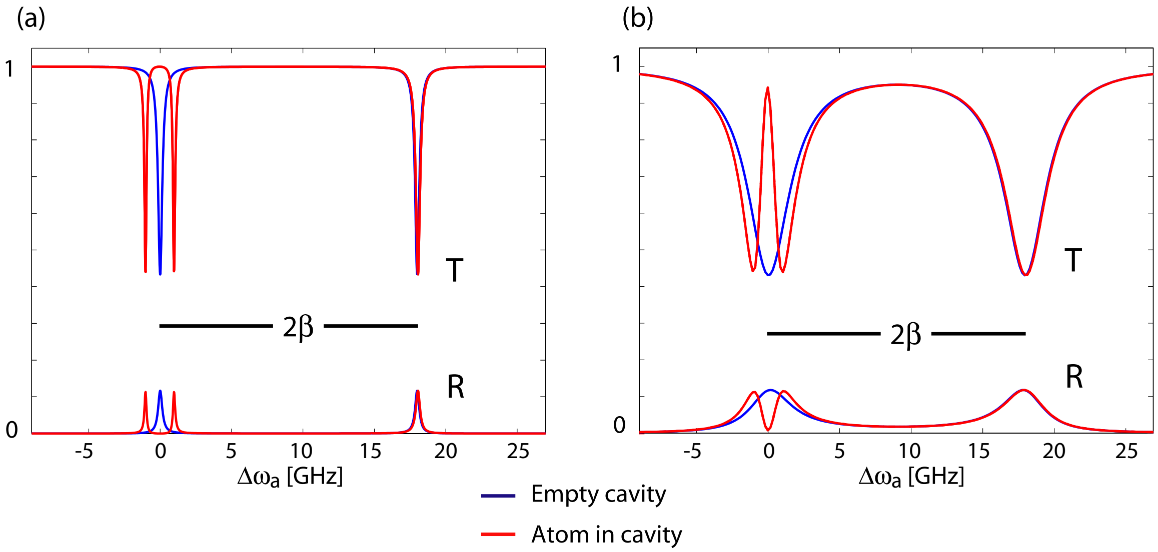

Figure 8.4: Same simulations as in Fig. 8.3, but with microcavity induced coupling between the degenerate whispering gallery modes ($|\beta|/2\pi = 9$ [GHz], β real). The atomic dipole is detuned by $-|\beta|$ from the uncoupled cavity resonance frequency, so that is spectrally aligned with the lower frequency standing wave mode. Although γ_e is unchanged from the simulation results in Figs. 8.3 and 8.2, in the standing wave basis $K \rightarrow K' = K/(K+1) = 0.34$. Also shown is the reflected waveguide signal. The semiclassical and fully-quantum results cannot be differentiated by eye.

presence of an atom, the cavity mode responds nearly identically to the single-mode cavities studied in Sec. 8.1.1, in both the strong- and bad-cavity regimes (Fig. 8.4(a,b), respectively). Notably, the on-resonance transmission when an atom enters the cavity, $T_{a,o}$, recovers to unity. The principle differences are that $g \rightarrow \sqrt{2}g$, due to the standing wave nature of the modes, and that for a given γ_e and γ_i, $T_{c,o}$ is larger, as expected from the discussion above. Additionally, the reflected waveguide signal is non-zero for the empty cavity, as the standing wave mode radiates into both the forward and backward propagating waveguide modes. The power dependence is not shown, but is similar to the single mode case, but with P_s renormalized to take into account the modified waveguide coupling.

8.2 Single atom detection: signal to noise

In the preceding section, we showed that a single atom interacting with the field of a microcavity can significantly alter the cavity response, so that in principle the presence of an atom can be detected as it transits the cavity field. However, to determine whether single atom transits are observable in the laboratory, the photon detection bandwidth and noise floor must be taken into account. In this section, we consider practical photon detection schemes, including single photon counting (SPC), avalanche photodiode (APD) detection, and heterodyne (HD) detection, using specifications for commercially available detectors. We quantitatively evaluate their suitability for single atom detection by calculating the maximum expected signal to noise obtainable with them, given the expected atom-induced change in cavity response and saturation cavity input power calculated in the previous section.

8.2.1 Signal to noise ratio

The signal to noise ratio (SNR) for single atom detection using a fiber-coupled microcavity can be defined in terms of the change in the observed waveguide output signal induced by one or more atoms interacting with the cavity relative to the amplitude of the noise on the output signal when there are no atoms interacting with the cavity. Writing S_c and S_a as the measured signal (e.g., voltage or number of photons) when there are no atoms and when one or more atoms are interacting with the cavity, respectively, a suitable definition for the SNR is

$$\mathrm{SNR} = \frac{\Delta S}{\sigma_S} = \frac{|S_a - S_c|}{\sigma_S}, \tag{8.49}$$

$$\sigma_S = \sqrt{\sigma_t^2 + \sigma_{sn}^2} \tag{8.50}$$

where σ_t and σ_{sn} are the standard deviations of S due to technical noise and shot noise (SN), respectively. Note that this SNR is defined in terms of optical power, and not electronic power. Technical noise is independent of S, and is determined by the detector and the operating bandwidth. Shot noise depends on the output signal, and one can present arguments for whether the shot noise on S_c (during the atom transit) or S_a (when the cavity is not interacting with an atom) should be considered. As in Ref. [173], here we take

$$\sigma_{sn} = \sqrt{\sigma_{sn,a}^2 + \sigma_{sn,c}^2}, \tag{8.51}$$

where $\sigma_{sn,a}$ and $\sigma_{sn,c}$ are the shot noise on S_a and S_c, respectively. This definition provides an accurate measure of the fidelity with which atom-cavity dynamics can be observed. An alternate definition, in which $\sigma_{sn} = \sigma_{sn,c}$, provides an exagerated measure of whether a change in signal can be prescribed to an atom transit, but does not take into account the possiblity of missing a transit due to shot noise fluctuations in the atom-induced signal.

Bandwidth requirements

In general, both the noise and signal amplitudes depend upon the detection bandwidth, $\Delta\nu$. For the experiment considered here, $\Delta\nu$ is determined by the time that an atom spends within the near field of the cavity. Atoms that are laser cooled such that they travel with mean thermal velocities of $\sim$ 2.5 cm/s [180] will transit the 250 nm thickness of a typical microdisk or photonic crystal microcavity in 10 μs [173]. This requires a detection bandwidth of $\Delta\nu = 0.1 - 1$ MHz, corresponding to integration times of $\tau = 1/2\Delta\nu \sim 0.5 - 5$ μs.

Photon collection efficiency

Using the waveguide-cavity coupling formalism presented above, imperfect cavity-waveguide coupling efficiency due to intrinsic cavity loss ("bad-loss") is taken into account by the coupling parameter K. However, broadband "insertion-loss" associated with scattering, radiation, or absorption within the waveguide needs to be taken into account. This insertion loss can be lumped together, and the transmission between the waveguide-microcavity coupling region and the photon detection apparatus can be simply expressed as η_w. In practice, $\eta_w \sim$ 0.5-0.8 is typical for a fiber taper permanently coupled to a microdisk and installed in the atom cooling vacuum chamber, as described in Ch. 7.

Idealized SNR

In a perfect photodetector, there is no technical noise, so that the SNR is only limited by the quantum fluctuations in the detected signal (shot noise), the transmission of the waveguide (η_w), and the quantum efficiency of the detector (η_d). Generally, the measured signal is the change in the measured number of photon counts per time bin when an atom interacts with the cavity (N_a) compared to when there is no atom interacting with the cavity (N_c). For a given integration time τ, S and σ_S are expressed in terms of the waveguide powers, P_a and P_c (in units of photons per unit time), transmitted past the waveguide-cavity coupling region:

$$S = \tau\eta_w\eta_d|P_a - P_c| = \tau\eta_w\eta_d\Delta P, \tag{8.52}$$

$$\sigma_S = \sqrt{\tau\eta_w\eta_d(P_a + P_c)}. \tag{8.53}$$

The SNR is then simply given by

$$\mathrm{SNR}\big|_{\mathrm{SN}} = \frac{\Delta P}{\sqrt{P_a + P_c}}\sqrt{\eta_w\eta_d\tau} = \frac{\Delta N}{\sqrt{N_a + N_c}}\sqrt{\eta_w\eta_d}, \tag{8.54}$$

where $\Delta N = |N_a - N_c|$. For on-resonance detection, in the case that $P_c = 0$ ($K \to 1$), Eq. (8.54) reduces to

$$\mathrm{SNR}\big|_{\mathrm{SN}} = \sqrt{\Delta N}\sqrt{\eta_w\eta_d}. \tag{8.55}$$

In practice, technical noise will always be present. Next, we discuss the limitations of practical photodetection schemes.

8.2.2 Photon detection schemes

Below we briefly review the noise properties of photodetection schemes in the context of single atom detection experiments.

Single photon counting

Commerically available single photon counting modules (SPCM) offer essentially shot noise limited detection "out of the box" for very low light levels. With dark count rate of less than 25 photons per second (Perkin Elmer SPCM-AQP-16), SPCMs have almost no electronic noise on the time scales over which atom transits are expected to occur. Their primary limitation from an atom detection point of view is their large dead time between successive photon counting events, which typically limits the maximum photon flux that they can measure to $\sim 10^7$ photons per second. Assuming that $\{\eta_w P_c, \eta_w P_a\} \leq P_{\mathrm{SPCM}}$, where P_{SPCM} is the saturation power of the SPCM, the SNR is simply given by Eq. 8.54. However, for $\{\eta_w P_c, \eta_w P_a\} > P_{\mathrm{SPCM}}$, the saturation power limits the SNR:

$$\mathrm{SNR}\big|_{\mathrm{SPCM}} < P_{\mathrm{SPCM}} \times \sqrt{\frac{\eta_d\tau}{P_c + P_a}}. \tag{8.56}$$

If $P_{\mathrm{SPCM}} = 10^7$ photons/second and $P_c = 0$, for a $\tau = 1$ μs integration time,

$$\mathrm{SNR}\big|_{\mathrm{SPCM}} < \sqrt{10\ \eta_d}. \tag{8.57}$$

APD detection

Avalanche photodiodes (APD) can provide high-bandwidth, low noise photodetection at low light levels. As with SPCMs, they are fabricated using reverse biased photodiodes, and rely upon avalanche multiplication of photo-generated electrons to provide gain without adding significant electronic noise. Unlike SPCMs, they are not reverse biased past their breakdown point, and can operate at higher powers and bandwidths.

For a given atom-induced change in optical power ΔP (photons per unit time), the signal measured using an APD-amplifier module is

$$S = \mathsf{R}\ \eta_w \Delta P, \tag{8.58}$$

where $\mathsf{R} = \mathsf{R_o}\hbar\omega$, and $\mathsf{R_o}$ is the lumped responsivity of the APD detector module (i.e., APD quantum efficiency, APD gain, and electronic amplifier transimpedance), usually expressed in units of V/W. The noise has contributions from both the APD (shot noise) and the amplifier electronics, and is written as σ_{APD} and σ_t, respectively. The total noise is:

$$\sigma_{S_c} = \sqrt{\sigma_{\mathrm{APD}}^2 + \sigma_t^2}. \tag{8.59}$$

The amplifier noise is typically quoted as a spectral density, $\overline{w}$, in units of W/$\sqrt{\mathrm{Hz}}$, so that

$$\sigma_t = \mathsf{R}\ w\sqrt{\Delta\nu} = \mathsf{R}\frac{w}{\sqrt{2\tau}}, \tag{8.60}$$

where $w = \overline{w}/\hbar\omega$. The APD noise,

$$\sigma_{\mathrm{APD}} = \mathsf{R}\sqrt{F}P_{sn}, \tag{8.61}$$

is fundamental, as it is proportional to the photon shot noise power [3]:

$$P_{sn} = \sqrt{\frac{\eta_w(P_c + P_a)}{\eta_d \tau}}. \tag{8.62}$$

The F term is the "noise factor" characteristic of any stochastic avalanche amplification process [202]; generally $F \geq 1$. Combining the above expressions, the APD SNR for atom detection is

$$\mathrm{SNR}\big|_{\mathrm{APD}} = \frac{\Delta P\ \eta_w}{\sqrt{F(P_c + P_a)\eta_w/\eta_d\tau + w^2/2\tau}}. \tag{8.63}$$

In the limit that electronic noise is small compared to shot noise, Eq. 8.63 becomes

$$\mathrm{SNR}\big|_{\mathrm{APD}} = \frac{\Delta P}{\sqrt{P_a + P_c}}\sqrt{\frac{\tau\eta_w\eta_d}{F}}, \qquad \text{for} \quad \eta_w(P_a + P_c) \gg w^2\eta_d/2F \tag{8.64}$$

which is the "ideal" shot noise limited result, Eq. 8.54, scaled by $F^{-1/2}$.

Heterodyne detection

Ideally, optical heterodyne detection [3, 203] can reach the shot noise limit at high bandwidths, even using photodetectors with large σ_t compared to the the signal of interest. Heterodyne detection measures the amplitude of a beat note formed by two spatially overlapping but frequency detuned optical beams incident on a photodetector. Given a signal with optical power, P_s (photons per unit time), the heterodyne signal is,

$$S = \mathsf{R}\ 2\eta_h\sqrt{P_s P_{\mathrm{lo}}}, \tag{8.65}$$

where R is the responsivity of the detector being used, and P_{lo} is the power of a frequency detuned local oscillator (LO) that is spatially overlapped with the P_s beam, and η_h is the heterodyne efficiency. In practice, η_h depends on the mode matching of the LO and the signal beams, and the mix-down electronics that filter for the beat note. If the LO is not phase locked relative to the signal, $\eta_h \leq 0.5$.

For $P_{\mathrm{lo}} \gg P_s$, the noise of the heterodyne signal is given by

$$\sigma_{S_c} = \sqrt{\sigma_h^2 + \sigma_{\mathrm{lo}}^2}, \tag{8.66}$$

where σ_h is the technical electronic heterodyne noise, and σ_{lo} is the LO shot noise. Ideally, the electronic noise is determined by the measurement bandwidth and the noise power spectral density, w, of the detector at the frequency of the beat note, ν_h:

$$\sigma_h = \mathsf{R}\ w(\nu_h)\sqrt{\Delta\nu}. \tag{8.67}$$

The LO shot is given by,

$$\sigma_{\mathrm{lo}} = \mathsf{R}\sqrt{\frac{P_{\mathrm{lo}}}{\eta_d \tau}}, \tag{8.68}$$

and the heterodyne SNR for atom detection is,

$$\mathrm{SNR}\big|_{\mathrm{HD}} = \frac{2\eta_h|\sqrt{\eta_w P_a P_{\mathrm{lo}}} - \sqrt{\eta_w P_c P_{\mathrm{lo}}}|}{\sqrt{P_{\mathrm{lo}}/\eta_d\tau + w^2/2\tau}}. \tag{8.69}$$

In the limit that $P_{\mathrm{lo}} \gg \eta_d w^2/2$, usually achieved by increasing P_{lo},

$$\mathrm{SNR}\big|_{\mathrm{HD}} = 2\eta_h|\sqrt{P_a} - \sqrt{P_c}|\sqrt{\eta_w\eta_d\tau}. \qquad \text{for} \quad P_{\mathrm{lo}} \gg \eta_d w^2/2 \tag{8.70}$$

If $P_c \sim 0$, this is simply

$$\mathrm{SNR}\big|_{\mathrm{HD}} = 2\eta_h\sqrt{P_a}\sqrt{\eta_w\eta_d\tau}, \tag{8.71}$$

$$= 2\eta_h\sqrt{\Delta N}\sqrt{\eta_w\eta_d}, \tag{8.72}$$

where ΔN is the atom induced change in photon counts per time bin, τ. Again, this corresponds to the "ideal" shot noise limited SNR, Eq. 8.54, scaled by $2\eta_h$.

8.2.3 Simulations

Using the expressions for SNR for the detectors described in Sec. 8.2.2, as well as the power-dependent atom-cavity response calculations from Sec. 8.1.3, we now calculate the SNR for realistic single atom detection, for varying cavity parameters and drive strength. Table 8.1 lists the detector parameters used in the calculations in this section. All of these parameters correspond to commercially available components, as listed in the table.

Figure 8.5 shows calculated atom-detection SNR for a single mode microcavity and a degenerate whispering gallery mode microcavity, assuming on-resonance detection, atom-photon interaction rate, $g/2\pi = 1$ GHz, and a $\tau = 3$ μs integration time, for $Q = \omega/\gamma_t = [10^6, 10^5, 10^4]$, as in Sec. 8.1.3. As discussed in Ch. 6, $[g/2\pi, Q] = [1\ \mathrm{GHz}, 10^6]$ should be achievable for a Cs atom interacting with a silicon nitride microdisk cavity [17]. In addition to considering APD, SPCM, and HD detection, the "ideal" shot noise limited SNR (for η_w and η_d given in Table 8.1) is shown as function of waveguide input power. Each of the detection schemes has an optimal input power at which the SNR is maximized. In the case of the SPCM, the SNR is maximized when the waveguide output power is $\sim P_{\text{SPCM}}/\eta_d$ as expected from Eq. 8.57. So long as $\eta_d \eta_w P_s > P_{\text{SPCM}}$ is satisfied, the maximum SPCM SNR is largely unaffected by g and γ_t. For the other detectors, with saturation powers far above $\eta_d \eta_w P_s$, P_s is a very good prognosticator of the input power at which the SNR is maximized. The maximum SNR obtainable with the degenerate whispering gallery mode cavity is essentially equal to that in the corresponding single mode cavity, albeit at a higher input power (recall that $P_s|_{\text{2-mode}} = 4P_s|_{\text{1-mode}}$), confirming our intuition from Sec. 8.1.2. The smaller change in cavity response characteristic of the degenerate cavity is only deterimental for the SNR for SPCM detection, where ΔP is limited by the detector saturation.

Table 8.1: Photodetector parameters

Detector	Parameter	Value	Units	Source
APD[a]	η_d	0.7	-	Specification
	$\overline{w}$	30	fW/$\sqrt{\text{Hz}}$	Measured[d]
	F	7	-	Specification
SPCM[b]	η_d	0.35	-	Specification
	P_{SPCM}	15×10^6	photons/s	Specification/Measured
HD[c]	η_d	0.7	-	Specification
	η_h	0.5	-	Ideal[e]
	P_{lo}	1	mW	As setup.
	$\overline{w}$	30	pW/$\sqrt{\text{Hz}}$	Specification[g]
Ideal SN	η_d	0.7	-	-
All	η_w	0.5	-	-

[a] Analog Modules 712A-4 (Perking Elmer 30902E APD)

[b] Perkin Elmer SPCM-AQR-16-FC

[c] In-house setup built around a New Focus 1801 detector

[d] Measured for a $\Delta\nu = 1.9$ MHz bandwidth; specification is 20 fW/$\sqrt{Hz}$.

[e] Without phase stabilization, assuming perfect mode matching.

[f] For a beatnote of frequency > 10 MHz

Given shot noise limited detectors with η_w and η_d specified in Table 8.1, from Fig. 8.5 we see that when $g = 1$ GHz, single atom detection should be possible for $Q > 10^5$, as SNR $\gg 1$. However, given the practical detectors under consideration here, the optimum obtainable SNR is far below the shot noise limited maximum. For microcavities with low P_s (e.g., the cavity with $Q = 10^5$), SPCM detectors offer the best performance. Although their small dynamics range limits $\text{SNR}\big|_{\text{SPCM}} \sim 5$, this should be sufficient for single atom detection, though the situation worsens as K decreases and the resonance contrast is reduced. The higher $Q = 10^6$ cavity supports stronger driving powers without saturating the atom. As a result, single-atom signals, ΔP, from these cavities can overcome the electronic noise

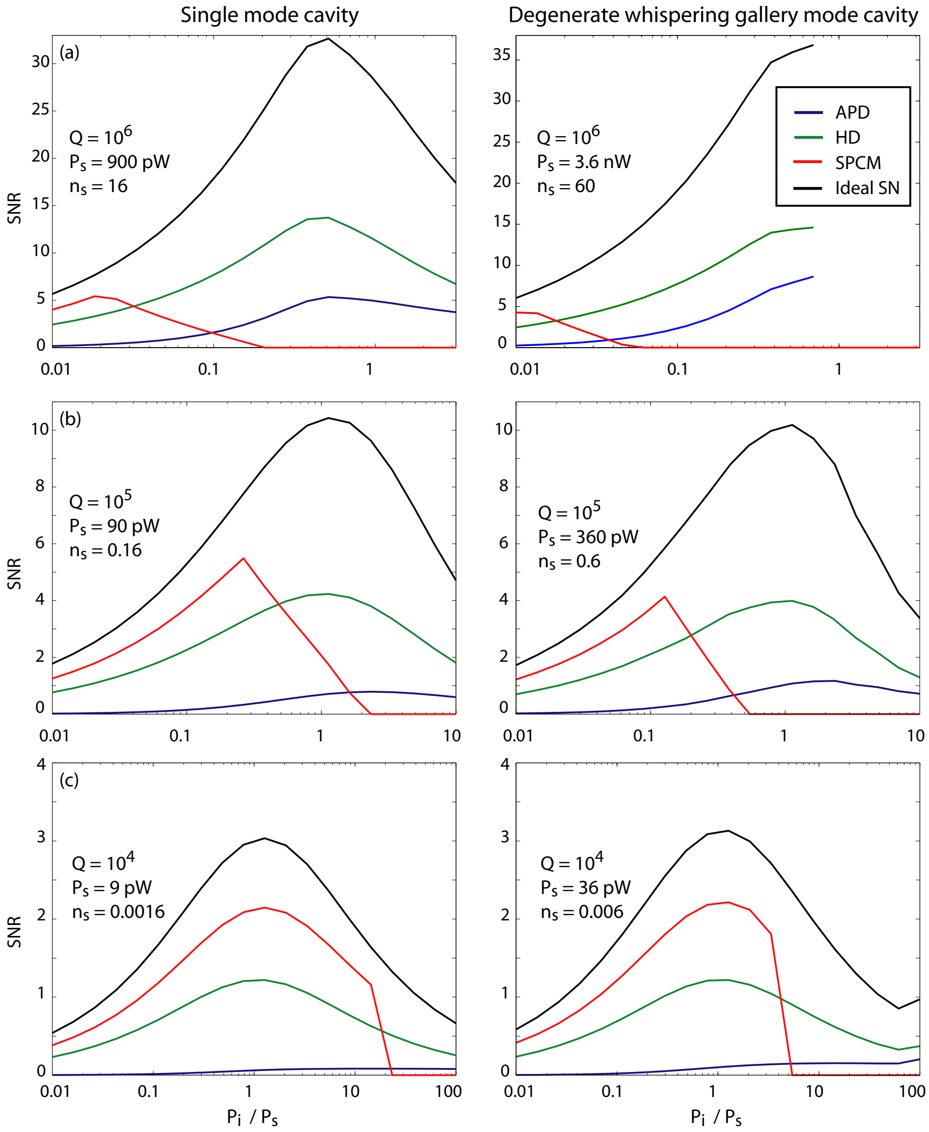

Figure 8.5: Calculated SNR for a fiber coupled single mode (left) and degenerate whispering gallery mode (right) microcavity with $g/2\pi = 1$ GHz and (a) $Q = 10^6$, (b) $Q = 10^5$, (c) $Q = 10^4$. In all of the calculations, $\lambda_o = 852$ nm, $\gamma_a/2\pi = 0.005$ GHz, $\Delta\omega_a = \Delta\omega_c = 0$, $K = 0.52$ ($T_{e,o} = 0.1$). The various detector parameters are given in Table 8.1. The power dependent calculation in (a) was limited to $P_i < P_s$ for computational reasons.

of the APD and HD detectors and provide improved performance: SNR $>$ 10 should be achievable.

Alternately, since $P_s = s_s^2$ scales with g^2/γ_t ($\propto Q/V$), the SNR can be improved by using a smaller mode volume cavity, so long as Q does not degrade too quickly as the mode volume shrinks. Figure 8.6 shows calculated SNR for a microcavity with $g/2\pi = 10$ GHz, and

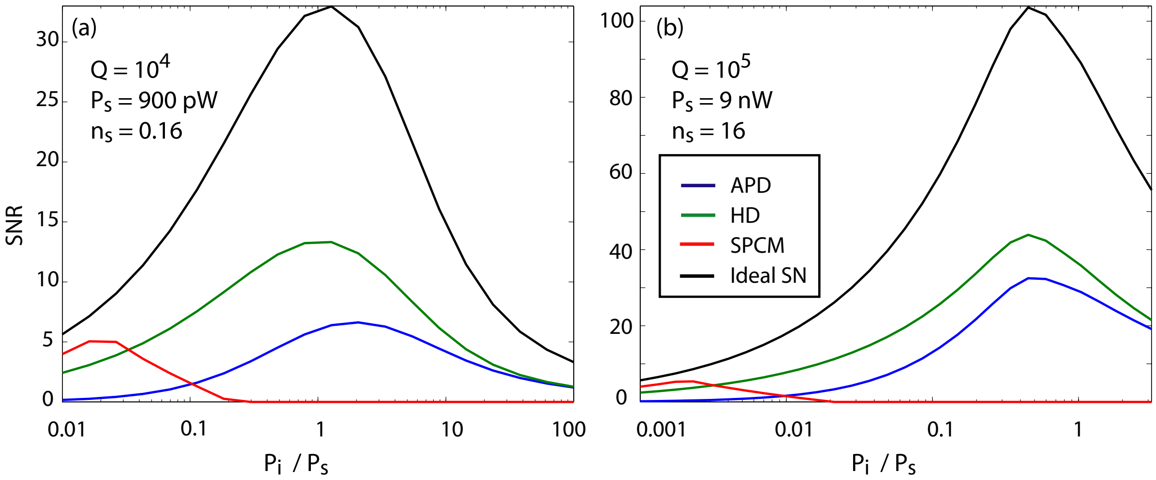

Figure 8.6: Calculated SNR for fiber coupled single mode microcavities with $g/2\pi = 10$ GHz and (a) $Q = 10^5$, (b) $Q = 10^4$. In all of the calculations, $\lambda_o = 852$ nm, $\gamma_a/2\pi = 0.005$ GHz, $\Delta\omega_a = \Delta\omega_c = 0$, $K = 0.52$ ($T_{e,o} = 0.1$). The various detector parameters are given in Table 8.1.

$Q = [10^4, 10^5]$. These parameters should be achievable using a high quality photonic crystal nanocavity [11, 12], such as that studied in Ch. 4, but fabricated from a material suitable for near-visible wavelengths. As expected, when $[g/2\pi, Q] = [10\ \text{GHz}, 10^4]$ [Fig. 8.6(a)], the microcavity performs similarly to the $[g/2\pi, Q] = [1\ \text{GHz}, 10^6]$ microcavity [Figure 8.5(a)]. Figure 8.6(b) shows the expected performance of a cavity with $[g/2\pi, Q] = [10\ \text{GHz}, 10^5]$. Shot noise limited SNR ~ 100 should be possible, and SNR > 30 is expected using direct APD detection. This is a significant improvement over the higher Q, but larger mode volume cavity, and promises high-quality single atom transit measurements. Beyond the benefit of improved single-atom sensitivity, an advantage of pursuing the route of miniturization, rather than working to further increase Q, is robustness. Mode volume is largely unaffected by fabrication imperfections, and lower Q cavities are less sensitive to surface contamination and spectral detuning.

8.3 Summary

In this section, we have shed light on the role of mode volume and quality factor on the sensitivity of a microcavity to single atom transits. In particular, through analytic analysis and verification with numerical simulations, we have shown that the relevant figure of merit is g^2/γ_t, which is proportional to Q/V. Using realistic detector noise parameters, we have studied the expected performance of a range of microcavities, and determined that single atom transits should be observable with the microdisk cavities studied in this thesis, but that larger Q/V devices, and/or longer atom-cavity interaction times, are necessary for high quality signals. It is expected that photonic crystal nanocavities will offer significantly improved detection fidelity.

Appendix A

Bloch modes and coupled mode theory

A physical problem of practical interest is the coupling between Bloch modes in seperate interacting electromagnetic waveguides. This problem arises when considering strongly periodic waveguides, such as those formed by line defects in high refractive index contrast photonic crystals [204, 52, 113, 58]. In these structures, it is not accurate to represent the fields of the unperturbed waveguides using a plane wave basis; a Bloch mode basis must be used. In this appendix an approximate coupled mode theory suitable for studying coupling between strongly period waveguides is derived. Additionally, some mathematical identities useful for working with and understanding the physical properties of Bloch modes are presented.

A.1 Formulating Maxwell's equations

In absence of free charge and current, and for fields with $e^{i\omega t}$ time dependance, Maxwell's equations are given by

$$\nabla \cdot \mathbf{D} = 0 \tag{A.1}$$

$$\nabla \times \mathbf{H} - i\omega \mathbf{D} = 0 \tag{A.2}$$

$$\nabla \times \mathbf{E} + i\omega \mathbf{B} = 0 \tag{A.3}$$

$$\nabla \cdot \mathbf{B} = 0, \tag{A.4}$$

where, for non-magnetic material,

$$\mathbf{D}(\mathbf{r}) = \epsilon(\mathbf{r})\mathbf{E}(\mathbf{r}) \tag{A.5}$$

$$\mathbf{B}(\mathbf{r}) = \mathbf{H}(\mathbf{r}). \tag{A.6}$$

It can be shown [69] that solutions to Maxwell's equations corresponding to a structure whose dielectric constant, $\epsilon(\mathbf{r})$, is periodic in $\hat{\mathbf{z}}$ with lattice constant Λ,

$$\epsilon(x, y, z + n\Lambda) = \epsilon(x, y, z) \tag{A.7}$$

$$n = 0, \pm 1, \pm 2, \ldots$$

can be written in Bloch form

$$\mathbf{E}_k(\mathbf{r}) = e^{-ikz}\mathbf{e}_k(\mathbf{r}), \tag{A.8}$$

where

$$\mathbf{e}_k(x, y, z + n\Lambda) = \mathbf{e}_k(x, y, z), \tag{A.9}$$

and a $e^{i\omega t}$ time dependance is assumed. Writing the field in Bloch form, taking the curl of (A.3) and substituting (A.2), we get

$$\boldsymbol{\nabla} \times \boldsymbol{\nabla} \times \mathbf{E}_k = \frac{\omega^2}{c^2}\epsilon(\mathbf{r})\mathbf{E}_k, \tag{A.10}$$

or, more explicitly,

$$\mathbb{H}_k\mathbf{e}_k(\mathbf{r}) = \left[-k^2\mathbf{z} \times \mathbf{z} \times -ik(\boldsymbol{\nabla} \times \mathbf{z} \times + \mathbf{z} \times \boldsymbol{\nabla}\times) + \boldsymbol{\nabla} \times \boldsymbol{\nabla}\times\right]\mathbf{e}_k(\mathbf{r}) = \frac{\omega^2}{c^2}\epsilon(\mathbf{r})\mathbf{e}_k(\mathbf{r}). \tag{A.11}$$

Equation (A.10) is often solved as an eigenvalue problem for ω parameterized by the wavenumber, k, giving a dispersion relation, $\omega = \omega(k)$. In general (A.10) will have multiple solutions for a given ω. Each of these solutions is a mode of the structure described by $\epsilon(\mathbf{r})$ and can be labeled by a wavenumber, $k = k_m$. To be explicit, $\mathbf{E}_k$ can be labeled as $\mathbf{E}_{k_m}$ to distinguish between modes. For radiating modes, k_m will form a continuum, while for bound modes, k_m will form a discrete set. It is important to note that for each mode $\mathbf{E}_{k_m}$, by time reversal symmetry, there is a corresponding eigenfunction, $\mathbf{E}_{-k_m}$, with eigenvalue $\omega(-k_m) = \omega(k_m)$, which represents a mode propagating in the $-\hat{\mathbf{z}}$ direction.

The relationship between the forward and backward propagating modes will be examined in subsequent sections. Additionally, for each $k_{m'} = k_m + n\,G$ where the reciprocal lattice vector $G = \frac{2\pi}{\Lambda}$ and n is any integer, there corresponds a mode that is physically identical to the mode labelled by k_m [69, 205]. As a result, in considering the space of eigenmodes, it is sufficient to restrict k to the first Brillouin zone: $|k| \leq \frac{G}{2}$.

A.1.1 Orthogonality of Bloch modes

Before deriving coupled mode equations, it is useful to derive an orthogonality relationship between modes. In [68] it is shown that $\mathbb{H}_k$ is Hermitian, so that for fixed k and varying eigenfrequencies, ω_m, equation (A.11) gives

$$\int_{\mathcal{V}} d\mathbf{r}\, \epsilon(\mathbf{r})\, \mathbf{e}^*_{k(\omega_n)}(\mathbf{r}) \cdot \mathbf{e}_{k(\omega_m)}(\mathbf{r}) = \delta_{\omega_n,\omega_m}, \qquad k(\omega_n) = k(\omega_m) \tag{A.12}$$

where the integration is over a single unit cell defined by $\mathcal{V} = \{\mathbf{r} \mid z_0 \leq z \leq z_0 + \Lambda\}$. In coupling between modes in linear dielectrics, however, ω is typically fixed to ensure non-zero time averaged power transfer between modes, while k varies between modes as described above.

Another othorgonality relation can be derived using a reciprocity theorem similar to that used in [72]. Define $\mathbf{F}$ as

$$\mathbf{F} = \mathbf{E}_{k_n} \times \mathbf{H}^*_{k_m} + \mathbf{E}^*_{k_m} \times \mathbf{H}_{k_n}, \tag{A.13}$$

where $\mathbf{E}_{k_{(n,m)}}$ and $\mathbf{H}_{k_{(n,m)}}$ are solutions to Maxwell's equations (A.1-A.4) for some $\epsilon_{(n,m)}$. Using Maxwell's equations and standard vector identities, the divegence of $\mathbf{F}$ is:

$$\boldsymbol{\nabla} \cdot \mathbf{F} = -i\omega \mathbf{E}_{k_n} \cdot \mathbf{E}^*_{k_m}[\epsilon_n(\mathbf{r}) - \epsilon^*_m(\mathbf{r})]. \tag{A.14}$$

From (A.14), if $\epsilon_n = \epsilon^*_m$, then $\boldsymbol{\nabla} \cdot \mathbf{F} = 0$, and integrating over a unit cell:

$$\begin{aligned} \int_{\mathcal{V}} \boldsymbol{\nabla} \cdot \mathbf{F}\, d\mathcal{V} &= \int_{\mathcal{S}} \mathbf{F} \cdot d\mathbf{S} && \text{(A.15)} \\ &= \left[\int_{z=z_0} -\hat{\mathbf{z}} + \int_{z=z_0+\Lambda} \hat{\mathbf{z}} \right] \cdot \mathbf{F}\, dx\, dy + \int_{\mathcal{S}_\infty} \mathbf{F} \cdot d\mathbf{S} && \text{(A.16)} \\ &= 0, \end{aligned}$$

where $\mathcal{S}$ is the surface bounding $\mathcal{V}$, and $\mathcal{S}_\infty$ represents the surface of $\mathcal{V}$ at $\rho = \sqrt{x^2+y^2} \to \infty$. Since the area of $\mathcal{S}_\infty \propto \rho\,\Lambda$ and $|\mathbf{F}| \propto 1/\rho^2$ (at most for physical fields) on $\mathcal{S}_\infty$, the last term in (A.16) does not contribute. Recalling that Bloch modes are eigenvectors of the translation operator:

$$\mathbb{T}_{\Lambda\hat{\mathbf{z}}}(\mathbf{E}_{k_m}, \mathbf{H}_{k_m}) = e^{-ik_m\Lambda}(\mathbf{E}_{k_m}, \mathbf{H}_{k_m}), \tag{A.17}$$

equation (A.16) becomes

$$\left[1 - e^{-i(k_n-k_m)\Lambda}\right] \int_{z=z_0} \left(\mathbf{E}_{k_n} \times \mathbf{H}^*_{k_m} + \mathbf{E}^*_{k_m} \times \mathbf{H}_{k_n}\right) \cdot \hat{\mathbf{z}}\, dx\, dy = 0. \tag{A.18}$$

By Bloch's theorem, the Bragg condition,

$$k_n - k_m = \frac{2\pi j}{\Lambda}, \qquad\qquad j = \pm 1, \pm 2 ... \tag{A.19}$$

can only be satisfied by modes that are identical moduolo a reciprocal lattice vector label. By restricting our eigmodes to the first Brillouin zone, Eq. (A.19) can never be satisfied, requiring that if $k_m \neq k_n$,

$$\int_z \left(\mathbf{E}_{k_n} \times \mathbf{H}^*_{k_m} + \mathbf{E}^*_{k_m} \times \mathbf{H}_{k_n}\right) \cdot \hat{\mathbf{z}}\, dx\, dy = 0, \tag{A.20}$$

for Eq. (A.18) to hold. Equation (A.20) is a power orthogonality relationship that has the advantage of not requiring integration in the propagation direction.

If $k_m = k_n$, assuming there are no degeneracies, modes n and m are identical and the "power" defined by the left hand side of (A.20) is non-zero; however, it can be shown that it is independant of z. We have:

$$\mathbf{F} = \mathbf{E}_{k_m} \times \mathbf{H}^*_{k_m} + \mathbf{E}^*_{k_m} \times \mathbf{H}_{k_m}. \quad (k_m = k_n) \tag{A.21}$$

Integrating $\boldsymbol{\nabla} \cdot \mathbf{F}$ over a plane of constant z, and using (A.14) as well as the 2-D divergence thereom (see [72])

$$\int_z \boldsymbol{\nabla} \cdot \mathbf{F}\, dx\, dy = \frac{\partial}{\partial z} \int_z \mathbf{F} \cdot \hat{\mathbf{z}}\, dx\, dy = 0 \tag{A.22}$$

or

$$\frac{\partial}{\partial z}\int_z \left(\mathbf{E}_{k_m}\times\mathbf{H}^*_{k_m}+\mathbf{E}^*_{k_m}\times\mathbf{H}_{k_m}\right)\cdot\hat{\mathbf{z}}=0. \tag{A.23}$$

This is simply a statement of power conservation: For modes propagating in the **z** direction, the power flux through any x-y plane is independent of z. Equations (A.20) and (A.23) state that the eigenmodes of a periodic $\epsilon(\mathbf{r})$ can be normalized by their power, and that they are power orthogonal. These relations will be critical in the developement of a coupled mode theory below.

A.1.2 Additional properties of Bloch modes

Because of the lack of translational invariance in a periodic $\epsilon(\mathbf{r})$, the standard relationships between forward and backward propagating modes derived in [72] do not hold for Bloch modes. Fortunately, by considering the symmetries of the system, some useful relationships can be derived.

First, consider time reversal symmetry. Since the operator defining $\mathbf{E}(\mathbf{r},t)$ obtained from Maxwell's equations is invariant under time reversal $t\to t'=-t$, the time reversed $\mathbf{E}(\mathbf{r},-t)$ is also a solution. From this, one can show that [69]

$$\begin{aligned}\mathbf{E}_{-k}&=\mathbf{E}^*_k\\ \mathbf{H}_{-k}&=-\mathbf{H}^*_k.\end{aligned} \tag{A.24}$$

We can arrive at this result directly from the eigenvalue equation for $\mathbf{e}_k$ without specifically considering time-reversal. From (A.11), it is clear that $\mathbb{H}_{-k}=\mathbb{H}^*_k$, so that the eigenvalue problem for $\mathbf{e}_{-k}$ can be written as

$$\mathbb{H}_{-k}\,\mathbf{e}_{-k}=\frac{\omega^2}{c^2}\epsilon\,\mathbf{e}_{-k} \tag{A.25}$$

$$\mathbb{H}^*_k\,\mathbf{e}_{-k}=\frac{\omega^2}{c^2}\epsilon\,\mathbf{e}_{-k} \tag{A.26}$$

$$\mathbb{H}_k\,\mathbf{e}^*_{-k}=\frac{\omega^2}{c^2}\epsilon\,\mathbf{e}^*_{-k} \tag{A.27}$$

for real ϵ. This implies that $\mathbf{e}^*_{-k}$ is an eigenmode of $\mathbb{H}_k$, but we know that the eigenmode of $\mathbb{H}_k$ is given by $\mathbf{e}_k$, so that

$$\mathbf{e}^*_{-k} = \mathbf{e}_k \tag{A.28}$$

or

$$\mathbf{e}_{-k} = \mathbf{e}^*_k \tag{A.29}$$

which is the relationship we are want. Next consider the Bloch part of the magnetic field which from Maxwell's equations is related to he Bloch part of the electric field by

$$\mathbf{h}_k = \frac{1}{i\,\omega}\left(-ik\hat{\mathbf{z}} + \boldsymbol{\nabla}\right) \times \mathbf{e}_k = \mathbb{B}_k\,\mathbf{e}_k. \tag{A.30}$$

Clearly $\mathbb{B}_{-k} = -\mathbb{B}^*_k$, so that

$$\mathbf{h}_{-k} = \mathbb{B}_{-k}\,\mathbf{e}_{-k} \tag{A.31}$$

$$= -\mathbb{B}^*_k\,\mathbf{e}^*_k \tag{A.32}$$

$$= -\left(\mathbb{B}_k\,\mathbf{e}_k\right)^* \tag{A.33}$$

$$= -\mathbf{h}^*_k \tag{A.34}$$

which is again the desired relation.

Next consider spatial inversion symmetry. Unlike translationally invariant waveguides, a periodic structure such as a photonic crystal waveguide only has inversion symmetry about a finite number of high symmertry points, and in some cases may not have inversion symmertry at all in the direction of propagation. If it does, i.e., if

$$\epsilon(x, y, -z) = \epsilon(x, y, z) \tag{A.35}$$

for $z = 0$ defined at an appropriate high symmetry point of the structure, then (see [69])

$$\left[\mathbb{O}_{\sigma_z}, \frac{1}{\epsilon(\mathbf{r})}\boldsymbol{\nabla} \times \boldsymbol{\nabla}\times\right] = 0 \tag{A.36}$$

and, as a result,

$$\begin{aligned}\frac{1}{\epsilon(\mathbf{r})}\boldsymbol{\nabla}\times\boldsymbol{\nabla}\times(\mathbb{O}_{\sigma_z}\mathbf{E}_k) &= \mathbb{O}_{\sigma_z}\left(\frac{1}{\epsilon(\mathbf{r})}\boldsymbol{\nabla}\times\boldsymbol{\nabla}\times\mathbf{E}_k\right)\\ &= \frac{\omega^2}{c^2}(\mathbb{O}_{\sigma_z}\mathbf{E}_k); \end{aligned} \tag{A.37}$$

i.e., $\mathbb{O}_{\sigma_z}\mathbf{E}_k$ is an solution to the original eigenvalue problem (A.10). Next, it can be shown that $\mathbb{O}_{\sigma_z}\mathbf{E}_k$ is a Bloch mode:

$$\begin{aligned}\mathbb{T}_{\Lambda\hat{\mathbf{z}}}(\mathbb{O}_{\sigma_z}\mathbf{E}_k) &= \mathbb{O}_{\sigma_z}(\mathbb{T}_{\sigma_z\Lambda\hat{\mathbf{z}}}\,\mathbf{E}_k)\\ &= \mathbb{O}_{\sigma_z}(e^{-ik(-\Lambda)}\mathbf{E}_k)\\ &= \mathbb{O}_{\sigma_z}(e^{-i(-k)\Lambda}\mathbf{E}_k)\\ &= e^{-i(-k)\Lambda}(\mathbb{O}_{\sigma_z}\mathbf{E}_k)\end{aligned} \tag{A.38}$$

i.e., $\mathbb{O}_{\sigma_z}\mathbf{E}_k$ is a Bloch state with wave number $-k$:

$$\mathbb{O}_{\sigma_z}\mathbf{E}_k = \mathbf{E}_{-k}. \tag{A.39}$$

But we can also operate directly on the eigenvector with the inversion operator:

$$\mathbb{O}_{\sigma_z}\mathbf{E}_k(x,y,z) = \sigma_z\mathbf{E}_k(x,y,-z). \tag{A.40}$$

These last two equations combine to give

$$\mathbf{E}_{-k}(x,y,z) = \sigma_z\,\mathbf{E}_k(x,y,-z). \tag{A.41}$$

Since the electric field **E** is a true vector [fundamentally defined by a vector (position) times a scalar (charge)] [206], under inversion it transforms as

$$\sigma_z\,\mathbf{E}\cdot(\hat{\mathbf{x}},\hat{\mathbf{y}},\hat{\mathbf{z}}) = \mathbf{E}\cdot(\hat{\mathbf{x}},\hat{\mathbf{y}},-\hat{\mathbf{z}}) \tag{A.42}$$

finally giving

$$\mathbf{E}_{-k}(x,y,z)\cdot(\hat{\mathbf{x}},\hat{\mathbf{y}},\hat{\mathbf{z}}) = \mathbf{E}_{k}(x,y,-z)\cdot(\hat{\mathbf{x}},\hat{\mathbf{y}},-\hat{\mathbf{z}}) \tag{A.43}$$
$$\mathbf{e}_{-k}(x,y,z)\cdot(\hat{\mathbf{x}},\hat{\mathbf{y}},\hat{\mathbf{z}}) = \mathbf{e}_{k}(x,y,-z)\cdot(\hat{\mathbf{x}},\hat{\mathbf{y}},-\hat{\mathbf{z}}).$$

A similar derivation can be followed with the magnetic field, with the only difference resulting from the fact that $\mathbf{H}$ is a pseudovector [fundamentally defined as the cross product of two vectors (postion and current density)] [206] so that under inversion

$$\sigma_z\,\mathbf{H}\cdot(\hat{\mathbf{x}},\hat{\mathbf{y}},\hat{\mathbf{z}}) = \mathbf{H}\cdot(-\hat{\mathbf{x}},-\hat{\mathbf{y}},\hat{\mathbf{z}}), \tag{A.44}$$

giving

$$\mathbf{H}_{-k}(x,y,z)\cdot(\hat{\mathbf{x}},\hat{\mathbf{y}},\hat{\mathbf{z}}) = \mathbf{H}_{k}(x,y,-z)\cdot(-\hat{\mathbf{x}},-\hat{\mathbf{y}},\hat{\mathbf{z}}) \tag{A.45}$$
$$\mathbf{h}_{-k}(x,y,z)\cdot(\hat{\mathbf{x}},\hat{\mathbf{y}},\hat{\mathbf{z}}) = \mathbf{h}_{k}(x,y,-z)\cdot(-\hat{\mathbf{x}},-\hat{\mathbf{y}},\hat{\mathbf{z}}).$$

Since $\mathbf{e}_k$ and $\mathbf{h}_k$ are periodic functions of z, at the edges and center of the unit cell, $z_n = \pm n\Lambda/2$, we have $\mathbf{e}_k(-z_n), \mathbf{h}_k(-z_n) = \mathbf{e}_k(z_n), \mathbf{h}_k(z_n)$ and

$$\mathbf{e}_{-k}(x,y,z_n)\cdot(\hat{\mathbf{x}},\hat{\mathbf{y}},\hat{\mathbf{z}}) = \mathbf{e}_{k}(x,y,z_n)\cdot(\hat{\mathbf{x}},\hat{\mathbf{y}},-\hat{\mathbf{z}}) \tag{A.46}$$
$$\mathbf{h}_{-k}(x,y,z_n)\cdot(\hat{\mathbf{x}},\hat{\mathbf{y}},\hat{\mathbf{z}}) = \mathbf{h}_{k}(x,y,z_n)\cdot(-\hat{\mathbf{x}},-\hat{\mathbf{y}},\hat{\mathbf{z}}).$$

These are the same relations that hold for all z (as opposed to the set of z_n, given here) in translationally invariant waveguides [72]. Combining these relations with the time reversal relations allows the phase of the components of the Bloch modes at these high symmetry points to be fixed. From (A.46) and (A.29, A.31) at the high symmertry points, z_n, we get

$$\mathbf{e}_{k}(x,y,z_n)\cdot(\hat{\mathbf{x}},\hat{\mathbf{y}},\hat{\mathbf{z}}) = \mathbf{e}_{k}^{*}(x,y,z_n)\cdot(\hat{\mathbf{x}},\hat{\mathbf{y}},-\hat{\mathbf{z}}) \tag{A.47}$$
$$\mathbf{h}_{k}(x,y,z_n)\cdot(\hat{\mathbf{x}},\hat{\mathbf{y}},\hat{\mathbf{z}}) = \mathbf{h}_{k}^{*}(x,y,z_n)\cdot(\hat{\mathbf{x}},\hat{\mathbf{y}},-\hat{\mathbf{z}})$$

i.e., the transverse parts are purely real and the longitudinal parts are purely imaginary at z_n. This property can be used to obtain a more compact orthogonality relationship at these points:

$$\int_{z_n} (\mathbf{e}^*_{k_m} \times \mathbf{h}_{k_n}) \cdot \hat{\mathbf{z}}\, dx\, dy = 0 \tag{A.48}$$

$$\frac{\partial}{\partial z} \int_{z_n} (\mathbf{e}^*_{k_n} \times \mathbf{h}_{k_n}) \cdot \hat{\mathbf{z}}\, dx\, dy = 0. \tag{A.49}$$

These equations are obtained by rewriting (A.20) and (A.23) with $k_m \to -k_m$, and adding the resulting equations to the originals using the properties presented above.

Since $\mathbf{e}_k$ and $\mathbf{h}_k$ obey the spatial inversion relations (A.43, A.45), we can more generally use the time reversal properties (A.29, A.31) to fix the parity of the real and imaginary parts away from the high symmetry points z_n. From (A.43, A.45) and (A.29, A.31)

$$\begin{aligned} \mathbf{e}_k(x,y,z) \cdot (\hat{\mathbf{x}}, \hat{\mathbf{y}}, \hat{\mathbf{z}}) &= \mathbf{e}^*_k(x,y,-z) \cdot (\hat{\mathbf{x}}, \hat{\mathbf{y}}, -\hat{\mathbf{z}}) \\ \mathbf{h}_k(x,y,z) \cdot (\hat{\mathbf{x}}, \hat{\mathbf{y}}, \hat{\mathbf{z}}) &= -\mathbf{h}^*_k(x,y,-z) \cdot (-\hat{\mathbf{x}}, -\hat{\mathbf{y}}, \hat{\mathbf{z}}) \end{aligned} \tag{A.50}$$

i.e., under inversion:

1. The real (imaginary) parts of $\{\mathbf{e}_k, \mathbf{h}_k\} \cdot (\hat{\mathbf{x}}, \hat{\mathbf{y}})$ must be even (odd).
2. The real (imaginary) part of $\{\mathbf{e}_k, \mathbf{h}_k\} \cdot (\hat{\mathbf{z}})$ must be odd (even).

A.2 Coupled mode equations: Lorentz reciprocity method

This section shows how to use the Lorentz reciprocity relation to derive approximate but self-consistent coupled mode equations describing two periodic waveguides. Each waveguide is defined by its dielectric constant, $\epsilon_a(\mathbf{r})$ for waveguide a and $\epsilon_b(\mathbf{r})$ for waveguide b. Assume that the modes of waveguides a and b in isolation are known,

$$\mathbf{E}_{k^a_m} = e^{-ik^a_m z} \mathbf{e}_{k^a_m}(\mathbf{r}) e^{i\omega t} \tag{A.51}$$

$$\mathbf{E}_{k^b_m} = e^{-ik^b_m z} \mathbf{e}_{k^b_m}(\mathbf{r}) e^{i\omega t}, \tag{A.52}$$

where $\mathbf{e}^a_{k^a_m}$ and $\mathbf{e}^b_{k^b_m}$ are periodic as in (A.9) and are solutions to the eigenvalue equation (A.11):

$$\mathbb{H}_{k^a_m}\,\mathbf{e}_{k^a_m}(\mathbf{r}) = \epsilon_a(\mathbf{r})\frac{w^2}{c^2}\mathbf{e}_{k^a_m}(\mathbf{r}) \tag{A.53}$$
$$\mathbb{H}_{k^b_m}\,\mathbf{e}_{k^b_m}(\mathbf{r}) = \epsilon_b(\mathbf{r})\frac{w^2}{c^2}\mathbf{e}_{k^b_m}(\mathbf{r})$$

To solve Maxwell's equations for the two waveguide system described by

$$\begin{aligned}\epsilon(\mathbf{r}) &= 1 + [\epsilon_a(\mathbf{r}) - 1] + [\epsilon_b(\mathbf{r}) - 1] \qquad\qquad (\text{for } (\epsilon_a - 1) \cap (\epsilon_b - 1) = 0)\\ &= 1 + \Delta\epsilon_a(\mathbf{r}) + \Delta\epsilon_b(\mathbf{r}) \end{aligned}\tag{A.54}$$

write the total field as a linear combination of the individual waveguide modes:

$$\mathbf{E}(\mathbf{r}) = \sum_m \left[A_m(z)\mathbf{E}_{k^a_m}(\mathbf{r}) + B_m(z)\mathbf{E}_{k^b_m}(\mathbf{r})\right] e^{i\omega t}. \tag{A.55}$$

Recall the reciprocity relation used in the previous sections. Let

$$\mathbf{F} = \mathbf{E}_1 \times \mathbf{H}_2^* + \mathbf{E}_2^* \times \mathbf{H}_1 \tag{A.56}$$

where $\mathbf{E}_{1,2}$ and $\mathbf{H}_{1,2}$ are solutions to Maxwell's equations for some $\epsilon_{1,2}$. Using Maxwell's equations and standard vector identities, the divegence of $\mathbf{F}$ is:

$$\boldsymbol{\nabla} \cdot \mathbf{F} = -i\omega \mathbf{E}_1 \cdot \mathbf{E}_2^* \left(\epsilon_1 - \epsilon_2^*\right). \tag{A.57}$$

Integrating (A.57) over a plane of constant z and using the two dimensional form of the divergence theorem gives the desired relation:

$$\frac{\partial}{\partial z}\int_z (\mathbf{E}_1 \times \mathbf{H}_2^* + \mathbf{E}_2^* \times \mathbf{H}_1)\cdot\hat{\mathbf{z}}\,dx\,dy = -i\omega\int_z \mathbf{E}_1 \cdot \mathbf{E}_2^*\left(\epsilon_1 - \epsilon_2\right)dx\,dy, \tag{A.58}$$

where it has been assumed that $\epsilon_{1,2}$ are real. Now let

$$\mathbf{E}_1 = \sum_n \left[A_n(z)\mathbf{E}^a_n(\mathbf{r}) + B_n(z)\mathbf{E}^b_n(\mathbf{r})\right] \tag{A.59}$$

$$\mathbf{E}_2 = \mathbf{E}^a_m \tag{A.60}$$

and, corespondingly, let

$$\epsilon_1(\mathbf{r}) = \epsilon(\mathbf{r}) \tag{A.61}$$

$$\epsilon_2(\mathbf{r}) = \epsilon_a(\mathbf{r}), \tag{A.62}$$

so that $\mathbf{E}_1$ represents the approximate field in the two waveguide structures, while $\mathbf{E}_2$ represents the field in a single isolated waveguide. Subsitituting these equations into (A.58) gives:

$$\begin{aligned}\sum_n \Bigg[\frac{dA_n}{dz}\int_z (\mathbf{E}_n^a \times \mathbf{H}_m^{a*} + \mathbf{E}_m^{a*} \times \mathbf{H}_n^a)\cdot\hat{\mathbf{z}}\,dx\,dy + \frac{dB_n}{dz}\int_z (\mathbf{E}_n^b \times \mathbf{H}_m^{a*} + \mathbf{E}_m^{a*} \times \mathbf{H}_n^b)\cdot\hat{\mathbf{z}}\,dx\,dy + \\ A_n\frac{d}{dz}\int_z (\mathbf{E}_n^a \times \mathbf{H}_m^{a*} + \mathbf{E}_m^{a*} \times \mathbf{H}_n^a)\cdot\hat{\mathbf{z}}\,dx\,dy + B_n\frac{d}{dz}\int_z (\mathbf{E}_n^b \times \mathbf{H}_m^{a*} + \mathbf{E}_m^{a*} \times \mathbf{H}_n^b)\cdot\hat{\mathbf{z}}\,dx\,dy\Bigg] \\ = -i\,\omega\sum_n\int_z (A_n\mathbf{E}_n^a + B_n\mathbf{E}_n^b)\cdot\mathbf{E}_m^{a*}\,(\epsilon-\epsilon_a)\,dx\,dy\end{aligned} \tag{A.63}$$

Recalling from (A.58) that

$$\frac{d}{dz}\int_z (\mathbf{E}_n^a \times \mathbf{H}_m^{a*} + \mathbf{E}_m^{a*} \times \mathbf{H}_n^a)\cdot\hat{\mathbf{z}}\,dx\,dy = 0 \tag{A.64}$$

$$\frac{d}{dz}\int_z (\mathbf{E}_n^b \times \mathbf{H}_m^{a*} + \mathbf{E}_m^{a*} \times \mathbf{H}_n^b)\cdot\hat{\mathbf{z}}\,dx\,dy = -i\,\omega\int_z \mathbf{E}_n^b\cdot\mathbf{E}_m^{a*}\,(\epsilon_b-\epsilon_a)\,dx\,dy, \tag{A.65}$$

equation (A.63) can be written as

$$\begin{aligned}\sum_n \Bigg[\frac{dA_n}{dz}\int_z (\mathbf{E}_n^a \times \mathbf{H}_m^{a*} + \mathbf{E}_m^{a*} \times \mathbf{H}_n^a)\cdot\hat{\mathbf{z}}\,dx\,dy + \frac{dB_n}{dz}\int_z (\mathbf{E}_n^b \times \mathbf{H}_m^{a*} + \mathbf{E}_m^{a*} \times \mathbf{H}_n^b)\cdot\hat{\mathbf{z}}\,dx\,dy + \Bigg] \\ = -i\,\omega\sum_n\left[A_n\int_z \mathbf{E}_n^a\cdot\mathbf{E}_m^{a*}\,(\epsilon-\epsilon_a)\,dx\,dy + B_n\int_z \mathbf{E}_n^b\cdot\mathbf{E}_m^{a*}\,(\epsilon-\epsilon_b)\,dx\,dy\right].\end{aligned} \tag{A.66}$$

Repeating this for $\mathbf{E}_2$ equal to each possible $\mathbf{E}_m^{(a,b)}$, we obtain a set of self-consistent coupled mode equations. The notation can be cleaned up considerably by replacing the set of indices $(\{a,b\},n)$ with a single index, j, and rewriting the amplitude coefficients as $C_j(z) = \{A_n, B_n\}(z)$. Then, (A.66) becomes

$$\sum_j \frac{dC_j}{dz}\int_z (\mathbf{E}_j \times \mathbf{H}_i^{*} + \mathbf{E}_i^{*} \times \mathbf{H}_j)\cdot\hat{\mathbf{z}}\,dx\,dy = -i\,\omega\sum_j C_j\int_z \mathbf{E}_j\cdot\mathbf{E}_i^{*}\,(\epsilon-\epsilon_j)\,dx\,dy, \tag{A.67}$$

which can be written in matrix form as

$$P_{ij}\frac{dC_j}{dz} = -i\,K_{ij}C_j \tag{A.68}$$

or

$$\mathbf{P}\frac{d\mathbf{C}}{dz} = -i\,\mathbf{KC} \tag{A.69}$$

where

$$P_{ij} = \int_z (\mathbf{E}_i^* \times \mathbf{H}_j + \mathbf{E}_j \times \mathbf{H}_i^*) \cdot \hat{\mathbf{z}}\,dx\,dy \tag{A.70}$$

$$K_{ij} = \omega \int_z \mathbf{E}_i^* \cdot \mathbf{E}_j\,(\epsilon - \epsilon_j)\,dx\,dy. \tag{A.71}$$

Note that, in general, the matrix elements, P_{ij}, can depend on z. However, as shown by (A.64) and (A.65), only elements corresponding to modes of different waveguides are z dependent, which is a consequence of power conservation.

A.2.1 Coupling between two periodic waveguides

We will now formulate the coupled mode equations for the specific case of coupling between periodic waveguides, each with a single forward and backward propagating mode. In this case, the electric field in the two waveguide system is approximated by

$$\mathbf{E}(\mathbf{r}) = A^+(z)\mathbf{E}_a^+(\mathbf{r}) + A^-(z)\mathbf{E}_a^-(\mathbf{r}) + B^+(z)\mathbf{E}_b^+(\mathbf{r}) + B^-(z)\mathbf{E}_b^-(\mathbf{r}) \tag{A.72}$$

and the coupled mode equations become (in a less general notation)

$$\begin{pmatrix} 1 & 0 & P_{ab}^{++} & P_{ab}^{+-} \\ 0 & -1 & P_{ab}^{-+} & P_{ab}^{--} \\ P_{ba}^{++} & P_{ba}^{+-} & 1 & 0 \\ P_{ba}^{-+} & P_{ba}^{--} & 0 & -1 \end{pmatrix} \frac{d}{dz} \begin{pmatrix} A^+ \\ A^- \\ B^+ \\ B^- \end{pmatrix} = -i \begin{pmatrix} K_{aa}^{++} & K_{aa}^{+-} & K_{ab}^{++} & K_{ab}^{+-} \\ K_{aa}^{-+} & K_{aa}^{--} & K_{ab}^{-+} & K_{ab}^{--} \\ K_{ba}^{++} & K_{ba}^{+-} & K_{bb}^{++} & K_{bb}^{+-} \\ K_{ba}^{-+} & K_{ba}^{--} & K_{bb}^{-+} & K_{bb}^{--} \end{pmatrix} \begin{pmatrix} A^+ \\ A^- \\ B^+ \\ B^- \end{pmatrix}$$

In calculating the matrix elements, P_{ij}, properties of Bloch modes in periodic structures derived earlier have been used. Specifically:

1. Modes of the same waveguide whose propagation constants do not differ by a reciprocal

lattice vector are power orthogonal (A.20).

2. Forward propagating modes can be normalized to carry unity power, so that $P_{aa}^{++} = P_{bb}^{++} = 1$, independent of z (see (A.64) or (A.23)).

3. Backward propagating modes are related to their forward propagating counterparts by $\mathbf{E}^-(\mathbf{r}) = \mathbf{E}^+(\mathbf{r})^*$ and $\mathbf{H}^-(\mathbf{r}) = -\mathbf{H}^+(\mathbf{r})^*$ (see A.24)), so that backward propagating modes are normalized to carry negative unity power (i.e., $P_{aa}^{--} = P_{bb}^{--} = -1$).

The exact form for the coupling coefficients is given by (A.71) in simplified notation. As discussed earlier, solutions to Maxwell's equations in period structures can be written in Bloch form (A.8). As a result, they can be expanded as a plane wave times a Fourier series. This aids in solving the coupled mode equations numerically, since, as a result, the z dependence of the coupling coefficients can be approximated as an easily evaluated Fourier series. The coupling coefficients in the specific notation used in the matrix expression are given by

$$\begin{aligned}
K_{ab}^{+-}(z) &= \omega \int_z \mathbf{E}_a^{+*} \cdot \mathbf{E}_b^- \, (\epsilon - \epsilon_b) \, dx \, dy & \text{(A.73)} \\
&= e^{i(k_a^+ - k_b^-)z} \, \omega \int_z \mathbf{e}_a^{+*} \cdot \mathbf{e}_b^- \, (\epsilon - \epsilon_b) \, dx \, dy & \text{(A.74)} \\
&= e^{i(k_a^+ - k_b^-)z} \sum_n (K_{ab}^{+-})_n \, e^{i(2\pi n/\Lambda)z}, & \text{(A.75)} \\
(K_{ab}^{+-})_n &= \frac{1}{\Lambda} \int_{z_0}^{z_0+\Lambda} e^{-i(2\pi n/\Lambda)z} \left(\omega \int_z \mathbf{e}_a^{+*} \cdot \mathbf{e}_b^- \, (\epsilon - \epsilon_b) \, dx \, dy \right) dz & \text{(A.76)}
\end{aligned}$$

for the various permutations of $\{a, b\}$ and $\{+, -\}$. Note that $k_{a,b}^- = -k_{a,b}^+$.

The cross terms in the "power matrix" on the left hand side of the matrix expression can be expanded in a similar manner:

$$\begin{aligned}
P_{ab}^{+-} &= \int_z (\mathbf{E}_a^{+*} \times \mathbf{H}_b^- + \mathbf{E}_b^- \times \mathbf{H}_a^{+*}) \cdot \hat{\mathbf{z}} \, dx \, dy & \text{(A.77)} \\
&= e^{i(k_a^+ - k_b^-)z} \int_z (\mathbf{e}_a^{+*} \times \mathbf{h}_b^- + \mathbf{e}_b^- \times \mathbf{h}_a^{+*}) \cdot \hat{\mathbf{z}} \, dx \, dy & \text{(A.78)} \\
&= e^{i(k_a^+ - k_b^-)z} \sum_n (P_{ab}^{+-})_n \, e^{i(2\pi n/\Lambda)z}, & \text{(A.79)} \\
(P_{ab}^{+-})_n &= \frac{1}{\Lambda} \int_{z_0}^{z_0+\Lambda} e^{-i(2\pi n/\Lambda)z} \left(\int_z (\mathbf{e}_a^{+*} \times \mathbf{h}_b^- + \mathbf{e}_b^- \times \mathbf{h}_a^{+*}) \cdot \hat{\mathbf{z}} \, dx \, dy \right) & \text{(A.80)}
\end{aligned}$$

Often these cross terms will be small compared to the diagonal elements of the P_{ij} matrix and can be ignored.

Before solving the coupled mode equations numerically it is useful to analyze the form of the coupled mode equations. From the coupling matrix, in absence of power matrix cross terms, it can be seen that coupling between two modes depends primarily on the magnitude of the DC component of the corresponding coupling term. If $k_{a,b}^{+;-}$ and $k_{a,b}^{+;-}$ do not differ by some reciprocal lattice vector, $2\pi n/\Lambda$, then there will be no DC component, and coupling between these modes modes will suffer.

A.2.2 Power conservation

Physically, we require the total power in the field to be conserved. For coupling between two waveguides, this total power includes the power in individual modes as well as "cross terms" that arise due to the non-power orthogonality of modes of differing waveguides. Specifically, we require that

$$\frac{dP_{total}}{dz} = \frac{d}{dz}(\mathbf{C}^{\dagger}\mathbf{P}\mathbf{C}) = 0 \tag{A.81}$$

giving

$$\frac{d\mathbf{C}^{\dagger}}{dz}\mathbf{P}\mathbf{C} + \mathbf{C}^{\dagger}\mathbf{P}\frac{d\mathbf{C}}{dz} + \mathbf{C}^{\dagger}\frac{d\mathbf{P}}{dz}\mathbf{C} = 0. \tag{A.82}$$

It can easily be seen that $\mathbf{P}$ is Hermitian, so that

$$\frac{d\mathbf{C}^{\dagger}}{dz}\mathbf{P} = \frac{d\mathbf{C}^{\dagger}}{dz}\mathbf{P}^{\dagger} = \left(\mathbf{P}\frac{d\mathbf{C}}{dz}\right)^{\dagger}. \tag{A.83}$$

Using the coupled mode equation (A.69), this gives

$$\frac{d\mathbf{C}^{\dagger}}{dz}\mathbf{P} = (-i\,\mathbf{K}\mathbf{C})^{\dagger} \tag{A.84}$$

and the power conservation relation becomes

$$(-i\,\mathbf{K}\mathbf{C})^\dagger\mathbf{C} + \mathbf{C}^\dagger(-i\mathbf{K}\mathbf{C}) + \mathbf{C}^\dagger\frac{d\mathbf{P}}{dz}\mathbf{C} = 0 \tag{A.85}$$

$$i\,\mathbf{C}^\dagger\mathbf{K}^\dagger\mathbf{C} - i\,\mathbf{C}^\dagger\mathbf{K}\mathbf{C} + \mathbf{C}^\dagger\frac{d\mathbf{P}}{dz}\mathbf{C} = 0 \tag{A.86}$$

$$\mathbf{C}^\dagger\left(i\mathbf{K}^\dagger - i\mathbf{K} + \frac{d\mathbf{P}}{dz}\right)\mathbf{C} = 0. \tag{A.87}$$

Writing the terms in the matrix explicitly

$$C_m^*\left(i\omega\int_z \mathbf{E}_n\cdot\mathbf{E}_m^*\,(\epsilon-\epsilon_m)\,dx\,dy - i\omega\int_z \mathbf{E}_m^*\cdot\mathbf{E}_n\,(\epsilon-\epsilon_n)\,dx\,dy + \frac{dP_{mn}}{dz}\right)C_n = 0 \tag{A.88}$$

and, once again recalling the reciprocity relation (A.58),

$$\frac{dP_{mn}}{dz} = \frac{d}{dz}\int_z(\mathbf{E}_m^*\times\mathbf{H}_n + \mathbf{E}_n\times\mathbf{H}_m^*)\cdot\hat{\mathbf{z}}\,dx\,dy \tag{A.89}$$

$$= -i\,\omega\int_z \mathbf{E}_n\cdot\mathbf{E}_m^*(\epsilon_n-\epsilon_m)dx\,dy, \tag{A.90}$$

we get

$$i\,\omega\,C_m^*C_n\int_z \mathbf{E}_n\cdot\mathbf{E}_m^*\,[(\epsilon-\epsilon_m)-(\epsilon-\epsilon_n)-(\epsilon_n-\epsilon_m)]\,dx\,dy = 0 \tag{A.91}$$

$$i\,\omega\,C_m^*C_n\int_z \mathbf{E}_n\cdot\mathbf{E}_m^*\,[(\epsilon-\epsilon)+(\epsilon_n-\epsilon_n)+(\epsilon_m-\epsilon_m)]\,dx\,dy = 0, \tag{A.92}$$

which clearly holds for all **C**, indicating that power is conserved.

Appendix B

Emitter-waveguide coupling

The goal of this calculation is to estimate the efficiency with which optical fiber tapers collect photons from a radiating source. Texts by Jackson [206] and by Snyder and Love [72] were refered to in deriving the following expressions. SI units are used throughout.

B.1 Coupled-mode analysis

Maxwells equations for a harmonic field (time dependence $e^{-i\omega t}$) are

$$\boldsymbol{\nabla} \cdot \mathbf{D} = \rho \tag{B.1}$$

$$\boldsymbol{\nabla} \times \mathbf{H} + i\omega\mathbf{D} = \mathbf{J} \tag{B.2}$$

$$\boldsymbol{\nabla} \times \mathbf{E} - i\omega\mathbf{B} = 0 \tag{B.3}$$

$$\boldsymbol{\nabla} \cdot \mathbf{B} = 0, \tag{B.4}$$

with

$$\mathbf{D}(\mathbf{r}) = \epsilon(\mathbf{r})\mathbf{E}(\mathbf{r}) \tag{B.5}$$

$$\mathbf{B}(\mathbf{r}) = \mu(\mathbf{r})\mathbf{H}(\mathbf{r}). \tag{B.6}$$

In the problem that we are concerned with, there is no free charge ($\rho = 0$), and the material is assumed to be non-magnetic ($\mu(\mathbf{r}) = \mu_0$). The fiber taper dielectric constant is represented by $\epsilon(\mathbf{r})$, and the radiating dipole source (for example a quantum dot, or nanocrystal) is described by the source current $\mathbf{J}(\mathbf{r})$. This source current can be related to a polarization source $\mathbf{P}(\mathbf{r})$ oscillating at frequency ω_p by $\mathbf{J}(\mathbf{r}) = i\omega_p\mathbf{P}(\mathbf{r})$.

From Maxwell's equation, we can derive the Lorentz Reciprocity theorem, which relates two solutions to Maxwell's equations:

$$\boldsymbol{\nabla}\cdot(\mathbf{E}_1\times\mathbf{H}_2^*+\mathbf{E}_2^*\times\mathbf{H}_1)=i\omega\mathbf{E}_1\cdot\mathbf{E}_2^*(\epsilon_1-\epsilon_2^*)-\mathbf{E}_1\cdot\mathbf{J}_2^*-\mathbf{E}_2^*\cdot\mathbf{J}_1 \tag{B.7}$$

Integrating both sides over a two dimensional plane perpendicular to the waveguide axis, and invoking Gauss' theorem,

$$\frac{d}{dz}\int(\mathbf{E}_1\times\mathbf{H}_2^*+\mathbf{E}_2^*\times\mathbf{H}_1)\cdot\hat{\mathbf{z}}\;dxdy= \tag{B.8}$$

$$i\omega\int\left(\mathbf{E}_1\cdot\mathbf{E}_2^*(\epsilon_1-\epsilon_2^*)-\mathbf{E}_1\cdot\mathbf{J}_2^*-\mathbf{E}_2^*\cdot\mathbf{J}_1\right)\;dxdy. \tag{B.9}$$

Now, let $\epsilon_1(\mathbf{r})=\epsilon_f(\mathbf{r})$ and $\mathbf{J}_1(\mathbf{r})=0$ describe the dielectric constant of the fiber, and $\epsilon_2(\mathbf{r})=\epsilon_f(\mathbf{r})$ and $\mathbf{J}_2(\mathbf{r})=\mathbf{J}(\mathbf{r})$ represent the combined fiber-polarization source. If the eigenmodes of Maxwell's equations for $\epsilon_1=\epsilon_f(\mathbf{r})$ are given by

$$\mathbf{E}_1=\mathbf{E}_n(\mathbf{r}), \tag{B.10}$$

we can write solutions for the combined fiber-polarization source systems as

$$\mathbf{E}_2=\sum_m a_m(z)\mathbf{E}_m(\mathbf{r}). \tag{B.11}$$

In the case of a translationally invariant waveguide such an optical fiber, the eigenmodes can be expressed in the form $\mathbf{E}_n(\mathbf{r})=e^{i\beta_n z}\mathbf{e}_n(x,y)$, and we write $a_m=a_m(z)$. Subsituting Eqs. (B.10) and (B.11) into Eq. (B.8), we get

$$\frac{d}{dz}\sum_m e^{i(\beta_n-\beta_m)z}a_m(z)\int(\mathbf{e}_n\times\mathbf{h}_m^*+\mathbf{e}_m^*\times\mathbf{h}_n)\cdot\hat{\mathbf{z}}\;dxdy=-\int e^{i\beta_m z}\mathbf{e}_m\cdot\mathbf{J}^*\;dxdy. \tag{B.12}$$

Using the Lorentz reciprocity relation for the case that $\epsilon_1=\epsilon_2$ and $\mathbf{J}_1=\mathbf{J}_2=0$, one can show that for $m\neq n$,

$$\int(\mathbf{e}_n\times\mathbf{h}_m^*+\mathbf{e}_m^*\times\mathbf{h}_n)\cdot\hat{\mathbf{z}}\;dxdy=0. \tag{B.13}$$

As a result, the coupled mode equations given above simplify to

$$\frac{da_m}{dz} = -\frac{1}{P_m^o}\int \mathbf{E}_m \cdot \mathbf{J}^* \; dxdy \tag{B.14}$$

where

$$P_m^o = \frac{1}{2}\mathrm{Re}\left[\int (\mathbf{e}_m \times \mathbf{h}_m^*) \cdot \hat{\mathbf{z}} \; dxdy\right], \tag{B.15}$$

is the power in mode m for $a_m = 1$. Integrating Eq. (B.14), we arrive at the following expression for the amplitude of mode m excited by the source, $\mathbf{J}$, assuming that z is past the source in the direction of propagation:

$$a_m(z) = -\frac{1}{4P_m^o}\int \mathbf{E}_m \cdot \mathbf{J}^* \; dxdydz. \tag{B.16}$$

If $\mathbf{J}$ is a current source which is small compared to the wavelength of light and positioned at $\mathbf{r}_o$, then we can approximate it as $\mathbf{J} = \mathbf{I_o}\delta^3(\mathbf{r} - \mathbf{r}_o)$ and the the above equation simplfies to

$$a_m(z) = -\frac{1}{4P_m^o}\mathbf{E}_m(\mathbf{r}_o) \cdot \mathbf{I_o}^*. \tag{B.17}$$

B.2 Field normalization

Next, we aim to write Eq. (B.17) in terms of normalized field strength and typical waveguide parameters. Note that P_m^o is the power propagating in mode m for $a_m = 1$. This can also be expressed as

$$P_m^o = \frac{v_g}{2}\int \epsilon_f(\mathbf{r})|\mathbf{e}_m(\mathbf{r})|^2 \; dxdy = \frac{1}{2}v_g A_m \epsilon_f^o |\mathbf{e}_m|^2_{\max} \tag{B.18}$$

where ϵ_f^o is the dielectric constant of the fiber material, v_g is the group velocity, and where the modal area A_m is a two dimensional analogue to mode volume given by

$$A_m = \frac{\int \epsilon_f |\mathbf{e}_m|^2 \; dxdy}{\epsilon_f^o |\mathbf{e}_m|^2_{\max}}. \tag{B.19}$$

Note that we have assumed that the field maximum is located in the fiber.

The power radiated by $\mathbf{J}$ into mode m is then given by

$$P_m = |a_m|^2 P_m^o = \frac{|\mathbf{e}_m(\mathbf{r}_o) \cdot \mathbf{I_o}^*|^2}{16 P_m^o} = \frac{\bar{e}_m^2(\mathbf{r}_o)}{8 v_g A_m \epsilon_f^o} I_o^2 |\hat{\mathbf{n}}_J^* \cdot \hat{\mathbf{n}}_m|^2 \tag{B.20}$$

where $\bar{e}_m^2(\mathbf{r}_o) = \frac{|\mathbf{e}_m^2(\mathbf{r}_o)|}{|\mathbf{e}_m^2(\mathbf{r})|_{\max}}$ is the normalized field intensity, and where $\hat{\mathbf{n}}_J$ and $\hat{\mathbf{n}}_m$ are the polarization unit vectors of $\mathbf{J}$ and $\mathbf{e}_m(\mathbf{r}_o)$, respectively.

B.3 Coupling efficiency

The metric that we are most interested in is the coupling efficiency between the total power radiated by $\mathbf{J_o}$ and mode m of the waveguide. From Jackson (3rd edition, Eq. (9.24)), the total power radiated by a dipole $\mathbf{p}$ in free space is

$$P_r = \frac{1}{12\pi}\frac{\omega^4}{c^2}|\mathbf{p}|^2. \tag{B.21}$$

A current source oscilating at frequency ω is related to $\mathbf{p}$ by $\mathbf{p} = i\mathbf{I_o}/\omega$. This gives

$$P_r = \frac{1}{12\pi}\sqrt{\frac{\mu_o}{\epsilon_o}}\frac{\omega^2}{c^2}|\mathbf{I_o}|^2. \tag{B.22}$$

The collection efficiency of the fiber taper mode m is given by

$$\begin{aligned}
\eta_m = \frac{P_m}{P_r} &= \left(\frac{\bar{e}_m^2(\mathbf{r}_o)}{8v_g A_m \epsilon_f}|\hat{\mathbf{n}}_J^* \cdot \hat{\mathbf{n}}_m|^2\right)\left(12\pi\sqrt{\frac{\epsilon_o}{\mu_o}}\frac{c^2}{\omega^2}\right) && \text{(B.23)}\\
&= \left(\frac{\bar{e}_m^2(\mathbf{r}_o)}{8v_g A_m \epsilon_f}|\hat{\mathbf{n}}_J^* \cdot \hat{\mathbf{n}}_m|^2\right)\left(12\pi\sqrt{\frac{\epsilon_o}{\mu_o}}\frac{\lambda^2}{4\pi^2}\right) && \text{(B.24)}\\
&= \left(\frac{3}{8\pi}\frac{\bar{e}_m^2(\mathbf{r}_o)\lambda^2}{v_g A_m \epsilon_f}|\hat{\mathbf{n}}_J^* \cdot \hat{\mathbf{n}}_m|^2\sqrt{\frac{\epsilon_o}{\mu_o}}\right). && \text{(B.25)}
\end{aligned}$$

Writing $v_g = c/n_g$, where n_g is the group index of mode m, and $\epsilon_f^o = n_f^2\epsilon_o$, where n_f is the fiber index of refraction, gives

$$\begin{aligned}
\eta_m &= \frac{3}{8\pi}\frac{(\lambda/n_f)^2}{A_m}\frac{\bar{e}_m^2(\mathbf{r}_o)}{c/n_g}|\hat{\mathbf{n}}_J^* \cdot \hat{\mathbf{n}}_m|^2\sqrt{\frac{1}{\epsilon_o\mu_o}} && \text{(B.26)}\\
&= \frac{3}{8\pi}\bar{e}_m^2(\mathbf{r}_o)\frac{(\lambda/n_f)^2}{A_m}n_g|\hat{\mathbf{n}}_J^* \cdot \hat{\mathbf{n}}_m|^2, && \text{(B.27)}
\end{aligned}$$

which is a satisfyingly simple expression for the fraction of radiated power emitted into mode m.

However, this expression has the disturbing property that for large n_g and small A_m (achievable in, for example, a photonic crystal waveguide), $\eta_m > 1$. The coupled mode equations derived from Lorentz reciprocity are implicitly power conserving, and the problem is related to Eq. (B.21). Equation (B.21) is valid for a dipole radiating in free space, but needs to be modified for a dipole located in a non-trivial environment with an altered density of states. The cylindrical symmetry of the fiber taper permits exact, albeit complicated, formulations of the local density of states in terms of the various fiber taper modes. This calculation requires solving for the radiation modes as well as for the usual guided modes of the fiber taper, and can be found in Refs. [207, 208]. Nonetheless, Eq. B.26 can be used as an initial estimate of the coupling efficiency, and is expected to be valid for $\eta_m << 1$.

Bibliography

[1] G. T. Reed and A. P. Knights, *Silicon Photonics: An Introduction* (Wiley, New York, NY, 2004).

[2] L. Pavesi and D. J. Lockwood, *Silicon Photonics* (Springer, New York, NY, 2004).

[3] A. Yariv, *Optical Electronics* (Saunder College Publishing, a division of Holt, Rinehart and Winston, Inc., Orlando, Florida, 1991), 4th edn.

[4] H. Mabuchi and A. C. Doherty, "Cavity Quantum Electrodynamics: Coherence in Context," Science **298**, 1372–1377 (2002).

[5] H. J. Kimble, "Strong interactions of single atoms and photons in cavity QED," Phys. Scr., T **T76**, 127–137 (1998).

[6] P. R. Berman, *Cavity quantum electrodynamics*, Advances in atomic, molecular, and optical physics (Academic Press, New York, NY, 1994).

[7] K. J. Vahala, "Optical microcavities," Nature **424**, 839–846 (2003).

[8] O. Painter, R. K. Lee, A. Yariv, A. Scherer, J. D. O'Brien, P. D. Dapkus, and I. Kim, "Two-Dimensional Photonic Band-Gap Defect Mode Laser," Science **284**, 1819–1824 (1999).

[9] K. Srinivasan, P. E. Barclay, O. Painter, J. Chen, A. X. Cho, and C. Gmachl, "Experimental demonstration of a high quality factor photonic crystal microcavity," Appl. Phys. Lett. **83**, 1915–1917 (2003).

[10] Y. Akahane, T. Asano, B.-S. Song, and S. Noda, "High-Q photonic nanocavity in a two-dimensional photonic crystal," Nature **425**, 944–947 (2003).

[11] K. Srinivasan, P. E. Barclay, M. Borselli, and O. Painter, "Optical-fiber based measurement of an ultra-small volume high-Q photonic crystal microcavity," Phys. Rev. B **70**, 081 306(R) (2004).

[12] B.-S. Song, S. Noda, T. Asano, and Y. Akahane, "Ultra-high-Q photonic double-heterostructure nanocavity," Nat. Mat. **4**, 207–210 (2005).

[13] M. L. Gorodetsky, A. A. Savchenkov, and V. S. Ilchenko, "Ultimate Q of optical microsphere resonators," Opt. Lett. **21**, 453–455 (1996).

[14] D. K. Armani, T. J. Kippenberg, S. M. Spillane, and K. J. Vahala, "Ultra-high-Q toroid microcavity on a chip," Nature **421**, 925–928 (2003).

[15] T. J. Kippenberg, S. M. Spillane, and K. J. Vahala, "Modal coupling in traveling-wave resonators," Opt. Lett. **27**, 1669–1671 (2002).

[16] M. Borselli, T. J. Johnson, and O. Painter, "Beyond the Rayleigh scattering limit in high-Q silicon microdisks: theory and experiment," Opt. Expr. **13**, 1515–1530 (2005).

[17] P. E. Barclay, B. Lev, K. Srinivasan, H. Mabuchi, and O. Painter, "Integration of fiber coupled high-Q SiNx microdisks with atom chips," Appl. Phys. Lett. **89**, 131 108 (2006).

[18] S. M. Spillane, T. J. Kippenberg, and K. J. Vahala, "Ultralow-threshold Raman laser using a spherical dielectric microcavity," Nature **415**, 621–623 (2002).

[19] T. J. Kippenberg, S. M. Spillane, D. K. Armani, and K. J. Vahala, "Ultralow-threshold microcavity Raman laser on a microelectronic chip," Opt. Lett. **29**, 1224–1226 (2004).

[20] B. Min, T. J. Kippenberg, and K. J. Vahala, "Compact, fiber-compatible, cascaded Raman laser," Opt. Lett. **28**, 1507–1509 (2003).

[21] T. J. Kippenberg, S. M. Spillane, and K. J. Vahala, "Kerr-Nonlinearity Optical Parametric Oscillation in an Ultrahigh-Q Toroid Microcavity," Phys. Rev. Lett. **93**, 083 904 (2004).

[22] T. J. Kippenberg, H. Rokhsari, T. Carmon, A. Scherer, and K. J. Vahala, "Analysis of Radiation-Pressure Induced Mechanical Oscillation of an Optical Microcavity," Phys. Rev. Lett. **95**, 033 901 (2005).

[23] H. Rokhsari, T. J. Kippenberg, T. Carmon, and K. J. Vahala, "Radiation-pressure-driven micro-mechanical oscillator," Optics Express **13**, 5293 (2005).

[24] V. R. Almeida and M. Lipson, "Optical bistability on a silicon chip," Opt. Lett. **29**, 2387–2389 (2004).

[25] P. E. Barclay, K. Srinivasan, and O. Painter, "Nonlinear response of silicon photonic crystal microresonators excited via an integrated waveguide and a fiber taper," Opt. Expr. **13**, 801–820 (2005).

[26] M. Notomi, A. Shinya, S. Mitsugi, G. Kira, E. Kuramochi, and T. Tanabe, "Optical bistable switching action of Si high-Q photonic-crystal nanocavities," Opt. Expr. **13**, 2678–2687 (2005).

[27] C. J. Hood, T. W. Lynn, A. C. Doherty, A. S. Parkins, and . H. J. Kimble, "The Atom-Cavity Microscope: Single Atoms Bound in Orbit by Single Photons," Science **287**, 1447–1453 (2000).

[28] P. W. H. Pinkse, T. Fischer, P. Maunz, and G. Rempe, "Trapping an atom with single photons," Nature **404**, 365–368 (2000).

[29] T. Aoki, B. Dayan, E. Wilcut, W. P. Bowen, A. S. Parkins, T. J. Kippenberg, K. J. Vahala, and H. J. Kimble, "Observation of strong coupling between one atom and a monolithic microresonator," Nature **443**, 671–674 (2006).

[30] T. Yoshie, A. Scherer, J. Hendrickson, G. Khitrova, H. Gibbs, G. Rupper, C. Ell, O. Shchekin, and D. Deppe, "Vacuum Rabi splitting with a single quantum dot in a photonic crystal nanocavity," Nature **432**, 200–203 (2004).

[31] J. Reithmaier, G. Sek, A. Loffler, C. Hofmann, S. Kuhn, S. Reitzenstein, L. Keldysh, V. Kulakovskii, and T. Reinecke, "Strong coupling in a single quantum dot-semiconductor microcavity system," Nature **432**, 197–200 (2004).

[32] E. Peter, P. Senellart, D. Martrou, A. Lemaitre, and J. Bloch, "Exciton photon strong-coupling regime for a single quantum dot in a microcavity," quant-ph/0411076 (2004).

[33] K. Hennessy, A. Badolato, M. Winger, D. Gerace, M. Atature, S. Gulde, S. Faelt, E. L. Hu, and A. Imamoglu, “Quantum nature of a strongly coupled single quantum dot-cavity system,” Nature **455**, 896–899 (2007).

[34] J. McKeever, A. Boca, A. D. Boozer, R. Miller, J. R. Buck, A. Kuzmich, and H. J. Kimble, “Deterministic Generation of Single Photons from One Atom Trapped in a Cavity,” Science **303**, 1992–1994 (2004).

[35] M. Hijlkema, B. Weber, H. P. Specht, S. C. Webster, A. Kuhn, and G. Rempe, “A single-photon server with just one atom,” Nat. Phys. **3**, 253–255 (2007).

[36] M. Pelton, C. Santori, J. Vuckovic, B. Zhang, G. Solomon, J. Plant, and Y. Yamamoto, “An Efficient Source of Single Photons: A Single Quantum Dot in a Micropost Microcavity,” Phys. Rev. Lett. **89**, 299 602 (2002).

[37] C. Santori, D. Fattal, J. Vučković, G. S. Solomon, and Y. Yamamoto, “Indistinguishable photons from a single-photon device,” Nature **419**, 594–597 (2002).

[38] J. I. Cirac, P. Zoller, H. J. Kimble, and H. Mabuchi, “Quantum State Transfer and Entanglement Distribution among Distant Nodes in a Quantum Network,” Phys. Rev. Lett. **78**, 3221–3224 (1997).

[39] A. D. Boozer, A. Boca, R. Miller, T. E. Northup, and H. J. Kimble, “Reversible state transfer between light and a single trapped atom,” /quant-ph/0702248 (2007).

[40] T. A. Birks and Y. W. Li, “The shape of fiber tapers,” J. Lightwave Tech. **10**, 432–438 (1992).

[41] R. P. Kenny, T. A. Birks, and K. P. Oakley, “Control of optical fibre taper shape,” IEE Elec. Lett. **27**, 1654–1656 (1991).

[42] J. Knight, G. Cheung, F. Jacques, and T. Birks, “Phase-matched excitation of whispering-gallery-mode resonances by a fiber taper,” Opt. Lett. **22**, 1129–1131 (1997).

[43] M. Cai, O. Painter, and K. Vahala, “Observation of critical coupling in a fiber taper to a silica-microsphere whispering-gallery mode system,” Phys. Rev. Lett. **85**, 74–77 (2000).

[44] M. Borselli, K. Srinivasan, P. E. Barclay, and O. Painter, “Rayleigh scattering, mode coupling, and optical loss in silicon microdisks,” Appl. Phys. Lett. **85**, 3693–3695 (2004).

[45] C. P. Michael, M. Borselli, T. J. Johnson, C. Chrystala, and O. Painter, “An optical fiber-taper probe for wafer-scale microphotonic device characterization,” Opt. Expr. **15**, 4745–4752 (2007).

[46] P. E. Barclay, K. Srinivasan, M. Borselli, and O. Painter, “Experimental demonstration of evanescent coupling from optical fibre tapers to photonic crystal waveguides,” IEE Elec. Lett. **39**, 842–844 (2003).

[47] P. E. Barclay, K. Srinivasan, M. Borselli, and O. Painter, “Probing the dispersive and spatial properties of planar photonic crystal waveguide modes via highly efficient coupling from optical fiber tapers,” Appl. Phys. Lett. **85**, 4–6 (2004).

[48] P. E. Barclay, K. Srinivasan, M. Borselli, and O. Painter, “Efficient input and output optical fiber coupling to a photonic crystal waveguide,” Opt. Lett. **29**, 697–699 (2004).

[49] V. R. Almeida, R. R. Panepucci, and M. Lipson, “Nanotaper for compact mode conversion,” Opt. Lett. **28**, 1302–1304 (2003).

[50] J. Reichel, “Microchip traps and Bose-Einstein condensation,” Appl. Phys. B **74**, 469–487 (2002).

[51] R. Folman, P. Krüger, J. Schmiedmayer, J. Denschlag, and C. Henkel, “Microscopic atom optics: From wires to an atom chip,” Ad. Mod. Phys. **48**, 263 (2002).

[52] M. Lončar, D. Nedeljković, T. Doll, J. Vučković, A. Scherer, and T. P. Pearsall, “Waveguiding in planar photonic crystals,” Appl. Phys. Lett. **77**, 1937–1939 (2000).

[53] M. Notomi, A. Shinya, K. Yamada, J. Takahashi, C. Takahashi, and I. Yokohama, “Structural Tuning of Guiding Modes of Line-Defect Waveguides of Silicon-on-Insulator Photonic Crystal Slabs,” IEEE J. Quan. Elec. **38**, 736–742 (2002).

[54] Y. Xu, R. K. Lee, and A. Yariv, “Adiabatic coupling between conventional dielectric waveguides and waveguide with discrete translational symmetry,” Opt. Lett. **25**, 755–757 (2000).

[55] A. Mekis and J. D. Joannopoulos, “Tapered Couplers for Efficient Interfacing Between Dielectric and Photonic Crystal Waveguides,” J. Lightwave Tech. **19**, 861–865 (2001).

[56] S. G. Johnson, P. Bienstman, M. A. Skorobogatiy, M. Ibanescu, E. Lidorikis, and J. D. Joannopoulos, “The adiabatic theorem and a continuous coupled-mode theory for efficient taper transitions in photonic crystals,” Phys. Rev. E **66**, 066 608 (2002).

[57] O. Mitomi, K. Kasaya, and H. Miyazawa, “Design of a Single-Mode Tapered Waveguide for Low-Loss Chip-to-Fiber Coupling,” IEEE J. Quan. Elec. **30**, 1787–1793 (1994).

[58] S. J. McNab, N. Moll, and Y. A. Vlasov, “Ultra-low loss photonic integrated circuit with membrane-type photonic crystal waveguides,” Opt. Expr. **11**, 2927–2939 (2003).

[59] W. Bogaerts, D. Taillaert, B. Luyssaert, P. Dumon, J. V. Campenhout, P. Bienstman, R. Baets, V. Wiaux, and S. Beckx, “Basic structures for photonic integrated circuits in silicon-on-insulator,” Opt. Expr. **12**, 1583–1591 (2004).

[60] A. R. Cowan, G. W. Rieger, and J. F. Young, “Nonlinear transmission of 1.5 m pulses through single-mode silicon-on-insulator waveguide structures,” Opt. Expr. **12**, 1611–1621 (2004).

[61] M. Cai, O. Painter, and K. Vahala, “Observation of critical coupling in a fiber taper to a silica-microsphere whispering-gallery mode system,” Phys. Rev. Lett. **85**, 74–77 (2000).

[62] J. Knight, N. Dubreuil, V. Sandoghdar, J. Hare, V. Lefèvre-Seguin, J. M. Raimond, and S. Haroche, “Characterizing whispering-gallery modes in microspheres by direct observation of the optical standing-wave pattern in the near field,” Opt. Lett. **21**, 698–700 (1996).

[63] P. E. Barclay, K. Srinivasan, and O. Painter, “Design of photonic crystal waveguides for evanescent coupling to optical fiber tapers and integration with high-Q cavities,” J. Opt. Soc. Am. B **20**, 2274–2284 (2003).

[64] J. C. Slater, *Microwave Electronics* (Dover, New York, NY, 1969).

[65] W.-P. Huang, “Coupled-mode theory for optical waveguides: and overview,” J. Opt. Soc. Am. A **11**, 963–983 (1994).

[66] C. M. de Sterke, D. G. Salinas, and J. E. Sipe, “Coupled-mode theory for light propagation through deep nonlinear gratings,” Phys. Rev. E **54**, 1969–1989 (1996).

[67] N. A. R. Bhat and J. E. Sipe, “Optical pulse propagation in nonlinear photonic crystals,” Phys. Rev. E **64**, 056 604–056 604 (2001).

[68] S. Mookherjea and A. Yariv, “Second-harmonic generation with pulses in a coupled-resonator optical waveguide,” Phys. Rev. E **65**, 026 607–026 607 (2002).

[69] K. Sakoda, *Optical Properties of Photonic Crystals* (Springer, New York, NY, 2001).

[70] A. A. Barybin and V. A. Dmitriev, *Modern Electrodynamics and Coupled-Mode Theory* (Rinton Press, Princeton, NJ, 2002).

[71] H. A. Haus, W. P. Huang, and A. W. Snyder, “Coupled-mode formulations,” Opt. Lett. **14**, 1222–1224 (1989).

[72] A. W. Snyder and J. D. Love, *Optical Waveguide Theory* (Chapman and Hall, New York, NY, 1983).

[73] W. P. Huang and H. A. Haus, “Power Exchange in Grating-Assisted Couplers,” J. Lightwave Tech. **7**, 920–924 (1989).

[74] P. Paddon and J. F. Young, “Two-dimensional vector-coupled-mode theory for textured planar waveguides,” Phys. Rev. B **61**, 2090–2101 (2000).

[75] H.-Y. Ryu, S.-H. Kim, H.-G. Park, J.-K. Hwang, Y.-H. Lee, and J.-S. Kim, “Square-lattice photonic band-gap single-cell laser operating in the lowest-order whispering gallery mode,” Appl. Phys. Lett. **80**, 3883–3885 (2002).

[76] K. Srinivasan and O. Painter, “Momentum Space Design of High-Q Photonic Crystal Nanocavities in Two-Dimensional Slab Waveguides,” Opt. Expr. **10**, 670–684 (2002).

[77] S. Kawakami, “Analytically Solvable Model of Photonic Crystal Structures and Novel Phenomena,” J. Lightwave Tech. **20**, 1644–1650 (2002).

[78] P. Yeh and H. F. Taylor, "Contradirectional frequency-selectice couplers for guided-wave optics," Appl. Opt. **19**, 2848–2855 (1980).

[79] P. R. Villeneuve, S. Fan, and J. D. Joannopoulos, "Microcavities in photonic crystals: Mode symmetry, tunability, and coupling efficiency," Phys. Rev. B **54**, 7837–7842 (1996).

[80] J. D. Joannopoulos, R. D. Meade, and J. N. Winn, *Photonic Crystals* (Princeton University Press, Princeton, New Jersey, 1995).

[81] J. S. Foresi, P. R. Villeneuve, J. Ferrera, E. R. Thoen, G. Steinmeyer, S. Fan, J. D. Joannopoulos, L. C. Kimerling, H. I. Smith, and E. P. Ippen, "Photonic-Bandgap microcavities in optical waveguides," Nature **390**, 143–145 (1997).

[82] S. Y. Lin, E. Chow, S. G. Johnson, and J. D. Joannopoulos, "Direct measurement of the quality factor in a two-dimensional photonic crystal microcavity," Opt. Lett. **26**, 1903–1905 (2001).

[83] S. Noda, A. Chutinan, and M. Imada, "Trapping and emission of photons by a single defect in a photonic bandgap structure," Nature **407**, 608–610 (2000).

[84] S. M. Spillane, T. J. Kippenberg, O. J. Painter, and K. J. Vahala, "Ideality in a Fiber-Taper-Coupled Microresonator System for Application to Cavity Quantum Electrodynamics," Phys. Rev. Lett. **91**, 043 902 (2003).

[85] M. Borselli, *High-Q Microresonators as Lasing Elements for Silicon Photonics*, Ph.D. thesis, California Institute of Technology (2006).

[86] I.-K. Hwang, S.-K. Kim, J.-K. Yang, S.-H. Kim, S. H. Lee, and Y.-H. Lee, "Curved-microfiber photon coupling for photonic crystal light emitter," Appl. Phys. Lett. **87**, 131 107 (2005).

[87] C. Grillet, C. Smith, D. Freeman, S. M. B. Luther-Davies, E. Magi, D. Moss, and B. Eggleton, "Efficient coupling to chalcogenide glass photonic crystal waveguides via silica optical fiber nanowires," Opt. Expr. **14**, 1070–1078 (2006).

[88] K. Srinivasan, *Semiconductor optical microcavities for chip-based cavity QED*, Ph.D. thesis, California Institute of Technology (2006).

[89] H. A. Haus, *Waves and Fields in Optoelectronics*, Prentice-Hall Series in Solid State Physical Electronics (Prentice-Hall, Englewood Cliffs, NJ, 1984).

[90] T. Tanabe, M.Notomi, S. Mitsugi, A. S. A, and E. Kuramochi, “Fast bistable all-optical switch and memory on a silicon photonic crystal on-chip,” Opt. Lett. **30**, 2575–2577 (2005).

[91] T. Uesugi, B. S. Song, T. Asano, and S. Noda, “Investigation of optical nonlinearities in an ultra-high-Q Si nanocavity in a two-dimensional photonic crystal slab,” Opt. Expr. **14**, 377–386 (2006).

[92] Y. T. Y, H. Kawashima, N. Ikeda, Y. Sugimoto, H. Kuwatsuka, T. Hasama, and H. Ishikawa, “Optical bistable operations in AlGaAs-based photonic crystal slab microcavity at telecommunication wavelengths,” IEEE Photonics Tech. Lett. **18**, 1996–1998 (2006).

[93] S. F. Preble, Q. Xu, B. S. Schmidt, and M. Lipson, “Ultrafast all-optical modulation on a silicon chip,” Opt. Lett. **30**, 2891–2893 (2005).

[94] O. Boyraz and B. Jalali, “Demonstration of directly modulated silicon Raman laser,” Opt. Expr. **13**, 796–800 (2005).

[95] H. Rong, Y.-H. Kuo, A. Liu, M. Paniccia, and O. Cohen, “High efficiency wavelength conversion of 10 Gb/s data in silicon waveguides,” Opt. Expr. **14**, 1182–1188 (2006).

[96] M. Dinu, F. Quochi, and H. Garcia, “Third-order nonlinearities in silicon at telecom wavelengths,” Appl. Phys. Lett. **82**, 2954–2956 (2003).

[97] T. Liang and H. Tsang, “Role of free carriers from two photon absorption in Raman amplification in silion-on-insulator waveguides,” Appl. Phys. Lett. **84**, 2745–2757 (2004).

[98] K. Kanamoto, S. Lan, N. Ikeda, Y. Tanaka, Y. Sugimoto, K. Asakawa, and H. Ishikawa, “Single Photonic-Crystal Defect Switch for All-Optical Ultrafast Operation Using Two Photon Absorption,” IEICE Trans. Electron. **E87-C**, 1142–1146 (2004).

[99] H. W. Tan, H. M. van Driel, S. L. Schweizer, R. B. Wehrspohn, and U. Gösele, "Nonlinear optical tuning of a two-dimensional silicon photonic crystal," Phys. Rev. B **70**, 205 110 (2004).

[100] G. P. Agrawal and N. K. Dutta, *Semiconductor Lasers* (Van Nostrand Reinhold, New York, NY, 1993).

[101] S. G. Johnson, M. Ibanescu, M. A. Skorobogatiy, O. Weisberg, J. D. Joannopoulos, and Y. Fink, "Perturbation theory for Maxwell's equations with shifting material boundaries," Phys. Rev. E **65**, 066 611 (2002).

[102] R. A. Soref and B. R. Bennett, "Electrooptical Effects in Silicon," IEEE J. Quan. Elec. **23**, 123–129 (1987).

[103] V. R. Almeida, C. A. Barrios, R. R. Panepucci, and M. Lipson, "All-optical control of light on a silicon chip," Nature **431**, 1081–1084 (2004).

[104] T. Carmon, L. Yang, and K. J. Vahala, "Dynamical thermal behavior and thermal self-stability of microcavities," Opt. Expr. **12**, 4742–4750 (2004).

[105] R. W. Boyd, *Nonlinear Optics* (Academic Press, San Diego, CA, 2003), 2nd edn.

[106] M. Soljačić, S. G. Johnson, Y. Fink, and J. D. Joannopoulos, "Optimal bistable switching in nonlinear photonic crystals," Phys. Rev. E **66**, 055 601 (2002).

[107] R. Claps, V. Raghunathan, D. Dimitropoulos, and B. Jalali, "Influence of nonlinear absorption on Raman amplification in Silicon waveguides," Opt. Expr. **12**, 2774–2780 (2004).

[108] H. Rong, A. Liu, R. Nicolaescu, M. Paniccia, O. Cohen, and D. Hak, "Raman gain and nonlinear optical absorption measurements in a low-loss silicon waveguide," Appl. Phys. Lett. **85**, 2196–2198 (2004).

[109] H. M. Gibbs, *Optical Bistability: Controlling Light with Light* (Academic Press, Orlando, FL, 1985).

[110] A. Cutolo, M. Iodice, P. Spirito, and L. Zeni, "Silicon Electro-Optic Modulator Based on a Three Terminal Device Integrated in a Low-Loss Single-Mode SOI Waveguide," J. Lightwave Tech. **15**, 505–518 (1997).

[111] G. Cocorullo and I. Rendina, “Thermo-optical modulation at 1.5 m in silicon etalon,” IEE Elec. Lett. **28**, 83–85 (1992).

[112] P.-T. Lee, J. R. Cao, S.-J. Choi, Z.-J. Wei, J. O’Brien, and P. D. Dapkus, “Operation of photonic crystal membrane lasers above room temperature,” Appl. Phys. Lett. **81**, 3311–3313 (2002).

[113] M. Notomi, A. Shinya, S. Mitsugi, and H.-Y. Ryu, “Waveguides, resonators and their coupled elements in photonic crystal slabs,” Opt. Expr. **12**, 1551–1561 (2004).

[114] C. P. Michael, K. Srinivasan, T. J. Johnson, O. Painter, K. H. Lee, K. Hennessy, H. Kim, and E. Hu, “Wavelength- and material-dependent absorption in GaAs and AlGaAs microcavities,” Appl. Phys. Lett. **90**, 051 108 (2007).

[115] T. L. Chu, C. H. Lee, and G. A. Gruber, “The Preparation and Properties of Amorphous Silicon Nitride Films,” J. Electrochem. Soc. **114**, 717–722 (1967).

[116] E. A. Taft, “Characterization of Silicon Nitride Films,” J. Electrochem. Soc. **118**, 1341–1346 (1971).

[117] W. Stutius and W. Streifer, “Silicon nitride films on silicon for optical waveguides,” Appl. Opt. **16**, 3218–3222 (1977).

[118] D. P. Poenar and R. F. Wolffenbuttel, “Optical properties of thin-film silicon-compatible materials,” Appl. Opt. **36**, 5122–5128 (1997).

[119] T. Inukai and K. Ono, “Optical Characteristics of Amorphous Silicon Nitride Thin Films Prepared by Electron Cyclotron Resonance Plasma Chemical Vapor Deposition,” Jpn. J. Appl. Phys. **33**, 2593–2598 (1994).

[120] B. E. Little, S. T. Chu, P. P. Absil, J. V. Hryniewicz, F. Seiferth, D. Gill, V. Van, O. King, and M. Traklo, “Very High-Order Microring Resonator Filters for WDM Applications,” IEEE Photonics Tech. Lett. **16**, 2263–2265 (2004).

[121] T. Barwicz, M. A. Popovic, P. T. Rakich, M. R. Watts, H. A. Haus, E. P. Ippen, and H. I. Smith, “Microring-resonator-based add-drop filters in SiN: fabrication and analysis,” Opt. Expr. **12**, 1437–1442 (2004).

[122] M. C. Netti, M. D. B. Charlton, G. J. Parker, and J. J. Baumberg, “Visible photonic band gap engineering in silicon nitride waveguides,” Appl. Phys. Lett. **76**, 991–993 (2000).

[123] C. H. Henry, R. F. Kazarinov, H. J. Lee, K. J. Orlowsky, and L. E. Katz, “Low loss Si3N4 - SiO2 optical waveguides on Si,” Appl. Opt. **26**, 2621–2624 (1987).

[124] N. Daldosso, M. Melchiorri, F. Riboli, M. Girardini, G. Pucker, M. Crivellari, P. Bellutti, A. Lui, , and L. Pavesi, “Comparison Among Various Si3N4 Waveguide Geometries Grown Within a CMOS Fabrication Pilot Line,” IEEE Photonics Tech. Lett. **22**, 1734–1740 (2004).

[125] F. Vollmer, D. Braun, A. Libchaber, M. Khoshsima, I. Teraoka, and S. Arnold, “Protein detection by optical shift of a resonant microcavity,” Appl. Phys. Lett. **80**, 4057–4059 (2002).

[126] A. Ksendzov, M. L. Homer, and A. M. Manfreda, “Integrated optics ring-resonator chemical sensor with polymer transduction layer,” IEE Elec. Lett. **40**, 63 (2004).

[127] J. Yota, J. Hander, and A. A. Saleh, “A comparative study on inductively-coupled plasma high-density plasma, plasma-enhanced, and low pressure chemical vapor deposition silicon nitride films,” J. Vac. S. Tech. A **18**, 372–376 (2000).

[128] M. Borselli, T. J. Johnson, and O. Painter, “Measuring the role of surface chemistry in silicon microphotonics,” Appl. Phys. Lett. **88**, 131 114 (2006).

[129] S. L. McCall, A. F. J. Levi, R. E. Slusher, S. J. Pearton, and R. A. Logan, “Whispering-gallery mode lasers,” Appl. Phys. Lett. **60**, 289–291 (1992).

[130] K. Srinivasan, M. Borselli, T. J. Johnson, P. E. Barclay, O. Painter, A. Stintz, and S. Krishna, “Optical loss and lasing characteristics of high-quality-factor AlGaAs microdisk resonators with embedded quantum dots,” Appl. Phys. Lett. **86**, 151 106 (2005).

[131] S. M. Spillane, T. J. Kippenberg, K. J. Vahala, K. W. Goh, E. Wilcut, and H. J. Kimble, “Ultrahigh-Q toroidal microresonators for cavity quantum electrodynamics,” Phys. Rev. A **71**, 013 817 (2005).

[132] D. A. Steck, "Cesium D Line Data," http://steck.us/alkalidata/ (2003).

[133] G. Davies and M. F. Hamer, "Optical studies of the 1.945 eV vibronic band in diamond," Proc. R. Soc. London. A. **348**, 285–298 (1976).

[134] C. Manolatou, M. J. Khan, S. Fan, P. R. V. nd H. A. Haus, and J. D. Joannopoulos, " Coupling of modes analysis of resonant channel add-drop filters," IEEE J. Quan. Elec. **35**, 1322–1331 (1999).

[135] Y. Xu, Y. Li, R. K. Lee, and A. Yariv, "Scattering-theory analysis of waveguide-resonator coupling," Phys. Rev. E **62**, 7389–7404 (2000).

[136] D. S. Weiss, V. Sandoghdar, J. Hare, V. Lefevreseguin, J. M. Raimond, and S. Haroche, "Splitting of high-Q mie modes induceds by light backscattering in silica microspheres," Opt. Lett. **20**, 1835–1837 (1995).

[137] D. M. Knotter and T. J. J. D. Denteneer, "Etching Mechanism of Silicon Nitride in HF Based Solutions," J. Electrochem. Soc. **148**, F43–F46 (2001).

[138] G. N. Parsons, J. H. Souk, and J. Batey, "Low hydrogen content stoichiometric silicon nitride films deposited by plasma-enhanced chemical vapor deposition," J. Appl. Phys. **70**, 1553 (1991).

[139] S. J. Choi, Z. Peng, Q. Yang, S. J. Choi, and P. D. Dapkus, "An eight-channel demultiplexing switch array using vertically coupled active semiconductor microdisk resonators," IEEE Photonics Tech. Lett. **16**, 2517–2519 (2004).

[140] A. Yariv, Y. Xu, R. K. Lee, and A. Scherer, "Coupled-resonator optical waveguide: a proposal and analysis," Opt. Lett. **24**, 711–713 (1999).

[141] J. E. Heebner and R. W. Boyd, "'Slow' and 'fast' light in resonator-coupled waveguides," J. Mod. Opt. **49**, 2629–2636 (2002).

[142] J. K. S. Poon, J. Scheuer, Y. Xu, and A. Yariv, "Designing coupled-resonator optical waveguide delay lines," J. Opt. Soc. Am. B **21**, 1665–1673 (2004).

[143] Y. Xu, R. K. Lee, and A. Yariv, "Propagation and second-harmonic generation of electromagnetic waves in a coupled-resonator optical waveguide," J. Opt. Soc. Am. B **17**, 387–400 (2000).

[144] S. Mookherjea and A. Yariv, “Coupled Resonator Optical Waveguides,” IEEE J. Sel. Top. Quan. Elec. **8**, 488–456 (2002).

[145] A. Yariv, *Quantum Electronics* (John Wiley & Sons, New York, NY, 1989), 3rd edn.

[146] E. T. Jaynes and F. W. Cummings, “Comparison of quantum and semiclassical radiation theories with application to the beam maser,” Proc. of the IEEE **51**, 89–109 (1963).

[147] E. M. Purcell, “Spontaneous emission probabilities at radio frequencies,” Phys. Rev. **69**, 681 (1946).

[148] A. Gruber, A. Dräbenstedt, C. Tietz, L. Fleury, J. Wratchtrup, and C. v. Borczyskowski, “Scanning confocal optical microscopy and magnetic resonance on single defect centers,” Science **276**, 2012–2014 (1997).

[149] A. Bevaratos, S. Kuhn, R. Brouri, T. Gacoin, J.-P. Poizat, and P. Grangier, “Room temperature stable single-photon source,” Eur. Phys. J. D **18**, 191–196 (2002).

[150] A. T. Collins, M. F. Thomaz, and M. I. B. Jorge, “Luminescence decay time of the 1.945 eV centre in type Ib diamond,” J. Phys. C, Solid State Phys. **16**, 2177–2181 (1992).

[151] P. Tamarat, T. Gaebel, J. R. Rabeau, M. Khan, A. D. Greentree, H. Wilson, L. C. L. Hollenberg, S. Prawer, P. Hemmer, F. Jelezko, and J. Wrachtrup, “Stark Shift Control of Single Optical Centers in Diamond,” Phys. Rev. Lett. **97**, 083 002 (2006).

[152] J. Reichel, W. Hänsel, P. Hommelhoff, and T. Hänsch, “Applications of integrated magnetic microtraps,” Appl. Phys. B **72**, 81–89 (2001).

[153] B. Lev, “Fabrication of micro-magnetic traps for cold neutral atoms,” Quantum Information and Computation **3**, 450–464 (2003).

[154] J. D. Weinstein and K. G. Libbrecht, “Microscopic magnetic traps for neutral atoms,” Phys. Rev. A **52**, 4004–4009 (1995).

[155] J. Reichel, W. Hänsel, and T. W. Hänsch, “Atomic Micromanipulation with Magnetic Surface Traps,” Phys. Rev. Lett. **83**, 3398–3401 (1999).

[156] N. H. Dekker, C. S. Lee, V. Lorent, J. H. Thywissen, S. P. Smith, M. Drndić, R. M. Westervelt, and M. Prentiss, "Guiding Neutral Atoms on a Chip," Phys. Rev. Lett. **84**, 1124–1127 (2000).

[157] R. Folman, P. Krüger, D. Cassettari, B. Hessmo, T. Maier, and J. Schmiedmayer, "Controlling Cold Atoms using Nanofabricated Surfaces: Atom Chips," Phys. Rev. Lett. **84**, 4749–4752 (2000).

[158] W. H. P. Hommelhoff, T. Hänsch, and J. Reichel, " Bose-Einstein condensation on a microelectronic chip," Nature **413**, 498–501 (2001).

[159] H. Ott, J. Fortagh, G. Schlotterbeck, A. Grossmann, and C. Zimmermann, "Bose-Einstein Condensation in a Surface Microtrap," Phys. Rev. Lett. **87**, 230 401 (2001).

[160] S. Aubin, S. Myrskog, M. H. T. Extavour, L. J. Leblanc, D. Mckay, A. Stummer, and J. H. Thysissen, "Rapid sympathetic cooling to Fermi degeneracy on a chip," Nat. Phys. **2**, 384–387 (2006).

[161] S. Du, M. B. Squires, Y. Imai, L. Czaia, R. A. Saravanan, V. Bright, J. Reichel, T. W. Hansch, and D. Z. Anderson, "Atom-chip Bose-Einstein condensation in a portable vacuum cell," Phys. Rev. A **70**, 053 606 (2004).

[162] H. Ott, J. Fortágh, S. Kraft, A. Günther, D. Komma, and C. Zimmermann, "Nonlinear Dynamics of a Bose-Einstein Condensate in a Magnetic Waveguide," Phys. Rev. Lett. **91**, 040 402 (2003).

[163] W. Hänsel, J. Reichel, P. Hommelhoff, and T. W. Hänsch, "Magnetic Conveyor Belt for Transporting and Merging Trapped Atom Clouds," Phys. Rev. Lett. **86**, 608–611 (2001).

[164] Y. Shin, C. Sanner, G.-B. Jo, T. A. Pasquini, M. Saba, W. Ketterle, D. E. Pritchard, M. Vengalattore, and M. Prentiss, "Interference of Bose-Einstein condensates split with an atom chip," Phys. Rev. A **72**, 021 604 (2005).

[165] Y.-J. Wang, D. Z. Anderson, V. M. Bright, E. A. Cornell, Q. Diot, T. Kishimoto, M. Prentiss, R. A. Saravanan, S. R. Segal, and S. Wu, "Atom Michelson Interferometer on a Chip Using a Bose-Einstein Condensate," Phys. Rev. Lett. **94**, 090 405 (2005).

[166] T. Schumm, S. Hofferberth, L. M. Andersson, S. Wildermuth, S. Groth, I. Bar-Joseph, J. Schmiedmayer, and P. Krger, "Matter-wave interferometry in a double well on an atom chip," Nat. Phys. **1**, 28–34 (2005).

[167] G.-B. Jo, Y. Shin, S. Will, T. A. Pasquini, M. Saba, W. Ketterle, D. E. Pritchard, M. Vengalattore, and M. Prentiss, "Long Phase Coherence Time and Number Squeezing of Two Bose-Einstein Condensates on an Atom Chip," Phys. Rev. Lett. **98**, 030 407 (2007).

[168] H. Mabuchi and H. J. Kimble, "Atom galleries for whispering atoms: binding atoms in stable orbits around an optical resonator," Opt. Lett. **19**, 749–751 (1994).

[169] P. Horak, B. G. Klappauf, A. Haase, R. Folman, J. Schmiedmayer, P. Domokos, and E. A. Hinds, "Towards single-atom detection on a chip," Phys. Rev. A **67**, 043 806 (2003).

[170] M. Rosenblit, P. Horak, S. Helsby, and R. Folman, "Single-atom detection using whispering-gallery modes of microdisk resonators," Phys. Rev. A **70**, 053 808 (2004).

[171] M. Rosenblit, Y. Japha, P. Horak, and R. Folman, "Simultaneous optical trapping and detection of atoms by microdisk resonators," Phys. Rev. A **73**, 063 805 (2006).

[172] S. Eriksson, M. Trupke, H. F. Powell, D. Sahagun, C. D. J. Sinclair, E. A. Curtis, B. E. Sauer, E. A. Hinds, Z. Moktadir, C. O. Gollasch, and M. Kraft, "Integrated optical components on atom chips," Eur. Phys. J. D **35**, 135–139 (2005).

[173] B. Lev, K. Srinivasan, P. E. Barclay, O. Painter, and H. Mabuchi, "Feasibility of detecting single atoms using photonic bandgap cavities," Nanotechnology **15**, S556–S561 (2004).

[174] A. Haase, B. Hessmo, and J. Schmiedmayer, "Detecting magnetically guide atoms with an optical cavity," Opt. Lett. **31**, 268–270 (2006).

[175] T. Steinmetz, Y. Colombe, D. Hunger, T. W. Hänsch, A. Balocchi, R. J. Warburton, and J. Reichel, "Stable fiber-based Fabry-Pérot cavity," Appl. Phys. Lett. **89**, 111 110 (2006).

[176] H. Mabuchi, Q. A. Tuchette, M. S. Chapman, and H. J. Kimble, “Real-time detection of individual atoms falling through a high-finesse optical cavity,” Opt. Lett. **21**, 1393–1395 (1996).

[177] K. M. Birnbaum, A. Boca, R. Miller, A. D. Boozer, T. E. Northup, and H. J. Kimble, “Photon blockade in an optical cavity with one trapped atom,” Nature **436**, 87–90 (2005).

[178] S. Nussmann, M. Hijlkema, B. Weber, F. Rohde, G. Rempe, and A. Kuhn, “Submicron Positioning of Single Atoms in a Microcavity,” Phys. Rev. Lett. **95**, 173 602 (2005).

[179] S. Nussmann, K. Murr, M. Hijlkema, B. Weber, A. Kuhn, and G. Rempe, “Vacuum-stimulated cooling of single atoms in three dimensions,” Nat. Phys. **1**, 122–125 (2005).

[180] B. Lev, *Magnetic microtraps for cavity QED, Bose-Einstein condensates, and atom optics*, Ph.D. thesis, California Institute of Technology (2005).

[181] K. Srinivasan and O. Painter, “Optical fiber taper coupling and high-resolution wavelength tuning of microdisk resonators at cryogenic temperatures,” Appl. Phys. Lett. **90**, 031 114 (2007).

[182] R. I. Abraham and E. A. Cornell, “Teflon feedthrough for coupling optical fibers into ultrahigh vacuum systems,” Appl. Opt. **37**, 1762–1763 (1998).

[183] R. G. Palmer, D. L. Stein, E. Abrahams, and P. W. Anderson, “Models of Hierachically Constrained Dynamics for Glassy Relaxation,” Phys. Rev. Lett. **53**, 958–961 (1984).

[184] M. Brause, D. Ochs, J. Günster, T. Mayer, B. Braun, V. Puchin, W. Maus-Friedrichs, and V. Kempter, “Cs adsorption on oxide films (Al_2O_3, MgO, SiO_2),” Surf. Sci. **383**, 216–225 (1997).

[185] S. Mosor, J. Hendrickson, B. C. Richards, J. Sweet, G. Khitrova, H. M. Gibbs, T. Yoshie, A. Scherer, O. B. Shchekin, and D. G. Deppe, “Scanning a photonic crystal slab nanocavity by condensation of xenon,” Appl. Phys. Lett. **87**, 141 105 (2005).

[186] K. Srinivasan and O. Painter, "Optical fiber taper coupling and high-resolution wavelength tuning of microdisk resonators at cryogenic temperatures," Appl. Phys. Lett. **90**, 031 114 (2007).

[187] K. M. Birnbaum, *Cavity QED with Multilevel Atoms*, Ph.D. thesis, California Institute of Technology (2005).

[188] S. Ghosh, A. R. Bhagwat, C. K. Renshaw, S. Goh, A. L. Gaeta, and B. J. Kirby, "Low-Light-Level Optical Interactions with Rubidium Vapor in a Photonic Band-Gap Fiber," Phys. Rev. Lett. **97**, 023 603 (2006).

[189] H. J. Metcalf and P. van der Straten, *Laser cooling and trapping* (Springer, New York, 1999).

[190] N. Schlosser, G. Reymond, I. Protsenko, and P. Grangier, "Sub-poissonian loading of single atoms in a microscopic dipole trap," Nature **411**, 1024–1027 (2001).

[191] J. McKeever, J. R. Buck, A. D. Boozer, A. Kuzmich, H.-C. Nägerl, D. M. Stamper-Kurn, and H. J. Kimble, "State-Insensitive Cooling and Trapping of Single Atoms in an Optical Cavity," Phys. Rev. Lett. **90**, 133 602 (2003).

[192] M. Trupke, E. A. Hinds, S. Eriksson, E. A. Curtis, Z. Moktadir, E. Kukharenka, and M. Kraft, "Microfabricated high-finesse optical cavity with open access and small volume," Appl. Phys. Lett. **87**, 211 106 (2005).

[193] C. J. Hood, M. S. Chapman, T. W. Lynn, and H. J. Kimble, "Real-Time Cavity QED with Single Atoms," Phys. Rev. Lett. **80**, 4157–4160 (1998).

[194] H. Carmichael, *An Open Systems Approach to Quantum Optics*, Lecture Notes in Physics (Springer-Verlag, Berlin Heidelberg, 1993).

[195] L. A. Lugiato, *Progress in Optics* (North-Holland, Amsterdam, 1984), Vol. XXI, chap. Theory of Optical Bistability.

[196] M. A. Armen and H. Mabuchi, "Low-lying bifurcations in cavity quantum electrodynamics," Phys. Rev. A **73**, 063 801 (2006).

[197] S. M. Tan, "A computational toolbox for quantum and atomic optics," J. Opt. B **1**, 424–432 (1999).

[198] K. Srinivasan and O. Painter, "Mode coupling and cavity–quantum-dot interactions in a fiber-coupled microdisk cavity," Phys. Rev. A **75**, 023 814 (2007).

[199] H. J. Carmichael, "Quantum trajectory theory for cascaded open systems," Phys. Rev. Lett. **70**, 2273–2276 (1993).

[200] L. Tian and H. J. Carmichael, "Quantum trajectory simulations of two-state behavior in an optical cavity containing one atom," Phys. Rev. A **46**, R6801–R6804 (1992).

[201] K. Mølmer, Y. Castin, and J. Dalibard, "Monte Carlo wave-function method in quantum optics," J. Opt. Soc. Am. B **10**, 524–538 (1993).

[202] R. J. McIntyre, "Multiplication noise in uniform avalanche diodes," IEEE Trans. Electon Devices **ED-13**, 164–168 (1966).

[203] B. E. A. Saleh and M. C. Teich, *Fundamentals of Photonics* (Wiley-Interscience, New York, NY, 1991).

[204] S. G. Johnson, P. R. Villeneuve, S. Fan, and J. D. Joannopoulos, "Linear waveguides in photonic-crystal slabs," Phys. Rev. B **62**, 8212–8222 (2000).

[205] N. W. Ashcroft and N. D. Mermin, *Solid State Physics* (Saunders College Publishing, New York, NY, 1976).

[206] J. D. Jackson, *Classical Electrodynamics* (John Wiley & Sons, Inc., New York, NY, 1975), 2nd edn.

[207] V. V. Klimov and M. Ducloy, "Spontaneous emission rate of an excited atom placed near a nanofiber," Phys. Rev. A **69**, 013 812 (2004).

[208] T. Søndergaard and B. Tromborg, "General theory for spontaneous emission in active dielectric microstructures: Example of a fiber amplifier," Phys. Rev. A **64**, 033 812 (2001).